AL/OE-SR-1996-0003

RADIO FREQUENCY RADIATION DOSIMETRY WORKSHOP: PRESENT STATUS AND RECOMMENDATIONS FOR FUTURE RESEARCH

William D. Hurt

OCCUPATIONAL AND ENVIRONMENTAL HEALTH DIRECTORATE RADIOFREQUENCY RADIATION DIVISION
8305 Hawks Road
Brooks Air Force Base, Texas 78235-5324

June 1996

Final Technical Report for Period March 1992 to July 1993

19960617 127 ɔTIC QUALITY INSPECTED 1

AIR FORCE MATERIEL COMMAND
BROOKS AIR FORCE BASE, TEXAS

ARMSTRONG LABORATORY

DISCLAIMER NOTICE

UNCLASSIFIED

Technical Report
distributed by

DEFENSE
TECHNICAL
INFORMATION
CENTER

DTIC

UNCLASSIFIED

THIS DOCUMENT IS BEST
QUALITY AVAILABLE. THE
COPY FURNISHED TO DTIC
CONTAINED A SIGNIFICANT
NUMBER OF PAGES WHICH DO
NOT REPRODUCE LEGIBLY.

NOTICES

This report is published as received and has not been edited by the staff of the Occupational and Environmental Health Directorate.

Publication of this report does not constitute approval or disapproval of the ideas or findings. It is published in the interest of scientific and technical information (STINFO) exchange.

When Government drawings, specifications, or other data are used for any purpose other than in connection with a definitely Government-related procurement, the United States Government incurs no responsibility or any obligation whatsoever. The fact that the Government may have formulated or in any way supplied the said drawings, specifications, or other data, is not to be regarded by implication, or otherwise in any manner construed, as licensing the holder or any other person or corporation; or as conveying any rights or permission to manufacture, use, or sell any patented inven-tion that may in any way be related thereto.
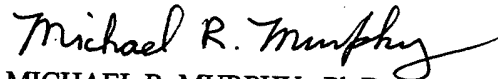
The Office of Public Affairs has reviewed this report, and it is releasable to the National Technical Information Service, where it will be available to the general public, including foreign nationals.

This report has been reviewed and is approved for publication.

Government agencies and their contractors registered with DefenseTechnical Information Center (DTIC) should direct requests for copies to: Defense Technical Information Center, 8725 John J. Kingman Rd., STE 0944, Ft. Belvoir, VA 22060-6218.

Non-Government agencies may purchase copies of this report from: National Technical Information Services (NTIS), 5285 Port Royal Road, Springfield, VA 22161-2103.

WILLIAM D. HURT
Project Scientist

MICHAEL R. MURPHY, Ph.D.
Chief, Radiofrequency Radiation
Division

REPORT DOCUMENTATION PAGE

Public reporting burden for this collection of information is estimated to average 1 hour per response, including the time for reviewing instructions, searching existing data sources, gathering and maintaining the data needed, and completing and reviewing the collection of information. Send comments regarding this burden estimate or any other aspect of this collection of information, including suggestions for reducing this burden, to Washington Headquarters Services, Directorate for Information Operations and Reports, 1215 Jefferson Davis Highway, Suite 1204, Arlington, VA 22202-4302, and to the Office of Management and Budget, Paperwork Reduction Project (0704-0188), Washington, DC 20503.

1. AGENCY USE ONLY (Leave blank)	2. REPORT DATE June 1996	3. REPORT TYPE AND DATES COVERED Final, March 1992 to July 1993

4. TITLE AND SUBTITLE

Radio Frequency Radiation Dosimetry Workshop: Present Status and Recommendations for Future Research

5. FUNDING NUMBERS

C - F33615-90-D-0606-Task 0010
PE - 62202F
PR - 7757
TA - 01
WU - 2L

6. AUTHOR(S)

William D. Hurt

7. PERFORMING ORGANIZATION NAME(S) AND ADDRESS(ES)

AL/OERS
8305 Hawks Road
Brooks AFB, TX 78235-5324

AUSA
18985 Tuggle Avenue
Cupertino, CA 95014-3658

8. PERFORMING ORGANIZATION

9. SPONSORING/MONITORING AGENCY NAME(S) AND ADDRESS(ES)

Armstrong Laboratory (AFMC)
Occupational and Evironmental Health Directorate
Radiofrequency Radiation Division
8305 Hawks Road
Brooks Air Force Base, TX 78235-5324

10. SPONSORING/MONITORING

AL/OE-SR-1996-0003

11. SUPPLEMENTARY NOTES

Armstrong Laboratoary Technical Monitor: Willliam D. Hurt, (210) 536-3167

12a. DISTRIBUTION/AVAILABILITY STATEMENT

Approved for public release; distribution is unlimited.

12b. DISTRIBUTION CODE

13. ABSTRACT *(Maximum 200 words)*
The goal of this project is to advance the state of the art of RFR dosimetry to a level of sophistication where computer graphically generated, high-resolution SAR distributions can be obtained and displayed with anatomical features for any section of the human body. Procedures are to be developed to allow modelling of the realistic exposure conditions for whole-body or partial-body irradiation due to spatially uniform or nonuniform (far-field or near-field) EM fields that are CW, pulsed, or transient in nature. Effects will also be directed at improving thermal models of the human body so that expected temperature distributions due to RFR exposure can be predicted and displayed graphically. Participants have generated recommendations for research in subspecialty areas relevant to the above, such as standard models of humans and animals, graphical display methods, numerical algorithms, validation of computer-generated data, extrapolation of SAR data to thermal physiology, and others.

14. SUBJECT TERMS
Radiation biology (dosimetry and health physics), Thermodynamics, Mathematical models, Numerical algorithms, Computer graphics, Thermal physiology models.

15. NUMBER OF PAGES
246

16. PRICE CODE

17. SECURITY CLASSIFICATION OF REPORT	18. SECURITY CLASSIFICATION OF THIS PAGE	19. SECURITY CLASSIFICATION OF ABSTRACT	20. LIMITATION OF ABSTRACT
Unclassified	Unclassified	Unclassified	UL

Table of Contents

Foreword

The primary objective of this invitational workshop was to provide a basis for further development of radio frequency radiation (RFR) dosimetry to a level of sophistication that would permit graphical displays of computer-generated, high-resolution anatomical distributions of specific absorption rates (SAR) within any section of the human body. Detailed recommendations were made toward development of methods for modeling SAR distributions under realistic conditions of whole-body and/or partial-body exposure to spatially uniform or nonuniform CW, pulsed, or transient RFR. Another objective was directed toward seeking means for improving thermal models of the human body, thereby enabling predictions and graphic displays of temperature distributions within the body due to exposure to RFR. A specific goal of the workshop was to recommend directions toward the development of a widely-accessible-on-line, computer-based dosimetry program to update and supplant the RFR Dosimetry Handbook previously developed under the aegis of the Armstrong Laboratory.

Toward these ends, the participants at the workshop presented the status of their research efforts on RFR dosimetry, and conducted sessions in which specific written recommendations were made regarding future research efforts in relevant subspecialty areas, such as the derivation of standard models of humans and various animal species, graphical display methods, numerical algorithms, validation of computer-generated data, and application of SAR data to thermal physiology. Summarized in this technical report are the in depth deliberations of the workshop participants, for use by the Armstrong Laboratory toward planning future research efforts on this subject.

RFR DOSIMETRY WORKSHOP

AGENDA

MONDAY, DECEMBER 7

Arrival at The Crockett Hotel. Cash Bar, Green Room, 6 p.m. - 7:30 p.m.

TUESDAY, DECEMBER 8

8:00 a.m.   Transportation (arranged by Air Force) from Crockett Hotel Lobby
             to Brooks Air Force Base. We will depart precisely at 8:00 a.m.

8:45 a.m.   D. Erwin, Chief, Radiofrequency Radiation Branch,
             Armstrong Laboratory, Brooks AFB.
             "WELCOME, INTRODUCTION AND REVIEW OF PURPOSE."

9:00 a.m.   C. Durney, "4TH EDITION OF RFR DOSIMETRY HANDBOOK.

9:30 a.m.   C.-K. Chou, "PHANTOMS AND SAR DETERMINATIONS."

10:00 a.m.   Break

10:15 a.m.   O. Gandhi/J. Lee,   "FORMATION OF STANDARD MODELS OF HUMANS AND
                  ANIMALS VIA HIGH-RESOLUTION MRI."

10:45 a.m.   W. Hurt, "OVERVIEW OF TISSUE PROPERTIES AND RFR DOSIMETRY."

11:15 a.m.   A. Taflove, "OVERVIEW OF FINITE-DIFFERENCE TIME-DOMAIN
                  TECHNIQUES."

11:45 a.m.   M. Hagmann, "PRACTICAL LIMITS ON THEORETICAL DOSIMETRY."

12 noon   Lunch at Officers' Club.

1:00 p.m.   O. Gandhi, "SOME RECENT APPLICATIONS OF FDTD FOR EM DOSIMETRY:
                  ELF TO MICROWAVE FREQUENCIES."

1:30 p.m.   R. Albanese/J. Blaschak/P. Petropoulos, "NUMERICAL ERROR AND
                  ELECTROMAGNETIC COMPUTATION."

2:00 p.m.   E. Adair/E. Wissler, "REVIEW OF THERMOPHYSIOLOGICAL MODELS."

2:30 p.m.   K. Foster, "SAR, BLOOD FLOW, AND TISSUE TEMPERATURE
                  DISTRIBUTION."

3:00 p.m.   Break

3:15 p.m.   O. Gandhi, "DISPLAY OF COMPUTER-GENERATED DOSIMETRY DATA: I."

3:45 p.m.   J. Toler, "DISPLAY OF COMPUTER-GENERATED DOSIMETRY DATA: II."

4:15 p.m.   C. Batishko, "DISPLAY OF MEASURED DOSIMETRY DATA."

5:00 p.m.   Transportation from Brooks AFB to hotel.

TUESDAY (continued)

        Evening free.

WEDNESDAY, DECEMBER 9

8:15 a.m.   Transportation from Crockett Hotel Lobby to Brooks Air Force Base.
<u>We will depart precisely at 8:15 a.m.</u>

9:00 a.m.   FORMATION OF WORKING GROUPS.
WORKING GROUP DELIBERATIONS ON FUTURE RESEARCH DIRECTIONS.
PREPARATION OF WRITTEN RECOMMENDATIONS BY WORKING GROUPS.

10:15 a.m.   Break

10:30 a.m.   CONTINUATION OF WORKING GROUP ACTIVITIES.

12 noon   Lunch at Officers' Club.

1:00 p.m.   VERBAL PRESENTATION OF SUMMARIES OF EACH WORKING GROUP.
(EACH GROUP TO APPOINT A RAPPORTEUR)
(APPROXIMATELY 6 GROUPS, 15 MINUTES EACH)

3:00 p.m.   CONCLUSION OF WORKSHOP.
Transportation from Brooks AFB To San Antonio Airport.

RFR DOSIMETRY WORKSHOP

LIST OF PARTICIPANTS

(# INDICATES PRESENTER)

DR. DAVID N. ERWIN #
AL/OEDR
BROOKS AFB, TX 78235-5324
(210) 536-3582
FAX: (210) 536-3945

DR. JOHNATHAN KIEL
AL/OEDR
BROOKS AFB, TX 78235-5324
(210) 536-3583
FAX: (210) 536-3945

PROF. CARL H. DURNEY #
DEPARTMENT OF ELECTRICAL
ENGINEERING
UNIVERSITY OF UTAH
MERRILL ENGINEERING BUILDING
SALT LAKE CITY, UT 84112
(801) 581-5096
FAX: (801) 581-5281

DR. C.-K. CHOU #
DEPARTMENT OF RADIATION RESEARCH
CITY OF HOPE NATIONAL MEDICAL
CENTER
1500 E. DUARTE ROAD
DUARTE, CA 91010
(818) 301-8355
FAX: (818) 357-1929

PROF. OM P. GANDHI #
DEPARTMENT OF ELEC. ENGINEERING
UNIVERSITY OF UTAH
3032 MERRILL ENGINEERING BUILDING
SALT LAKE CITY, UT 84112
(801) 581-7743
FAX: (801) 581-5281

PROF. JAMES N. LEE #
MEDICAL IMAGING RESEARCH
LABORATORY
AC 213 SCHOOL OF MEDICINE
UNIVERSITY OF UTAH
SALT LAKE CITY, UT 84132
(801) 581-4228
FAX: (801) 585-3592

MR. WILLIAM D. HURT   #
AL/OEDR
BROOKS AFB, TX 78235-5301
(210) 536-3185
FAX: (210) 536-3977

PROF. ALLEN TAFLOVE #
DEPARTMENT OF ELECTRICAL
ENGINEERING AND COMPUTER SCIENCE
NORTHWESTERN UNIVERSITY
EVANSTON, IL 60201
(708) 491-4127
FAX: (708) 491-4455

PROF. MARK J. HAGMANN   #
DEPARTMENT OF ELECTRICAL
AND COMPUTER ENGINEERING
FLORIDA INTERNATIONAL UNIVERSITY
MIAMI, FL 33199
(305) 348-3017
FAX: (305) 348-3707

DR. RICHARD ALBANESE   #
AL/OEDA
BROOKS AFB, TX 78235-5301
(210) 536-3884
FAX: (210) 536-3450

DR. JEFFREY BLASCHAK #
AL/OEDA
BROOKS AFB, TX 78235-5301
(210) 536-3884
FAX: (210) 536-3450

DR. PETER PETROPOULOS   #
AL/OEDA
BROOKS AFB, TX 78235-5301
(210) 536-3884
FAX: (210) 536-3450

DR. RICHARD MEDINA
AL/OEDA
BROOKS AFB, TX 78235-5301
(210) 536-3884
FAX: (210) 536-3450

DR. ELEANOR R. ADAIR #
THE JOHN B. PIERCE FOUNDATION
YALE UNIVERSITY
290 CONGRESS AVENUE
NEW HAVEN, CT 06519
(203) 562-9901 x218
FAX: (203) 624-4950

PROF. EUGENE WISSLER #
OFFICE OF GRADUATE STUDIES
MAIN BUILDING 101
UNIVERSITY OF TEXAS AT AUSTIN
AUSTIN, TX 78712
(512) 471-7213
FAX: (512) 471-7620

PROF. KENNETH R. FOSTER #
DEPARTMENT OF BIOENGINEERING
UNIVERSITY OF PENNSYLVANIA
220 S. 33RD STREET
PHILADELPHIA, PA 19104-6392
(215) 898-8534
FAX: (215) 573-2071

MR. JAMES C. TOLER #
BIOENGINEERING CENTER
GEORGIA INSTITUTE OF TECHNOLOGY
OIP/0329
ATLANTA, GA 30332-0130
(404) 894-3964
FAX: (404) 894-7025

DR. WESLEY SHELTON
BIOENGINEERING CENTER
GEORGIA INSTITUTE OF TECHNOLOGY
OIP/0327
ATLANTA, GA 30332-0130
(404) 894-7026
FAX: (404) 894-7025

MR. JOHN PEIFER
BIOENGINEERING CENTER
GEORGIA INSTITUTE OF TECHNOLOGY
OIP/0334
ATLANTA, GA 30332-0130
(404) 894-7028
FAX: (404) 894-7025

DR. CHARLES R. BATISHKO #
BATTELLE PACIFIC NORTHWEST
LABORATORIES
P.O. BOX 999
RICHLAND, WA 99352
(509) 375-2588
FAX: (509) 375-3614

DR. KURT A. STAHL
BATTELLE PACIFIC NORTHWEST
LABORATORIES
P.O. BOX 999
RICHLAND, WA 99352
(509) 375-2209
FAX: (509) 375-3614

DR. ARTHUR W. GUY
BIOELECTRICAL CONSULTING
18122 60TH PLACE, NE
SEATTLE, WA 98155
(206) 486-6439
FAX: (206) 485-5963

PROF. JAMES C. LIN
COLLEGE OF ENGINEERING
M/C 154
UNIVERSITY OF ILLINOIS AT CHICAGO
851 SOUTH MORGAN STREET
CHICAGO, IL 60607-7053
(312) 413-1052
FAX: (312) 413-0024

DR. JAN STOLWIJK
DEPARTMENT OF EPIDEMIOLOGY
AND PUBLIC HEALTH
YALE UNIVERSITY SCHOOL OF
MEDICINE
60 COLLEGE STREET
NEW HAVEN, CT 06510
(203) 785-6373
FAX: (203) 785-7296

DR. KEN H. JOYNER
TELECOM AUSTRALIA RESEARCH LABORATORY
770 BLACKBURN ROAD
CLAYTON, VICTORIA 3168
AUSTRALIA
011-61-3-253-6315
FAX: 011-61-3-253-6365

DR. CAMELIA GABRIEL
PHYSICS DEPARTMENT
KINGS COLLEGE
STRAND
LONDON WC2R 2LS
ENGLAND
011-44-081-989-5055
FAX: 011-44-081-989-6658

2

DR. PETER J. DIMBYLOW
NATIONAL RADIOLOGICAL PROTECTION
BOARD
CHILTON, DIDCOT
OXON OX11 0RQ
UNITED KINGDOM
011-44-0235-831-600
FAX: 011-44-0235-833-891

DR. MICHAEL H. REPACHOLI
VISITING SCIENTIST
AUSTRALIAN RADIATION LABORATORY
LOWER PLENTY ROAD
YALLAMBIE, VICTORIA 3085
AUSTRALIA
011-61-3-433-2391
FAX: 011-61-3-432-1835

DR. ALAN J. FENN
LINCOLN LABORATORY
MASSACHUSETTS INSTITUTE OF
TECHNOLOGY
244 WOOD STREET
LEXINGTON, MA 02173-9108
(617) 981-7630
FAX: (617) 981-0143

PROF. MARIA A. STUCHLY
DEPARTMENT OF ELECTRICAL
AND COMPUTER ENGINEERING
UNIVERSITY OF VICTORIA
P.O. BOX 3055
VICTORIA, BC
CANADA V8W 3P6
(604) 721-6029
FAX:(604) 721-6052

PROF. RICHARD L. MAGIN
DEPARTMENT OF ELECTRICAL
AND COMPUTER ENGINEERING
1406 W. GREEN STREET
UNIVERSITY OF ILLINOIS
URBANA, IL 61801
(217) 333-6347
FAX: (217) 244-0105

PROF. TADEUSZ M. BABIJ
DEPARTMENT OF ELECTRICAL
AND COMPUTER ENGINEERING
FLORIDA INTERNATIONAL UNIVERSITY
MIAMI, FL 33199
(305) 348-2683
FAX: (305) 348-3707

DR. SARAH NUNNELEY
AL/CFTO
BROOKS AFB, TX 78235-5301
(210) 536-3814
FAX: (210) 536-2761

PROF. GREGORY KRIEGSMANN
DEPARTMENT OF MATHEMATICS
NEW JERSEY INSTITUTE OF
TECHNOLOGY
UNIVERSITY HEIGHTS
NEWARK, NJ 07102
(201) 596-5785
FAX: (201) 596-6467

DR. DENNIS M. SULLIVAN
DEPARTMENT OF RADIATION ONCOLOGY
STANFORD UNIVERSITY SCHOOL OF
MEDICINE
STANFORD, CA 94305
(415) 725-6208
FAX: (415) 725-8231

COORDINATORS:

DR. PETER POLSON
AUSA
18985 TUGGLE AVENUE
CUPERTINO, CA 95014-3658
(408) 257-3376
FAX: (408) 257-3376

MR. LOUIS N. HEYNICK
CONSULTANT
833 RICHARDSON COURT
PALO ALTO, CA 94303
(415) 494-6585
FAX: (415) 494-1151

Introduction and Review of Purpose

David N. Erwin
Radiofrequency Radiation Division
Armstrong Laboratory
Brooks AFB, TX 78235

The goal of this project is to advance the state of the art of RFR dosimetry to a level of sophistication where computer graphically generated, high-resolution SAR distributions can be obtained and displayed with anatomical features for any section of the human body. Procedures are to be developed allow modelling of the realistic exposure conditions for whole-body or partial-body irradiation due to spatially uniform or nonuniform (far-field or near-field) EM fields that are CW, pulsed, or transient in nature. Efforts will also be directed at improving thermal models of the human body so that expected temperature distributions due to RFR exposure can be predicted and displayed graphically.

Participants will generate recommendations for research in subspecialty areas relevant to the above, such as standard models of humans and animals, graphical display methods, numerical algorithms, validation of computer-generated data, extrapolation of SAR data to thermal physiology, etc.

The final product of the workshop will be an Armstrong Laboratory Technical Report containing overview papers presented at the workshop and recommendations for research generated by the working groups. The Technical Report will assist the Radiofrequency Radiation Division in planning for future efforts in this area.

FOURTH EDITION OF THE RADIOFREQUENCY RADIATION DOSIMETRY HANDBOOK

Carl H. Durney
Department of Electrical Engineering and Department of Bioengineering
University of Utah
Salt Lake City, UT 84112

1. The Beginning

The genesis of the dosimetry handbooks stems from research in dosimetry sponsored by the US Air Force School of Aerospace Medicine (USAFSAM) at Brooks AFB, Texas in the early 1970s. Curtis C. Johnson returned to the University of Utah as chairman of the newly created Bioengineering Department in 1972 after spending five years at the University of Washington. At the University of Washington, he had worked with Arthur W. Guy and others in bioelectromagnetics, including dosimetry calculations in spherical models of the human body. When he returned to the University of Utah, he continued that work.

Stewart Allen at Brooks AFB had been measuring power absorption in monkeys and had observed that more power was absorbed when the incident electric field was parallel to the long axis of the monkeys than when it was not. Since spherical models could not predict that orientation effect, Curt Johnson and I extended the dosimetry calculations to spheroidal models. We used a long-wavelength approximation which did predict the orientation effect, but was limited to the lower frequency ranges, up to about 30 MHz for human models.

The idea of a dosimetry handbook came out of conversations of Curtis Johnson with John C. Mitchell and Stewart J. Allen of USAFSAM, which was funding our dosimetry research. They felt that a handbook consisting of a compilation of dosimetry calculations and other information useful to those doing research in dosimetry would be valuable. With that in mind, we began to make dosimetry calculations for pertinent models of humans and other animals and to collect the information that was to be in the first edition of the Radiofrequency Radiation Dosimetry Handbook.

2. The First Edition

The first edition of the Radiofrequency Radiation Dosimetry Handbook was published in September, 1976. Dosimetric calculations were based on homogeneous spheroidal and ellipsoidal models of humans and other animals. Specific absorption rates (SARs) were calculated by the long-wavelength method in the lower frequency range. Habib Massoudi made the long-wavelength calculations, extending them from the prolate spheroidal models to ellipsoidal models. Peter Barber, who did his PhD work at UCLA on a technique called the extended boundary condition method (EBCM), joined us at the University of Utah and used the EBCM to calculate SARs in spheroidal models. The EBCM was used to calculate SARs above the range for which the long-wavelength method was valid. It provided data nearly to the 80 MHz resonance frequency for the average man model, and slightly beyond resonance for some animal models. The upper frequency limit was a function of the aspect ratio of the model. A geometrical optics approximation valid when the wavelength was small compared to the size of the model was used to calculate SARs in the high-frequency range. Interpolations were made in the range where no calculations were yet available.

The first edition included some rules of thumb for dosimetry, specifications for spheroidal and ellipsoidal models of humans and other animals, a graph of permittivity of muscle as a function of frequency, and graphs of SAR versus frequency for animal models in the frequency range of 10 kHz to 1.5 GHz for up to six different polarizations (orientation of the incident fields with respect to the model).

Figure 1 (Fig. 4, first edition) shows a typical SAR graph from the first edition for an ellipsoidal model in the lower frequency range calculated by the long-wavelength approximation. Figure 2 (Fig. 27, first edition) shows the SAR versus frequency for an average-man model, with the dashed lines showing the interpolated values.

3. The Second Edition

In May, 1978, the second edition of the dosimetry handbook was published. In it, the frequency range was broadened to the 10 MHz to 100 GHz range with dosimetric data extended to include absorption of models irradiated by planewaves in free space, absorption of models on or near ground planes, heat-response calculations, and some scattering data. Empirical relations for calculating the specific absorption rates (SARs), some rules of thumb, and data from the literature for metabolic rates, dielectric constants, and conductivities were also included, as well as tables summarizing the experimental data and theoretical techniques found in the literature.

The frequency range of SAR calculations was extended from just above resonance to the geometrical-optics range by using cylindrical models (except for K polarization). Figure 3 (Fig. 16, second edition) shows how the SARs were calculated by various techniques in the various frequency ranges.

Om Gandhi and Mark Hagmann made SAR calculations using a block model of man and the moment method. Figure 4 (Fig. 49, second edition) shows the block model and Fig. 5 (Fig. 48, second edition) shows average SARs calculated from the block model and those calculated from spheroidal models. The block model calculations showed additional resonances attributed to the head and arms and legs, features not included in the spheroidal models. An empirical relation was developed by Magdy Iskander that provided a simple calculation for SARs for various spheroidal models, thus providing a way to get dosimetric data for models not included in the handbook. James L. Lords and David Ryser made heat-response calculations and contributed thermoregulatory information.

4. The Third Edition

The third edition of the handbook (August, 1980) was published mainly to provide new data on near-field absorption: SARs for spheroids and cylinders irradiated by short dipoles and small loops, and a block model of man irradiated by simple aperture fields. Tables from the second edition were also updated and included, although generally speaking, material contained in the first and second editions was not included in the third edition. Contents of the third edition include a section on qualitative electromagnetics, experimental dosimetric techniques, some in-vivo tissue properties, recipes for phantoms, a summary of theoretical methods, experimental SAR data, calculated SAR data (including layer effects, near-fields due to small dipoles and small apertures), and qualitative explanations of SAR behavior.

The frequency range of SAR calculations was extended by use of the surface integral equation (SIE) method, which was based on a model consisting of a finite-cylinder capped by hemispheres on each end. Figure 6 (Fig. 9, third edition) illustrates
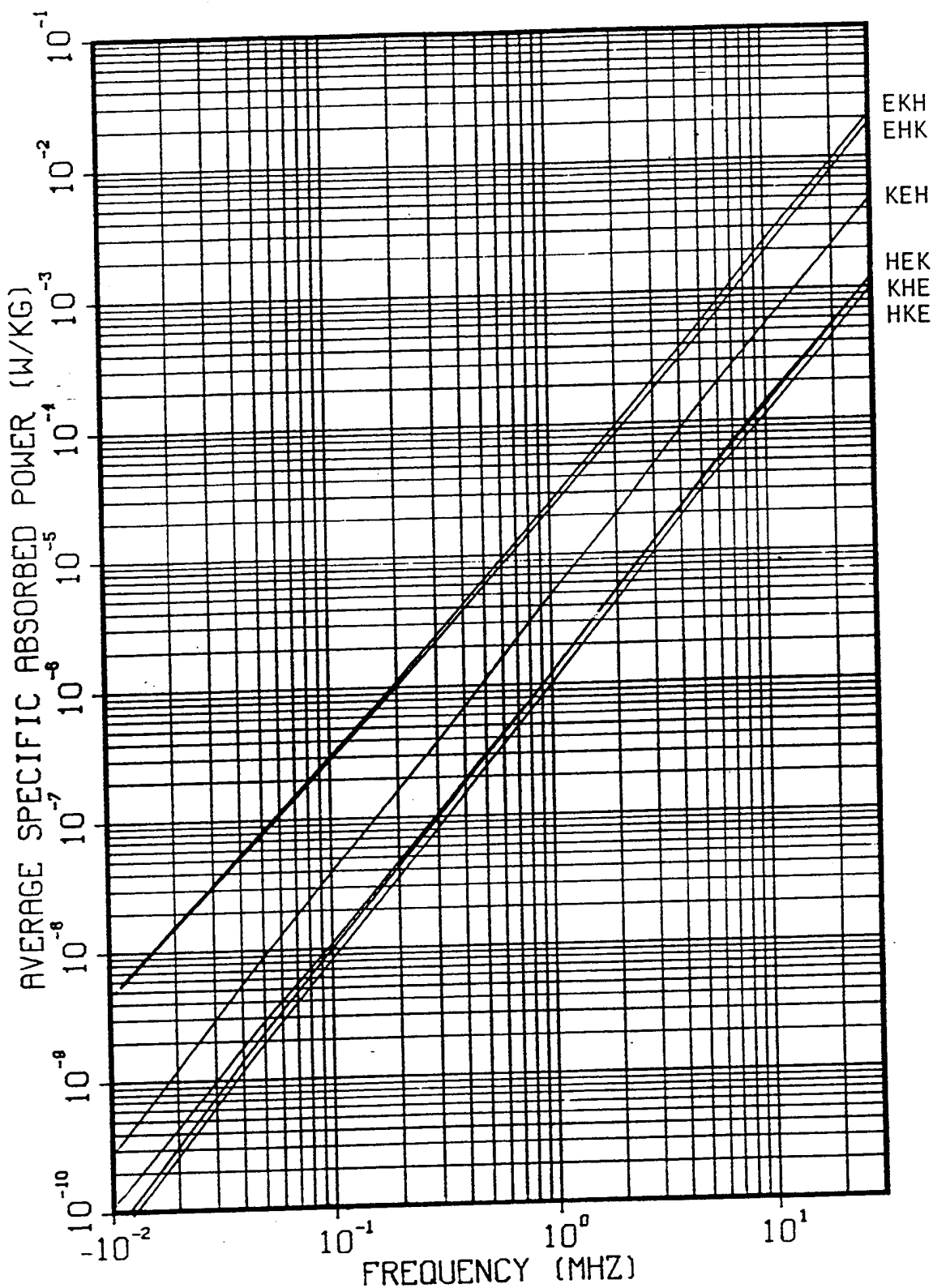
Fig. 1. (Fig. 4, first edition) Average specific absorbed power in an ellipsoidal model of an average man, for the six standard polariations. a = 0.875 m, b/c = 2, V = 0.07 m³. Incident power density is 1 mW/cm².
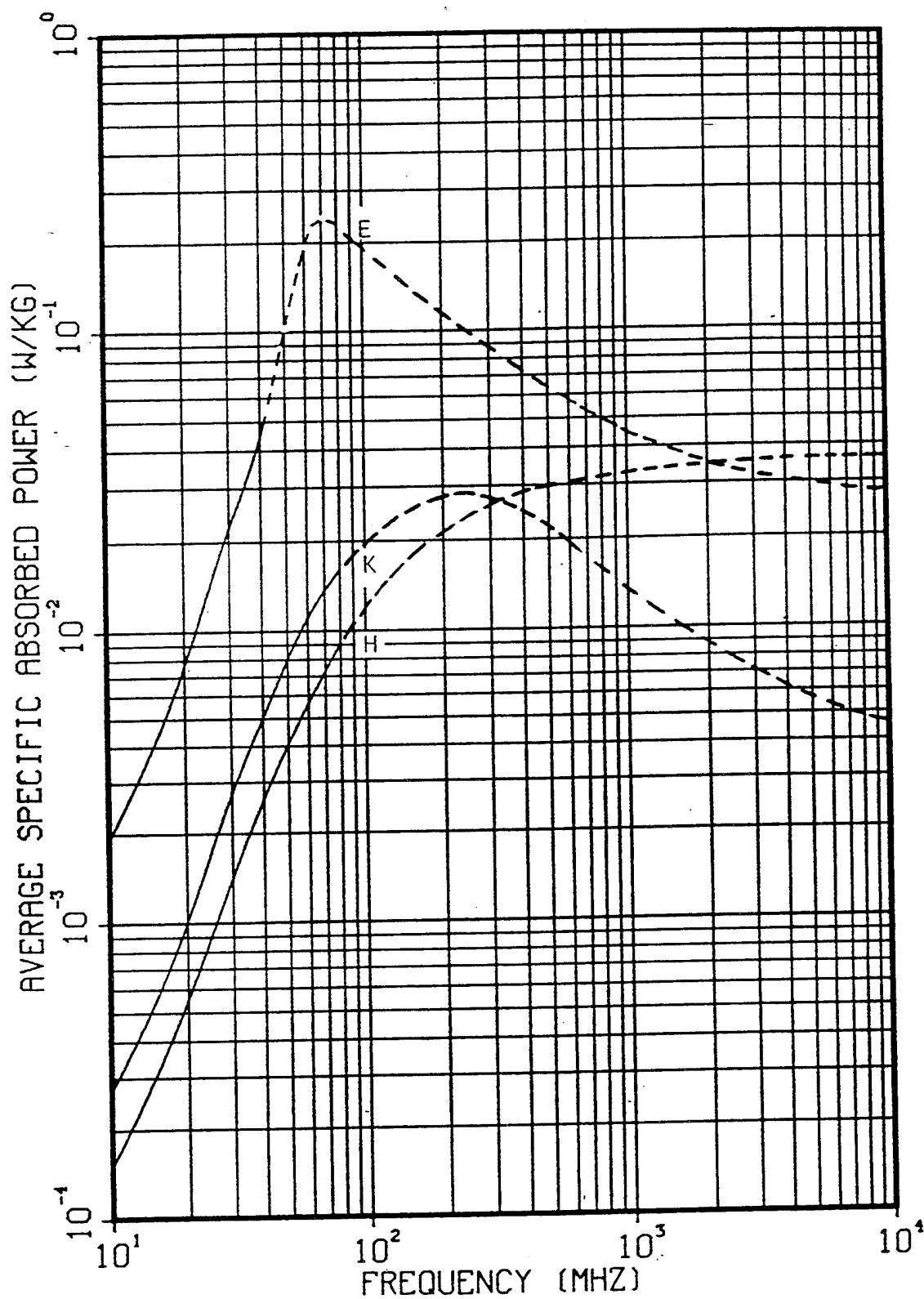
Fig. 2. (Fig. 27, second edition) Average specific absorbed power in a prolate spheroidal model of an average man, for the three standard polarizations. a = 0.875 m, V = 0.07 m³. Incident power density is 1 mW/cm².
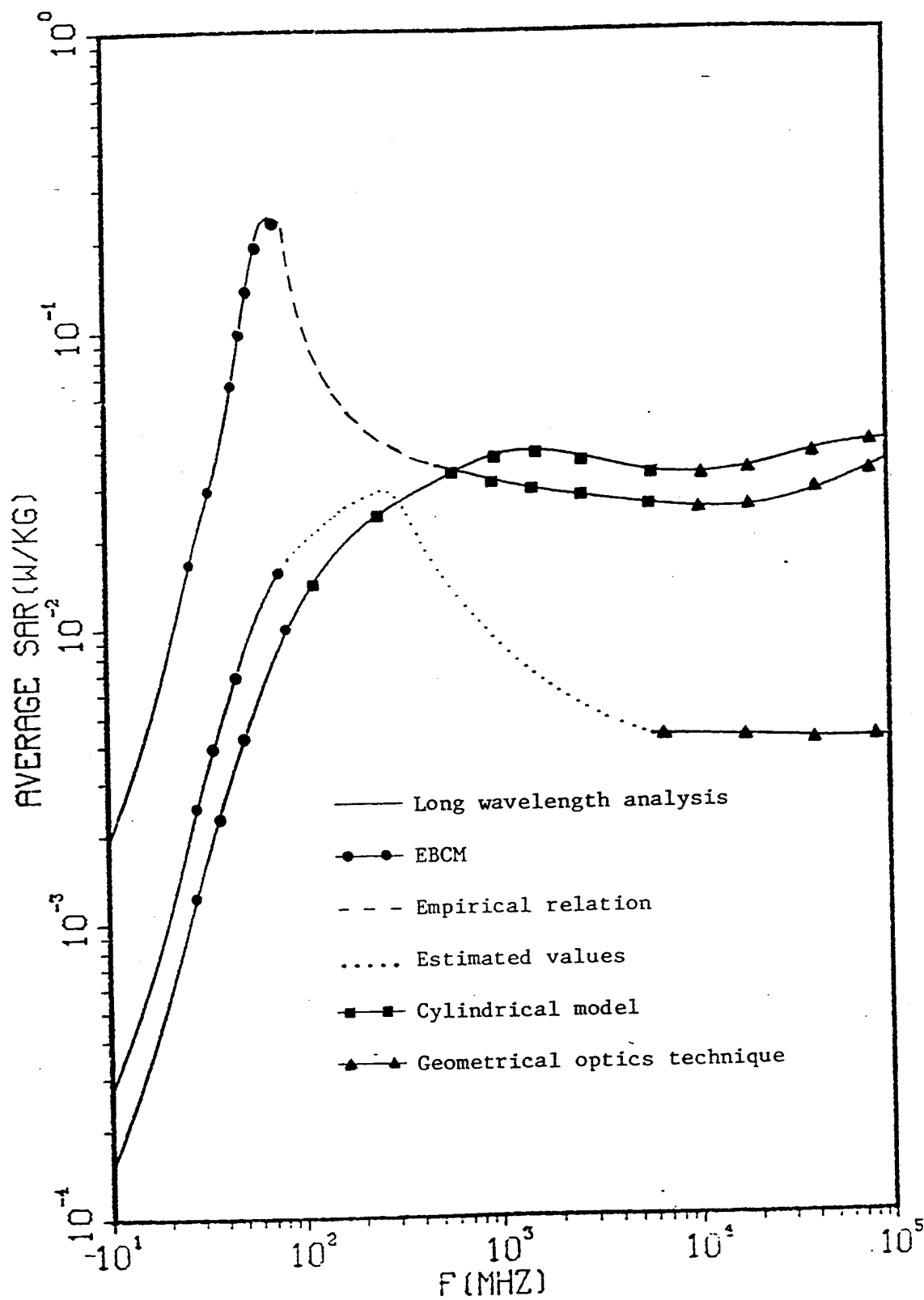
Fig. 3. (Fig. 16, second edition) Illustration of different techniques, with their frequency limits, used for calculating SAR data for models of an average man.

BACK
- LAYER

MIDDLE
LAYER

FRONT
LAYER
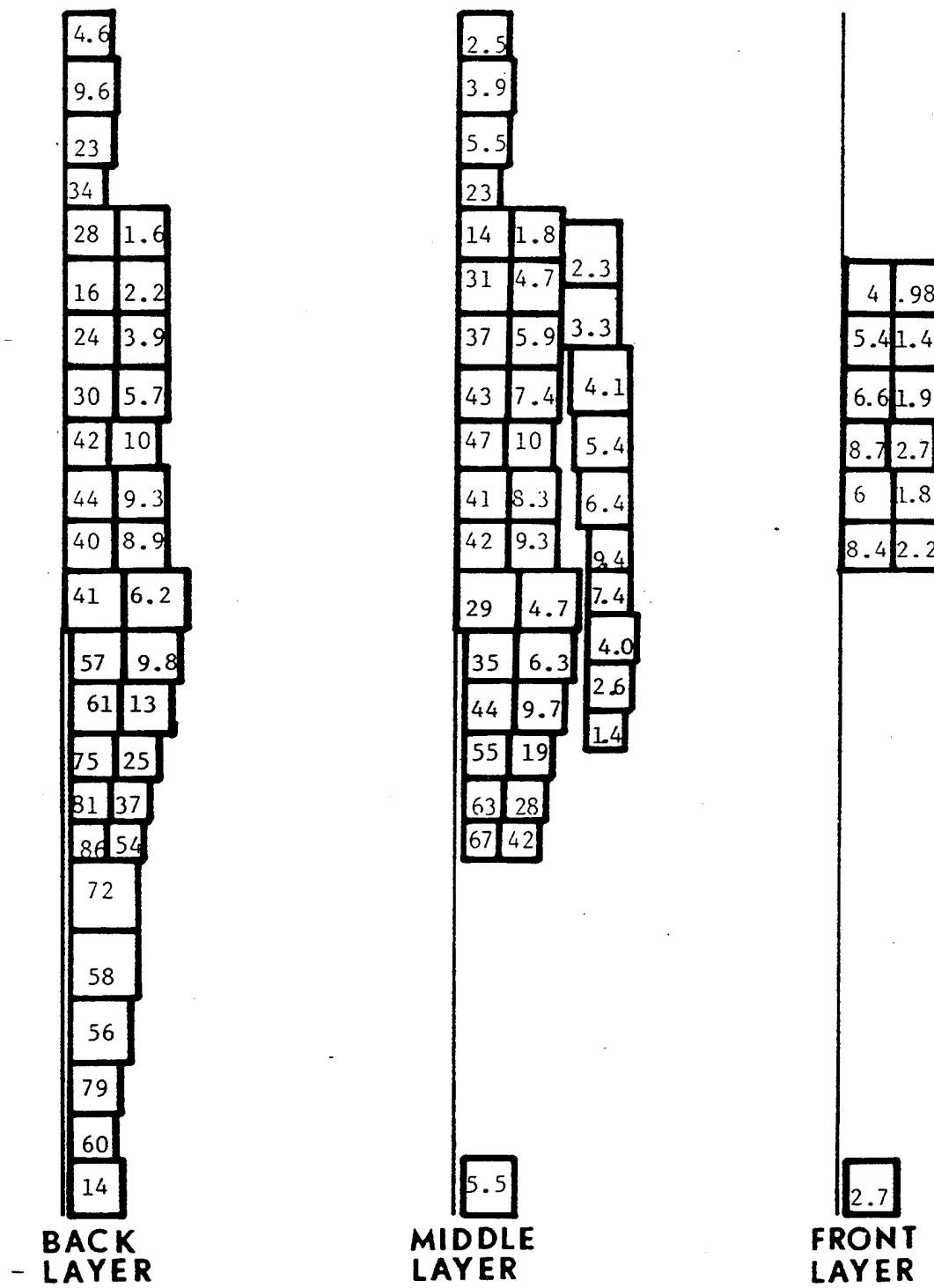
Fig. 4. (Fig. 49, second edition)   Local SAR values (W/kg per mW/cm^2) x 100 for homogeneous block model of man with vertical polarization at 80 MHz
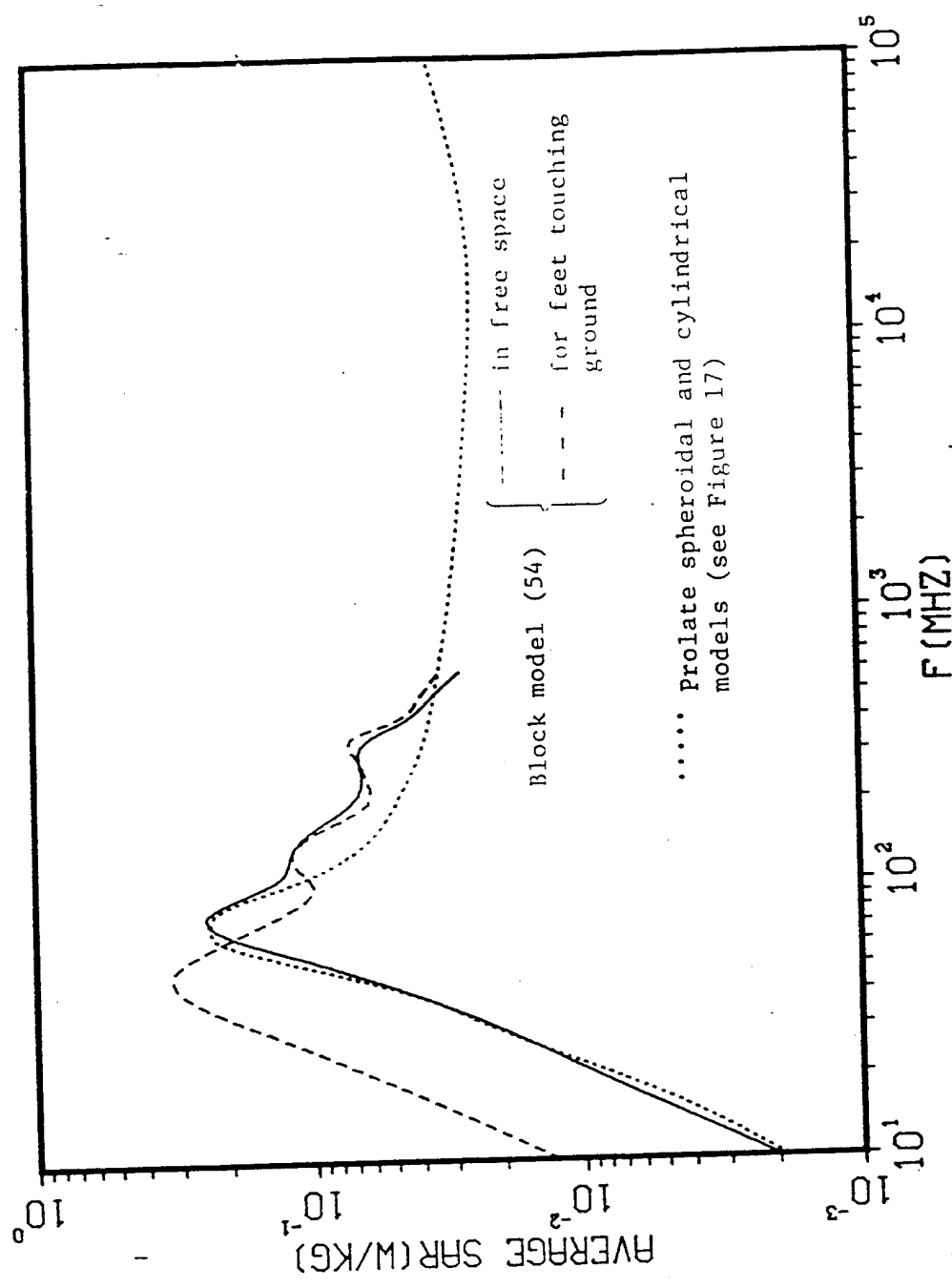
Fig. 5. (Fig. 48, second edition) Comparison of the average SAR in models of an average man, E polarization. Incident power density is 1 mW/cm².
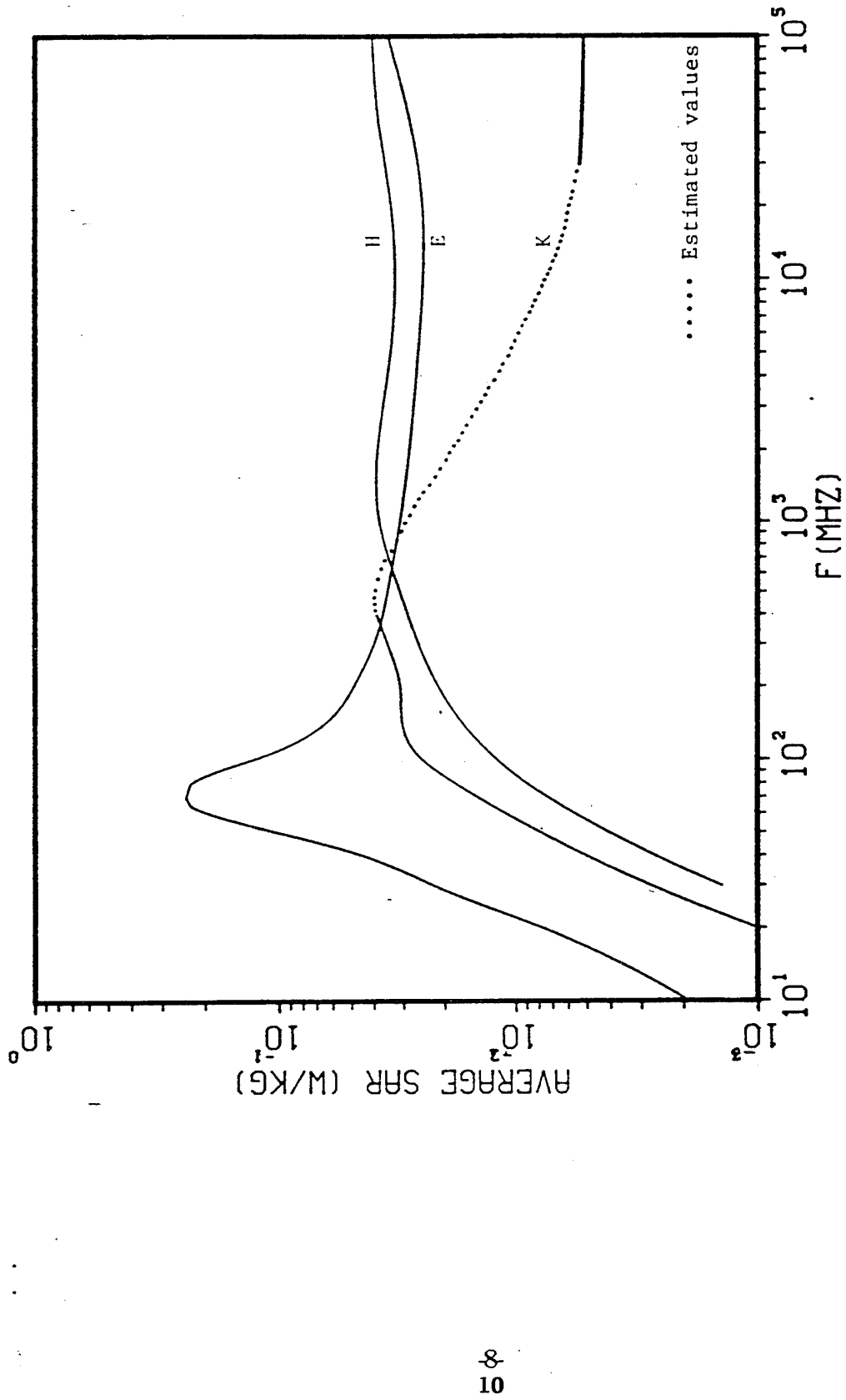
Fig. 6. (Fig. 9, third edition) Calculated average SAR in a prolate spheroidal model of an average man for an incident power density of 1 mW/cm^2 for three polarizations; a = 0.875 m, b = 0.138 m, V = 0.07 m^3.

the SAR calculation, with considerably less interpolation than in previous editions. Figure 7 (Fig. 19, third edition) illustrates the effects of layers, such as skin and fat, on the calculated SAR. The layers produce additional resonances at the higher frequencies, where the thickness of the layers is near a half wavelength. Figure 8 (Fig. 24, third edition) illustrates the kind of near-field SAR data that was included in the third edition. Figure 9 (Fig. 60, third edition) shows some internal SAR distributions calculated in the block model by Indira Chatterjee and Om Gandhi for irradiation by leakage near fields. Figure 10 (Fig. 72, third edition) illustrates the qualitative explanations given for the SARs as a function of polarization. For example, when the electric field is parallel to the long axis of the body, the SAR is generally higher than when the electric field is perpendicular to the long axis of the body.

5. The Fourth Edition

The purpose of the fourth edition of the handbook (October, 1986) was to provide one convenient source of dosimetry information, including that contained in the previous editions. Significant new information was added, and for the first time, the handbook was formally reviewed by six reviewers, Stewart J. Allen, Kenneth R. Foster, Donald I. McRee, Richard G. Olsen, Herman P. Schwan, and Thomas S. Tenforde, whose comments were valuable for improving the book.

In the fourth edition, one chapter explains the basics of electromagnetics for readers who are not physicists or engineers. The emphasis in this chapter is on qualitative explanations, as opposed to mathematical relations. Herman Schwan contributed a chapter about tissue permittivities, and updated compilations of published tissue properties were included. Techniques of theoretical dosimetry were also explained, along with a tabulation of published theoretical work and data for models of biological systems. Calculated dosimetric data for spheroidal models were extended well beyond the resonant frequency range by a new technique developed at the University of Utah by Magdy Iskander called the iterative extended boundary condition method. Stewart Allen contributed a chapter on experimental dosimetry , including a history of experimental dosimetry (adapted from Bill Guy's writings) and a discussion of experimental techniques. Information on very-low-frequency radiation dosimetry, which was not included in previous editions, was also included in the fourth edition. Eleanor Adair contributed a chapter on heat-response that included information from a previous edition written by James Lords. John Mitchell contributed a chapter on radiofrequency radiation safety standards. The fourth edition consists of 11 chapters, 508 pages, 222 figures, and 400 references.

The fourth edition of the Radiofrequency Radiation Dosimetry Handbook is a benchmark work in the sense that it is a compilation of dosimetry information resulting from the work of many people, containing the best information available at the time it was published.

6. What's Next?

Since publication of the fourth edition of the handbook, significant advances have been made in numerical electromagnetic techniques. Much greater computer power is now readily available. Improved computer graphics techniques are commonly in use. By taking full advantage of these added resources, a much advanced new edition of the dosimetry handbook could and should be developed.
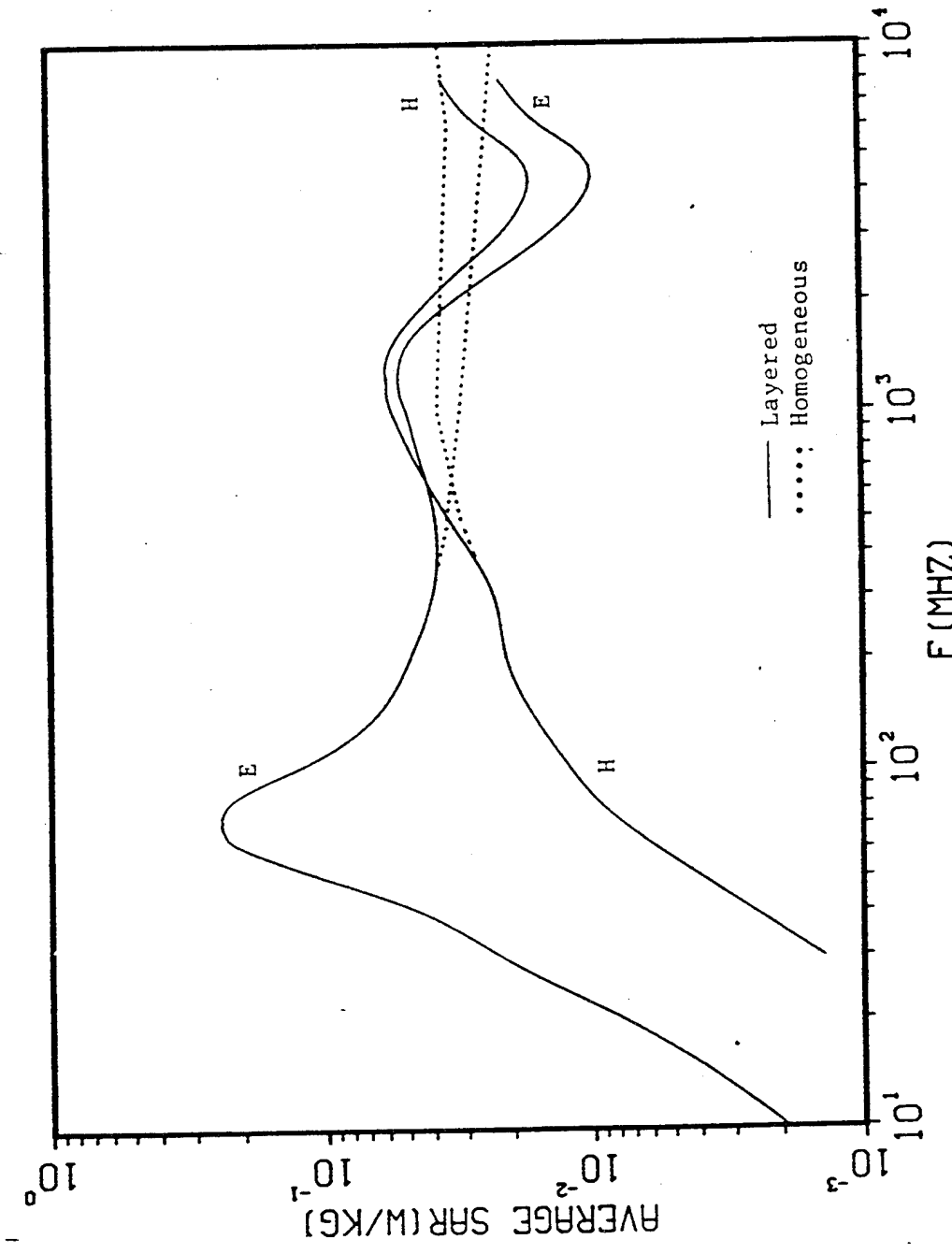
Fig. 7. (Fig. 19, third edition) Calculated average SAR in homogeneous and multilayered models of an average man for an incident power density of 1 mW/cm² for two polarizations.
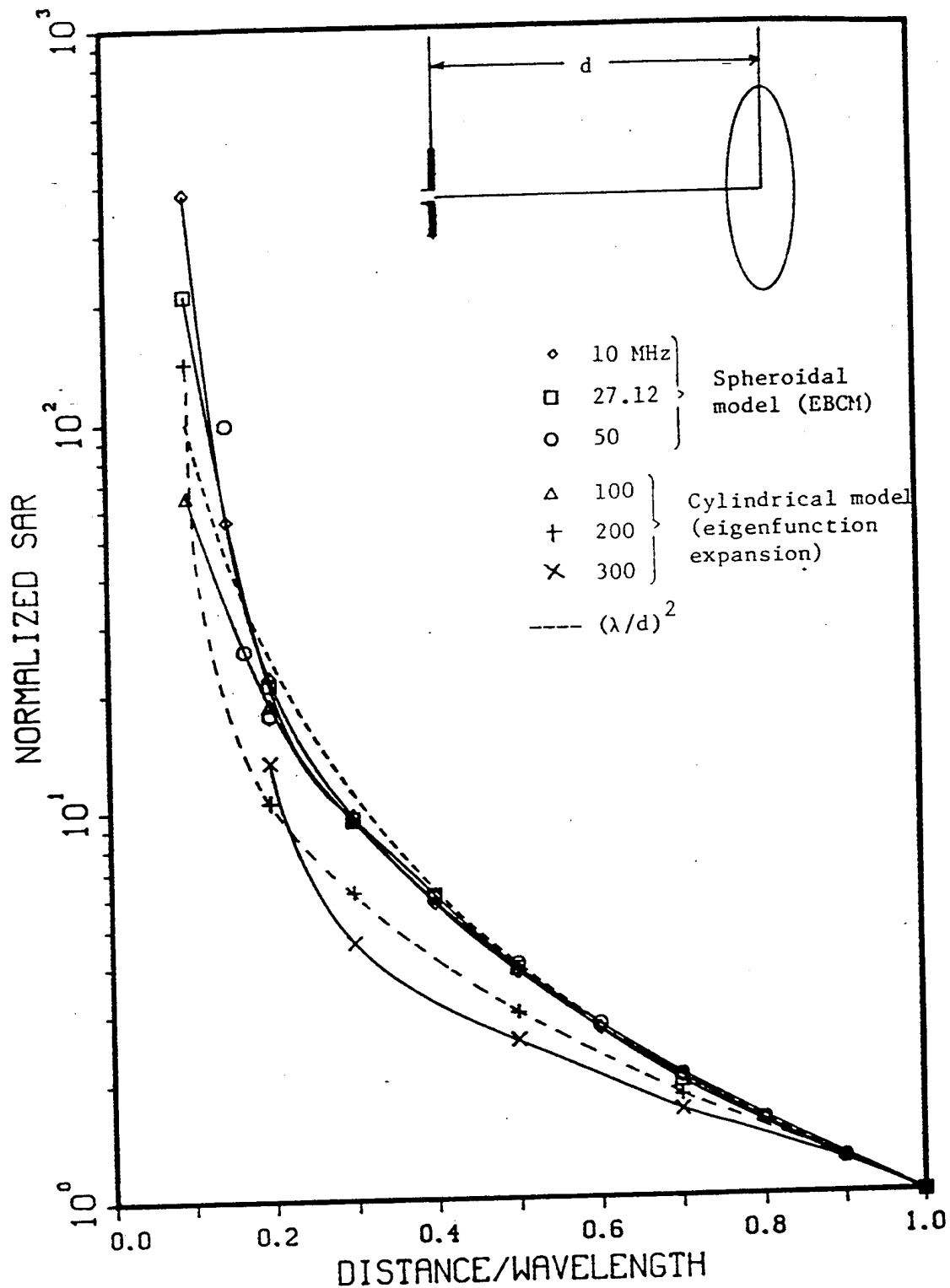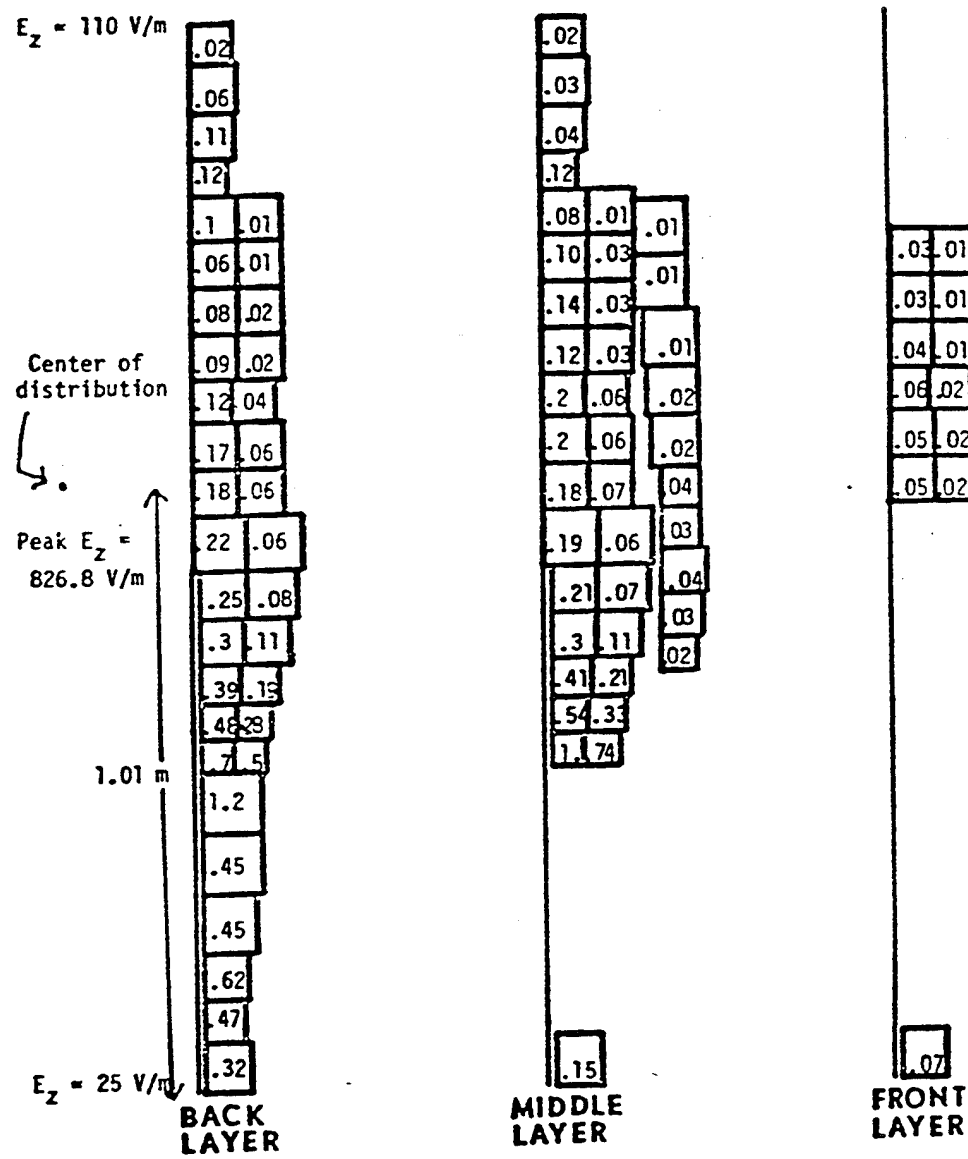
Fig. 8.(Fig. 24, third edition) Calculated normalized average SAR in a prolate spheroidal model of an average man as a function of the electric dipole location for E polarization.

The numbers indicated are in watts/kg. The numbers in parentheses are for normal planewave irradiation.

Whole-body average:	0.16 (1.22)	Neck:	0.12 (1.9)
Torso:	0.08 (0.68)	Leg:	0.38 (2.5)
Head:	0.05 (0.79)	Arm:	0.02 (0.17)

Fig. 9. (Fig. 60, third edition) Distribution of SAR in the block model of man placed in the leakage field of a 27.12-MHz RF sealer, assuming a zero phase difference in the incident field E_z; peak $E_z = 826.8$ V/m.
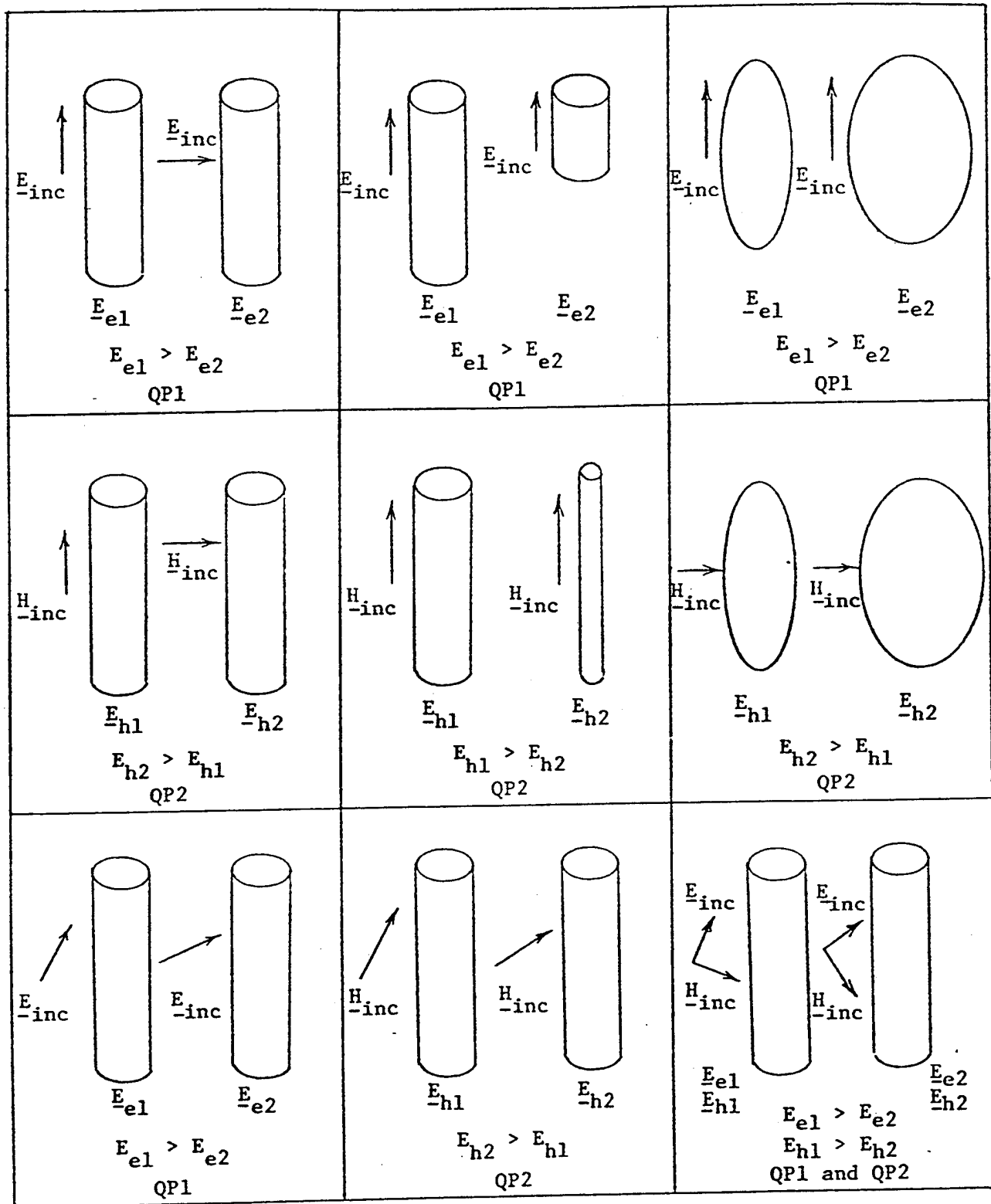
Fig. 10. (Fig. 72, third edition) Qualitative evaluation of the internal fields based on qualitative principle QP1 and QP2. $\underline{E}_e$ is the internal electric field generated by $\underline{E}_{inc}$, the incident field, and $\underline{E}_h$ is the internal electric field generated by $\underline{H}_{inc}$, the incident H field.

With techniques like the finite-difference time-domain (FDTD) method, calculations of SAR distributions can now be made using models composed of millions of cells, which was not possible during the time of the fourth edition. Using theseadvanced techniques, new dosimetry calculations using refined models of humans and other animals should be made for inclusion in a new dosimetry handbook. In particular, nonrectangular mathematical cells should be implemented in these models, since they can be much more conforming to nonrectangular boundaries, thus leading to improved efficiency in terms of accuracy for a given number of cells. Methods for using course cells in areas of least interest and finer meshes in areas of greater interest should also be developed. More work is needed in modeling exposure fields. Methods should be developed for modeling sources of exposure fields from measurements, so that dosimetry calculations could be made for specific exposure conditions. Ways for linking temperature and SAR calculations in a unified method should be developed.

A new area in dosimetry that should be explored is transient electromagnetic field exposure. People are continually exposed to literally thousands of transient electromagnetic fields. Some initial work has been done in measuring and characterizing these transient fields, but very little work has been done in calculating transient fields inside the human body produced by these transient exposure fields, and very little is known about how these transient fields affect people.

The next edition of the dosimetry handbook should be a combination of printed material and software. Much of the reference and tutorial material in the handbook would be most useful in printed form. Software that would allow calculation of SARs and temperatures for specific conditions and that would provide visual display of the calculated data would be an ideal complement to the printed reference material. Such a dosimetry handbook is well within the reach of present technology, and certainly should be developed.

Phantoms and SAR Determinations

Chung-Kwang Chou, Ph.D.
Department of Radiation Research
City of Hope National Medical Center
Duarte, California 91010

ABSTRACT

Extrapolation of research results from animals to man presents many difficulties. In addition to species differences in biological parameters, there are formidable dosimetric problems in non-ionizing radiation research. Phantom models with dielectric properties and geometry similar to tissues have been used to simulate biological bodies exposed to radiofrequency electromagnetic fields. Specific absorption rate (SAR) is widely accepted as a quantification unit. SAR can be calculated from measurements of temperature rise in tissues exposed briefly to high power electromagnetic fields or from electric fields in the tissues at normal incident power densities. The induced electric fields or current densities in the tissues can be calculated from the SAR data. Measurement of temperature rise is a method of determining SAR and has no implication as to the mechanism of any biological effects.

INTRODUCTION

Many experiments that cannot be ethically performed on humans can be performed on animals, but the results obtained are not always directly applicable to man; extrapolation of data is fraught with complications. In non-ionizing radiation research, one must not only consider differences in biological endpoints, but also deal with the difficult problem of physical extrapolation (Chou & Guy 1985). Unlike ionizing radiation, the same intensity of non-ionizing radiation can result in markedly different biological effects in animals of different species because of variation in the quantity of energy absorbed from electromagnetic (EM) fields. For example, if a behavioral effect in a rat exposed to a 2450-MHz field at 0.5 mW/cm^2 is observed, one cannot conclude that microwave irradiation at the same power density will elicit that behavior in human beings.

Since energy coupling to tissues is a complex function of many different variables, the incident field intensity (e.g., in mW/cm^2 or V/m) provides little insight into dose response relationship. Therefore, it is difficult to extrapolate the results from research on laboratory animals to predict human effects based solely on power density or the strength of the incident EM field. A basic law of Grothus-Draper is that a physical agent cannot have a physical effect if it is not imparted to a body. Consequently, the question arises as to the most suitable parameter(s) for the quantification of EM fields interaction with biological

1

systems. Wacker & Bowman (1971) suggested the use of the square of the electric field or the energy density in a volume of tissues for quantification. Schwan (1971) proposed the use of induced current density in tissue. A simpler alternative is to use the strength of the electric field in the tissues. Yet another alternative is the mass-normalized rate of energy absorption, the dose rate, which was introduced into microwave research in the late 1960's (Justesen & King, 1970; Justesen, 1975). Many investigators now rely on the dose rate as a measure, which has also been termed "absorbed power density" (Johnson & Guy, 1972) and is defined as the Specific Absorption Rate (SAR) by the National Council of Radiation Protection and Measurements (NCRP, 1981). Technically, it makes no difference which of the above parameters is chosen, as they are all related by simple equations:

$$SAR = \frac{1}{10^3}\frac{\sigma}{\rho}E^2 \quad (W/kg)$$

$$E = \sqrt{\frac{\rho 10^3}{\sigma}SAR} \quad (V/m)$$

$$j = \sqrt{\sigma\rho 10^3 SAR} \quad (A/m^2)$$

where E is the electric field, j is the current density, ρ is tissue density in g/cm^3, and σ is the conductivity of tissue in S/m. What is essential is the quantification of EM fields in the exposed tissues. In this paper we will first discuss phantom materials, and then SAR measurement techniques.

PHANTOM TISSUES

Various cuts of pork or beef and saline solutions have been used by many investigators as phantoms for qualitative evaluation of diathermy applicators or as a load for heating equipment (Cetas, 1982). However, meat is messy, has a short lifetime and, most importantly, has an inconsistent tissue composition. The convection in saline solutions quickly alters the heat pattern. These problems make the above phantoms unacceptable for quantitative measurements. Guy et al. (1968) published formulas for making high water content muscle and low water content fat and bone which have dielectric constant and conductivity similar to real tissues for a frequency range of 200 to 2450 MHz.

Table 1 lists the composition and properties of the phantom materials published by Guy et al. (1971). In high water content tissue, the dielectric constant can vary over a wide range by changing the percentage of polyethylene powder, and conductivity can be controlled by the salinity. The properties of synthetic fat can be changed to simulate other tissues of

2

low water content by alternating the amounts of aluminum powder to control the dielectric constant and acetylene black to control the conductivity. Thermal properties of several phantom materials have been studied by Leonard et al. (1984). Procedures for making these phantoms are described below.

Preparation of phantom muscle

Chou et al. (1984) described the methods of preparing muscle phantoms for frequencies of 13.56 to 2450 MHz. The mixture consisted of various proportions of TX151 (a gelling agent, formerly known as "super stuff", supplied by Oil Center Research, P.O. Box 71871, Lafayette. LA 70501), polyethylene powder (to reduce the dielectric constant, 20-mesh low-density powder, obtained from Wedco CA Inc., 2102 Curry Street, Long Beach, CA 90805), water, and NaCl (to increase the conductivity, reagent grade) for simulating tissue above 200 MHz. If the frequency is at or below 100 MHz, and the dielectric constant of tissue is higher than water, polyethylene powder is no longer applicable. Balzano et al. (1979) demonstrated that aluminum powder can be used to increase the dielectric constant of the phantom. Therefore, for the frequency range of 13.56 to 100 MHz, aluminum powder (Baker's USP, reagent grade, obtained from J. T. Baker Chemical Co., Phillipsburg, NJ) is added to the phantom muscle mixture. It is essential that industrial grade aluminum powder not be used because of the nonuniform particle size and powder impurity.

Table 2 shows the composition of the phantom muscle tissue for various radiofrequencies (Chou et al. 1984). Percentages are by weight. The NaCl percentage was maintained to three significant figures since the conductivity of the mixture was highly sensitive to small changes in NaCl. The measured dielectric constants and conductivities of the phantom tissue (mean $\pm$ standard deviation, N = 5) at 22°C are very similar to that of muscle tissue at 37°C (Burdette et al. 1980, Schepps & Foster, 1980, Stuchly & Stuchly, 1980, Stuchly et al. 1981).

The specific heat and density of the phantom muscle are as indicated in Table 1. The thermal conductivity is 0.55-0.60 W/m°C (depending on aluminum content). These values are in close agreement with those of tissue (Guy et al. 1974).

The phantom muscle for 200 to 2,450 MHz is prepared as follows: a) Determine weights from percentages and weigh all ingredients. b) Mix ingredients (except TX151), including one drop of household liquid detergent to wet the polyethylene powder, in 14-20°C water with a 10-cm shear stirrer rotating at 450 rpm on a variable speed drill press until all polyethylene powder is wet. c) Add TX151 and increase drill press speed to 1200 rpm. d) Mix for 45-120 seconds. When the mixture becomes thick, slow the drill press to about 800 rpm to avoid generation of air bubbles. Since the setting time of TX151 varies with age and different batches, proper water temperature and mixing time must be determined by experience. If stirred too long, the mixture will become too hard to pour, and if stirred insufficiently, the polyethylene powder will float.

3

For a frequency range of 13.56-100 MHz, the procedures are as follows: a) Weigh all ingredients as before. b) Mix NaCl and aluminum powder in water add TX151 after the aluminum is wet and mix with a 10 cm shear stirrer rotating at 1,200 rpm for 45-120 seconds on a drill press, following the same precautions as discussed above. c) If the stirring time is not sufficient, the aluminum powder will sink. Since air bubbles are easily formed in this mixture, it is necessary to rotate the mixing bucket constantly and move the stirrer up and down to insure proper mixing. Decreasing the speed of the drill press to 800 rpm is essential when the mixture starts to set to avoid trapping air bubbles. d) Pour the mixture into the mold slowly to allow the air bubbles to escape from the mixture.

Preparation of phantom fat and bone

According to the formulas in Table 1, for a small quantity, place everything but the catalyst in a one-quart round container, and stir until blended. Care must be taken with the acetylene black. It is light and electrostatic and therefore must be mixed into the polyester resin by hand. The stirring machine is a small drill press with 1/4" drill operating at 1000 rpm, and with a vertically oscillating- rotating table. The vertical oscillation and rotation is about one cycle per second. The stirring device is a 5 cm shear stirrer. When the ingredients are blended, the catalyst is added and stirring is continued for precisely 20 minutes, after which the mixture is poured. For large mixtures, a 10 cm shear stirrer, a large drill press, a stainless steel can 20 cm in diameter and 30 cm high, and a heavier vertically oscillating table are used. Table rotation is 40 rpm and vertical oscillation is 50 times per minute. Molds for our models are coated with paraffin wax to ease removal. After 3 hours setting, the models are firm and may be removed from the molds. The top and bottom of the final casting will have to be machined to remove air pockets and settled aluminum powder.

Preparation of phantom brain

For 915 MHz and 2450 MHz, the brain can be simulated by mixing 7.01% TX-150, 29.8% polyethylene powder, 62.61% water and 0.58% of NaCl. This material should have a dielectric constant of 34.37 and 33.56, and a conductivity of 0.77 and 1.24 S/m at 915 and 2450 MHz, respectively. The specific heat of the material is 0.83 kcal/kg°C and specific density of 0.96 g/cm^3.

The mixing procedure is essentially the same as for the muscle phantom, but due to the larger amount of polyethylene powder, it is very difficult to tell the correct pouring time; therefore, when the mixture looks "soupy", pour it into a plastic bag and let it set, then force it into a model. It should not be stirred too long, otherwise air may be beaten into it.

In addition to the formulas presented above, Table 3 lists the published compositions of various phantom tissues to be used at specific frequencies. For detailed mixing methods, the readers should refer to the original publications. Bini et al. (1984) used a transparent

4

20

material polyacrylamide for shortwave range applications. At millimeter wave range, formulas are given by Steel & Sheppard (1988).

MEASUREMENT OF SAR

The SAR can be easily calculated from the temperature rise in tissues caused by a short exposure to high intensity EM fields. The equation for the SAR calculation is:

$$SAR \simeq \frac{4186c\Delta T}{t} \quad (W/kg)$$

where c, in kcal/kg °C, is the specific heat of the tissues under study, 4186 is the kilocalorie-to-joules conversion factor, ΔT in K or °C is the increment temperature, and t the exposure duration in seconds. The symbol of approximation over the equation equal sign implies that accuracy is based on negligible loss of thermal energy by the irradiated body. Irradiations at a high power level (> 200 mW/cm^2) and for a short time (< 30 seconds) are needed to accurately quantify the temperature increase and minimize dissipation of thermal energy. The lower SAR used in most animal studies can be linearly extrapolated from the SAR measured at higher powers. For example, the measured whole-body SAR in a rat is 60 W/kg exposed at 300 mW/cm^2. For a 0.5 mW/cm^2 exposure level used in a low-level study, the SAR in the rats was extrapolated to (60/300) x 0.5 = 0.1 W/kg.

Point SAR

Before non-perturbing temperature probes were available, the thermocouple and glass tubing method was used to measure point SAR (Johnson & Guy, 1972). Later, several microwave-transparent temperature probes became commercially available (Bowman, 1976; Rozzell et al., 1975; Christensen 1977, Wickersheim & Alves, 1979, Wickersheim & Sun 1987). Because of the inhomogeneous energy deposition in a body (the electrical "hot spot" phenomenon which can yield thermal hot spots), multiple probing is necessary in quantifying SAR distribution. Mapping along a track with steeping motor has been reported (Gibbs, 1983). Linear array sensors are also useful for stationary mapping (Vaguine et al. 1984).

SAR can be calculated from electric fields in tissue with known electric conductivity. Electric field sensitive diodes have been used to map the field distributions in phantoms (Stuchly et al. 1984, Guy et al. 1987).

Two-dimensional SAR

Guy (1971) developed a thermographic technique for rapid measurement of the SAR on an internal plane of the animal or phantom. The accuracy of this technique depends on the size of the object, since heat loss between the time of exposure and taking of

5

thermograms becomes relatively large for smaller animals or phantoms. This method uses a thermographic camera for recording RF-induced temperature changes over an internal surface of the exposed object. Models are designed to separate along planes so that cross-sectional heating patterns can be measured. Silk screens are placed over precut surfaces on each half of the model to hold the phantom tissue and provide electrical contact between the two halves. The model is exposed for a short time at power levels much higher than normally used, then the model is quickly disassembled and the temperature pattern over the surface of separation is recorded by means of a thermograph. Since the thermal conductivity of the tissue model is low, the rate of the change in temperature distribution after heating per time interval will closely approximate the heating distribution over the flat surface. In regions of high temperature gradient errors may occur because of appreciable heat diffusion. The thermographic technique described for use with phantom models can be used in a similar way to quantify the SAR pattern in scaled models (Guy et al. 1976, Guy et al. 1984) in terminated animals exposed to electromagnetic fields (Johnson & Guy 1972, Chou et al. 1984) and in live animals measured on their skin surface (Guy et al. 1978). Recently, the magnetic resonance diffusion imaging technique has been applied to measure temperature non-invasively inside exposed body (Samulski et al. 1992). The heating equipment and applicators must be compatible with the MRI facility. In addition, the high cost of the facility is a problem.

Whole body SAR

Whole-body-averaged SAR in animals can be determined by twin-well calorimetry (Phillips et al., 1975; Blackman & Black, 1977; Allen & Hunt, 1979). Two animals of similar body weight were euthanatized and equilibrated at the twin well base line temperature, then one of the animals was exposed to microwaves. Immediately after exposure, the two carcasses were placed in the twin-well calorimeter. The averaged SAR in the exposed animal can be calculated from the differential heat of the two animals. In contrast to the thermographic technique, twin-well calorimetry is a better method for smaller animals; the long heat diffusion time for larger animals creates problems in twin-well calorimetry because the larger subject animals lose heat more slowly and the measurement time can take several days to reach equilibrium. During this time, decomposition generates additional heat which introduces errors in SAR measurement. A gradient layer calorimeter was used by Olsen et al. (1980) to measure partial or whole body average SAR of monkey or human models.

DISCUSSION

Most research on animals has the ultimate goal of applying the results for the benefit of mankind. Therefore, when effects are observed in animals, it should be discerned whether the effects can occur in exposed humans and, if so, under what exposure conditions. Without quantification of EM fields action on biological tissues, it would be impossible to extrapolate the results and to predict safe exposure levels for human beings. The SAR is now widely accepted by researchers in this field as a common unit for comparing and

6

extrapolating laboratory results to predict safe exposure levels for humans. The techniques for measuring SAR are complicated and still primitive. Although whole-body-averaged SAR provide a first step in quantification, distributive two dimensional SAR are also needed to make meaningful comparisons across species. For example, the SAR in the brain and spinal cord might be more appropriate than the whole-body SAR for determining thresholds and mechanisms of combined microwave-and-drug effects on behavior. In addition to biological effect research, the phantom materials and SAR determination methods are equally applicable in medical applications such as hyperthermia. For heating application, the quantification of heating pattern can be directly expressed in heating rate (°C/min) instead of SAR. The advantages of this have been discussed by Chou (1990).

Mistakes have often been made by investigators attempting to measure SAR in subjects exposed at low power-density levels, exposed over a long period of time, or both. Loss of thermal energy via blood flow and thermal diffusion will occur at low power levels; then the measured changes in temperature are low and do not reflect the actual energy deposition.

Concerning the modulation characteristics of the applied EM waves, the SAR should also be modified to reflect the time-varying nature of the field. For example, microwaves hearing effect can be induced by a single pulse (Chou et al., 1982). It is improper to quantify the effect by SAR as averaged over time. Instead, specific absorption (SA, the product of SAR and exposure time) for each pulse is a more suitable quantification. Another example of modulation is the effect of microwave exposure on Ca^{++} efflux (Bawin et al., 1975). This effect occurs only when the EM field is modulated, especially at 16 Hz. In this case, a time-varying element of 16 Hz should also be specified.

There is a misconception in the field about the validity of using the SAR in biological effects research involving both thermal and athermal ("field specific") effects. That is, since the SAR can be indexed by ΔT, some investigators regard that SAR is a thermal unit. It should be emphasized that temperature measurement is not required in measuring the SAR. The SAR can also be determined by measurement of the electrical field in a subject during exposure (to a weak or an intense incident field) by an electric-field probe. Measurement of ΔT resulting from a brief exposure to an intense field is merely a simple method of determining SAR, but has no implications as to mechanism of a field-body interaction.

ACKNOWLEDGEMENT

7

REFERENCES

1. Allen, S.J. and W.D. Hunt. Calorimetric measurements of microwave energy absorption by mice after simultaneous exposure of 18 animals. Radio Sci 14(6S):1-4 (1979).

2. Q. Balzano, O Garay, FR Steel. An attempt to evaluate the exposure of operators of portable radios to 30 MHz. Conf Rec 29th IEEE Trans Vehicular Tech Soc, Arlington Heights, FL, pp 187-188 (1979).

3. Bawin S.M., L.K. Kaczmarek, and W.R. Adey. Effects of modulated VHF fields on the central nervous system. Ann NY Acad Sci 247:74-81 (1975).

4. Bini, M.G., A. Ignesti, L. Millanta, R. Olmi, N. Rubino, and R. Vanni. The polyacrylamide as a phantom material for electromagnetic hyperthermia studies. IEEE Trans Biomed Eng 31:317-322, (1984).

5. Blackman, C.F. and J.A. Black. Measurement of microwave radiation absorbed by biological systems. In: Analysis by Dewar-flask Calorimetry. Radio Sci 12(6S):9-14 (1977)

6. Bowman, R.R.. A probe for measuring temperature in radio frequency heated material. IEEE Trans Microwave theory Tech 24:43-45 (1976).

4. Burdette, E.C., F.L. Cain, and J. Seals. In-vivo probe measurement technique for determining dielectric properties of VHF through microwave frequencies. IEEE Trans Microwave Theory Tech MTT 28, 414-427 (1980)

5. Cetas, T.C.. The philosophy and use of tissue-equivalent electromagnetic phantoms. In Physical Aspects of Hyperthermia, American Institute of Physics, NY, pp 441-461, (1982).

6. Chou, C.K., A.W. Guy, and R. Galambos. Auditory perception of radiofrequency electromagnetic field. 80th review and tutorial paper. J Acoust Soc Am Vol. 71(6):1321-1334 (1982).

7. Chou, C.K., G.W. Chen, A.W. Guy, and K.H. Luk. Formulas for preparing phantom muscle tissue at various radiofrequencies. Bioelectromagnetics 5(4):435-441, 1984.

8. Chou, C.K., A.W. Guy, and R.B. Johnson. SAR in Rats Exposed in 2450-MHz Circularly Polarized Waveguide. Bioelectromagnetics 5(4):389-398, 1984.

9. Chou, C.K., and A.W. Guy. Research on nonionizing radiation: Physical aspects in extrapolating infrahuman data to man. In Behavioral effects of microwave radiation absorption. J.C. Monahan and J.A. D'Andrea (Eds), HHS Publication FDA 85-8238:135-149, (1985).

10. Chou, C.K.. Use of Heating Rate (HR) and Specific Absorption Rate (SAR) in the Hyperthermia Clinic. Int. J. Hyperthermia 6(2):367-370, 1990.

11. Christensen, D.A.. A new nonperturbing temperature probe using semiconductor band edge shift. J Bioeng. 1, 541-545 (1977).

12. Gibbs, F.A.. Thermal mapping in experimental cancer treatment with hyperthermia: description and use of a semi-automatic system. Int. J. Rad. Oncol. Phys. 9, 1057-1063 (1983)-

13. Guy, A.W., J.F. Lehmann, J.A. McDougall, and C.C. Sorensen. Studies on therapeutic heating by electromagnetic energy. In Thermal Problems in Biotechnology, ASME,

8

United Engineer Center, New Yorker, pp. 26-45, (1968).

14. Guy, A.W.. Analyses of electromagnetic fields induced in biological tissues by thermographic studies on equivalent phantom models. IEEE Trans Microwave Theory Tech 19:205-214 (1971).

15. Guy, A.W., J.F. Lehmann, and J.B. Stonebridge. Therapeutic applications of electromagnetic energy. Proc IEEE 62, 55-75 (1974).

16. Guy, A.W., M.D. Webb, and C.C. Sorenson. Determination of power absorption in man exposed to high frequency electromagnetic fields by thermographic measurements on scale models. IEEE Trans Biomed Eng BME-23, 361-371 (1976).

17. Guy, A.W., M.D. Webb, A.F. Emery, and C.K. Chou. Measurement of Power Distribution at Resonant and Non-Resonant Frequencies in Experimental Animals and Models. Scientific Report No. 11, Bioelectromagnetics Research Laboratory, University of Washington School of Medicine, Seattle, Washington, March, 1978. Final Report prepared for USAF/Sam Contract No. F41609-76-C-0032.

18. Guy, A.W., C.K. Chou, and B. Neuhaus. Average SAR and SAR Distributions in Man Exposed to 450 MHz Radiofrequency Radiation. IEEE Transactions on MTT Vol. MTT-32(8):752-763, 1984

19. Guy, A.W., C.K. Chou, J.A. McDougall, and C.C. Sorensen. Measurement of shielding effectiveness of microwave protective suits. IEEE Trans. Microwave Theory and Tech. MTT-35(11):984-994, 1987.

20. Hartsgrove G, A. Kraszewski, and A. Surowiec. Simulated biological materials for electromagnetic radiation absorption studies. Bioelectromag 8(1):29-36, 1987.

21. Johnson, C.C. and A.W. Guy. Nonionizing electromagnetic wave effects in biological materials and systems. Proc IEEE 60(2):692-718 (1972).

22. Justesen, D.R. and N.W. King. Behavioral effects of low level microwave irradiation in the close-space situation: Biological effects and health implications of microwave radiation. In: Symposium Proceedings. S.F. Cleary, Ed., pp. 154-179, BRH/DBE 70-2, (1970).

23. Justesen, D.R.. Toward a prescriptive grammar for the radiobiology of non-ionizing radiations: Quantities, definitions, and units of absorbed EM energy--An assay. J Microwave Power 10:343-356 (1975).

24. Lagendijk, J.J.W. and P. Nilsson. Hyperthermia dough: a fat and bone equivalent phantom to test microwave/radiofrequency hyperthermia heating systems. Phys. Med. Biol. 30, 709-712 (1985).

25. Leonard, J.B., K.R. Foster, and T.W. Athey. Thermal properties of tissue equivalent phantom materials. IEEE Trans Biomed Eng BME 31, 533-536 (1984).

26. Matsuda, T., S. Takatsuka, Y. Nikawa, and M. Kikuchi. Heating characteristics of a 430 MHz microwave heating system with a lens applicator in phantoms and miniature pigs. Int J Hyperthermia 6(3):685-696, (1990).

27. NCRP. Radiofrequency electromagnetic fields; properties, quantities and units, biophysical interaction, and measurements. National Council on Radiation Protection and Measurements, Report 67 (March 1, 1981).

28. Olsen, R.G., T.A. Griner and G.D. Prettyman. Far-field microwave dosimetry in a rhesus monkey model. Bioelectromagnetics 1:149-160 (1980).

9

29. Phillips, R.D., E.L. Hunt, and N.W. King. Field measurements,f absorbed dose and biologic dosimetry of microwaves. Ann NY Acad Sci 247:499-509 (1975).

30. Rozzell, T.C., C.C. Johnson, C.H. Durney, J.L. Lords, and R.G. Olsen. A nonperturbing temperature sensor for measurements in electromagnetic fields. J Microwave Power 9:241-248 (1975).

31. Samulski, T.V., J. MacFall, Y. Zhang, W. Grant, and C. Charles. Non-invasive thermometry using magnetic resonance diffusion imaging: potential for application in hyperthermia oncology. Int J Hyperthermia 8(6):819-829, (1992).

32. Schepps, J.L. and K.R. Foster. The UHF and microwave dielectric properties of normal and tumor tissues: variation in dielectric properties with tissue water content. Phys Med Biol 25, 1149-1159 (1980).

33. Schwan, H.P.. Interaction of microwave and radiofrequency radiation with biological systems. IEEE Trans Microwave Theory Tech 19:146-152 (1971).

34. Steel, M.C. and R.J. Sheppard. The dielectric properties of rabbit tissue, pure water and various liquids suitable for tissue phantoms at 35 GHz. Phy Med Biol 33(4):467-472, (1988).

35. Stuchly, M.A., T.W. Athey, S.S. Stuchly, G.M. Samaras, and G. Taylor. Dielectric properties of animal tissues on vivo at frequencies 10 MHZ-1 GHz. Bioelectromag 2, 93-103 (1981).

36. Stuchly, M.A. and S.S. Stuchly. Dielectric properties of biological substances-tabulated. J Microwave Power 15, 19-26 (1980).

37. Stuchly, M.A., A. Kraszewski, and S.S. Stuchly. Implantable electric field probes-some performance characteristics. IEEE Trans Biomed Eng 31:526-530, (1984).

38. Vaguine, V.A., D.A. Christensen, J.H. Lindley and T.E. Walston. Multiple sensor optical thermometry system for application in clinical hyperthermia. IEEE Trans Biomed Eng 31:168-172 (1984).

39. Wacker, P.F. and R.R. Bowman. Quantify hazardous electromagnetic fields: Scientific basis and practical considerations. IEEE Trans Microwave Theory Tech 19:178-187 (1971).

40. Wickersheim, K.A., and R.B. Alves. Recent advances in optical temperature measurement. Indus Res Devel 21(12):82-89 (1979).

41. Wickersheim, K.A., and M.H. Sun. Fiberoptic thermometry and its application. J Microwave Power and Electromag Energy 22:85-94, (1987).

10

Table 1 Composition and Properties of Phantom Modeling Materials for Human Tissues (200- 2450 MHz)

Modeling Material	Composition (percentages by weight)	Dielectric Constant	Loss Tangent	Specific Heat	Density
Fat and bone (dry solid plastic)	84.81 laminac polyester resin 0.45 catalyst 0.24 acetylene black 14.5 aluminum powder	4.6-6.2	0.17-0.55	0.24-0.30	1.30
Muscle (moist gel)	76.5 saline solution (12-g salt/l) 15.2 powdered polyethylene 8.4 "Super Stuff" (a gelling agent)	49-58	0.33-1.7	0.86	1.0

From Guy (1971).

11

Table 2 Composition of Phantom Muscle Tissues for Various Radiofrequencies

Frequency (MHz)	Actual tissue (37°C)		Phantom tissue (22°C)						
	Dielectric constant	Conductivity (S/m)	Dielectric constant	Conductivity (S/m)	TX-151 (%)	PEP (%)	Al (%)	H$_2$O (%)	NaCl (%)
2450	47.0	2.17	47.4 ± 0.9	2.17 ± 0.08	8.46	15.01	--	75.48	1.051
915	51.0	1.28	51.1 ± 0.6	1.27 ± 0.02	8.42	15.44	--	75.15	0.996
750	52.0	1.25	52.5 ± 0.6	1.26 ± 0.04	8.42	15.44	--	75.15	0.996
433	53.0	1.18	53.5 ± 0.5	1.21 ± 0.01	8.42	15.44	--	75.15	0.996
300	54.0	1.15	54.8 ± 0.7	1.17 ± 0.01	8.42	15.44	--	75.15	0.996
200	56.5	1.00	56.7 ± 0.7	1.06 ± 0.02	8.39	15.79	--	74.92	0.894
100	71.7	0.89	71.5 ± 1.1	0.89 ± 0.01	9.81	--	2.12	87.59	0.482
70	84.0	0.79	84.7 ± 0.5	0.76 ± 0.01	10.36	--	2.72	86.50	0.424
40.68	97.0	0.68	97.9 ± 3.8	0.70 ± 0.02	9.68	--	9.20	80.82	0.303
27.12	113.0	0.60	113 ± 3.0	0.62 ± 0.02	9.70	--	9.06	80.97	0.270
13.56	149.0	0.62	149 ± 3.0	0.62 ± 0.03	9.69	--	9.15	80.88	0.280

From Chou et al (1984)

12

Table 3 Compositions of other phantom materials

Tissue	f(MHz)	ε'	σ(S/m)	Composition
Skin	2450	43	--	60% H_2O, 1% NaCl, 39% cellulose paper
Muscle	10	65.8	1.17	75.5% H_2O, 0.9% NaCl, 15.2% PEP, 8.4% TX150
	50	44.1	1.20	
	100	44.8	1.43	
	100-1000			52.4% H_2O, 45% sugar, 1.4% NaCl, 1% hydroxyetheylcellulose (HEC), 0.1% bacteriacide
	13.56		0.69	90% H_2O, 0.5% NaCl, 9.5% TX150
	30	110	0.65	76.57% H_2O, 0.153% NaCl, 13.78% Al powder, 9.495% TX150
	430	72	1.19	95.4% H_2O, 4% Agar, 0.55% NaCl, 0.05% NaN_3
	2450	50	2.18	69% H_2O, 30% gelatine, 1% NaCl
	8500	34-48	4.5-7.1	H_2O, NaCl, PEP, TX150
	10000	30-45	5.6-8.3	for formulas see original reference
Brain	100-1000			40.4% H_2O, 56% sugar, 2.5% NaCl, 1% HEC, 0.1% bacteriacide
	2450	42	2.59	59% H_2O, 1% NaCl, 40% gelatine
Viscera	13.56		0.43	90% H_2O, 0.26% NaCl, 9.7% TX150
Lung	13.56		0.12	82.15% polyester resin, 16.65% Al powder, 1.19% acetylene black, MEK catalyst
	100-1000			47% muscle and 53% microsheres
Fat and bone	13.56		0.23	83.71% polyester resin, 14.9% Al powder, 1.37% acetylene black, MEK catalyst
	30	19	0.28	79% Laminac 4110, 20.72% Al powder, 0.28% acetylene black, MEK catalyst
	451	7.3	0.038	66.67% flour, 30% oil, 3.33% of 0.9% NaCl solution
	100-1000	Castable		36% Epoxy, 36% hardener, 28% 2M KCl solution
	100-1000	Liquid		57% TWEEN, 28.5% n-Amyl alcohol, 9.5% paraffin oil, 4.5% H_2O, 0.5% NaCl

References: Cetas, 1982, Lagendijk & Nilsson, 1985, Leonard et al., 1984, Hartsgrove et al., 1987, Matsuda et al., 1990.

13

MODELS OF THE HUMAN BODY: A HISTORICAL PERSPECTIVE

James N. Lee[1] and Om P. Gandhi[2]

[1] Medical Imaging Research Laboratory, School of Medicine
[2] Department of Electrical Engineering
University of Utah
Salt Lake City, Utah 84112

Abstract

This paper gives a chronological development of the models used for electromagnetic (EM) dosimetric calculations. Starting with planar-layered models, which were followed by homogeneous and layered sphere and cylinder models, prolate spheroidal and ellipsoidal models, and relatively coarse, inhomogeneous block models, model development has advanced to a stage where resolutions on the order of millimeters are possible. We describe the development of a high-resolution model based on the MRI scans of an adult male volunteer. The MRI scans were taken with a slice thickness of 3 mm and a pixel size of 1.875 mm. We plan to use partial-body versions of this model for dosimetry at microwave frequencies for localized near-field sources such as cellular phones and police radar, at power-line frequencies to properly account for the important tissue interfaces and the anisotropic properties of the various tissues, and for design of applicators for expanding biomedical applications of EM fields.

INTRODUCTION

As the field of bioelectromagnetics has progressed, there has been a need for increasingly sophisticated models of the human body so that realistic sources of electromagnetic fields may be modeled for assessment of safety. Higher-resolution models are needed because nonuniform electromagnetic fields from several of the sources of concern are highly localized, and, at times, of microwave frequencies that do not penetrate the body more than a few tens of millimeters. Some examples of these sources are cellular phones, police radar, hair dryers, electric power drills, etc. Whereas simpler models, such as prolate spheroidal models were quite adequate for determining whole-body-averaged SARs, particularly for far-field plane-wave irradiation conditions in the early years of bioelectromagnetics, for the last ten to fifteen years, the focus has been on near-field, partial-body exposures that are encountered in real life. Since the safety guidelines of whole-body-averaged SAR of 0.4 W/kg for controlled environments and 0.08 W/kg for uncontrolled environments [1] are hardly ever exceeded in real life, the focus in recent years has been to ascertain that peak local SARs do not exceed 8.0 and 1.6 W/kg for any 1 g of tissue for the aforementioned environments, respectively.

A HISTORICAL PERSPECTIVE

The earliest of the models for absorbed EM energy calculations involved planar-layered models by Schwan and Li [2] with later analyses done by Johnson et al [3]. Although these models were useful at that time, they were incapable of taking

1

dimensionally dependent responses into account. These models were subsequently followed by lossy homogeneous and layered sphere models by Kritikos and Schwan [4], Lin et al. [5], Joines and Spiegel [6], Weil [7], and others. An advantage of using spherical shapes was that the classical Mie series solution [8] could be written for the various layers of the sphere. Though easy to handle analytically, use of the spheres revealed that the SARs are very shape-dependent. Furthermore, it was obvious that they were incapable of accounting for different polarizations of incident plane-wave irradiation. To account for the polarization effects, Johnson, Durney, and their colleagues developed prolate spheroidal, ellipsoidal, and layered cylindrical models that were relatively simple to use and provided excellent information on the whole-body-averaged SARs as a function of frequency for different polarizations of irradiation [9-13].

Since it was becoming apparent that homogeneous models are incapable of providing information on the distribution of the specific absorption rates, block models composed of cubical cells were developed for the human body by Livesay and Chen [14] and Chen et al. [15, 16], who used the method of moments to calculate the SAR distributions. To improve on the shape used by these authors, Hagmann et al. [17, 18] used a new model of the human body where 180 cubical cells of different sizes were used to form the volume most closely resembling that of an average man as given by the biometric data. Since the local SARs are of interest, special care was taken to make the size and shape of the block model as realistic as possible. Also, different complex permittivities based on the tissues for the various regions of the body were used for the block model. To improve the resolution for SAR calculations, somewhat smaller cell sizes were subsequently used, resulting in the human body being represented by 1132 cells [19].

Since the early days of bioelectromagnetics, there has been a desire to obtain SAR distributions modeling the nonuniformity of the incident fields as realistically as possible. It has also been known that electromagnetic fields associated with several of the sources do not extend to more than a small fraction of the human body. Commonly used sources such as radiofrequency sealers, for example, create leakage fields that decrease rapidly in the vertical direction with fields dropping off to a small fraction of the maximum values within 10-20 cm in each direction along the vertical axis. For biomedical applications, too, the applicators are generally quite small to apply the electromagnetic energy to the desired parts of the body. With the advent of efficient numerical techniques such as the impedance method [20, 21] and the finite-difference time-domain method [22-24], it became possible to obtain SAR distributions with the human body or parts thereof being represented by several hundred thousand cells rather than 180-1132 cells that had been possible using the method of moments. Anatomically based models of the human body were, therefore, developed [21, 23, 24] using the sectional diagrams given in the book by Eycleshymer and Schoemaker [25]. As detailed in the companion paper [26], these models defined the predominant tissue type (one of sixteen tissues such as muscle, fat, bone, blood, brain, etc.) with a resolution of 0.25 × 0.25 inch for each of the sectional diagrams. Since the sectional diagrams were available [25] for somewhat variable separations, typically 2.3-2.7 cm, a new set of equispaced layers were defined at 0.25" (0.635 cm) intervals by interpolating the data on to these layers. The database at this stage consisted of fractional volumes occupied by the various tissues in each of the cubical subvolumes or cells of dimension 0.635 cm (0.25") for each of the sides. Since the number of cells representing the human body (approximately 360,000 cells) were not

2

easy to handle with the readily accessible computers at that time (mid-1980s), two coarser models of cell dimensions 1.27 cm (0.5") and 2.54 cm (1") were then developed by combining the data for $2 \times 2 \times 2 = 8$ or $4 \times 4 \times 4 = 64$ of the original cells. Without changes in the anatomy, this process allows some variations in the total height and weight of the models. To obtain the biometrically correct height and weight of 175.5 cm and 69.6 kg for the "average" man, we had to slightly increase the cell size to 1.31 and 2.62 cm for the two models, respectively. These models of 45,024 and 5,628 cells representing the human body, respectively, were then used for a number of applications involving whole-body or partial-body exposures due to spatially uniform or nonuniform (far-field or near-field) sinusoidally varying EM fields, or for electromagnetic pulses [26-28].

With increasing computer memory and improving efficiencies of the numerical codes, it is now possible to obtain SAR distributions for coupled parts of the body represented by 1-5 million cells. Higher-resolution models with cell sizes on the order of millimeters are, therefore, being developed both in our laboratory and by Peter Dimbylow at NRPB, U. K. These millimeter-resolution models are needed to extend dosimetric calculations to microwave frequencies where the penetration depths are generally less than 1 or 2 cm. They are also needed for nonuniform, at times highly localized, electromagnetic fields where the exposed region is of the dimensions of a few centimeters. Some examples of such sources are cellular phones and police radar at microwave frequencies, and hair dryers and power drills at power-line frequencies. In the following, we describe the development of a millimeter-resolution model of the human body that is presently underway in our laboratory.

MILLIMETER-RESOLUTION MODEL OF THE HUMAN BODY

We are currently developing a high-resolution model of the human body based on MRI scans. MRI has the advantages that it uses no ionizing radiation, is capable of 1- or 2-millimeter resolution, and has high intrinsic soft-tissue contrast. High resolution allows small parts such as the lens of the eye to be represented by its own pixels, rather than be averaged in a generic "eye area". The high tissue contrast can be illustrated by comparing the physical parameters that determine contrast for fat and muscle. For 100 kev X-rays, the mass attenuation coefficient of fat is 0.163, and for muscle it is 0.167, giving a difference of 2%. For MRI at 1.5 Tesla, the T_1 relaxation time of fat is 259 ms, and for muscle it is 869 ms, giving a difference of over 300%.

The images we have acquired for this model are of a male 176.4 cm tall and weighing 64 kg. A complete set of axial images was acquired, with the imaged volume extending from the top of the head to the sole of the foot. Each image has a slice thickness of 3 mm, and a matrix of 256×256 pixels with a 48 cm field-of-view, giving a pixel size of 1.875 mm. The pulse sequence used in the acquisition is spin echo, with repetition time (TR) 600 ms, and echo time (TE) 23 ms. The short TR was chosen to enhance T_1 differences among soft tissues. Of the three main parameters determining tissue contrast in MR (T_1, T_2, and spin density), T_1 differences produce the highest contrast among soft tissues. Saturation pulses were added outside the imaging slice to reduce pulsatile blood flow artifacts.

3

The images were acquired in an interleaved, multislice format to reduce the acquisition time. For example, after acquiring a signal from slice 1, there is a wait of 600 ms before another signal can be acquired from that slice. During that time, signals are acquired from several other slices so that no time is wasted. Even with multislice imaging, the total acquisition time for the images was over 6 hours. Without multislice imaging, the acquisition time would have been about 24 hours.

The images are being segmented into 27 tissue types whose electrical properties have been established. The tissue types are fat, muscle, bone, cartilage, skin, brain/nerve, cerebral spinal fluid, intestine, spleen, pancreas, heart, blood, eye, eye humor, eye sclera, eye lens, liver, kidney, lung, bladder, stomach, ligament, compact bone, testicle, spermatic cord, prostate gland, and erectile tissue. In image segmentation, each image is separated into its component tissues. For instance, the region of the liver is outlined on the screen, and then the image pixels in that region are replaced with the number chosen to represent liver tissue. Later, when the segmented images are used in computer simulations, the computer program will invoke the frequency-dependent electrical properties of liver tissue wherever it encounters that number.

Image segmentation is being done by anatomy students using a software package from the Mayo Clinic called ANALYZE. This package allows the students to indicate a region of the image either by drawing on the screen with a mouse, or by automatic thresholding. Anatomy students were chosen because of their familiarity with cross-sectional axial images of the body. The high-resolution nature of the model is illustrated in Fig. 1 by means of a typical cross section of the head. In Table 1 we compare the weights for some of the organs for our model with those for a "reference man" [29]. There is a reasonable agreement between the two sets of weights.

It is said that before you do something right, you must do it at all. After acquiring this data set, there are two things we would do differently if we did it again. We would take into account the shift of fat relative to muscle and other water-based tissues, and the motion of the heart which causes blurring in the images.

Fat has a slightly different resonant frequency than water. This frequency shift is expressed in ppm (parts per million) of the resonant frequency of protons in the static field. For instance, at a field of 1.5 Tesla, the resonant frequency of protons is 64 MHz, and the difference in resonant frequency between fat and water is 3.5 ppm times 64 MHz, or 225 Hz.

Since position is encoded by frequency in MR imaging, fat will appear to shift in the direction of the read gradient with respect to its true position. The amount of the shift is given by

$$\Delta x = \frac{\Delta v}{\gamma G}$$

where Δx is the shift in spatial position, Δv is the difference in resonant frequency, γ is the gyromagnetic ratio for protons, and G is the amplitude of the read gradient. There is no shift in the phase encoding direction because the phase difference between fat and water from one phase encoding point to the next is constant and does not accumulate.

4

In the images we acquired, the fat shift was approximately 2 pixels. This is most easily seen in the images of the leg, where the rim of fat is shifted slightly with respect to the muscle it surrounds. We have simply told the anatomy students working on the segmentation to try and ignore the shift, and encode the images as if it weren't there.

If we acquired the images again, there are two ways to reduce the fat shift. One is to acquire the images at a lower static field strength. Since the frequency difference between fat and muscle depends on the resonant frequency, lowering the static field will reduce the shift. A second way to reduce the fat shift is to increase the amplitude of the readout gradient, and sample the spin echo faster. Unfortunately, both these cures reduce the signal-to-noise in the images, so there is a tradeoff that must be accepted. If the shift were reduced to less than one pixel in the images, it would probably not be noticeable.

The motion of the heart caused great blurring in the images acquired at the level of the heart. If we acquired the images again, we would synchronize the image acquisition to the motion of the heart so the heart would appear to remain still. The drawback is that in order to do this synchronization, one cannot interleave the slice acquisition as we did to reduce acquisition time. One solution would be to synchronize the acquisition only of those images at the level of the heart, and then acquire the rest in a multislice format as we did. This would increase the total acquisition time by only 1/2 hour, and would give a much more faithful representation of heart anatomy.

CONCLUDING REMARKS

We hope to use the new millimeter-resolution model of the human body for dosimetry at microwave frequencies for localized near-field sources such as cellular phones and police radar. In fact, the new model of the head and neck has already been used to calculate SAR distributions for an experimental cellular phone that operates at a frequency of several GHz when the phone is held against the right ear or the left ear, respectively. For this device, the antenna was not symmetrically placed and, hence, placement against the right and left ears resulted in different SAR distributions. We also plan to use the new model for dosimetric calculations at power-line frequencies where it is necessary to model the various tissue interfaces and also the anisotropic properties of some of the tissues. For such applications, we plan to use a two-step approach where a coarser model will be used to calculate the currents induced for the various subsections of the body. High-resolution equivalent-impedance models of these subsections with a proper modeling of tissue interfaces would then be used to calculate internal current densities and electric fields for the various parts of the body. The new high-resolution model of the body will also be useful for design of applicators for biomedical applications. Some of these applications are for hyperthermia, selective heating for hypothermia, and for electro- and magneto-therapy.

REFERENCES

1. IEEE C95.1-1991, "IEEE Standard for Safety Levels with Respect to Human Exposure to Radio Frequency Electromagnetic Fields, 3 kHz to 300 GHz," published by the Institute of Electrical and Electronics Engineers, Inc., 345 East 47th Street, New York, New York, 10017, April 17, 1992.

2. H. P. Schwan and K. Li, "Hazards Due to Total Body Irradiation," *Proc. IRE*, Vol. 44, pp. 1572-1581, 1956.

3. C. C. Johnson, C. H. Durney, and H. Massoudi, "Electromagnetic Power Absorption in Anisotropic Tissue Media," *IEEE Transactions on Microwave Theory and Techniques*, Vol. MTT-23, pp. 529-532, 1975.

4. H. N. Kritikos and H. P. Schwan, "Hot Spots Generated in Conducting Spheres by Electromagnetic Waves and Biological Implications," *IEEE Transactions on Biomedical Engineering*, Vol. BME-19, pp. 53-58, 1972.

5. J. C. Lin, A. W. Guy, and C. C. Johnson, "Power Deposition in a Spherical Model of Man Exposed to 1-20 MHz Electromagnetic Fields," *IEEE Transactions on Microwave Theory and Techniques*, Vol. MTT-21, pp. 791-797, 1973.

6. W. T. Joines and R. J. Spiegel, "Resonance Absorption of Microwaves by the Human Skull," *IEEE Transactions on Biomedical Engineering*, Vol. BME-21, pp. 46-48, 1974.

7. C. M. Weil, "Absorption Characteristics of Multilayered Sphere Models Exposed to UHF/Microwave Radiation," *IEEE Transactions on Biomedical Engineering*, Vol. BME-22, pp. 468-476, 1975.

8. J. A. Stratton, *Electromagnetic Theory*, McGraw-Hill, New York, Section 9.25, 1941.

9. C. H. Durney, C. C. Johnson, and H. Massoudi, "Long-Wavelength Analysis of Planewave Irradiation of a Prolate Spheroid Model of Man," *IEEE Transactions on Microwave Theory and Techniques*, Vol. MTT-23, pp. 246-254, 1975.

10. C. C. Johnson, C. H. Durney, and H. Massoudi, "Long-Wavelength Electromagnetic Power Absorption in Prolate Spheroidal Models of Man and Animals," *IEEE Transactions on Microwave Theory and Techniques*, Vol. MTT-23, pp. 739-747, 1975.

11. H. Massoudi, C. H. Durney, and C. C. Johnson, "Long-Wavelength Analysis of Planewave Irradiation of an Ellipsoidal Model of Man," *IEEE Transactions on Microwave Theory and Techniques*, Vol. MTT-25, pp. 41-46, 1977.

12. H. Massoudi, C. H. Durney, P. W. Barber, and M. F. Iskander, "Electromagnetic Absorption in Multilayered Cylindrical Models of Man," *IEEE Transactions on Microwave Theory and Techniques*, Vol. MTT-27, pp. 825-830, 1979.

6

13. C. H. Durney, "Electromagnetic Dosimetry for Models of Humans and Animals: A Review of Theoretical and Numerical Techniques," *Proceedings of the IEEE*, Vol. 68, pp. 33-40, 1980.

14. D. E. Livesay and K. Chen, "Electromagnetic Fields Induced Inside Arbitrary Shaped Biological Bodies, *IEEE Transactions on Microwave Theory and Techniques*, Vol. MTT-22, part II, pp. 1273-1280, 1974.

15. K. M. Chen and B. S. Guru, "Internal EM Field and Absorbed Power Density in Human Torsos Induced by 1-500-MHz EM Waves," *IEEE Transactions on Microwave Theory and Techniques*, Vol. MTT-25, pp. 746-755, 1977.

16. K. M. Chen and B. S. Guru, "Induced EM Fields Inside Human Bodies Irradiated by EM Waves of up to 500 MHz," *Journal of Microwave Power*, Vol. 12, pp. 173-183, 1977.

17. M. J. Hagmann, O. P. Gandhi, and C. H. Durney, "Numerical Calculation of Electromagnetic Energy Deposition for a Realistic Model of Man," *IEEE Transactions on Microwave Theory and Techniques*, Vol. MTT-27, pp. 804-809, 1979.

18. M. J. Hagmann and O. P. Gandhi, "Numerical Calculation of Electromagnetic Energy Deposition in Man with Ground and Reflector Effects," *Radio Science*, Vol. 14, No. 6 (S), pp. 23-29, 1979.

19. J. F. DeFord, O. P. Gandhi, and M. J. Hagmann, "Moment-Method Solutions and SAR Calculations for Inhomogeneous Models of Man with a Large Number of Cells," *IEEE Transactions on Microwave Theory and Techniques*, Vol. MTT-31, pp. 848-851, 1983.

20. O. P. Gandhi, J. F. DeFord, and H. Kanai, "Impedance Method for Calculation of Power Deposition Patterns in Magnetically Induced Hyperthermia," *IEEE Transactions on Biomedical Engineering*, Vol. BME-31, pp. 644-651, 1984.

21. O. P. Gandhi and J. F. DeFord, "Calculation of EM Power Deposition for Operator Exposure to RF Induction Heaters," *IEEE Transactions on Electromagnetic Compatibility*, Vol. EMC-30, pp. 63-68, 1988.

22. A. Taflove and M. E. Brodwin, "Computation of the Electromagnetic Fields and Induced Temperatures Within a Model of the Microwave Irradiated Human Eye," *IEEE Transactions on Microwave Theory and Techniques*, Vol. MTT-23, pp. 888-896, 1975.

23. D. M. Sullivan, D. T. Borup, and O. P. Gandhi, "Use of the Finite-Difference Time-Domain Method in Calculating EM Absorption in Human Tissues," *IEEE Transactions on Biomedical Engineering*, Vol. BME-34, pp. 148-157, 1987.

7

24. D. M. Sullivan, O. P. Gandhi, and A. Taflove, "Use of the Finite-Difference Time-Domain Method for Calculating EM Absorption in Man Models," *IEEE Transactions on Biomedical Engineering*, Vol. BME-35, pp. 179-186, 1988.

25. A. C. Eycleshymer and D. M. Schoemaker, *A Cross-Section Anatomy*, Appleton-Century-Crofts, New York, 1970.

26. O. P. Gandhi, "Some Recent Applications of FDTD for EM Dosimetry: ELF to Microwave Frequencies," companion paper, this issue.

27. O. P. Gandhi, "Numerical Methods for Specific Absorption Rate Calculations," Chapter 6 in *Biological Effects and Medical Applications of Electromagnetic Energy*, Om P. Gandhi, Editor, published by Prentice Hall, Englewood Cliffs, New Jersey, 1990.

28. J. Y. Chen and O. P. Gandhi, "Currents Induced in an Anatomically Based Model of a Human for Exposure to Vertically Polarized Electromagnetic Pulses," *IEEE Transactions on Microwave Theory and Techniques*, Vol. 39, pp. 31-39, 1991.

29. International Commission on Radiological Protection No. 23, "Report of the Task Group on Reference Man," published by Pergamon Press, Elmsford, New York, 1992.

8

Table 1. Comparison of weights of organs in the MRI-based high-resolution model with "reference man [29]".

| Organ	No. of Cells	Weight in Grams	
		our model	"reference man"
Brain	140012	1636.7	1400.0
Eye	1153	13.5	15.4
Skull	78453	917.1	918.5
Pancreas	9394	109.8	100.0
Liver	148979	1741.6	1800.0
Kidney	24841	290.4	310
Heart	59236	692.5	570 *
Testicle	2980	34.8	35
Intestine	84513	988.0	1010.0
Bladder	11505	134.5	71.0

* diastole without blood

9
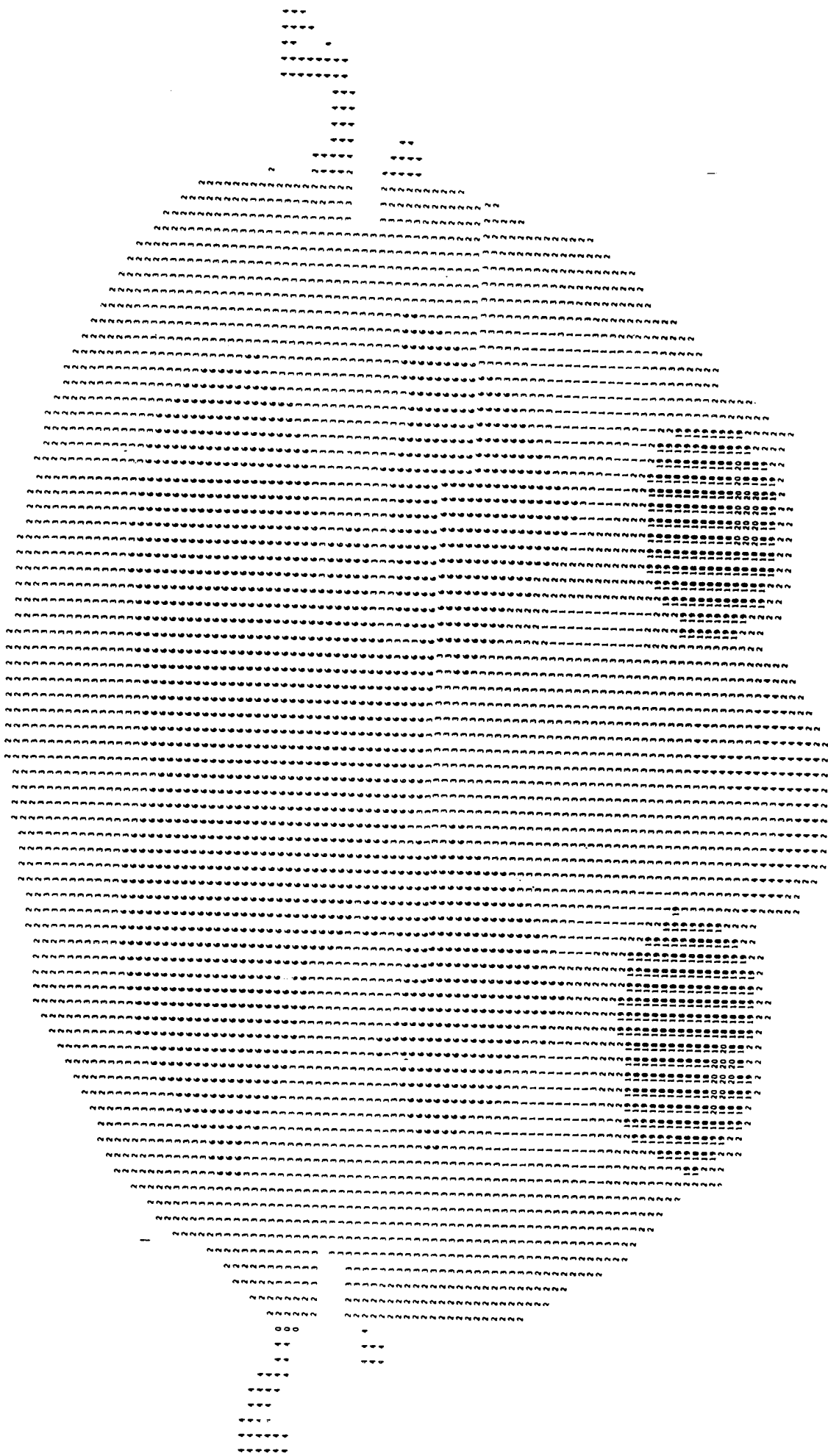
Fig. 1. A typical cross section for the MRI-based high-resolution model of the human body. Shown with a grid size of 1.875 × 1.875 mm for this section of the head are the various tissues such as brain (6), eye humor (18), fat (2), bone (3), etc.

OVERVIEW OF TISSUE PROPERTIES AND RFR DOSIMETRY

William D. Hurt
Radiofrequency Radiation Division
Armstrong Laboratory
Brooks AFB, TX 78235

INTRODUCTION

The most crucial tissue property for radio frequency (RF) dosimetry is the frequency dependent complex quantity referred to as permittivity which describes the electrical properties of the tissue. The real part of permittivity is equal to the dielectric of the tissue and the imaginary part is proportional to the conductivity. Permittivity, as well as geometry and orientation, affects how RF energy is absorbed by a body. In order for usable dose distribution estimates to be made, the various tissue types that make up the body must be considered. Accurate permittivity information about these tissue types is needed. Several researchers have reported on measurements of permittivity and least square fit techniques have been performed with two-term Debye expressions on some of these data. These results are offered for consideration when selecting permittivity values to be used for RF dosimetry calculations.

PERMITTIVITY MEASUREMENT TECHNIQUES

Measurements of the permittivity properties can be performed by numerous methods employing various sample sizes and shapes. The permittivity of the sample material is calculated from the measured reflection for nonresonant methods and from the measured resonant frequency and Q-factor for resonant methods.

A parallel-plate capacitor is sometimes used as the test cell or sample holder for dielectric disk specimens [1]. Both a two-terminal-type holder for roughly 0.01 Hz to 1 GHz [2] and a three-terminal-type for roughly less than 100 kHz are used.

The complex capacitance, which gives the permittivity, may be observed in several ways. Bridges at various frequencies may measure the change of capacitance and of conductance due to putting the sample in and out [1-3]. A symmetrically disposed bridge of capacitors has been used for permittivity measurements over the range 8 to 500 MHz [4].

The short-circuited transmission-line method is simply explained and historically referenced by Dakin and Works [5]. The method is especially easy for nonbrittle materials that may be squeezed into the line tightly to avoid air-gap errors. The

1

calculations utilize impedance methods. The reflection coefficient may be measured by a slotted line or a network analyzer, or by forming a resonator terminated by the sample [6].

The cavity resonator, at least in the TE_{01} mode, is very convenient for dielectric measurements over a wide range. The main difficulty is that commercial cavities are not available; also, any one cavity is rather narrow-banded. Either a disk sample or a coaxial rod sample may be used. An advantage of this method is that the fit error, either of a gap around a disk sample or of a top hole for inserting a rod sample, is small and easily calculated. The analysis with a disk sample is essentially the same as in the transmission-line case.

The cavity perturbation method pioneered by Birnbaum and Franeau [7] is often simple, convenient, and reasonably accurate. A simple rectangular waveguide resonator in a TE_{103} or TE_{105} mode may be constructed by squeezing thin diaphragms with irises between waveguide flanges that are suitably separated [8]. Observed data are the volumes of the cavity and the sample, and the frequency and Q, without the sample, and with the sample.

Re-entrant coaxial (hybrid) cavity resonators [9 & 10] are used in the range 0.1 to 1 GHz. A parallel-plate capacitor region for the sample is formed by a gap in the center conductor. The capacitance of this variable gap versus separation is calibrated at a low frequency [1].

Sample holders which utilize TEM lines operate over a broad frequency range. Those that are suitable for nonresonant methods can be used for measurements in the time domain [11 & 12]. The open-ended coaxial line offers flexibility, ease of sample preparation, and accuracy in measurements in vivo [13 & 14]. Until recently it was assumed, for the end-of-line-admittance model, that the probe was not radiating and was only capacitive in nature. There is significant error with this assumption for frequencies above a few GHz. Gabriel [15] has introduced admittance models in which the radiating element of the probe is explicitly treated together with inductive and capacitive components. The results show that the technique is suitable for measurements on lossy materials to 20 GHz.

PERMITTIVITY DATA

Information about the permittivity of biological systems is essential to RF dosimetry. This information is important in both experiments and calculations that include the interaction of electromagnetic fields with biological systems. Since there is some variability in the permittivity of people and other animals and some uncertainty in the measurement of permittivity of tissue-equivalent materials, knowing something about specific

2
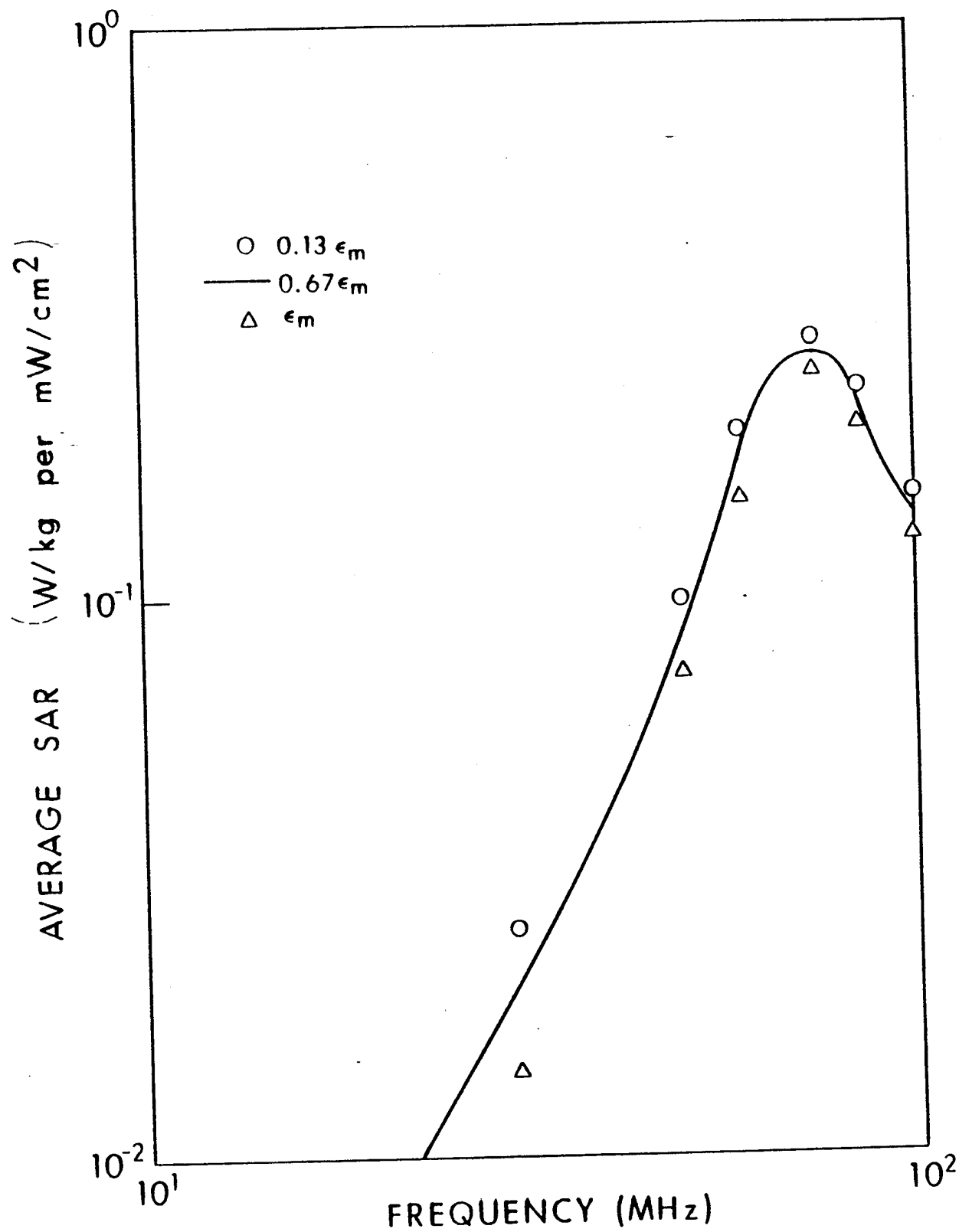
Figure 1. Calculated average SAR in a prolate spheroidal model of an average man, as a function of frequency for several values of permittivity. ϵ_m is the permittivity of muscle tissue.

3

absorption rate (SAR) sensitivity to permittivity changes is important. Figure 1 shows calculated average SAR as a function of frequency for several permittivity values in a prolate spheroidal model of an average man [16]. For this case the SAR is not extremely sensitive to changes in permittivity. This appears to be generally true for whole body average values. Since the effect of permittivity variations for local SAR cannot be reliably extrapolated from this whole body average SAR situation, it is also important to study how sensitive localized SAR values are to perturbations in permittivity. This will help in assigning appropriate levels of concern and importance to such considerations as dependence of permittivity on temperature and accuracy of measured values for the various tissue types.

A large body of data on the permittivity of biological materials has been accumulated, starting with the 1950s work of H. F. Cook and a mammoth contribution of H. P. Schwan and his colleagues. Data representative of this, as well as more recent work, [16-27] has been used to fit, by least square technique, two-term Debye expressions for several tissue types. The expression is as follows:

$$\epsilon^* = \epsilon' + j\epsilon'' = \epsilon_\infty - j\sigma_o/(2\pi\epsilon_o f) + \epsilon_1/[1+j(f/f_1)] + \epsilon_2/[1+j(f/f_2)]$$

where ϵ^* = relative permittivity,
ϵ' = relative dielectric,
ϵ'' = imaginary part of relative permittivity,
ϵ_∞ = high frequency limit of relative dielectric,
σ_o = d. c. conductivity (S/m),
ϵ_o = 8.85 X 10^{-12} F/m,
f = frequency (Hz),
ϵ_1 = contribution due to dispersion #1,
f_1 = dispersion frequency #1 (Hz),
ϵ_2 = contribution due to dispersion #2, and
f_2 = dispersion frequency #2 (Hz).

Table 1 contains the results of the two-term Debye least squares fits for frequencies greater than 10 MHz. For the instances where the best fit to the data did not occur for $1 < \epsilon_\infty < 10$, the value of 4.3 was assigned to ϵ_∞.

Interest in minimizing computer memory use for storing permittivity parameters has been expressed on the part of those performing RF dosimetry calculations on anatomically-based models of the human body. Therefore, fits were also performed for two-term Debye expressions with fixed dispersion frequencies. From the entries contained in Table 1, the values of 50 MHz and 20 GHz seem to be the two most appropriate frequencies. The results of this exercise are presented in Table 2, and the associated curves are plotted with the averaged measured values in Figures 2-12.

4

Table 1. Two-term Debye Parameters

Tissue	ϵ_∞	σ_o (S/m)	f_1 (MHz)	ϵ_1	f_2 (GHz)	ϵ_2
Blood	4.3	0.768	37.8	136	21.3	54.3
Bone	4.9	3.1×10^{-7}	2360	2.22	20.4	1.8
Brain	7.5	0.313	43.3	122	16.5	38.7
Fat	3.4	-0.0193	17.1	58.2	6.3	1.63
Heart	4.3	0.63	90.6	49.4	15.6	55.9
Kidney	4.3	0.551	24.7	166	24.5	43.2
Liver	4.3	0.406	44.2	136	21.6	41.6
Lung	4.3	0.325	81.8	69.1	15.1	28.3
Muscle	4.3	0.301	8.3	475	15.2	49.9
Skin	3.3	0.231	137	34.3	17.7	32
Spleen	4.3	0.44	26.6	289	19.8	48.1

Table 2. Two-term Debye Parameters for 0.05 and 20 GHz.

Tissue	ϵ_∞	σ_o (S/m)	$\epsilon_{.05}$	ϵ_{20}
Blood	8.6	0.778	103	50.7
Bone	4.2	3.09×10^{-7}	1.63	3.23
Brain	6	0.32	109	39.4
Fat	2.8	0.00642	12.5	1.96
Heart	4.3	0.595	105	57
Kidney	4.3	0.565	86.1	41.2
Liver	8.8	0.416	120	37.5
Lung	4.3	0.257	127	29
Muscle	4.3	0.423	46.6	50.3
Skin	4.3	0.177	105	32
Spleen	5.7	0.511	145	45.6

5

CONCLUSIONS

Permittivity measurements need to be made over a broader
frequency range for bone, the heart, and the lungs as indicated
in Figures 3, 6, and 9 respectively. Also, the reason for the
scatter in some of the data should be resolved, especially for
fat as evidenced in Figure 5. However, just as essential is an
understanding of the magnitude of the effect that variations in
permittivity have on RF dosimetry calculations. Such knowledge
will put into perspective the effort and expense appropriate for
the determination of the permittivity values of different types
of biological tissue.

$$\epsilon^* = 8.6 - 14j/f + 103/[1+j(f/.05)] + 50.7/[1+j(f/20)]$$
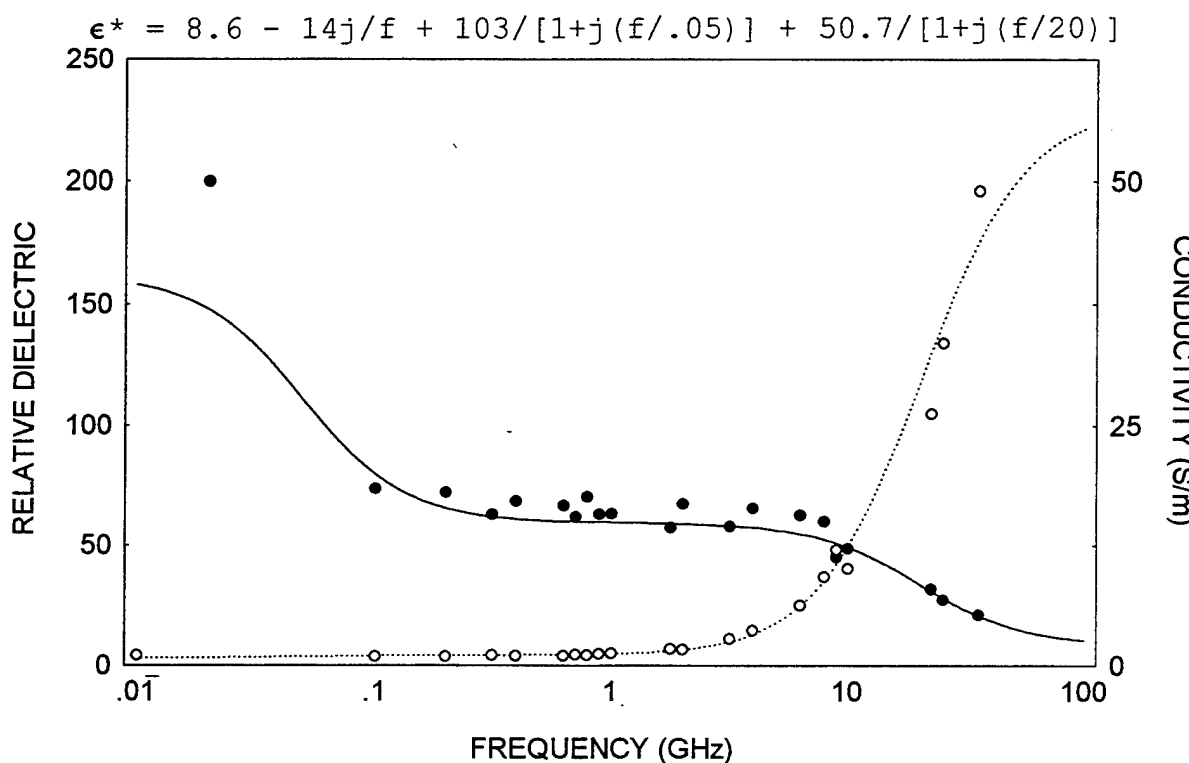
Figure 2. Permittivity of blood [16, 17, 22, 23].

6

$$\epsilon* = 4.2 + 1.63/[1+j(f/.05)] + 3.23/[1+j(f/20)]$$
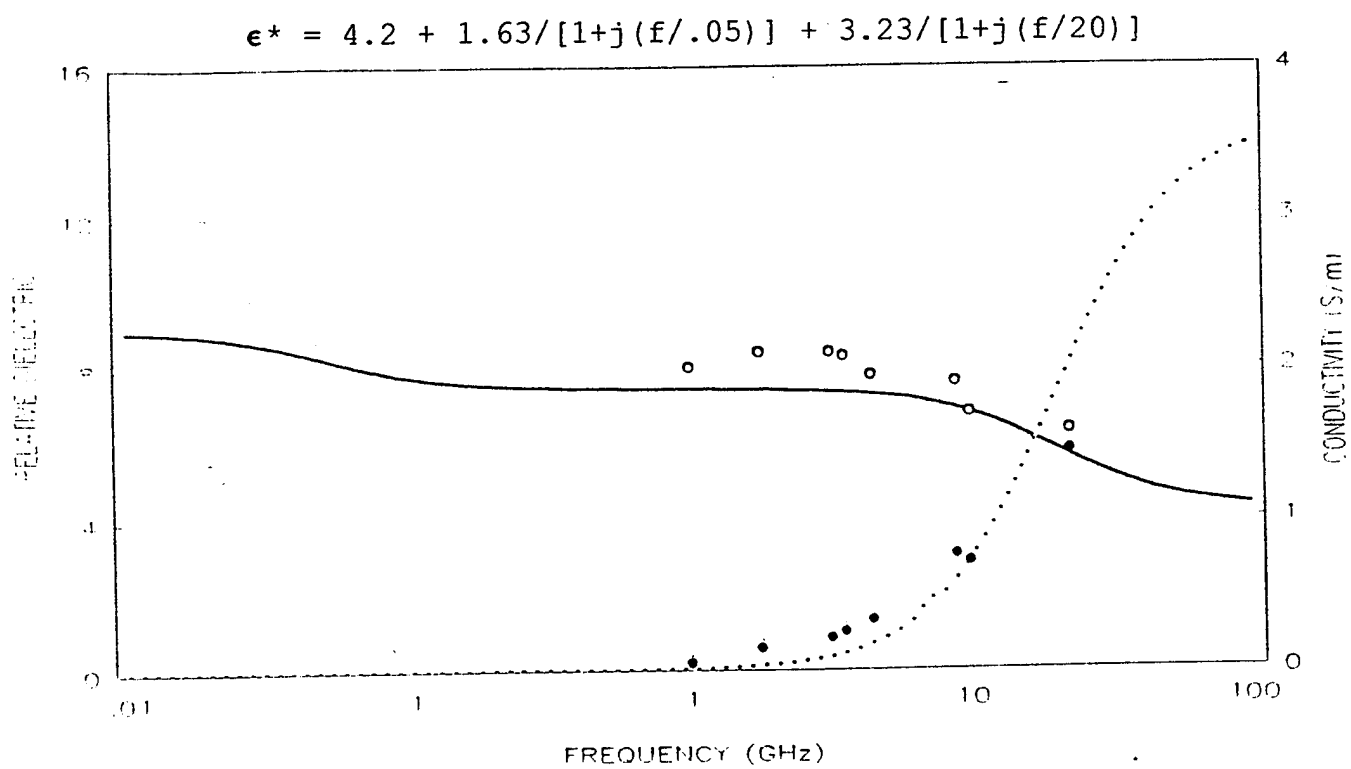
Figure 3.   Permittivity of bone [16, 17].

$$\epsilon* = 6 - 5.76j/f + 109/[1+j(f/.05)] + 39.4/[1+j(f/20)]$$
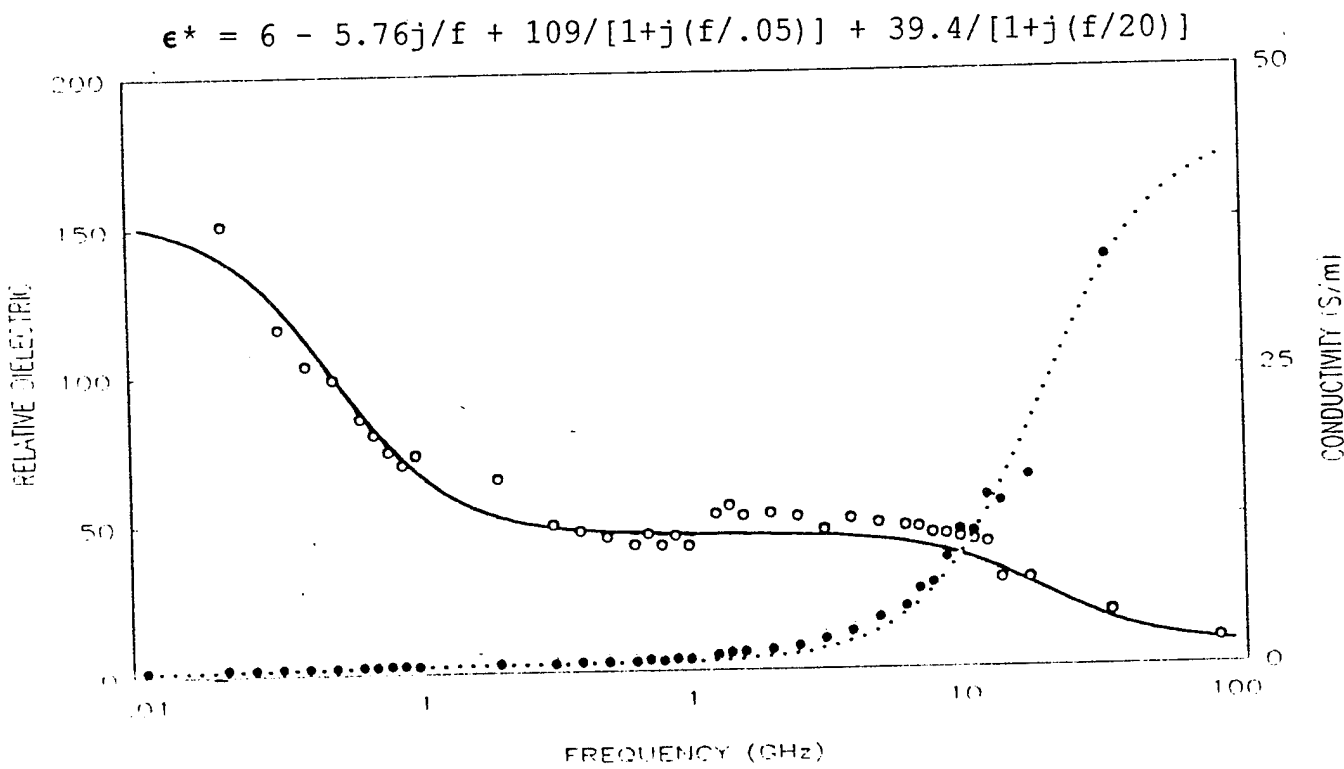
Figure 4.   Permittivity of brain tissue [16-20, 23, 26].

7

$$\epsilon^* = 2.8 - .115j/f + 12.5/[1+j(f/.05)] + 1.96/[1+j(f/20)]$$
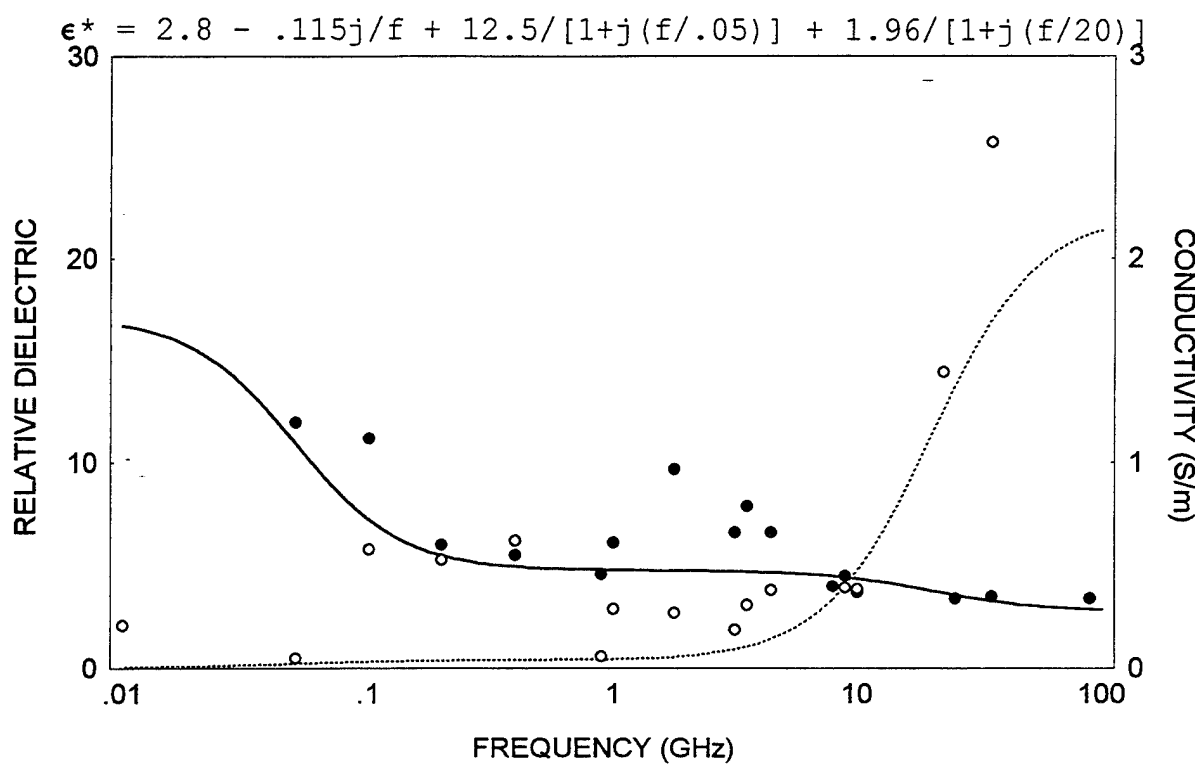
Figure 5. Permittivity of fat tissue [16, 17, 23, 26].

$$\epsilon^* = 4.3 - 10.7j/f + 105/[1+j(f/.05)] + 57/[1+j(f/20)]$$
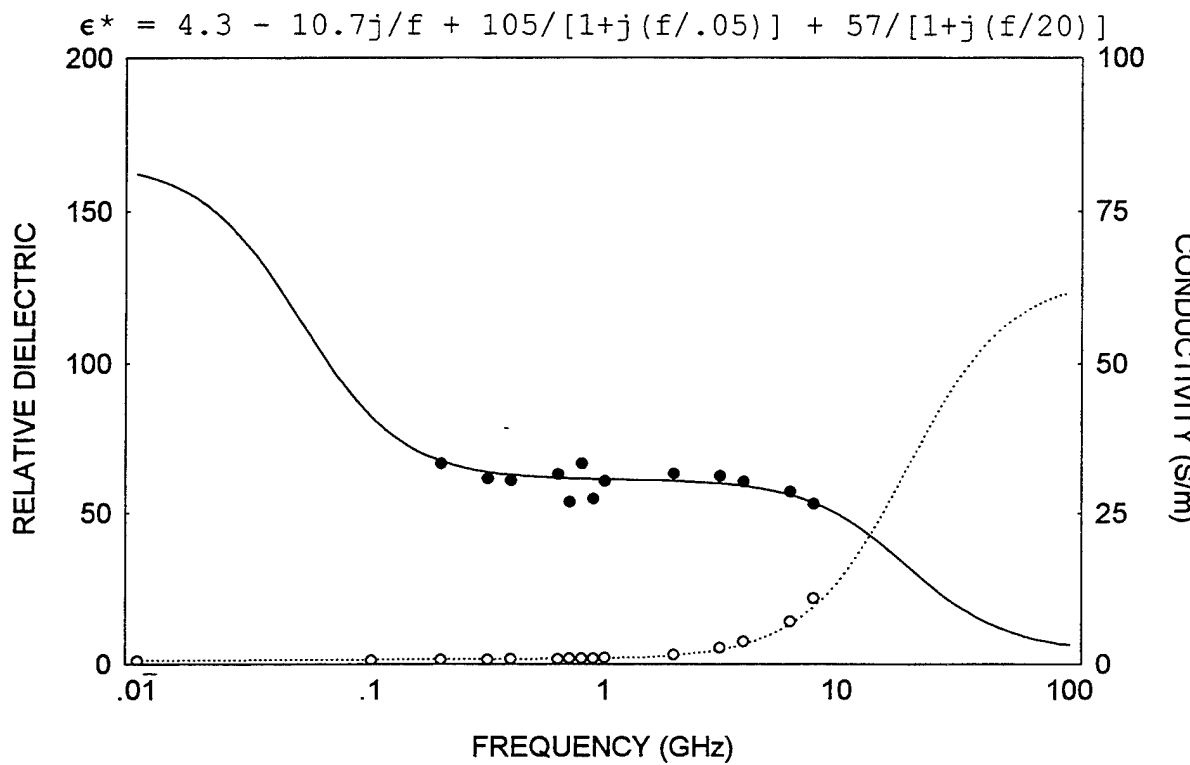
Figure 6. Permittivity of heart tissue [16, 17, 22].

8

$$\epsilon^* = 4.3 - 10.2j/f + 86.1/[1+j(f/.05)] + 41.2/[1+j(f/20)]$$
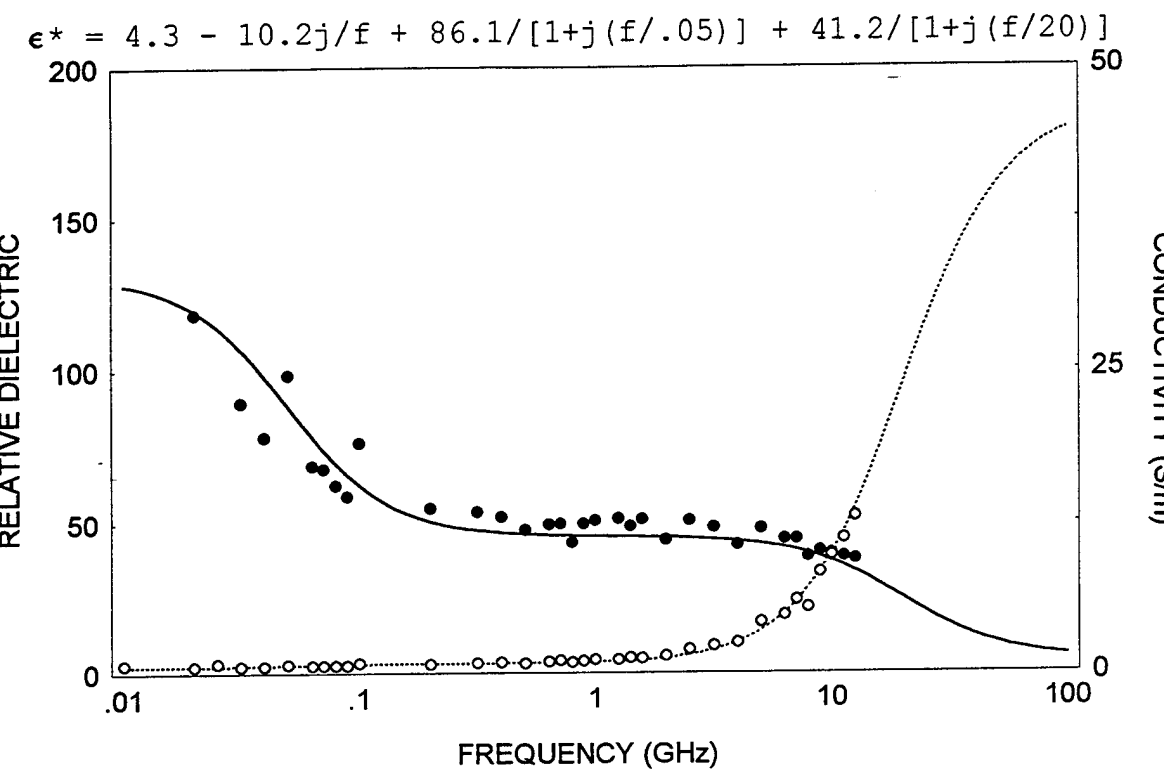
Figure 7. Permittivity of kidney tissue [16-19, 24].

$$\epsilon^* = 8.8 - 7.48j/f + 120/[1+j(f/.05)] + 37.5/[1+j(f/20)]$$
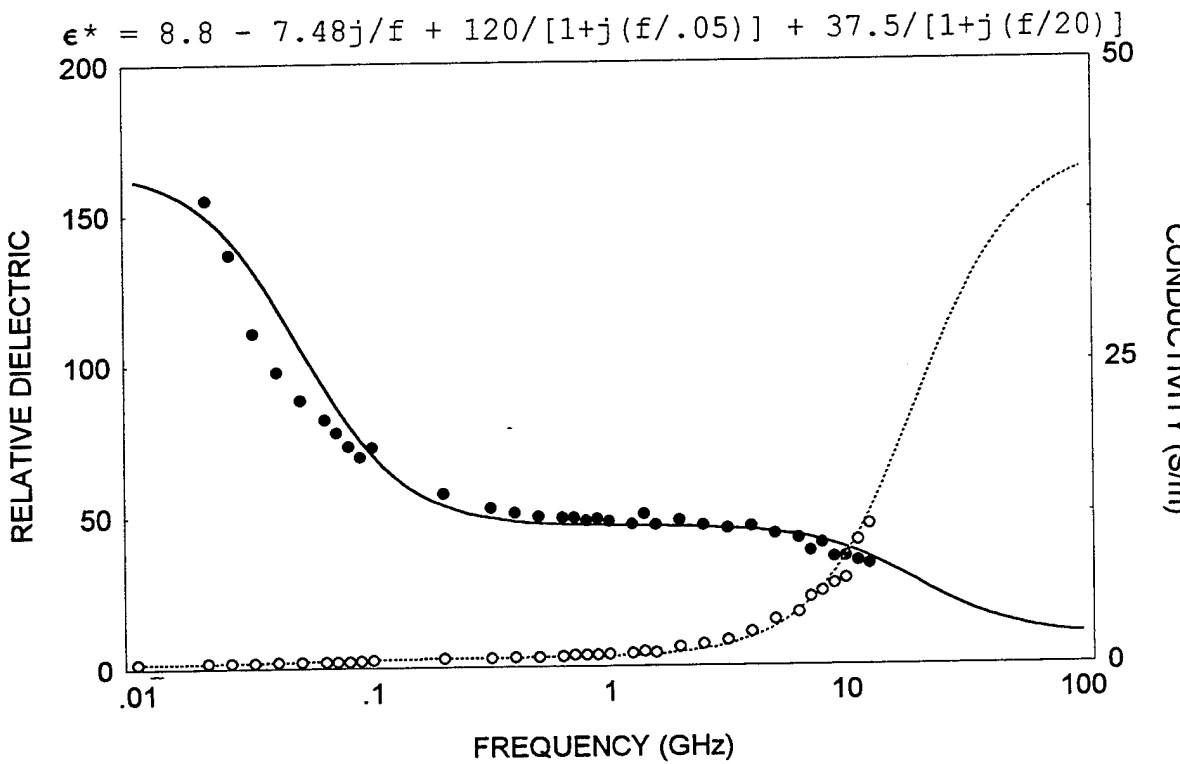
Figure 8. Permittivity of liver tissue [16-19, 24].

9

$$\epsilon* = 4.3 - 4.62j/f + 127/[1+j(f/.05)] + 29/[1+j(f/20)]$$
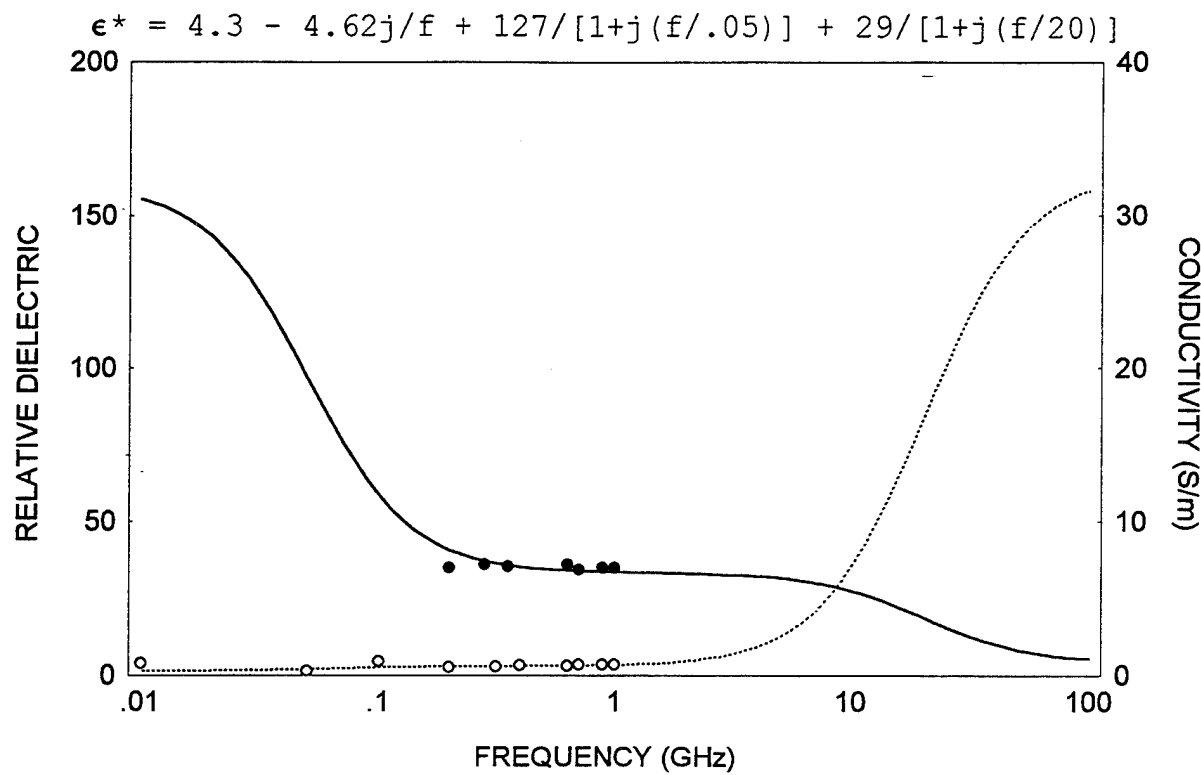
Figure 9. Permittivity of lung tissue [16, 17].

$$\epsilon* = 4.3 - 7.6j/f + 46.6/[1+j(f/.05)] + 50.3/[1+j(f/20)]$$
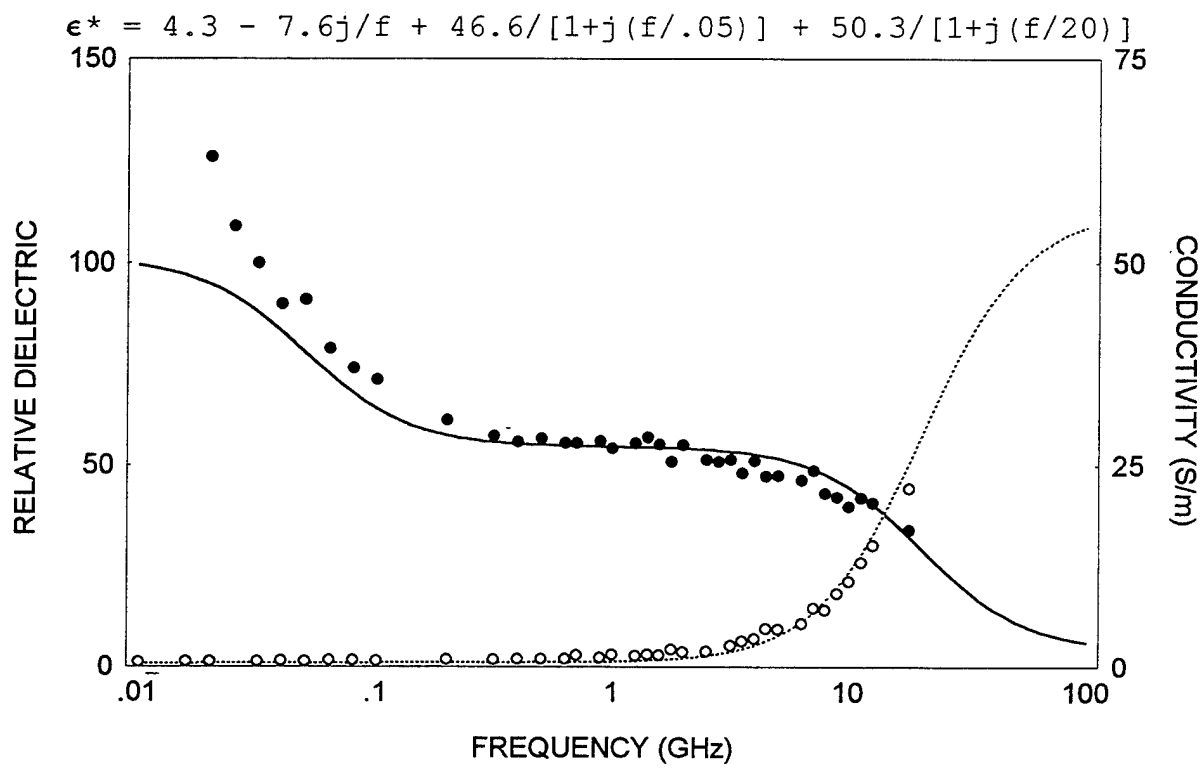
Figure 10. Permittivity of muscle tissue [16-19, 21-24].

10

$$\epsilon^* = 4.3 - 3.19j/f + 105/[1+j(f/.05)] + 32/[1+j(f/20)]$$
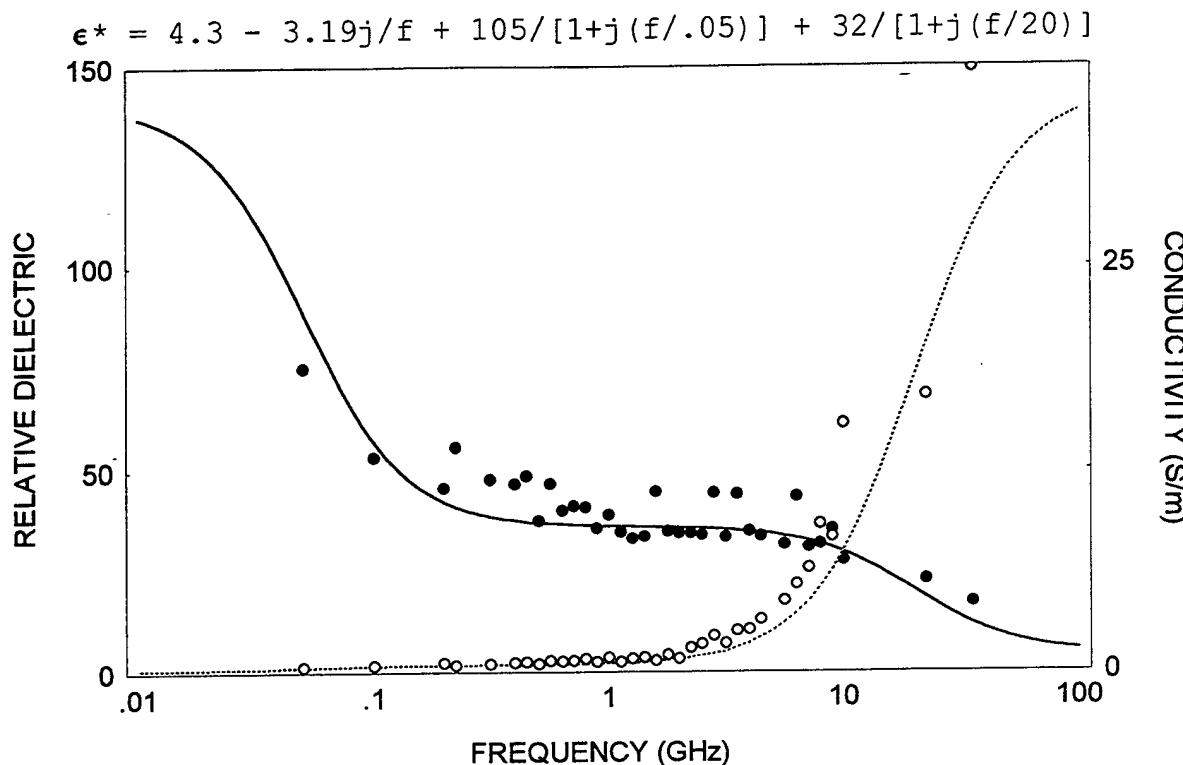
Figure 11. Permittivity of skin tissue [16, 17, 22, 23, 25, 27].

$$\epsilon^* = 5.7 - 9.2j/f + 145/[1+j(f/.05)] + 45.6/[1+j(f/20)]$$
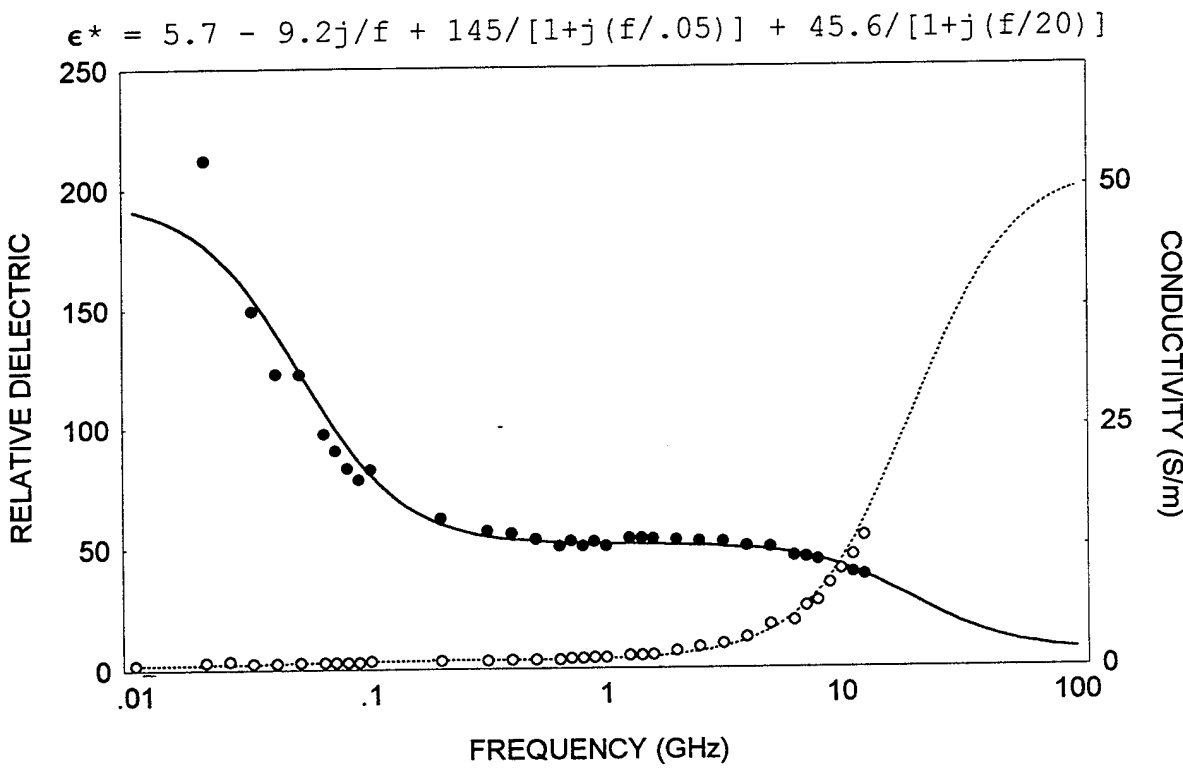
Figure 12. Permittivity of spleen tissue [16-19, 24].

11

REFERENCES

1. Hartshorn, L. and W. H. Ward. The measurements of permittivity and power factor of dielectrics at frequencies from 10^4 to 10^8 cps, J. IEE (London), Vol. 79: 567-609, Nov. 1936.

2. Broadhurst, M. G. and A. J. Bur. Two-terminal dielectric measurements up to 6×10^8 Hz, J. Res. NBS, Vol. 69C: 165-172, July 1963.

3. Dielectric Materials and Applications, A. R. von Hippel, Ed. Cambridge, Mass.: M.I.T. Press, 1954.

4. Epshtein, S. L. Izmeritel'naya Teknika, pp. 49-51, June 1963; English transl.: Measuring the parameters of insulating materials in the meter and decimeter wavelength range, Meas. Tech.: 516-517, June 1963.

5. Dakin, T. W. and C. N. Works. Microwave dielectric measurements, J. Appl. Phys., Vol. 18: 789-796, Sep. 1947.

6. Stuchly, S. S., M. A. Stuchly, and B. Carraro. Permittivity measurements in a resonator terminated by an infinite sample, IEEE Trans. Instrum. Meas., Vol. IM-27: 436-439, 1978.

7. Birnbaum, G. and J. Franeau. Measurement of the dielectric constant and loss of solids and liquids by a cavity perturbation method, J. Appl. Phys., Vol. 20: 817-818, 1949.

8. Bussey, H. E. Measurement of RF properties of materials - A survey, Proc. IEEE, Vol. 55: 1046-1053, 1967.

9. Works, C. N. Resonant cavities for dielectric measurements, J. Appl. Phys., Vol. 18: 605-612, 1947.

10. Beardsley, J. H. A variable length re-entrant cavity for dielectric measurements from 100 to 400 Mc, Rev. Sci. Instr., Vol. 24, No. 2: 180-181, 1953.

11. Nicolson, A. M. and G. F. Ross. Measurement of the intrinsic properties of materials by time-domain techniques, IEEE Trans. Instrum. Meas., Vol. IM-19: 377-382, 1970.

12. Iskander, M. F. and S. S. Stuchly. A time-domain technique for measurement of the dielectric properties of biological substances, IEEE Trans. Instrum. Meas., Vol. IM-21: 425-429, 1972.

13. Burdette, E. C., F. L. Cain, and J. Seals. In vivo probe measurement technique for determining dielectric properties

12

at VHF through microwave frequencies, IEEE Trans. Microwave Theory Tech., Vol. MTT-28: 414-427, 1980.

14. Stuchly, M. A. and S. S. Stuchly. Coaxial line reflection methods for measuring dielectric properties of biological substances at radio and microwave frequencies-A review, IEEE Trans. Instrum. Meas., Vol. IM-29: 176-183, 1980.

15. Gabriel, C. Permittivity probe modelling, AL-TR-1991-0055, Occupational and Environmental Health Directorate, Brooks Air Force Base, TX 78235-5000, Nov. 1991.

16. Durney, C. H., H. Massoudi, and M. F. Iskander. Radio frequency radiation dosimetry handbook (fourth edition), USAFSAM-TR-85-73, USAF School of Aerospace Medicine, Brooks Air Force Base, TX 78235-5301, Oct. 1986.

17. Stuchly, M. A. and S. S. Stuchly. Dielectric properties of biological substances - Tabulated, J. Microwave Power, Vol. 15: 19-26, 1980.

18. Stuchly, M. A., T. W. Athey, S. S. Stuchly, G. M. Samaras, and G. Taylor. Dielectric properties of animal tissues in vivo at frequencies 10 MHz - 1 GHz, Bioelectromagnetics, Vol. 2: 93-103, 1981.

19. Kraszewski, A, M. A. Stuchly, S. S. Stuchly, and A. M. Smith. In vivo and in vitro dielectric properties of animal tissues at radio frequencies, Bioelectromagnetics, Vol. 3: 421-432, 1982.

20. Grant, E. H. Accurate determination of the permittivity and conductivity biological tissue at centimetre and millimetre wavelength, USAFSAM-TR-84-33, USAF School of Aerospace Medicine, Brooks Air Force Base, TX 78235-5301, April 1986.

21. Hurt, W. D. Multiterm Debye dispersion relations for permittivity of muscle, IEEE Trans. Biomed. Eng., Vol. BME-32: 60-64, Jan. 1985.

22. Schwartz, J. L. and G. A. R. Mealing. Dielectric properties of frog tissues in vivo and in vitro, Phys. Med. Biol., Vol. 30: 117-124, 1985.

23. Sheppard, R. J. Accurate determination of the complex permittivity of biological tissue around 35 GHz, USAFSAM-TR-87-13, USAF School of Aerospace Medicine, Brooks Air Force Base, TX 78235-5301, Sep. 1988.

24. Scrowiec, A., S. S. Stuchly, L. Eidus, and A. Swarup. In vitro dielectric properties of human tissues at radio frequencies, Phys. Med. Biol., Vol. 32: 615-621, 1987.

13

25. Grant, J. P., R. N. Clarke, G. T. Symm, and N. M. Spyrou.
    In vivo dielectric properties of human skin from 50 MHz to
    2.0 GHz, Phys. Med. Bio., Vol. 33: 607-612, 1988.

26. Sheppard, R. J. Accurate determination of the complex
    permittivity of biological tissue at 90 GHz, 70 GHz, and
    over a broad band around 35 GHz, Interim Technical Report
    AFOSR-87-0393, European Office of Aerospace Research and
    Development, London, U. K., Feb. 1989.

27. Gabriel, C. Personal communication, June 1990.

14

RE-INVENTING ELECTROMAGNETICS: SUPERCOMPUTING SOLUTION OF MAXWELL'S EQUATIONS VIA DIRECT TIME INTEGRATION ON SPACE GRIDS

A. TAFLOVE

Department of Electrical Engineering and Computer Science, McCormick School of Engineering,
Northwestern University, Evanston, IL 60208-3118, U.S.A.

Abstract—This paper summarizes the present state and future directions of applying finite-difference and finite-volume time-domain techniques for Maxwell's equations on supercomputers to model complex electromagnetic wave interactions with structures. Applications so far have been dominated by radar cross-section technology, but by no means are limited to this area. In fact, the gains we have made place us on the threshold of being able to make tremendous contributions to non-defense electronics and optical technology. Some of the most interesting research in these commercial areas is summarized.

1. INTRODUCTION

Defense requirements for aerospace vehicles having low radar cross-section (RCS) have driven the development of large-scale methods in computational electromagnetics. We have an anomaly that the effectiveness and cost of such state-of-the-art systems depends upon our ability to develop engineering understanding of century-old basic science, Maxwell's equations (*ca* 1870). Recently, direct space-grid time-domain Maxwell's solvers have been the subject of intense interest for this application, challenging previously dominant frequency-domain integral equation approaches.

This paper summarizes the history, present state, and possible future of applying space-grid time-domain techniques for Maxwell's equations to model complex electromagnetic wave interactions. As teraflop-class supercomputers permit structures of amazing complexity and size to be modeled, the old/new theme of Maxwell's equations/RCS design will be seen to recur in areas that cut a wide swath through the core of electrical engineering. We will consider:

- The state of the full-matrix method of moments.
- The history of space-grid time-domain techniques for Maxwell's equations.
- The state of existing algorithms and meshes: basis, primary types, predictive dynamic range.
- Scaling to problems of $>10^9$ field unknowns.
- Future defense electromagnetics needs: 70 dB dynamic range; modeling of complex and composite materials; optimization of materials and shapes for RCS; integrated RCS and aerodynamics design and optimization; target identification.
- Future dual-use electromagnetics needs: antenna design; microwave and millimeter wave inte-

grated circuits; bio-electromagnetic systems; high-speed interconnects and packaging for electronic digital circuits; incorporation of models of active devices; all-optical devices, including femtosecond switches and logic gates.

Overall, advances in supercomputing solutions of Maxwell's equations based on their direct time integration on space grids place us on the threshold of being able to make large contributions to dual-use electronics and optical technology as well as RCS technology. In fact, I claim that solving Maxwell's equations at ultra-large scales will permit us to design devices having working bandwidths literally from d.c. to light.

2. THE STATE OF THE FULL-MATRIX METHOD OF MOMENTS

The modeling of engineering systems involving EM wave interactions has been dominated by frequency-domain integral equation techniques and high-frequency asymptotics. This is evidenced by the almost universal use of the method of moments (MoM)[1,2] to provide a rigorous boundary value analysis of structures and the geometrical theory of diffraction (GTD)[3,4] to provide an approximate analysis valid in the high-frequency limit. However, a number of important contemporary problems in EM wave engineering are not adequately treated by such models. Complexities of structure shape and material composition confound the GTD analysts; and structures of even moderate electrical size (spanning five or more wavelengths in three dimensions) present very difficult computer resource scaling problems for MoM.

The latter problem is particularly serious since MoM has provided virtually the only means of dealing with the non-metallic materials now

153

commonly used in aerospace design. Consider the following:

Define d_{span} as the characteristic span of a flat-configured target and λ_0 as the wavelength of the impinging radar beam such that the electrical surface area of the target (in square wavelengths) is $2(d_{span}/\lambda_0)^2$. Assume a standard triangular surface patching implementation of the electric field integral equation with the surface area of the target discretized at R divisions per λ_0. Then, the number of triangular surface patches is given by $4R^2(d_{span}/\lambda_0)^2$; and N, the number of field unknowns, is given by $6R^2(d_{span}/\lambda_0)^2$. In fact, N is the order of the MoM system matrix. With R usually taken as 10 or greater to properly sample the induced electric current distribution on the target surface, we see that N rises above 10,000 for d_{span} greater than $4\lambda_0$. Further, we see that N increases quadratically as λ_0 drops (radar frequency increases) and the computational burden for LU decomposition increases as the *sixth power* of frequency (order of N^3).

Let us see what this means in terms of program running time for the recently introduced CRAY C-90 supercomputer. First, assume that d_{span} is on the order of 10 m, perhaps typical of a jet fighter. N rises above 40,000 at a radar frequency of 240 MHz and the CRAY C-90 running time is projected to be less than 3 h, based upon much experience with the CRAY Y-MP/8 machine.[5] Up an octave to 480 MHz, N increases to 160,000 and the C-90 running time projects to be 8 days, a 64-fold (2^6) increase. Up still another octave to 960 MHz, N increases to 640,000 and the C-90 running time projects to be 1 year, 5 months. The latter assumes that: (a) we have enough disk drives to store the trillion-word MoM matrix; (b) we find acceptable the error accumulation resulting from the million-trillion floating-point operations on MoM matrix elements having precisions of only perhaps 1 part in 10,000; and (c) the computer system stays up continuously for over 1 year.

It is quite clear that the traditional, full-matrix MoM computational modeling of an entire aerospace structure such as a fighter plane is at present impractical at radar frequencies much above 500 MHz, despite advances in supercomputer hardware and software. However, radar frequencies of interest go much higher than 500 MHz, in fact up to 10 GHz or more. Much research effort has been expended in deriving alternative iterative frequency-domain approaches (conjugate gradient, spectral, etc.) that preserve the rigorous boundary-integral formulation of MoM while realizing dimensionally reduced computational burdens. These would permit, in principle, entire aircraft modeling at radar frequencies well above 500 MHz. However, these alternatives may not be as robust as the full-matrix MoM, that is, providing results of engineering value for a wide class of structures without the user wondering if the algorithm is converged.

3. HISTORY OF SPACE-GRID TIME-DOMAIN TECHNIQUES FOR MAXWELL'S EQUATIONS

The problems involved in applying frequency-domain, dense-matrix MoM technology to large-scale RCS modeling have prompted a rapid recent expansion of interest in an alternative class of non-matrix approaches: direct space-grid time-domain solvers for Maxwell's time-dependent curl equations. The new approaches appear to be as robust and accurate as MoM, but have dimensionally-reduced computational burdens to the point where whole-aircraft modeling for RCS is becoming possible at frequencies above 1 GHz. They are analogous to existing mesh-based solutions of fluid-flow problems in that the numerical model is based upon a direct, time-domain solution of the governing partial differential equation. Yet, they are very non-traditional approaches to CEM for engineering applications, where frequency-domain methods (primarily MoM) have dominated.

Table 1 summarizes key developments and publications in the history of direct space-grid time-domain solvers for Maxwell's time-dependent curl equations. As can be seen, both the pace and range of applications of FD-TD and other time-domain grid-based models of Maxwell's equations are expanding rapidly. These efficient volumetric solutions in the time domain are making possible applications in areas far beyond those of the method of moments. In this regard, this paper seeks to explore selected areas of high promise.

4. STATE OF EXISTING ALGORITHMS AND MESHES

4.1. Basis

FD-TD and FV-TD are direct solution methods for Maxwell's equations. They employ no potentials. Rather, they are based upon volumetric sampling of the unknown near-field distribution (E and H fields) within and surrounding the structure of interest, and over a period of time. The sampling in space is at a sub-wavelength (sub-λ_0) resolution set by the user to properly sample (in the Nyquist sense) the highest near-field spatial frequencies thought to be important in the physics of the problem. Typically, 10–20 samples per illumination wavelength are needed. The sampling in time is selected to insure numerical stability of the algorithm.

Overall, FD-TD and FV-TD are marching-in-time procedures which simulate the continuous actual EM waves by sampled-data numerical analogs propagating in a computer data space. Time-stepping continues as the numerical wave analogs propagate in the space grid to causally connect the physics of all regions of the target. All outgoing scattered wave analogs ideally propagate through the lattice truncation planes with negligible reflection to exit the region. Phenomena such as induction of surface currents, scattering and multiple scattering, aperture penetration and cavity excitation are modeled time

Table 1. Partial history of space-grid time-domain techniques for Maxwell's equations

1966	Yee[6] described the basis of the first space-grid time-domain technique, later called the finite-difference time-domain (FD-TD) method. FD-TD implements the spatial derivatives of the curl operators using finite differences in regular interleaved (dual) Cartesian space meshes for the electric and magnetic fields. Simple leapfrog time integration is employed
1975	Taflove and Brodwin published the correct numerical stability criterion for Yee's algorithm and the first grid-based time-integration of a two-dimensional EM scattering problem all the way to the sinusoidal steady state,[7] as well as the first three-dimensional grid-based computational model of EM wave absorption in complex, inhomogeneous biological tissues[8]
1977	Holland[9] and Kunz and Lee[10] applied the Yee algorithm to electromagnetic pulse (EMP) interaction problems
1980	Taflove coined the term "FD-TD" and published the first validated FD-TD models of EM wave penetration of a three-dimensional metal cavity[11]
1981	Mur published an accurate and numerically stable second-order radiation boundary condition for the Yee grid[12]
1982, 1983	Umashankar and Taflove published the first FD-TD EM wave scattering models computing near fields, far fields and RCS for two-dimensional structures[13] and three-dimensional structures[14]
1987, 1988	Kriegsmann and coworkers introduced modern radiation boundary condition theory to the engineering EM community[15,16]
1987–	Sullivan, Gandhi, Taflove and coworkers commenced publishing a series of articles applying FD-TD to model EM wave interactions, especially hyperthermia, with complex three-dimensional models of humans[17-20]
1987–	Taflove, Umashankar and coworkers introduced contour-path, subcell techniques to permit FD-TD modeling of EM wave coupling to thin wires and wire bundles,[21] EM wave penetration through cracks in conducting screens[22] and conformal surface treatments of curved structures[23]
1988–	Finite-element time-domain (FE-TD), body-fitted finite-volume time-domain (FV-TD) and unstructured or partially unstructured meshes for Maxwell's equations were introduced by Cangellaris et al.,[24] Shankar et al.,[25] McCartin et al.,[26] and Madsen and Ziolkowski[27]
1989–	FD-TD modeling of digital circuit interconnects and microstrips was introduced by Liang et al.,[28] Shibata and Sano,[29] Sheen et al.[30] and Ko and Mittra[31]
1990–	FD-TD modeling of frequency-dependent dielectric permittivity was introduced by Luebbers et al.,[32] and Joseph et al.[33]
1990–	FD-TD modeling of antennas was introduced by Maloney et al.,[34] Tirkas and Balanis[35] and Katz et al.[36]
1990–	FD-TD modeling of picosecond optoelectronic switches was introduced by Sano and Shibata[37] and El-Ghazaly et al.[38]
1991–	FD-TD modeling of the propagation of femtosecond optical pulses in non-linear dispersive media was introduced by Goorjian and Taflove[39] and Ziolkowski and Judkins[40]
1992–	FD-TD modeling of lumped-circuit elements (resistors, inductors, capacitors, diodes and transistors) in a two-dimensional EM wave code was introduced by Sui et al.[41]

step by time step by the action of the curl equations analog. Self-consistency of these modeled phenomena is generally assured if their spatial and temporal variations are well resolved by the space and time sampling process. In fact, the goal is to provide a self-consistent model of the mutual coupling of all of the electrically-small volume cells comprising the structure and its near field, even if the structure spans tens of λ_0 in three dimensions and there are tens of millions of space cells.

Time-stepping is continued until the desired late-time pulse response or steady-state behavior is observed. An important example of the latter is the sinusoidal steady state, wherein the incident wave is assumed to have a sinusoidal dependence and time-stepping is continued until all fields in the sampling region exhibit sinusoidal repetition. This is a consequence of the limiting amplitude principle. Extensive numerical experimentation has shown that the number of complete cycles of the incident wave required to be time-stepped to achieve the sinusoidal steady state is a function of:

(1) *Target electrical size*. For many targets, this requires a number of time steps sufficient to permit at least two front-to-back-to-front traverses of the target by a wave analog. For example, assuming a target spanning $10\lambda_0$, at least 40 cycles of the incident wave should be time-stepped to approach the sinusoidal steady state. For a grid resolution of $\lambda_0/10$, this corresponds to 800 time steps for FD-TD.

(2) *Target Q factor*. Targets having well-defined low-loss cavities or low-loss dielectric compositions may require the number of complete cycles of the incident wave to be time-stepped to approach the Q factor of the resonance; because Q can be large even for electrically moderate size cavities, this can dictate how many time steps the FD-TD or FV-TD code must be run.

In the RCS area, target electrical size may often be the dominant factor. Cavities for RCS problems (such as engine inlets) tend to be open and therefore moderate Q; and the use of radar-absorbing material (RAM) serves further to reduce the Q factors of structures.

4.2. *Primary types*

The primary FD-TD and FV-TD algorithms used today are fully explicit second-order accurate grid-based solvers employing highly vectorizable and concurrent schemes for time-marching the six vector components of the EM near field at each of the

volume cells. The explicit nature of the solvers is maintained by either leapfrog or predictor–corrector time integration schemes. Second-order accurate radiation boundary conditions are used to simulate the extension of the problem space to infinity, thereby minimizing error due to the artifactual reflection of outgoing numerical wave modes at the mesh outer boundary.

Present methods differ primarily in how the space grid is set up. In fact, gridding methods can be categorized according to the degree of structure or regularity in the mesh:

(1) *Almost completely structured.* Space cells more than one or two cells from the structure of interest are organized in a completely regular manner, for example, using a uniform Yee Cartesian mesh. Only the cells adjacent to the structure are modified in size and shape to conformally fit the structure surface.[23,27]

—Advantage: computationally efficient, because there are relatively few modified cells requiring special storage to locate the cells in the mesh and special computations to perform the field updates. In fact, the number of modified cells (proportional to the surface area of the structure) becomes arbitrarily small compared with the number of regular mesh cells as structure size increases. As a result, the computer memory and running time needed to implement a fully conformal model can be indistinguishable from that required for a stepped-surface model. Further, an ultra-fast, minimal memory, Yee-like algorithm can be used for the regular space cells.

—Advantage: mapping of the mesh onto a parallel–vector computer or massively parallel computer is straightforward.

—Advantage: artifacts due to refraction and reflection of numerical wave modes propagating across global mesh distortions are not present. This is especially important for three-dimensional structures having substantial EM coupling between electrically disjoint sections, or reentrant regions.

—Disadvantage: geometry generation software for this type of meshing has not reached the mature state achieved for other types. Considerable work remains.

—Disadvantage: thin target surface coatings do not conform to mesh boundaries. These are best modeled here using surface impedances.

(2) *Body-fitted.* The space grid is globally distorted to fit the shape of the structure of interest.[25] Effectively, a coordinate transformation between a non-Cartesian physical mesh and a Cartesian logical mesh is implemented.

—Advantage: well-developed geometry generation software is available from the CFD community. Aerodynamic shapes appropriate for the RCS problem are nicely handled.

—Advantage: thin target surface coatings naturally conform to mesh boundaries.

—Advantage: mapping of the logical mesh onto a parallel–vector computer or massively parallel computer is straightforward.

—Disadvantage: relative to the baseline Yee algorithm, extra computer storage must be allocated to account for the three-dimensional position and stretching factors of each space cell. Further, extra computer arithmetic operations must be performed to implement Maxwell's equations at each cell and/or to enforce EM field continuity at the interfaces of adjacent cells. As a result, the number of floating point operations needed to update the six field components at a space cell over one time step can exceed that of the Yee algorithm by as much as 20:1, thereby increasing running times by the same amount with respect to FD-TD.

—Disadvantage: artifacts due to refraction and reflection of numerical wave modes propagating across global mesh distortions will be present. These errors arise because the phase velocity of numerical wave modes propagating in the mesh is a function of position in the mesh, as well as angle of propagation. These artifacts are important for three-dimensional structures having substantial EM coupling between electrically disjoint sections, or reentrant regions, and may limit the predictive dynamic range (thereby limiting the ability to model low-observable structures).

(3) *Completely unstructured.* The space containing the structure of interest is completely filled with a collection of solid cells of varying sizes and shapes, but conforming to the structure surface.[26]

—Advantage: geometry generation software is available. This software is appropriate for modeling extremely complicated three-dimensional shapes possibly having volumetric inhomogeneities, for example inhomogeneous radar absorbing material.

—Disadvantages: the same as for the body-fitted meshes.

—Another disadvantage: mapping of the logical mesh onto a parallel–vector computer or massively parallel computer is not straightforward.

At present, the optimal choice of computational algorithm and mesh is not obvious. Clearly, there are important tradeoff decisions to be made. For the next several years, we can expect considerable progress in this area as various groups develop their favored approaches and perform validations.

4.3. *Predictive dynamic range*

For computational modeling of the RCS of aerospace vehicles (especially low-observable vehicles) using space-grid time-domain codes, it is useful to define a predictive dynamic range, D, analogous to the "quiet zone" figure of merit for an experimental anechoic chamber:

$$D = 10 \log(P^{inc}/P^{scat,min}) \text{ decibels,}$$

where P^{inc} is the power density of a modeled incident plane wave in the space grid, and $P^{scat,min}$ is the minimum observable local power density of a modeled scattered wave at any bistatic angle. At levels lower than this the accuracy of the computed scattered field degrades to poorer than 1 dB (or some other criterion).

This definition succinctly quantifies the reality that weak, physical numerical wave analogs propagating in the space grid exist in an additive noise environment due to the non-physical propagating wave analogs caused by the imperfect radiation boundary conditions. In addition to additive noise, the desired physical wave analogs undergo gradual progressive deterioration while propagating due to accumulating numerical dispersion artifacts, including phase velocity anisotropies and inhomogeneities within the mesh.

Since 1982, researchers have accumulated solid evidence for a predictive dynamic range of the order of 40 dB for the present class of second-order accurate space-grid time-domain codes when used to calculate monostatic and bistatic RCS. This value is reasonable if one considers the additive noise due to imperfect radiation boundaries to be the primary limiting factor, since existing second-order radiation boundary conditions yield effective reflection coefficients of about 1% (-40 dB), with an additional factor of perhaps -10 dB provided by the normal $r^{-1/2}$ rolloff (in two dimensions) or r^{-1} rolloff (in three dimensions) experienced by the outgoing scattered waves before reaching the radiation boundaries. Figure 1 illustrates a typical result for bistatic RCS dynamic range when using Cartesian-grid FD-TD with automated local mesh contouring to conform to curved target surfaces. Here, the scattering geometry consists of two 1 λ_0-diameter metal spheres separated by 1 λ_0 air gap, and the FD-TD grid has a uniform space resolution of 0.05 λ_0. The benchmark data are provided by a quasi-analytic frequency-domain approach, the generalized multipole technique (GMT).[42]
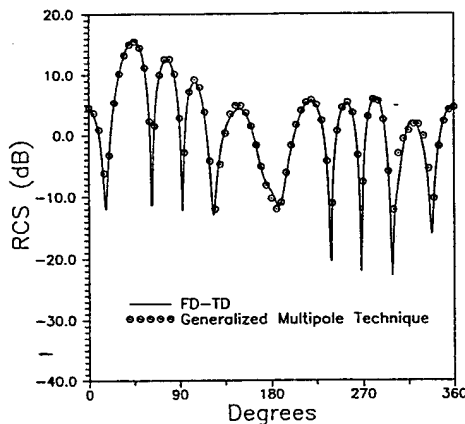

Fig. 1. Comparison of FD-TD and generalized multipole technique data for the bistatic RCS of two 1-λ diameter spheres separated by a 1-λ air gap, illuminated at oblique incidence.

Is more dynamic range needed? Certainly yes, if a better job is to be done in modeling specially shaped targets having low observability features. A good example of such a shape is the NASA almond,[43] which has been demonstrated to have monostatic RCS variations of 60 dB or more occurring over broad angular ranges. However, going from 40 to 60 or 70 dB will not be simple: We will require the development of advanced radiation boundary conditions having effective reflection coefficients of 0.1% or better, thereby reducing this contribution to the grid noise by 20 dB or more; and we will have to shift to space-sampling, time-integration algorithms having dimensionally better accuracy than the second-order procedures common today. A 20 dB reduction in the grid noise contribution due to dispersive effects accumulating on propagating numerical waves is needed to permit the use of grid resolutions no finer than those of today's algorithms.

5. SCALING TO PROBLEMS OF GREATER THAN 10^9 FIELD UNKNOWNS

5.1. Why this problem size is needed

Three-dimensional electromagnetic wave interaction problems modeled on volumetric space grids at the size level of 10^9 unknowns begin to have major engineering applications. For example, these might include: entire fighter planes illuminated by radar at 1 GHz and above; entire personal-computer-size multi-layer circuit boards modeled layer by layer for digital signal propagation, crosstalk and radiation; and entire microstrip circuits and antennas.

At this level, the goals are to achieve algorithm/computer architecture scaling such that for N field unknowns to be solved on M processors, we wish to approach an order (N/M) scaling of the computational modeling time.

5.2. Algorithm scaling factors

Is there a "best" EM computational algorithm to approach the ideal order (N) scaling of the computational modeling time? A consensus appears to be emerging that the class of non-matrix, space-grid time-domain solvers has the most promise. If robust algorithms for spatial or domain decomposition[44] cannot be achieved, the class of matrix-based frequency-domain methods may fade as a viable alternative because of difficult computational and error propagation problems associated with any large matrix, whether dense or sparse.

Let us now consider the factors involved in determining the computational burden for the class of non-matrix, space-grid time-domain solvers.

(1) *Number of grid cells*, N. The six vector electromagnetic field components located at each grid cell must be updated at every time step. This yields by itself an order (N) scaling.

(2) *Number of time steps*. A completely self-consistent solution in the time domain mandates that

numerical wave analogs propagate over time scales sufficient to causally connect each portion of the structure of interest. Therefore, in three dimensions, it can be argued that the number of time steps increases as a characteristic electrical length of the structure and thus a fractional power function of N such as $N^{1/3}$. The number of time steps must also be adequate to march through "ring-up" and "ring-down" times of energy storage features such as cavities and cavity-backed apertures.

(3) *Cumulative propagation errors.* Additional computational burdens may arise due to the need for either progressive mesh refinement or progressively higher-accuracy algorithms to bound cumulative positional/phase errors for propagating numerical modes in progressively enlarged meshes. Any need for progressive mesh refinement would feed back to Factor 1.

It appears likely that for most RCS problems, Factors 2 and 3 will be weaker functions of the size of the modeled structure than Factor 1. This is because geometrical scattering features at increasing electrical distances from each other become more and more weakly coupled due to radiative and other losses acting on electromagnetic wave energy propagating between these features. However, at this time there is insufficient experience in the grid-based modeling community with three-dimensional structures in this electrically-large size regime to provide meaningful comment.

5.3. *Computer architecture scaling factors*

Is there a "best" computer architecture to approach the ideal 1/order(M) scaling of the computational modeling time as the number of processors, M, increases? At present, the optimum connectivity of multi-processors is not clear. In 1993, the following manufacturers will offer massively parallel machines of varying architectures having claimed peak performances exceeding 100 Gflops (0.1 Tflop):

Intel:	Paragon
Cray Research:	MPP0
Thinking Machines:	CM-5.

In addition, Cray Research continues to develop its line of conventional general purpose vector-processing supercomputers descending from the CRAY Y-MP and C-90 machines. This will lead to a 100 + Gflop general purpose machine, the CRAY C-95, in 1994–1995.

5.4. *Results to date*

A number of groups have implemented large-scale grid-based Maxwell's equation solvers on vector-processing and massively parallel supercomputers.[5,25,45–47] Sufficient experience has been accumulated to justify the following statements:

(1) Concurrencies very close to 100% (i.e. an algorithm speedup factor equal to eight if the number of available processors equals eight) have been achieved with the CRAY Y-MP/8 under the CRAY autotasking (automatic multitasking) compiler for FD-TD and FV-TD. Average processing rates exceeding 1.6 Gflops were achieved for full FORTRAN programs. Performance scaling looks excellent at least through 16 high-performance (CRAY C-90 class) processors.

(2) Good to very good concurrencies for FD-TD can also be achieved using the JPL/Intel Hypercube. Performance scaling looks good into the hundreds of moderate-performance (Intel I-860 class) processors.

(3) For grid-based Maxwell's solvers, the CRAY Y-MP and JPL/Intel Hypercube machines were much easier to program and achieved substantially better fractions of their peak speeds than the CM-2 Connection Machine, when the CM-2 was programmed using the PARIS assembler.

(4) The volumetric space-grid time-domain solvers are already more efficient than surface-patching MoM. In one example,[5,47] FD-TD was used to conformally model an electrically large ($25 \lambda_0 \times 10 \lambda_0 \times 10 \lambda_0$) three-dimensional serpentine jet engine inlet. Here, the projected CRAY C-90 time is only 30 s per illumination angle (involving time-marching 23,000,000 vector field components over 1800 time steps), or 1.6 days for 5000 angles. In comparison, the standard full-matrix MoM set up a dense matrix of approximately 450,000 equations, assuming that the $1500 \lambda_0^2$ area of the engine inlet is discretized at 10 divisions per λ_0. The projected CRAY C-90 running time for LU decomposition and backsolve of this matrix is about 4 months for 5000 angles. Overall, the speedup when using FD-TD would be at least 75:1, with speedup factors much larger than this if we account for the likelihood of using FD-TD to evaluate the inlet RCS simultaneously for many frequencies by using an impulsive excitation and discrete Fourier transformation of the scattered field.

5.5. *The jet fighter model*

Consider again modeling a jet fighter, but now in the context of FD-TD. Assuming dimensions of $20 \times 20 \times 5$ m for the space grid and assuming a radar frequency of 1 GHz ($\lambda_0 = 0.3$ m; resolution = 3 cm), the space grid would be of the order of 75,000 λ_0^3 (450,000,000 vector field components) and the FD-TD central memory requirement would be about 1.3 Gword. This central memory size is currently feasible with 1–4 billion-word memory options of the CRAY Y-MP series. Running time on the C-90 is projected to be in the range 20–25 min per illumination angle. Modeling of the fighter at radar frequencies of 2 GHz and higher would be possible using well-known asynchronous out-of-core techniques that permit I/O to and from multiple disk drives to be performed concurrently with the floating point operations.

6. FUTURE DEFENSE ELECTROMAGNETICS NEEDS

Goals for computational electromagnetics modeling capabilities in the defense area have been and remain driven by the design of low-observable aircraft and missiles. Some of these goals are now summarized.

6.1. 70 dB predictive dynamic range

As noise-cancelling anechoic chambers become more sophisticated and attain effective quiet zones deeper than -70 dB, it is desired to extend numerical modeling capabilities to this dynamic range to balance theory and measurements. Clearly, larger predictive and measurement dynamic ranges permit structures of lower radar cross-section to be modeled and tested. Note that attainment of 70 dB predictive dynamic ranges is equivalent to the ability to suppress all sources of computational noise to amplitudes no larger than about 10^{-4} that of the incident wave. This will be a very difficult challenge for any computational electromagnetics model.

With respect to space-grid time-domain algorithms, a primary challenge will occur in the area of advanced radiation boundary conditions (RBCs). In comparison with today's codes, a 40-dB (100:1) improvement is needed here in reducing the effective reflection coefficient of the outer grid boundaries relative to outward propagating numerical modes. It is not clear that this will be possible without a fundamental advance in RBC theory or direct numerical emulation of the noise cancellation used in the 70-dB anechoic chambers.

6.2. Modeling of complex and composite materials

The usage of multilayer composites and cellular materials for structural and electromagnetic purposes in aerospace design has markedly increased. These materials can have inhomogeneities and anisotropies of their electric and magnetic properties at distance scales of a few microns, the thickness of one lamina in a composite sandwich. Further, the electric and magnetic properties can be functions of the frequency of radar illumination. Any conceivable electromagnetic analysis code will be very strongly challenged by the requirement to simultaneously model distance scales ranging over six orders of magnitude (from micrometers to meters) and frequencies ranging over three orders of magnitude (from megahertz to gigahertz).

In fact, it may be unfeasible in the time frame of the next decade to successfully attack the micrometers-to-meters distance-scale problem by direct modeling. Most likely, this problem will be approached by developing advanced electromagnetic field boundary conditions applied at the surface of complex composite media to nearly equivalence the field physics of the underlying media without having to refine the computational mesh beyond that used in the air region outside. If this is the case, the problem of modeling composite media in meshes is one of fundamental electromagnetic theory rather than numerical methods.

6.3. Optimization of materials and shapes for RCS

Analogous to CFD, the availability of increasingly sophisticated and accurate numerical analysis tools for RCS presents the possibility of optimizing target materials and shapes on the computer before any models are constructed. Space-grid time-domain models of scattering appear to be particularly useful for this purpose because of their potential for containing entire aircraft and their time-domain formulation. The latter permits modeling a very wideband [and even ultrawideband (UWB)] radar illumination in a single modeling run, as well as natural time-windowing of the scattering response to focus attention on the behavior of specific scattering centers.

For example, at least one published paper[48] reports an algorithm to automatically optimize the RCS of a structure using space-grid time-domain techniques. The algorithm of Ref. 48 optimizes broadband absorptive coatings for two-dimensional structures by embedding a FD-TD forward-scattering code in a numerical feedback loop with the Levenberg–Marquardt (LM) non-linear optimization routine. LM is used to adjust the many geometric and constitutive parameters that characterize the target, while FD-TD is used to obtain the broadband RCS response for each target adjustment. A recursive improvement process is established to minimize the broadband RCS response over a selected range of bistatic angles using the available engineering degrees of freedom. The solution is valid over the potentially broad bandwidth (frequency decade or more) of the illuminating pulse used in the FD-TD model.

This approach compactly treats the scatterer shape and coating specifications as a single point in an N-dimensional space (N-space) of geometrical and electrical parameters. By repeatedly recalculating the forward problem to obtain one or more figures of merit for the near or far-field response, this method implements a gradient-based search strategy in the N-space to obtain locally optimum monostatic or bistatic RCS reductions over the bandwidth of the illuminating plane wave pulse. More globally optimum searches can be conducted by seeding the algorithm with a variety of starting points in the N-space. The non-linear optimizer also permits adding constraints so that the search path in the N-space weights manufacturability and cost, and avoids possible forbidden zones.

Figure 2 illustrates the use of this method to synthesize an absorbing coating for a canonical two-dimensional structure, the infinite, perfectly conducting right-angle wedge subject to transverse magnetic (TM) illumination. As shown in Fig. 2a, the wedge coating is a single homogeneous 5 mm thick absorbing layer to the left and bottom of the wedge
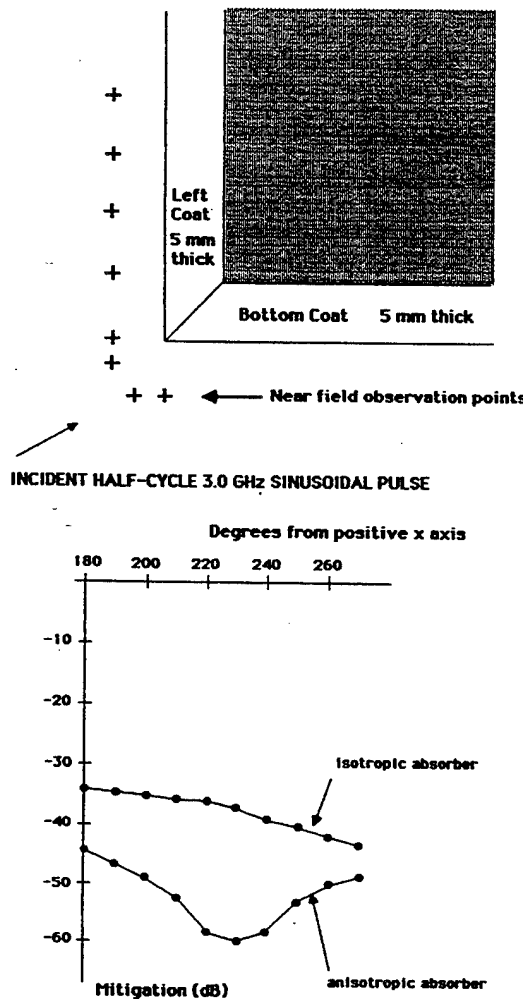
Fig. 2. FD-TD/LM synthesis of broadband absorbing coatings on an infinite conducting right-angle wedge, two-dimensional™ case: (a) wedge and coating geometry, showing the near-field observation points; (b) optimized mitigation of the broadband scattered pulse in the far field for bistatic angles bracketing the monostatic return, isotropic and anisotropic coating cases.

vertex, joined via a miter. In one case considered, the coating is assumed to be isotropic and independent of position, while in the other the coating is permitted to have an anisotropy of the magnetic loss that is dependent upon location (either in the left or bottom coat). The broadband illumination, a half-cycle 3.0 GHz sinusoidal pulse, is highly resolved everywhere by using a space discretization of $\lambda_0/200$. LM non-linear optimization is employed to minimize a weighted average of scattered near-field energy as observed at the eight near-field points indicated in Fig. 2a. From Fig. 2b, we see that the optimized broadband bistatic RCS mitigation in the far field (ratio of the peak scattered pulse power with coating to the peak scattered pulse power without coating) for bistatic angles bracketing the monostatic return is -34 to -42 dB for the isotropic coating and -44 to -60 dB for the anisotropic coating.

This case was purposefully selected to represent a coating N-space of low dimensionality, i.e. no coating layering was permitted. Given the simplicity of the coating examined here, it is likely that expanding the dimensionality of the automated search procedure would significantly increase the broadband RCS mitigation, increase the range of bistatic angles mitigated for RCS and decrease the sensitivity of the RCS mitigation to the illumination angle.

Methods such as the above appear to be ideal for implementation on massively parallel, multiple instruction multiple datastream (MIMD) computers. Here, systematic global searches of the N-space of interest could be implemented by assigning to each of the hundreds of processors (or groups of processors) a specific seed, or starting point, in the N-space. The searches could proceed independently of each other, culminating in an optimized engineering design for RCS.

6.4. Integrated RCS and aerodynamics design and optimization

In principle, the above ideas can be taken a large step further by performing simultaneous, linked modeling and optimization of RCS and aerodynamic performance, since these separate engineering goals can strongly mutually interact and even directly conflict. Needless to say, automated, integrated RCS/aero design is an ambitious goal—a true grand challenge—well worthy of the teraflop computers and 70 dB dynamic range electromagnetic modelers hopefully to come by the year 1997.

An interesting issue here is: "Should we use the same computational mesh for both the RCS model and the aero model?" At first glace this appears to be desirable, since target geometry and meshing could then be shared by both disciplines and the non-linear optimization software would deal with only a single geometry data base. However, it is less clear that the extraordinary 70 dB dynamic range needed by the electromagnetics model can be achieved by "shoehorning" Maxwell's equations into current CFD meshes. The physics involved in the two disciplines may be sufficiently different to mandate a Maxwell-specific mesh for the electromagnetics model. The computer storage and running time of the electromagnetics code and complexity of the umbrella non-linear optimization software may also factor into the choice of mesh for the electromagnetics model.

6.5. Target identification

An interesting observation is that the technique of embedding a space-grid time-domain Maxwell's solver within a non-linear optimization algorithm, considered above in the context of synthesizing scatterers having desired RCS properties, appears to be useful in reconstructing the shape (and even the composition) of a target from its broadband radar signature.[49]

Again, consider the FD-TD/LM non-linear optimization algorithm, but with the optimizer geared to replicate some finite measured impulsive scattering response rather than replicate a zero desired scattering response. Now, FD-TD generates a test pulse response for a parameterized trial target shape or composition, the test pulse is compared to the measured pulse, and an error signal is developed. Working on this error signal, the LM algorithm perturbs the original trial point in the N-space of parameters, effectively conducting a gradient search through this N-space. Upon repeated iterations, the trials ideally converge to the actual target geometry and composition. The advantage of working in the time domain is that causality can be exploited to permit progressive and cumulative target reconstruction as the incident pulse wavefront moves across the target. This reduces the complexity of reconstruction since only a portion of the target is being generated at each iteration.

Figure 3 provides examples of the ability of the FD-TD/LM non-linear optimization technique to exploit causality and reconstruct a dielectric J-shaped target from minimal two-dimensional TM near-field data contaminated by additive Gaussian noise.[49] Here, a single field observation point was assumed to be located approximately 10 target spans from the

front vertex of the J-target, with the incident plane wave pulse having a spatial width comparable with the J-target span and headed toward the front vertex of the J. The principal *a priori* information provided to the optimizer here is the target composition: lossless dielectric ($\epsilon_r = 2.1$).

Figure 3 exemplifies hundreds of FD-TD/LM reconstruction attempts where varying samples of Gaussian noise (provided by a random number generator) are added to the simulated measured scattered waveform (a sequence of FD-TD-generated numbers). Using this technique, the probability of exact reconstruction of the J-shaped target has been estimated as a function of the signal-to-noise (S/N) power ratio. It has been found that the probability of exact reconstruction exceeds 0.9 when S/N ratios exceed 40 dB. For lower S/N ratios, the reconstruction process appears to degrade gracefully, as shown.

We see that space-grid time-domain Maxwell's solvers combined with non-linear optimizers that exploit causality hold promise for the classic inverse-scattering problem. Further progress awaits study of this problem by more groups in the Maxwell's equations gridding community. Perhaps this will occur in the next 5 years.

7. FUTURE DUAL-USE ELECTROMAGNETICS NEEDS

By the mid-1990s, we will be implementing space-grid time-domain Maxwell's solvers on the 0.1–1 Tflop supercomputers of the day to model the radar cross-section of entire low-observable fighter aircraft at frequencies up to at least 2 GHz through dynamic ranges up to 70 dB; but, perhaps of more importance to the interests of society, we will be using these same Maxwell's solvers implemented on the same supercomputers to model electromagnetic wave problems that arise in cutting-edge commercial applications.

This discussion will start with extensions of existing commercial applications of electromagnetic wave interactions and proceed to highly innovative applications that best represent the dual-use nature of modeling Maxwell's equations on large scales.

7.1. *Antenna design*

This area includes the design of UHF/microwave data links for worldwide personal wireless telephony, cellular communications, remote computing and advanced automotive electronics (particularly car location and navigation).

Here, we are seeing that space-grid time-domain Maxwell's solvers are permitting the modeling of complicated antennas, especially those having finite ground planes that cannot be analyzed using conventional frequency-domain analyses based upon the Green's function technique. Key recent examples include:

(1) Maloney *et al.*[34]—FD-TD models of body-of-revolution-type monopoles and conical monopoles over finite ground planes. Here, computed results


(a)

(b)

(c)
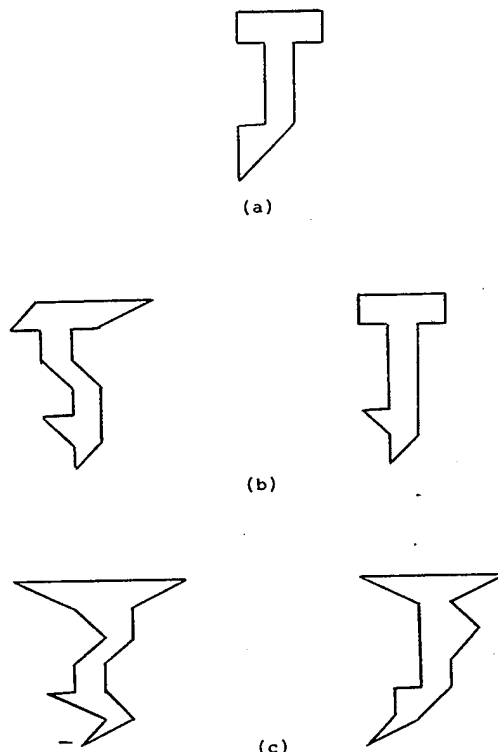
Fig. 3. Typical effects of Gaussian noise upon FD-TD/LM non-linear optimization inverse scattering reconstruction of a two-dimensional dielectric target having reentrant features: (a) $S/N = 40$ dB, exact reconstruction; (b) $S/N = 30$ dB, examples of imperfect reconstruction; (c) $S/N = 25$ dB, examples of imperfect reconstruction.

for the transient reflected waveforms in the feeding coaxial line and for the input impedances were found to agree with measurements to better than 1%.

(2) Katz et al.[36]—surface-conforming FD-TD models of two-dimensional waveguide-fed horn antennas and horn-excited parabolic reflectors. Here, the computed results for near-fields in the antenna apertures were found to agree with frequency-domain MoM numerical data to within 1% in magnitude and phase.

(3) Tirkas and Balanis[35]—surface-conforming FD-TD models of three-dimensional waveguide-fed horn antennas. Here, the computed results for far-field radiation patterns were found to agree very well with measurements over a 55-dB dynamic range.

(4) Thiele and Taflove[50]—in perhaps the most complex modeling so far, the authors are constructing three-dimensional FD-TD models of 6–18 GHz Vivaldi flares (tapered slot antennas) constructed from three-layer circuit board. Here, both single flares, double flares, quad elements comprised of perpendicular double-flares and arrays of up to eight quad elements are being modeled. The latter involve the solution of up to 60,000,000 vector field unknowns. Results are being obtained for radiation pattern and input impedance. The variation of the input impedance with phasing of the array of quad elements is also being studied.

As detailed FD-TD modeling proceeds in this area, it is possible that commercial application areas will include the design of mass-produced surface-conforming antennas for: homes (rooftop-mounted antennas for satellite reception); automobiles (rooftop-mounted antennas for two-way satellite communication, license-plate-mounted antennas for automated collision avoidance and programmed route-following); and laptop computers (computer-case-mounted antennas for two-way cellular and satellite communication).

7.2. Microwave circuits

Stripline microwave circuits, including filtering elements and couplers, are being studied for the first time by applying grid-based time-domain Maxwell's solvers. Key recent examples include:

(1) Sheen et al.[30]—FD-TD models of microstrip interconnects.

(2) Ko and Mittra[31]—three-dimensional FD-TD models yielding the broadband S-parameters of microstrip filters, couplers and hybrids.

This work is leading to the modeling of microwave and millimeter wave integrated circuits (MIMIC) in regimes of electrical size and complexity that cannot be handled by any existing finite-element or boundary integral method.

7.3. Bioelectromagnetic systems

Grid-based time-domain Maxwell's solvers are now being extensively applied in clinical settings for patient-specific electromagnetic hyperthermia. This technology uses electromagnetic absorption at RF, UHF, or microwave frequencies to heat cancerous tumors inside the human body, thereby rendering the tumors more vulnerable to ionizing radiation or chemotherapy. Recent examples of work include:

(1) Sullivan[19]—three-dimensional FD-TD models of RF hyperthermia for human patients.

(2) Piket-May et al.[20]—three-dimensional FD-TD models of UHF hyperthermia specifically tailored to patients by using computed tomography (CT) imaging to establish a three-dimensional dielectric medium data base unique to each patient's tissue structure.

This work is leading to the routine clinical usage of electromagnetic hyperthermia for cancer treatment. Time-domain solution of Maxwell's equations on grids is essential to this process because it permits an efficient, individual modeling of each patient to accommodate the electromagnetic field physics unique to his or her tissue geometry and selection of field applicators.

7.4. Packaging and metallic interconnect design for digital circuits

This area involves engineering problems in the propagation, crosstalk and radiation of electronic digital pulses, and has important implications in the design of the multi-layer circuit boards and multi-chip modules that are widely used in modern digital technology. Most existing computer-aided circuit design tools (primarily SPICE) are inadequate when digital clock speeds exceed about 250 MHz. These tools cannot deal with the physics of UHF/microwave electromagnetic wave energy transport (along metal surfaces like ground planes, or in the air away from metal paths) that predominate above 250 MHz. Effectively, electronic digital systems develop substantial analog wave effects when clock rates are high enough, and full-vector (full-wave) Maxwell's equations solvers become necessary for their understanding.

Key recent examples include:

(1) Liang et al.[28]—three-dimensional FD-TD modeling of picosecond pulse propagation along co-planar waveguides above gallium arsenide.

(2) Shibata and Sano[29]—three-dimensional FD-TD modeling of propagation along metal–insulator–semiconductor lines.

(3) Lam et al.[51]—three-dimensional FD-TD modeling of digital signal propagation and radiation for VLSI packaging.

(4) Maeda et al.[52]—three-dimensional FD-TD modeling of digital pulse propagation through vias in a three-layer circuit board.

(5) Piket-May et al.[53]—in perhaps the most complex modeling so far, the authors constructed three-dimensional FD-TD models of sub-nanosecond digital pulse propagation and crosstalk behavior in

Z-Axis Connector System
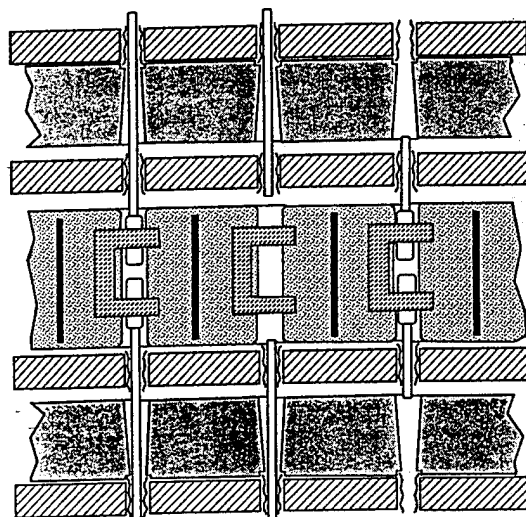
Fig. 4. Vertical cut through the four-circuit-board, three-connector geometry showing the via pins spaced 0.1 in apart.

modules consisting of four 22-layer circuit boards connected by three 100-pin connectors. The entire space was modeled with a uniform resolution of 0.004 in, permitting each layer, via and pin of the circuit boards and connectors to be modeled. A maximum of 60,000,000 vector field unknowns was solved per modeling run, a factor of perhaps 600 times larger than the capacity of the largest SPICE or finite-element CAD tool available. Color videos of digital signal propagation and crosstalk were constructed to vividly illustrate these phenomena.

Figure 4 depicts the geometry of the four-board, three-connector stack as seen in a vertical cut through the stack. Each 22-layer circuit board is shown as a cross-hatched horizontal slab, and each vertical via pin (spaced at a 0.1 in interval) is shown in proper relation to the surrounding boards and connectors. (Recall that each 0.004 in-thick metal–dielectric layer of each board is modeled.)

Figure 5 is a color plate showing the plan view of an outwardly propagating electromagnetic wave within a single 22-layer board generated by the passage of a sub-nanosecond pulse down one of the via pins. Although the relatively intense magnetic field adjacent to the excited via (shown by the yellow color) is quite localized, moderate-level magnetic fields (shown by light blue) emanate throughout the entire transverse cross-section of the board and link all of the adjacent via pins, shown as dark dots in a diamond pattern. The complete color video of this phenomenon shows repeated bursts of outward propagating waves linking all points within transverse cross-sections of the board as the digital pulse passes vertically through the 22 metal–dielectric–metal layers of the board.

Figure 6 is a color plate showing the magnitude and direction of currents instantaneously flowing along the vertical cross-section of Fig. 4 for a sub-nanosecond digital pulse assumed to excite a single vertical via pin in the upper 22-layer board. The currents were calculated in a post-processing step by numerically evaluating the curl of the magnetic field obtained from the three-dimensional FD-TD model. The color red was selected to denote downward-directed current, while the color green was selected to denote upward-directed current. At the time of this visualization, current had proceeded down the excited via through all four boards and all three connectors; but upward-directed (green) current is seen to flow on the adjacent vias. This represents undesired ground-loop coupling to the digital circuits using these vias. Ironically, the far-left-hand and far-right-hand vias showing downward-directed (red) currents were designated by the designers of this structure to be the ground return pins and should have been the only pins carrying upward-directed (green) current. In other words, this interconnection module wound up working nearly in an opposite manner relative to what its designers had intended.

This work is leading to the direct time-domain Maxwell's equations modeling of the metallic interconnects and packaging of general-purpose digital circuits operating at clock speeds about 250 MHz. From the example shown, it is clear that the analog coupling effects for such devices can be so complex that there may be no way to design them—no way to make them work in a timely and reliable manner—without such modeling.


Fig. 5. Color plate showing the plan view of an outwardly propagating electromagnetic wave within a single circuit board of Fig. 4 generated by the passage of a sub-nanosecond pulse down one of the via pins. Color scale: yellow = maximum; green = moderate; dark blue = negligible.
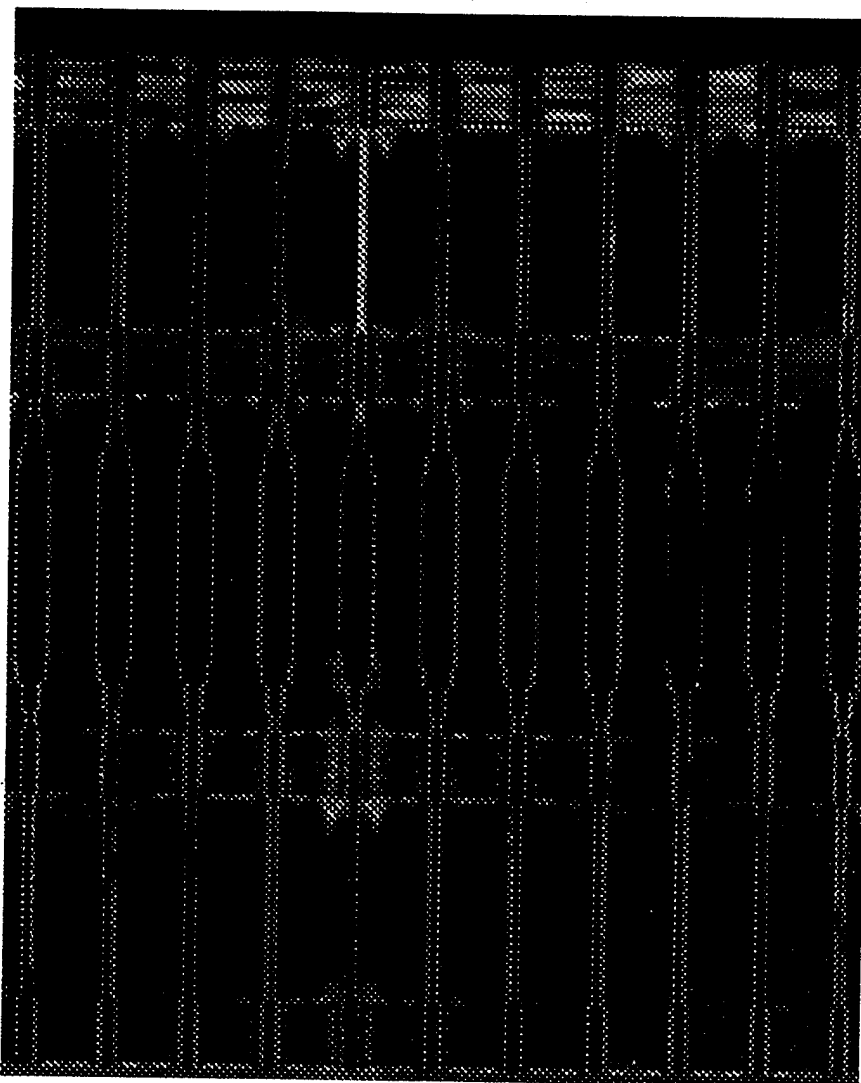
Fig. 6. Color plate showing the magnitude and direction of currents instantaneously flowing along the vertical cross-section of Fig. 4 for a sub-nanosecond digital pulse assumed to excite a single vertical via pin in the upper 22-layer board. Color scale: red = net downward-directed current; green = net upward-directed current; dark blue = negligible.

7.5. *Incorporation of models of active devices*

It is a short distance from modeling device packaging and interconnects, as discussed above, to including the active devices themselves. Work has begun in this area. The best examples are:

(1) Sano and Shibata[37]—incorporation of a self-consistent drift-diffusion charge-transport model of gallium arsenide in the three-dimensional FD-TD solver. This work modeled picosecond-regime pulse generation for an optically excited gallium arsenide device.

(2) El Ghazaly et al.[38]—incorporation of a self-consistent Monte Carlo charge-transport model of gallium arsenide in the three-dimensional FD-TD solver. This work also modeled picosecond-regime pulse generation for an optically excited gallium arsenide device.

(3) Sui et al.[41]—two-dimensional FD-TD modeling of lumped-circuit elements (resistors, inductors, capacitors, diodes and transistors).

By 1995, this work will probably lead to the incorporation of SPICE models of arbitrary linear and non-linear circuit elements into three-dimensional space-grid time-domain Maxwell's solvers. This will expand full-vector electromagnetic modeling of digital interconnects to include the voltage–current characteristics of the connected logic devices. It should result in a virtual replacement of SPICE for most problems involved in digital interconnect design above 250 MHz.

A recently initiated 3-year cooperative program between Cray Research and Los Alamos National Laboratory recognizes the possibility that the design of the digital microchips themselves will mandate

full-vector EM modeling, especially when clock speeds exceed 3 GHz. In this regime, wave propagation and coupling effects within the chips may render their operation just as problematic as that of today's circuit board modules operating at 300 MHz.

Subsequently, the Cray/Los Alamos program seeks to explore Maxwell's equations modeling of digital chips having clock speeds well above 10 GHz. The reasoning here is that when the logic pulse rise time becomes comparable with the charge transport time, existing approaches for modeling semiconductors which assume a quasi-static formulation for Maxwell's equations (the Poisson equation) will no longer have validity. In this regime, the simple circuit concept of a digital signal toggling a transistor may have to be considered at the most elemental level. Namely, the digital signal and transistor actually comprise a three-dimensional electromagnetic pulse scattering geometry: the digital signal is really a three-dimensional propagating field distribution having a specific temporal response and the transistor is really a three-dimensional charge density distribution that reacts non-linearly to the impinging electromagnetic pulse. Self-consistent Maxwell's equations field transport and semiconductor charge transport modeling are required to properly understand this non-linear scattering situation.

7.6. Application to all-optical devices

Work has begun to appear on first-principles modeling of the propagation and switching of femtosecond optical pulses in non-linear dispersive media. Again, time-domain grid-based Maxwell's solvers are being used:

(1) Joseph et al.[33]—demonstrated and rigorously validated an efficient one-dimensional FD-TD analysis of femtosecond pulse propagation and reflection effects for a linear Lorentz (resonant dispersive) medium. This work pioneered direct Maxwell's equations modeling of second-order dispersion, providing extremely accurate physics over instantaneous bandwidths of literally d.c. to light for reflection coefficients and Sommerfeld and Brillouin impulsive precursors.

(2) Goorjian and Taflove[39]—demonstrated an efficient one-dimensional FD-TD analysis of femtosecond optical soliton propagation and collision in a second-order non-linear dispersive medium. This work obtained for the first time optical solitons from Maxwell's equations, with quantum physics such as the Kerr and Raman interactions incorporated into the Maxwell's equations at distance scales larger than about 10 nm.

(3) Ziolkowski and Judkins[40]—two-dimensional FD-TD analysis of femtosecond optical pulse propagation and self-focusing in a first-order non-linear dispersive medium.

Consider qualitatively the key results of Ref. 39. Fig. 7a depicts the FD-TD computed propagation of a 50 fs duration infrared optical pulse observed at
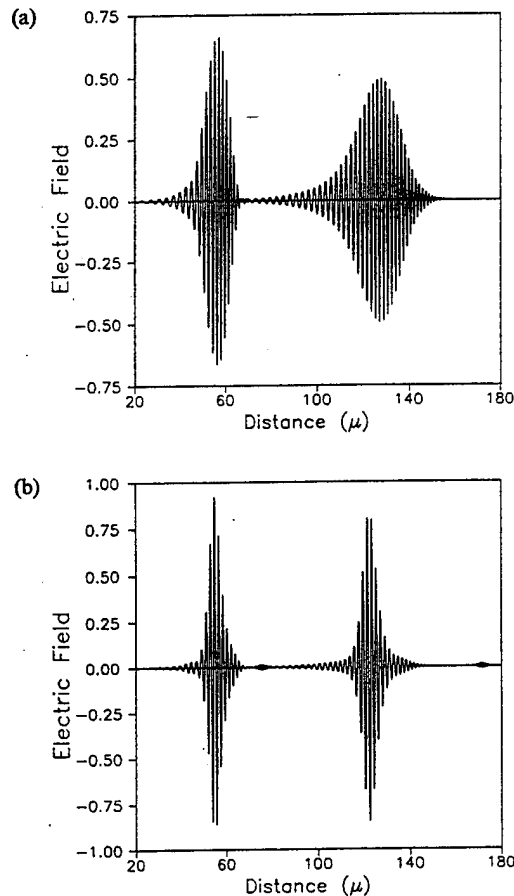

Fig. 7. FD-TD computed propagation of a 50 fs duration infrared optical pulse observed at propagation distances of 55 and 126 μm from the source in a medium having anomalous dispersion due to a single Lorentzian relaxation: (a) linear case, showing pulse attenuation, broadening, and frequency modulation; (b) dispersive non-linear case, showing the formation of a soliton pulse and precursor.

propagation distances of 55 and 126 μm from the source in a linear medium having anomalous dispersion. Note pulse broadening, diminishing amplitude and carrier frequency modulation ($>f_c$ on the leading side, $<f_c$ on the trailing side) which causes an asymmetrical shifting of the envelope, a higher-order dispersive effect. In Fig. 7b, sufficient non-linearity is introduced to yield a soliton that retains its amplitude and width when observed at the same propagation distances as Fig. 7a. However, a low-amplitude precursor is seen to move out ahead of the soliton. The carrier frequency of this precursor is upshifted to approximately 3.6 times that of the main pulse.

Figure 8 depicts the Fourier spectrum of the solitons shown in Fig. 7b. The figure shows a red shift and sharpening of the spectrum as the pulse propagates. This red shift is predicted due to the Raman effect occurring as a higher-order dispersive non-linearity modeled by the non-linear Maxwell's equations solver.

Finally, Ref. 39 considers the collision of two counter-propagating solitons. Each is identical and
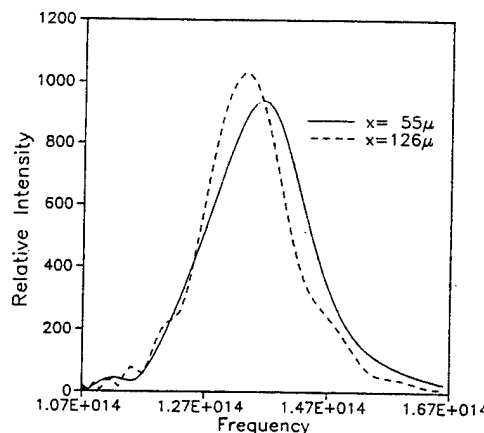
Fig. 8. Red shift of the Fourier spectrum of the propagating soliton of Fig. 7b.

has all of the parameters of the previous case. As is characteristic of colliding solitons, after the collisions the pulses separate without changing their general appearance. However, there are lagging phase shifts due to the collision, up to 31° for the carrier in the precursor. To illustrate this, Fig. 9 plots the space dependence of the central part of the precursor for the uncollided case and the collided case. Such phase shifts, not easily detected by previous theory, may be a basis for optical switching devices.

Unlike all previous soliton theory based upon the pulse-envelope approach, the direct Maxwell's equations model of Ref. 39 assumes nothing about the homogeneity or isotropy of the optical medium, the magnitude of its non-linearity, the nature of its $\omega - \beta$ variation, or the shape or duration of the optical pulse. By retaining the optical carrier, the new Maxwell's equations method solves for fundamental quantities—the optical electric and magnetic fields in space and time—rather than a non-physical envelope function. Thus, it is extendible to full-vector optical fields in two and three dimensions to permit rigorous boundary value problem studies of non-linear vector-wave polarization, diffraction, scattering and interference effects. This is being actively pursued.
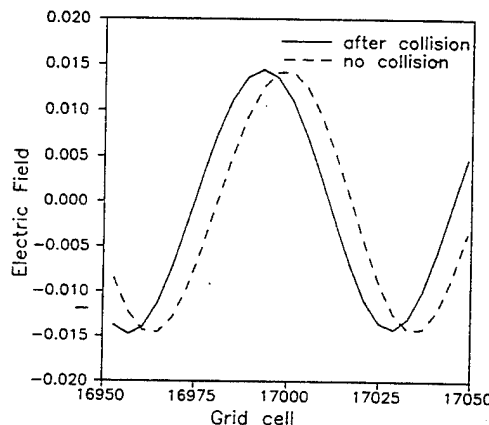

Fig. 9. Phase lag of the precursor pulse as a result of counterpropagating soliton–soliton collision.

This work may lead to the modeling of all-optical digital logic devices switching potentially in 10–50 fs at room temperature. This is about 1000 times faster than the best transistor today and 100 times faster than a Josephson junction operating under liquid helium. The implications may be profound for the realization of "optonics", a proposed successor technology to electronics in the 21st century that would integrate optical fiber interconnects and all-optical processors into systems of unimaginable information processing capability.

8. CONCLUSIONS

Supercomputers of the mid-1990s, which promise to achieve rates from 0.1 to 1 Tflop, will permit us to attack some "grand challenges" in electromagnetics. One such "challenge" remains from the RCS technology side—the airplane-in-the-grid. In fact, using the new class of machines and the new class of space-grid time-domain Maxwell's solvers, it will certainly be possible to obtain whole low-observable fighter-airplane models in the 1–3 GHz range and jet-engine-inlet models up to perhaps 5–10 GHz, with predictive dynamic ranges up to 70 dB. In addition, time-domain non-linear optimization algorithms will probably be used to achieve engineering goals with respect to observability and aerodynamics. But, of arguably more importance to society, the same algorithms implemented on the same computers could attack other "grand challenges" in electromagnetics:

- the satellite-antenna-in-the-grid;
- the cancer-patient-in-the-grid;
- the digital-microchip-module-in-the-grid;
- the microwave/millimeter wave integrated circuit-in-the-grid;
- the array-of-picosecond-transistors-in-the-grid;
- the femtosecond-all-optical-switch-in-the-grid, etc.

I assert that ultra-large-scale solution of Maxwell's equations using time-domain grid-based approaches may be fundamental to the advancement of our technology as we continue to push the envelope of the ultra-complex and the ultra-fast. Simply speaking, Maxwell's equations provide the physics of electromagnetic phenomena from d.c. to light and their accurate modeling is essential to understand high-speed signal effects having wave transport behavior. Let us aim for the computational unification of:

- full-vector electromagnetic waves in three dimensions;
- charge transport in transistors, Josephson junctions and electro-optic devices;
- surface and volumetric wave dispersions, including those of superconductors; and
- non-linearities due to quantum effects.

Then, we can attack some computational "grand challenges" to directly benefit our society.

REFERENCES

1. R. F. Harrington, *Field Computation by Moment Methods*, Macmillan, New York, 1968.
2. K. R. Umashankar, "Numerical analysis of electromagnetic wave scattering and interaction based on frequency-domain integral equation and method of moments techniques," *Wave Motion* 10, 493 (1988).
3. J. B. Keller, "Geometrical theory of diffraction," *Journal of the Optical Society America* 52, 116 (1962).
4. R. G. Kouyoumjian and P. H. Pathak, "A uniform geometrical theory of diffraction for an edge in a perfectly conducting surface," *Proceedings of the IEEE* 62, 1448 (1974).
5. J. P. Brooks, K. K. Ghosh, E. Harrigan, D. S. Katz and A. Taflove, "Progress in Cray-based algorithms for computational electromagnetics," in *Progress in Electromagnetics Research (PIER)* edited by T. Cwik, Vol. 7, Elsevier, New York, 1992.
6. K. S. Yee, "Numerical solution of initial boundary value problems involving Maxwell's equations in isotropic media," *IEEE Transactions Antennas and Propagation* 14, 302 (1966).
7. A. Taflove and M. E. Brodwin, "Numerical solution of steady-state electromagnetic scattering problems using the time-dependent Maxwell's equations," *IEEE Transactions Microwave Theory Tech.* 23, 623 (1975).
8. A. Taflove and M. E. Brodwin, "Computation of the electromagnetic fields and induced temperatures within a model of the microwave-irradiated human eye," *IEEE Transactions Microwave Theory Tech.* 23, 888 (1975).
9. R. Holland, "Threde: a free-field EMP coupling and scattering code," *IEEE Transactions Nuclear Science* 24, 2416 (1977).
10. K. S. Kunz and K. M. Lee, "A three-dimensional finite-difference solution of the external response of an aircraft to a complex transient EM environment I: the method and its implementation," *IEEE Transactions Electromagnetic Compat.* 20, 328 (1978).
11. A. Taflove, "Application of the finite-difference time-domain method to sinusoidal steady-state electromagnetic penetration problems," *IEEE Transactions Electromagnetic Compat.* 22, 191 (1980).
12. G. Mur, "Absorbing boundary conditions for the finite-difference approximation of the time-domain electromagnetic field equations," *IEEE Transactions Electromagnetic Compat.* 23, 377 (1981).
13. K. R. Umashankar and A. Taflove, "A novel method to analyze electromagnetic scattering of complex objects," *IEEE Transactions Electromagnetic Compat.* 24, 397 (1982).
14. A. Taflove and K. R. Umashankar, "Radar cross section of general three-dimensional scatterers," *IEEE Transactions Electromagnetic Compat.* 25, 433 (1983).
15. G. A. Kriegsmann, A. Taflove and K. R. Umashankar, "A new formulation of electromagnetic wave scattering using an on-surface radiation boundary condition approach," *IEEE Transactions Antennas and Propagation* 35, 153 (1987).
16. T. G. Moore, J. G. Blaschak, A. Taflove and G. A. Kriegsmann, "Theory and application of radiation boundary operators," *IEEE Transactions Antennas and Propagation* 36, 1797 (1988).
17. D. T. Borup, D. M. Sullivan and O. P. Gandhi, "Comparison of the FFT conjugate gradient method and the finite-difference time-domain method for the 2-D absorption problem," *IEEE Tranactions Microwave Theory Tech.* 35, 383 (1987).
18. D. M. Sullivan, O. P. Gandhi and A. Taflove, "Use of the finite-difference time-domain method in calculating EM absorption in man models," *IEEE Transactions Biomedical Engineering* 35, 179 (1988).
19. D. M. Sullivan, "Three-dimensional computer simulation in deep regional hyperthermia using the finite-difference time-domain method," *IEEE Transactions Microwave Theory Tech.* 38, 204 (1990).
20. M. J. Piket-May, A Taflove, W.-C. Lin, D. S. Katz, V. Sathiaseelan and B. Mittal, "Initial results for automated computational modeling of patient-specific electromagnetic hyperthermia," *IEEE Transactions Biomedical Engineering* 39, 226 (1992).
21. K. R. Umashankar, A. Taflove and B. Beker, "Calculation and experimental validation of induced currents on coupled wires in an arbitrary shaped cavity," *IEEE Transactions Antennas and Propagation* 35, 1248 (1987).
22. A. Taflove, K. R. Umashankar, B. Beker, F. Harfoush and K. S. Yee, "Detailed FD-TD analysis of electromagnetic fields penetrating narrow slots and lapped joints in thick conducting screens," *IEEE Transactions Antennas and Propagation* 36, 247 (1988).
23. T. G. Jurgens, A. Taflove, K. R. Umashankar and T. G. Moore, "Finite-difference time-domain modeling of curved surfaces," *IEEE Tranactions Antennas and Propagation* 40, 357 (1992).
24. A. C. Cangellaris, C. C. Lin and K. K. Mei, "Point-matched time-domain finite element methods for electromagnetic radiation and scattering," *IEEE Transactions Antennas and Propagation* 35, 1160 (1987).
25. V. Shankar, A. H. Mohammadian and W. F. Hall, "A time-domain finite-volume treatment for the Maxwell's equations," *Electromagnetics* 10, 127 (1990).
26. B. J. McCartin, L. J. Bahrmasal and G. Meltz, "Application of the control region approximation to two-dimensional electromagnetic scattering," in *Progress in Electromagnetics Research* (edited by M. A. Morgan), Vol. 2, Ch. 5, Elsevier, New York, 1990.
27. N. K. Madsen and R. W. Ziolkowski, "A three-dimensional modified finite volume technique for Maxwell's equations," *Electromagnetics* 10, 147 (1990).
28. G.-C. Liang, Y.-W. Liu and K. K. Mei, "Full-wave analysis of coplanar waveguide and slotline using the time-domain finite-difference method," *IEEE Transactions Microwave Theory Tech.* 37, 1949 (1989).
29. T. Shibata and E. Sano, "Characterization of MIS structure coplanar transmission lines for invesigation of signal propagation in integrated circuits," *IEEE Transactions Microwave Theory Tech.* 38, 881 (1990).
30. D. M. Sheen, S. M. Ali, M. D. Abouzahra and J. A. Kong, "Application of the three-dimensional finite-difference time-domain method to the analysis of planar microstrip circuits," *IEEE Transactions Microwave Theory Tech.* 38, 849 (1990).
31. W. L. Ko and R. Mittra, "A combination of FD-TD and Prony's methods for analyzing microwave integrated circuits," *IEEE Transactions Microwave Theory Tech.* 39, 2176 (1991).
32. R. Luebbers, F. P. Hunsberger, K. S. Kunz, R. B. Standler and M. Schneider, "A frequency-dependent finite-difference time-domain formulation for dispersive materials," *IEEE Transactions Electromagnetic Compat.* 32, 222 (1990).

33. R. M. Joseph, S. C. Hagness and A. Taflove, "Direct time integration of Maxwell's equations in linear dispersive media with absorption for scattering and propagation of femtosecond electromagnetic pulses," *Optics Letters* **16**, 1412 (1991).

34. J. G. Maloney, G. S. Smith and W. R. Scott, Jr, "Accurate computation of the radiation from simple antennas using the finite-difference time-domain method," *IEEE Transactions Antennas and Propagation* **38**, 1059 (1990).

35. P. A. Tirkas and C. A. Balanis, "Finite-difference time-domain technique for radiation by horn antennas," 1991 *IEEE Antennas and Propagation Society International Symposium Digest*, Vol. 3, pp. 1750–1753, London, Ontario, Canada, 1991.

36. D. S. Katz, M. J. Piket-May, A. Taflove and K. R. Umashankar, "FD-TD analysis of electromagnetic wave radiation from systems containing horn antennas," *IEEE Transactions Antennas and Propagation* **39**, 1203 (1991).

37. E. Sano and T. Shibata, "Fullwave analysis of picosecond photoconductive switches," *IEEE Journal Quantum Electronics* **26**, 372 (1990).

38. S. M. El-Ghazaly, R. P. Joshi and R. O. Grondin, "Electromagnetic and transport considerations in subpicosecond photoconductive switch modeling," *IEEE Transactions Microwave Theory Tech.* **38**, 629 (1990).

39. P. M. Goorjian and A. Taflove, "Direct time integration of Maxwell's equations in nonlinear dispersive media for propagation and scattering of femtosecond electromagnetic solitons," *Optics Letters* **17**, 180 (1992).

40. R. W. Ziolkowski and J. B. Judkins, "Full-wave vector Maxwell equation modeling of the self-focusing of ultrashort optical pulses in a nonlinear Kerr medium exhibiting a finite response time," *Journal Optical Society of America B*, submitted.

41. W. Sui, D. A. Christensen and C. H. Durney, "Extending the two-dimensional FD-TD method to hybrid electromagnetic systems with active and passive lumped elements," *IEEE Transactions Microwave Theory Tech.* **40**, 724 (1992).

42. A. C. Ludwig, General Research Corporation, private communication.

43. S. W. Lee (ed.), *High Frequency Scattering Data Book*, Electromagnetic Laboratory, University of Illinois at Urbana-Champaign, 1989.

44. K. R. Umashankar, S. Nimmagadda and A. Taflove, "Numerical analysis of electromagnetic scattering by electrically large objects using spatial decomposition technique," *IEEE Transactions Antennas and Propagation*, in press.

45. A. T. Perlik, T. Opsahl and A. Taflove, "Predicting scattering of electromagnetic fields using FD-TD on a Connection Machine," *IEEE Transactions Magnetics* **25**, 2910 (1989).

46. J. E. Patterson, T. Cwik, R. D. Ferraro, N. Jacobi, P. C. Liewer, T. G. Lockhart, G. A. Lyzenga, J. W. Parker and D. A. Simoni, "Parallel computation applied to electromagnetic scattering and radiation analysis," *Electromagnetics* **10**, 21 (1990).

47. D. S. Katz, A. Taflove, J. P. Brooks and E. Harrigan, "Large-scale methods in computational electromagnetics," in *Cray Channels*, Cray Research, 1991.

48. M. A. Strickel and A. Taflove, "Time-domain synthesis of broadband absorptive coatings for two-dimensional conducting targets," *IEEE Transactions Antennas and Propagation* **38**, 1084 (1990).

49. M. A. Strickel, A. Taflove and K. R. Umashankar, "Finite-difference time-domain formulation of an inverse scattering scheme for remote sensing. Part II—Two-dimensional case: conducting and dielectric targets," *Journal of Electromagnetic Waves and Applications*, in press.

50. E. Thiele and A. Taflove, "FD-TD analysis of Vivaldi tapered slot antennas," in preparation.

51. C. W. Lam, S. M. Ali, R. T. Shin and J. A. Kong, "Radiation from discontinuities in VLSI packaging structures," *Proceedings of the Progress in Electromagnetics Research Symposium*, Boston, Massachusetts, p. 567, July 1991.

52. S. Maeda, T. Kashiwa and I. Fukai, "Full wave analysis of propagation characteristics of a through hole using the finite-difference time-domain method," *IEEE Transactions Microwave Theory Tech.* **39**, 2154 (1991).

53. M. Piket-May and A. Taflove, "First-principles supercomputing simulation of crosstalk in high-speed digital interconnects," 1992 Joint Symposia, URSI Radio Science Meeting Digest, p. 451, Chicago, IL, 1992.

Practical Limits on Theoretical Dosimetry

Mark J. Hagmann

Department of Electrical and Computer Engineering
Florida International University, Miami, FL 33199

Abstract

Theoretical dosimetry should be used to determine the approximate whole-body average SAR, and to highlight the effects of various parameters on the distribution of SAR in regions of the body. Solutions giving the SAR at thousands of locations should not be taken too seriously because they are beyond the appropriate level of precision for the calculations. Furthermore, if such a solution were accurate it would be valid for such a limited range of exposure parameters that it would have little practical value.

There have been many recent papers in which supercomputers were used to calculate the rate of energy deposition (specific absorption rate or SAR) at thousands of locations within a human exposed to electromagnetic fields. In any engineering problem there is an appropriate level of precision, and these elaborate computations appear to be well beyond this limit.

It is reasonable to calculate the whole-body average SAR. Simple models such as prolate spheroids have been used to determine the average SAR in man and animals. Handbooks based on these calculations [1] are used by researchers studying electromagnetic bioeffects. These handbooks show that the average SAR depends upon frequency, polarization, near-field/far-field conditions and the distance to ground or nearby objects, as well as the height, weight and muscle/fat ratio of the subject.

It is also reasonable to calculate the average SAR in large regions of the body. This was first done for block models with the method of moments (MoM). These calculations successfully predicted neck heating, an arm resonance at 150 MHz, and a head resonance which was confirmed experimentally with phantom figurines and animal models [2]. Other procedures, such as finite elements [3] and finite-difference time-domain (FDTD) [4], may also be used for this purpose. Regional averages of SAR calculated from the FDTD solutions for thousands of cells should be more accurate than MoM calculations. However, the use of greater detail makes these solutions highly specific, being limited to one person in one exact posture with fixed surroundings, and one source of radiation. Thus, the practical value of even regional

1

averages of SAR found using FDTD may be questioned. Tests of accuracy with canonical problems, where the object is well-defined and the answer is known, should not be used to infer the suitability for computing the SAR within the human body. Some of the reasons why the thousands of computed local values of SAR should not be taken too seriously are listed below:

1. The current state of knowledge regarding the dielectric properties of human tissues is inadequate for such detailed calculations. Much of the data were determined in vitro, and there is considerable scatter. In high resolution calculations it is not sufficient to consider the body to be made of a limited number of tissues having specific properties. The properties of a single tissue type such as "muscle" show variability and others such as "bone" are heterogeneous. The gastrointestinal tract, which occupies a large fraction of the torso, has contents that vary greatly in water content, so the dielectric properties are both unknown and variable.

2. The dielectric properties of tissues are variable, depending on the water content and temperature. The fat content of the liver varies during a 24 hour period, so this large organ has variable dielectric properties.

3. Both muscle and nerve tissues are anisotropic, an effect which has not been modeled, and would be difficult to model with suitable precision.

4. In FDTD, as with MoM, the model is an array of cubes with flat surfaces that do not coincide with the boundaries between different media in the subject. With MoM we have found it necessary to arrange the cells carefully (staircasing cells, and using cells with different sizes) to minimize the errors at boundaries [5]. Similar errors occur when representing boundaries with FDTD [6], but rectangular arrays of identical cubical cells have generally been required in the FDTD computations for models of man.

5. Chen and Gandhi [4] have tried to reduce the errors due to representing irregular boundaries in FDTD by assigning each cube dielectric properties equal to the volume average of the media it represents. For example, cubes on the surface of the body have the volume-weighted properties of air and muscle. This procedure appears satisfactory in tests for canonical problems such as homogeneous spheres, where few cells are on the boundary and the boundary has low curvature. However, when modeling a highly heterogeneous subject such as the human body, the effects of this procedure are unknown. Each boundary is smeared in the model, which is likely to result in increased transmission.

6. We question the use of volume weighting to compute the effective dielectric properties of each cubical cell because it is known that the effective dielectric properties of a mixture of

2

dielectrics depend strongly on the shapes and distributions of the components as well as the frequency and orientation of the electric field. Various formulations have been considered as mixing rules, such as the logarithmic rule of Lichtenecker, but they have been shown to have limited validity [7].

7. Measurements of SAR in an amputated human leg heated with a mini-annular phased array (MAPA) hyperthermia applicator showed [8] that the local SAR depends on the detailed structure of the tissue interfaces. The dielectric heterogeneity of the human body increases upon closer examination in a manner that is almost fractal in nature. Thus, it is necessary to model at a much finer level than that at which the SAR is reported.

8. Even if an accurate solution could be obtained giving the SAR at thousands of locations within the human body, the specificity of the solution would cause it to have little practical value. Open-field measurements using a non-invasive current probe [9] with a man-sized phantom have shown that the current in the calf varies as the legs and arms are moved, or when various objects are brought near the phantom. These open-field measurements are consistent with earlier numerical simulations and experiments with animal models highlighting the effects of reflectors and other objects on the SAR [10]. We would expect greater variation in local values of SAR than that which is seen in current measurements because the latter represent an average over a cross section of the thigh.

9. Order of magnitude errors were found [11] when measurements of local SAR in a heterogeneous phantom model of man were compared with FDTD calculations. Even greater errors would be anticipated if the calculations were compared to measurements in a human since there would be less knowledge and control of the dielectric properties and configuration of the subject. Measured foot currents, like the whole body SAR, represent an integrated response of the body so they are not likely to be as subject to error as are the local values of SAR.

10. A thermal basis is generally assumed for biological effects, so temperatures should be determined as well as the SAR. Careful thermal modeling [12] suggests that the distribution of temperature is quite different from that of the SAR. The bioheat-transfer equation itself has been questioned, and it is necessary to allow for counter-current heat transfer in the extremities. Furthermore, the perfusion of tissues has not been characterized well enough to permit meaningful calculations of temperature.

We would suggest that there is a need for measurements of local SAR with animal models, as well as further studies with human body parts, in order to determine the actual values of SAR under a variety of conditions. Measurements made in an amputated human leg [8] showed several effects that would not have been

3

anticipated from numerical modeling. For example, a significant SAR was measured in the bone, which is surprising because the leg was located on the axis of an applicator that produces an electric field that is predominantly axial in orientation. One would be led to believe that under these conditions the electric field intensity would be approximately constant from tissue to tissue, but the deviations from coaxial geometry were found to have significant effects. The data suggest that there is likelihood of bone necrosis in hyperthermia.

We would suggest that experiments with animal models and human body parts be closely correlated with numerical solutions in order to determine the level of precision that is appropriate for the solutions. That is, to determine whether whole-body, part-body, or high-resolution calculations should be used. It is essential that the probes used in these measurements be minimaly-perturbing and have the smallest possible size. For example, 0.25 mm diameter fluoroptic temperature probes may be more appropriate than the electric field probes that are presently available [13].

References

1. C. H. Durney, M. F. Iskander, H. Massoudi, S. J. Allen and J. C. Mitchell, Radiofrequency Radiation Dosimetry Handbook, 3rd ed., SAM-TR-80-32, USAF School of Aerospace Medicine, Brooks AFB, Texas, 1980.

2. M. J. Hagmann, O. P. Gandhi, J. A. D'Andrea and I. Chatterjee, "Head Resonance: Numerical Solutions and Experimental Results," IEEE Trans. Microwave Theory Tech., vol. 27, pp. 809-813, September 1979.

3. K. D. Paulsen, J. W. Strohbehn and D. R. Lynch, "Theoretical Electric Field Distributions Produced by Three Types of Regional Hyperthermia Devices in a Three-Dimensional Homogeneous Model of Man," IEEE Trans. Biomed. Eng., vol. 35, pp. 36-45, January 1988.

4. J.-Y. Chen and O. P. Gandhi, "Numerical Simulation of Annular-Phased Arrays of Dipoles for Hyperthermia of Deep-Seated Tumors," IEEE Trans. Biomed. Eng., vol. 39, pp. 209-216, March 1992.

5. M. J. Hagmann, H. Massoudi, C. H. Durney and M. F. Iskander, "Comments on 'Limitations of the Cubical Block Model of Man in Calculating SAR Distributions," IEEE Trans. Microwave Theory Tech., vol. 33, pp. 347-350, April 1985.

6. A. C. Cangellaris and D. B. Wright, "Analysis of the Numerical Error Caused by the Stair-Stepped Approximation of a Conducting Boundary in FDTD Simulations of Electromagnetic Phenomena," IEEE Trans. Antennas Propagat., vol. 39, pp. 1518-1525, October 1991.

7. A. R. Von Hippel, Dielectrics and Waves, (M.I.T Press, Cambridge, Massachusetts, 1954), pp. 228-232.

8. C. K. Charny, J.-L. Guerquin-Kern, M. J. Hagmann, S. W.

4

Levin, E. E. Lack, W. F. Sindelar, A. Zabell, E. J. Glatstein and R. L. Levin, "Human Leg Heating using a Mini-Annular Phased Array," Medical Physics, vol. 13, pp. 449-456, July/August 1986.

9. M. J. Hagmann and T. M. Babij, "Non-Invasive Measurement of Current in the Human Body for Electromagnetic Dosimetry," IEEE Transactions on Biomedical Engineering (in press).

10. O. P. Gandhi, M. J. Hagmann and J. A. D'Andrea, "Part-Body and Multibody Effects on Absorption of Radio Frequency Electromagnetic Energy by Animals and by Models of Man," Radio Science, vol. 14, pp. 15-21, November-December 1979.

11. R. J. Spiegel, M. B. A. Fatmi, S. S. Stuchly and M. A. Stuchly, "Comparison of Finite-Difference Time-Domain SAR Calculations with Measurements in a Heterogeneous Model of Man," IEEE Trans. Biomed. Eng., vol. 36, pp. 849-855, August 1989.

12. C. K. Charny, M. J. Hagmann and R. L. Levin, "A Whole Body Thermal Model of Man during Hyperthermia," IEEE Trans. Biomed. Eng., vol. 34, pp. 375-387, May 1987.

13. T. M. Babij, M. J. Hagmann, C. F. Gottlieb, A. A. Abitbol, A. A. Lewin, J. G. Schwade and P. V. Houdek, "Evaluation of Heating Patterns of Microwave Interstitial Applicators using Miniature Electric Field and Fluoroptic Temperature Probes," International Journal of Hyperthermia, vol. 7:3, 485-492, 1991.

5

SOME RECENT APPLICATIONS OF FDTD FOR EM DOSIMETRY: ELF TO MICROWAVE FREQUENCIES

Om P. Gandhi
Department of Electrical Engineering
University of Utah
Salt Lake City, Utah 84112

Abstract

In this paper, we describe some of the recent applications of the finite-difference time-domain (FDTD) method for a number of problems in bioelectromagnetics. This method, used in the past for whole-body or partial-body exposures due to spatially uniform or nonuniform (far-field or near-field) sinusoidally varying electromagnetic fields, and for low-frequency transient fields, such as those for an electromagnetic pulse, has now been modified and used for the following new applications:

1. For short nanosecond pulses with ultrawide bandwidths, a frequency-dependent FDTD has been formulated, which uses frequency-variable properties of the various tissues using the best-fit two-relaxation-constant Debye equations.

2. The FDTD code has been modified and used for SAR calculations for RF magnetic fields typical of new and emerging magnetic resonance imaging (MRI) techniques.

3. Using scaled higher quasi-static frequencies, the FDTD method has been used for calculations of internal fields and induced current densities in an anatomically based model of the human body for electric, magnetic, or combined EM fields at power-line frequencies.

We also describe a new convolution method to alleviate the problem of having to run computer-memory-intensive anatomically based models repeatedly as the incident fields are varied in time and/or space domains. In this method, the impulse response of the heterogeneous model in time and space domains is obtained and stored. This may then be convolved with the prescribed time and/or space variations of the incident fields. Since convolution integrals are relatively easy to calculate and do not need a large computer memory, high-resolution dosimetric calculations should be possible using smaller computers or PCs.

INTRODUCTION

Great strides have been made in the last few years in the area of numerical dosimetry using anatomically based models of the human body. Perhaps the most successful and the most promising of the numerical methods for SAR calculations at the present time is the finite-difference time-domain (FDTD) method [1-7]. For numerical calculations this method requires a computer memory and cpu time proportional to N as opposed to N^3 for the competing Method of Moments (MOM), where N is the number of cells into which an absorbing body is divided. For bioelectromagnetic applications, use of the FDTD

1

method has, therefore, allowed us to obtain SAR distributions for an anatomically based 45,024-cell model of the human body as opposed to the 100-500-cell models that were possible with MOM, permitting a degree of resolution that would have been unthinkable just four or five years ago.

The FDTD method has been found to be extremely versatile and has been used for whole-body or partial-body exposures due to spatially uniform or nonuniform (far-field or near-field) sinusoidally varying electromagnetic fields, and for low-frequency transient fields such as those for an electromagnetic pulse (EMP). We have also recently extended the use of the FDTD method to obtain SAR and induced current distributions in a 45,024-cell sixteen-tissue, anatomically based model of the human body to frequencies as high as 915 MHz [8]. This work has allowed us to obtain SARs for the various organs (brain, eyes, heart, lungs, liver, kidneys, and intestines) as well as the various parts of the body (head and neck, torso, legs, and arms) as a function of frequency in the band 100-915 MHz. Special attention was given to the frequency band 110-200 MHz to see if we could predict the high SARs that had been observed for the neck by Stuchly et al. [9] at 160 MHz using a four-tissue (skeleton, brain, lungs,and muscle) heterogeneous model of a human. In this work, only three frequencies, 160, 350, and 915 MHz, and an isolated human model had been studied. By calculating SAR distributions at frequency intervals of 10 MHz, we found that the highest layer-averaged SAR for the neck section was obtained not at 160 MHz, but rather at 200 MHz, where the highest local SAR of 3.32 W/kg was calculated for the center of the neck.

The FDTD algorithm has recently been modified and used for the following newly emerging applications:

1. For ultrashort pulses where extremely wide bandwidths (on the order of 1 GHz) are involved, the code has been modified to include frequency-dependent properties of the tissues using the best-fit two relaxation Debye equations [10, 11]. This frequency-dependent finite-difference time-domain ((FD)^{2}TD) method can also be used to determine SAR distributions at multiple frequencies based on a single numerical run with an impulse using the Fourier components at various frequencies.

2. The FDTD code has also been used to calculate SARs in the exposed parts of the human body due to RF magnetic fields that are used in magnetic resonance imaging (MRI). Newer techniques for MRI are leading to the use of higher static magnetic fields and correspondingly higher RF magnetic fields. Based on the solution of a complete set of Maxwell's equations, the FDTD method is usable at any frequency, including RF magnetic-field frequencies as high as about 200 MHz that are proposed for the MRIs of the future [12].

3. For one of the recent applications, the FDTD code has been adapted for calculations of internal E and H fields and induced current densities for human -exposure to electromagnetic fields (EMFs) at power-line frequencies [7]. For these calculations, both the magnetic and electric incident fields have been considered and use is made of a scaled higher quasi-static frequency [13] on the order of 5-10 MHz to help reduce the computation time by over five orders of magnitude.

2

4. To alleviate the problem of having to run the computer-memory-intensive anatomically based model of the human body repeatedly as the incident fields are varied in time and/or space domains, we are developing simple and efficient techniques based on the convolution theory [14]. In this approach, the impulse response of the heterogeneous model is obtained and stored using an impulse in the time domain or space domain (spatially localized incident fields) or both, and convolved with the prescribed variations of the incident fields in time and space domains. Since convolution integrals are relatively easy to calculate and do not need a large computer memory, high-resolution dosimetric calculations should therefore be possible using a small computer or a personal computer (PC), as long as the direction of incidence on the body is maintained. This method inherently assumes that coupling back to the source is negligible, which is true for all far-field sources and for several near-field sources such as leakage fields of RF sealers, microwave ovens, etc.

THE FINITE-DIFFERENCE TIME-DOMAIN METHOD

The finite-difference time-domain method for electromagnetic calculations has been described in a number of publications [see, e.g., 15, 16 for a review of the procedure]. We have used the method for calculations of the distributions of electromagnetic (EM) fields and SARs in sixteen-tissue anatomically based models of the human body for whole-body or partial-body exposures due to far-field (plane-wave) or near-field irradiation conditions [1-8]. In this method, the time-dependent Maxwell's curl equations

$$\nabla \times \mathbf{E} = -\mu \frac{\partial \mathbf{H}}{\partial t} \ , \quad \nabla \times \mathbf{H} = \sigma \mathbf{E} + \varepsilon \frac{\partial \mathbf{E}}{\partial t} \tag{1}$$

are implemented for a lattice of subvolumes or "cells" that may be cubical or parallelipiped with different dimensions δ_x, δ_y, and δ_z in x-, y-, or z-directions, respectively. The components of $\mathbf{E}$ and $\mathbf{H}$ are positioned about each of the cells as shown in Fig. 1 and calculated alternately with half-time-steps where the time step $\delta t = \delta/2c$, where δ is the smallest of the dimensions used for each of the cells and c is the maximum phase velocity of the fields in modeled space. Since some of the modeled volume is air, c corresponds to the velocity of EM waves in air.

In the FDTD method, it is necessary to represent not only the scatterer/absorber such as the human body or a part thereof, but also the EM source/s, including their shapes, excitations, etc., if these sources are in the near-field region [4, 5]. The far-field sources, on the other hand, are described by means of incident plane-wave fields prescribed for a "source" plane [1-3, 6-8], typically 6-10 cells away from the exposed body. The source-body interaction volume is subdivided into cells of the type shown in Fig. 1. The interaction space consisting of several hundred thousand to a few million cells is truncated by means of absorbing boundaries. The prescribed incident fields are tracked in time for all cells of the interaction space. The problem is considered completed when either the fields have died off or, for sinusoidal excitation, when a sinusoidal steady-state behavior for $\mathbf{E}$ and $\mathbf{H}$ is observed for the interaction space.

3

THE FREQUENCY-DEPENDENT FDTD METHOD

As previously mentioned, the frequency-dependent FDTD or $(FD)^2TD$ method is needed for short pulses where wide bandwidths are generally involved. Two general approaches have been used for the $(FD)^2TD$ method. One approach is to convert the complex permittivity from the frequency domain to the time domain and convolve this with the time-domain electric fields to obtain time-domain fields for dispersive material. This discrete time-domain method may be updated recursively for some rational forms of complex permittivity, which removes the need to store the time history of the fields and makes the method feasible. This method has been applied to materials described by a first-order Debye relaxation equation [17-19], a second-order Lorentz equation with multiple poles [20], and to a gaseous plasma [21].

A second approach is to add a differential equation relating the electric flux density **D** to the electric field **E** and solve this new equation simultaneously with the standard FDTD equations. This method has been applied to 1D and 2D examples with materials described by a first-order Debye equation or second-order single-pole Lorentz equation [22], and to 3D sphere and homogeneous two-thirds muscle-equivalent man model with properties described by a second-order Debye equation [10, 23]. In the following we describe this differential equation approach, which has now been used for induced current and SAR calculations for a heterogeneous model of the human body [11].

The time-dependent Maxwell's curl equations used for the FDTD method are:

$$\nabla \times \mathbf{E} = -\frac{\partial \mathbf{B}}{\partial t} = -\mu \frac{\partial \mathbf{H}}{\partial t} \tag{2}$$

$$\nabla \times \mathbf{H} = \frac{\partial \mathbf{D}}{\partial t} \tag{3}$$

where the flux density vector **D** is related to the electric field through the complex permittivity $\varepsilon^*(\omega)$ of the local tissue by the following equation:

$$\mathbf{D} = \varepsilon^*(\omega)\, \mathbf{E} \tag{4}$$

Since Eqs. 2 and 3 are solved iteratively in the time domain, Eq. 4 must also be expressed in the time domain. This may be done by choosing a rational function for $\varepsilon^*(\omega)$ such as the Debye equation with two relaxation constants:

$$\varepsilon^*(\omega) = \varepsilon_0 \left[\varepsilon_\infty + \frac{\varepsilon_{s1} - \varepsilon_\infty}{1 + j\,\omega\,\tau_1} + \frac{\varepsilon_{s2} - \varepsilon_\infty}{1 + j\,\omega\,\tau_2} \right] \tag{5}$$

4

Rearranging Eq. 5 and substituting in Eq. 4 gives

$$D(\omega) = \varepsilon^*(\omega)\, E(\omega) = \varepsilon_o \frac{\varepsilon_s + j\,\omega\,(\varepsilon_{s1}\,\tau_2 + \varepsilon_{s2}\,\tau_1) - \omega^2\,\tau_1\,\tau_2\,\varepsilon_\infty}{1 + j\,\omega\,(\tau_1 + \tau_2) - \omega^2\,\tau_1\,\tau_2}\, E(\omega)$$

(6)

where the dc (zero frequency) dielectric constant is given by

$$\varepsilon_s = \varepsilon_{s1} + \varepsilon_{s2} - \varepsilon_\infty$$

(7)

Assuming $e^{j\omega t}$ time dependence, we can write Eq. 6 as a differential equation in the time domain

$$\tau_1\,\tau_2\,\frac{\partial^2 D}{\partial t^2} + (\tau_1 + \tau_2)\,\frac{\partial D}{\partial t} + D =$$

$$\varepsilon_o \left[\varepsilon_s\, E + (\varepsilon_{s1}\,\tau_2 + \varepsilon_{s2}\,\tau_1)\,\frac{\partial E}{\partial t} + \varepsilon_\infty\,\tau_1\,\tau_2\,\frac{\partial^2 E}{\partial t^2} \right]$$

(8)

For the (FD)^{2}TD method, we need to solve Eqs. 2 and 3 subject to Eq. 8. As in references 10 and 23, we write these equations in the difference form, solve Eq. 8 to find E, Eq. 2 to find H, and Eq. 3 to find D at each cell location. The E $\rightarrow$ H $\rightarrow$ D loop is then repeated until the pulse has died off.

ANATOMICALLY BASED MODELS OF HUMANS

For most of the calculations given in this paper, the anatomically based model described in our earlier publications [2-7] has been used. This model is based on the cross-sectional diagrams of the human body given in the book by Eycleshymer and Schoemaker [24]. This book contains cross-sectional diagrams of the human body which were obtained by making cross-sectional cuts at spacings of about one inch in human cadavers. The process for creating the data base of the man model was the following: first of all, a quarter-inch grid was taken for each single cross-sectional diagram and each cell on the grid was assigned a number corresponding to one of the sixteen tissue types (muscle, fat, bone, blood, intestine, cartilage, liver, kidney, pancreas, spleen, lung, heart, nerve, brain, skin, eye) or air. Thus the data associated with a particular layer consisted of three numbers for each square cell: x and y positions relative to some anatomical reference point in this layer, usually the center of the spinal cord; and an integer indicating which tissue that cell contained. Since the cross-sectional diagrams available in [24] are for somewhat variable separations, typically 2.3-2.7 cm, a new set of equispaced layers was defined at 1/4-in

5

(0.635 cm) intervals by interpolating the data onto these layers. Because the 1/4-in cell size is too small for the memory space of readily accessible computers, the proportion of each tissue type was calculated next for somewhat larger cells of size 1/2 in (1.27 cm) combining the data for $2 \times 2 \times 2 = 8$ cells of the smaller dimension. Without changes in the anatomy, this process allows some variability in the height and weight of the body. We have taken the final cell size of 1.31 cm (rather than 1/2 in) to obtain the total height and body weight of 175.5 cm and 69.6 kg, respectively. With a resolution of 1.31 cm, the model consists of a total of 45,024 cells that are either totally or partially within the human body. If the shoe-wearing condition of the model is needed, this is simulated by using a separation layer of rubber ($\varepsilon_r = 4.0$) that is 2 layers or 2.62 cm thick between the feet and the ground plane.

MODELING OF THE TISSUE PROPERTIES WITH THE DEBYE EQUATION

For ultrawideband calculations using the $(FD)^2TD$ method, the measured properties for the various tissues have been fitted to the Debye equation 5 with two relaxation constants [10, 11, 23]. The measured properties of biological tissues (muscle, fat, bone, blood, intestine, cartilage, lung, kidney, pancreas, spleen, lung, heart, brain/nerve, skin, and eye) were obtained from [25]. Optimum values for ε_{s1}, ε_{s2}, ε_{∞}, τ_1, and τ_2 in Eq. 5 were obtained by nonlinear least squares matching to the measured data for fat and muscle. All other tissues have properties falling roughly between these two. Optimum values shown in Table 1 for ε_{s1}, ε_{s2}, and ε_{∞} for all tissues were then obtained with τ_1 and τ_2 being the average of the optimized values for fat and muscle. This was done to facilitate volume averaging of the tissue properties in cells of the heterogeneous man model. Having τ_1 and τ_2 constant for all tissues allowed linear (volume) averaging of the ε values for each tissue in a given cell to calculate ε values for that cell. The measured tissue properties and those computed from the Debye equation with τ_1 and τ_2 being the average of fat muscle are shown in Fig. 2 for fat and muscle. Similar comparisons were also obtained for the other tissue types.

COUPLING OF AN ULTRAWIDEBAND PULSE TO THE HUMAN BODY

The $(FD)^2TD$ method has been used to calculate coupling of an ultrashort pulse to the heterogeneous model of the human body. From the calculated internal fields we calculated the vertical currents passing through the various layers of the body by using the following equation:

$$I_z(t) = \delta^2 \sum_{i,j} \frac{\partial D_z}{\partial t}$$

(9)

where δ is the cell size (= 1.31 cm), and the summation is carried out for all cells in a given layer. We also calculated the layer-averaged absorbed energy density or specific absorption (SA) and the total energy W absorbed by the whole body using the following relationships:

6

$$SA\Big|_{\text{layer }k} = \frac{\delta t}{N_k} \sum_t \frac{E(i,j,k,t)}{\rho(i,j,k)} \bullet \frac{\partial D(i,j,k,t)}{\partial t} \quad (10)$$

$$W = \delta t \bullet \delta^3 \sum_t E(i,j,k,t) \bullet \frac{\partial D(i,j,k,t)}{\partial t} \quad (11)$$

In Eqs. 10 and 11, δt is the time step (= $\delta/2c$ = 0.02813 ns) used for the time-domain calculations, N_k is the number of cells in layer k of the body, and $\rho(i,j,k)$ is the mass density in kg/m^3 for each of the cells in the corresponding layers.

For the various calculations, we have used both the isolated model of the human body as well as the model standing vertically on a conducting ground plane.

A typical ultrawideband pulse with a prescribed peak amplitude of 1.1 V/m is shown in Fig. 3 in the time domain. The pulse shape was provided on a diskette by Jim O'Loughlin of Kirtland Air Force Base, New Mexico, courtesy of Dr. David N. Erwin of Armstrong Laboratory, Brooks Air Force Base, Texas. It is interesting to note that the pulse has a rise time of about 0.2 ns and a total time domain of about 7-8 ns. We have calculated the Fourier spectrum of the prescribed pulse which is shown in Fig. 4. Most of the energy in the pulse is concentrated in the 200-900 MHz band with the peak of the energy being at about 500 MHz.

We assumed the incident fields to be vertically polarized, since this polarization is known to result in the strongest coupling for standing individuals. Using the (FD)^{2}TD procedure described earlier, we have calculated the temporal variations of total vertical currents for the various sections of the body, for both the shoe-wearing grounded, and ungrounded exposure conditions of the model, respectively. The current variations for a couple of representative sections such as those through the eyes and the bladder are given in Figs. 5a and 5b, respectively. The calculated peak currents for the various sections are on the order of 1.1 to 3.2 mA/(V/m). It is interesting to note that there is very little difference in the induced currents whether the model is grounded or not. This is on account of the fact that most of the energy in the pulse is at frequencies in excess of 300 MHz, where the effect of the ground plane on the induced currents or the SARs is minimal [8].

In Fig. 6 we have plotted the peak current for each section of the body with a resolution of 1.31 cm. The maximum peak current of 3.5 mA, which is 3.2 mA/(V/m) occurs at a height of 96.3 cm above the bottom of the feet. A very similar result had previously been observed for calculations using isolated and grounded models of the human body for plane-wave exposures at frequencies of 350-700 MHz, where the highest induced currents on the order of 3.0-3.2 mA/(V/m) were calculated for sections of the body that are at heights of 85-100 cm relative to the feet [8].

Using Eqs. 10 and 11, we have also calculated the specific absorptions (SA) and the total absorbed energy for exposure to the ultrawideband pulse of Fig. 3. The specific absorptions are plotted in Fig. 7 as a function of height above the feet of the various

7

sections of the body for isolated and shoe-wearing conditions. Note that because of the very limited time duration of the pulse (7-8 ns), the specific absorptions are on the order of 0.02 to 0.20 pJ/kg. Using Eq. 11, the total energy absorbed by the body as a function of time has been calculated and is shown in Fig. 8. The energy is virtually all absorbed in the first 6 to 8 ns. The total energy absorbed by the body exposed to a single pulse is calculated to be 2.0 and 1.91 pico Joules for isolated and shoe-wearing grounded conditions, respectively.

SAR DISTRIBUTIONS DUE TO RF MAGNETIC FIELDS OF MRI

Magnetic Resonance Imaging (MRI) is becoming an increasingly important tool for medical diagnostic applications. New and emerging technologies are leading to use of higher static magnetic fields (up to 4T) and associated higher RF frequencies (up to 200 MHz) [26]. Recently suggested safety guidelines by the USFDA [27] and the NRPB (UK) [28] limit the SARs within the body for exposure to the RF magnetic fields used for the MRI. We have, in the past, used the impedance method to calculate the SAR distributions in the 1.31-cm-resolution anatomically based model of the human body [29]. Because of the quasi-static approximation, the impedance method cannot, however, be used for frequencies in excess of 30-40 MHz. To alleviate this frequency limitation, we have been investigating the applicability of FDTD for SAR calculations for parts of the body that are exposed to RF magnetic fields of magnetic resonance imagers. For this application, we have modified the FDTD algorithm so that a sinusoidal uniform equiphase magnetic field either linearly or circularly polarized is postulated for each of the cells for the exposed parts of the body as the initial excitation. Solution of the Maxwell's equations for subsequent times give rise to the spatial nonuniformities and creation of internal (and external) electric fields.

To test the feasibility of using the FDTD method for such calculations, we have used a test case of a lossy sphere of radius 20 cm. We initially used a lower frequency of 5 MHz, where the results could be compared with the analytical solution that can be obtained from Faraday's law of induction.

$$\oint \mathbf{E} \cdot d\boldsymbol{\ell} = - \frac{\partial}{\partial t} \int \mathbf{B} \cdot d\mathbf{S}$$

(12)

For a circularly symmetric model such as a sphere

$$\mathbf{E} = E_\phi \hat{\phi} = - \frac{j \omega \mu_o H r}{2} \hat{\phi}$$

(13)

In Fig. 9, curve a shows the plot of magnitude of E_z (= $|E_\phi|$) along the central y axis of the sphere obtained from the analytical Eq. 13 and the results obtained by using the modified FDTD algorithm. For the calculations, properties assumed for the sphere were ε_r = 340, σ = 0.5 S/m, corresponding to the properties for high-water-content tissues such as

8

muscle at 5 MHz [30]. Agreement of the FDTD-calculated results with the analytical results (curve a) is excellent.

After verifying the feasibility of using the FDTD method, we next applied it for calculations of induced RF electric fields for an applied $H = H_x \hat{x} = 1$ A/m at 200 MHz. For these calculations, we assumed $\varepsilon_r = 37.0$ and $\sigma = 0.85$ S/m, corresponding to the properties of 2/3 muscle at 200 MHz [30]. The calculated variation of $|E_z|$ along the central y axis is shown as curve b in Fig. 9. For comparison, we have also plotted the linear variation given in by Eq. 13 as curve c in Fig. 9. It is interesting to note that the induced E fields (and, hence, SARs) based on the solution of the complete set of Maxwell's equations (the FDTD method) are considerably lower than those that will be given by solving just the Faraday's law of induction Eq. 13. This is not surprising, since the latter procedure is valid only for low frequencies where quasi-static approximations can be made.

We have also carried out calculations for another test case for which a homogeneous muscle-equivalent cylinder of dimensions 20 cm was used for calculations at 10, 30, and 100 MHz. The calculated SAR variations for this test case were found to be similar to those given in a paper by Bottomley and Andrew [31]. It was interesting to note both in the test case for the sphere (Fig. 9) and the cylinder that the SARs at higher frequencies do not increase as rapidly as ω^2 and there is a dramatic reduction of the RF magnetic field in the interior of these homogeneous bodies for frequencies in excess of about 30 MHz. We are presently in the process of extending this procedure for calculations of SARs and of internal magnetic-field variations for the anatomically based model of the human body.

NUMERICAL DOSIMETRY AT POWER-LINE FREQUENCIES

As described in reference 7, the FDTD method has also been adapted for calculations of internal E and H fields and induced current densities for exposure to purely electric, purely magnetic, or combined electric and magnetic fields (EMFs) at power-line frequencies. It is recognized that the conductivities of several tissues (skeletal muscle, bone, etc.) are highly anisotropic for power-line frequencies. This has, however, been neglected in the first instance and will be included in the future when models based on separate identification of these tissues are available.

Both sinusoidal and prescribed time-varying incident fields can be used with the FDTD procedure -- hence the method is well-suited also for transient exposures that are often of interest at power-line-related frequencies. For sinusoidally varying fields, the solution is completed when a sinusoidal steady-state behavior for E and H fields is observed for each of the cells. For lossy biological bodies this typically takes a stepped time on the order of 3 to 4 time periods of oscillation. Since δt is fixed for a given cell size, a larger number of iterations is therefore needed at lower frequencies. Because of the horrendous number of iterations, the FDTD procedure would be clearly inapplicable for calculations at power-line frequencies were it not for the quasi-static nature of the coupling as previously pointed out by Kaune and Gillis [32] and Guy et al. [13]. Using a logic similar to these authors, the fields outside the body depend not on the internal tissue properties, but only on the shape of the body as long as the quasi-static approximation is valid, i.e., the size of the body is a factor of 10 or more smaller than the wavelength, and $|\sigma + j\omega\varepsilon| \gg \omega\varepsilon_o$ where σ and ε are the conductivity and the permittivity of the tissues, respectively, $\omega = 2\pi f$

9

is the radian frequency, and ε_0 is the permittivity of the free space outside the body. Under these conditions, the electric fields in air are normal to the body surface and the internal tissue electric fields are given from the boundary conditions in terms of the fields outside

$$j\omega\varepsilon_0\hat{n} \cdot \mathbf{E}_{air} = (\sigma + j\omega\varepsilon)\hat{n} \cdot \mathbf{E}_{tissue} \tag{14}$$

A higher quasi-static frequency f′ may therefore be used for irradiation of the model and the internal fields E′ thus calculated may be scaled back to frequency f of interest, e.g., 60 Hz. From Eq. 14 we can write

$$\mathbf{E}_{tissue}(f) = \frac{\omega}{\omega'} \frac{(\sigma' + j\omega\varepsilon')}{(\sigma + j\omega\varepsilon)} \mathbf{E}'_{tissue}(f')$$

$$\approx \frac{f\,\sigma'}{f'\,\sigma} \mathbf{E}'_{tissue}(f') \tag{15}$$

assuming that $\sigma + j\omega\varepsilon \approx \sigma$ at both f′ and f.

For our calculations, we have used a full-scale anatomically based model of the human body and a frequency f′ of 5-10 MHz to reduce the computation time by orders of magnitude. Since in the FDTD method, one needs to calculate in the time domain until convergence is obtained (typically 3-4 time periods), this frequency scaling to 5-10 MHz for f′ reduces the needed number of iterations by over 5 orders of magnitude. At the higher irradiation frequency f′, we have taken $\sigma' = \sigma$, i.e., conductivities of the various tissues at 60 Hz. Furthermore, we have taken the incident E field $\mathbf{E}_i(f') = 60\,\mathbf{E}_i(f)/f'$ to obtain $\mathbf{E}_{tissue}(f)$ at say $\mathbf{E}_i(f) = 10$ kV/m. The incident magnetic field $\mathbf{H}_i(f')$ has similarly been taken to be considerably lower ($= 60\,\mathbf{H}_i(f)/f'$) to account for the fact that the induced current densities and internal electric fields are proportional to the frequency of the incident fields and would therefore be higher at the assumed frequency f′.

After verifying the accuracy of this approach with test cases using homogeneous and layered spheres [7] where the results for the internal field variations could be compared with those using the analytic Mie series solutions [33], we also checked the results against the experimental data on a mannequin given by Deno [34] and the variations of the induced currents calculated along the height of the body by DiPlacido et al. [35]. The agreement with the results of these two authors who had used a vertical electric field such as that under a high-voltage power line was found to be very good.

Shown in Fig. 10 are the calculated results using the anatomically based model where the conductivities used for the various tissues are as given in Table 2. Recognizing the anisotropy in the conductivity of the skeletal muscle, two different values of muscle conductivities are taken for curves (1) and (2). For these curves a higher conductivity of 0.52 S/m is taken for the skeletal muscle and an average value of 0.11 S/m is taken for the muscle in the interior of the body. For curves (3) and (4), however, a lower conductivity of 0.11 S/m is taken for all of the muscle, interior or skeletal. The results shown in Fig. 10 curves (1), (3), and (4) are for $\mathbf{E}_{inc} = 10$ kV/m (vertical) and $\mathbf{H}_{inc} = 26.5$ A/m from side to

10

side of the model. To point out the preponderance of the induced currents due to incident electric field, $H_{inc} = 0$ is assumed for the calculations shown in curve (2). It is interesting to note that the layer currents due to E-field exposure alone are almost 98-99 percent of the currents calculated for the combined electric and magnetic fields. It is also interesting to note that the calculated foot currents of 155-160 μA are in excellent agreement with 165 μA that would be projected from the measurements of Deno [34] for the human.

For the combined electric- and magnetic-field exposure condition of curve (1), the current density distributions for three representative sections through the brain, the heart, and the ankles are shown in Figs. 11a-c, respectively. For each of the sections the letter F denotes the front of the body. For comparison the current density distributions for the same sections due to incident magnetic field alone ($H_{inc} = 26.5$ A/m or B = 33 μT) are shown in Figs. 11d-f. It is interesting to note that considerably smaller current densities are obtained due to magnetic fields alone, as compared to the combined EMFs.

A NEW CONVOLUTION PROCEDURE FOR NUMERICAL DOSIMETRY

To alleviate the problem of having to run computer-memory-intensive anatomically based models of the human body repeatedly, we are developing simple and efficient techniques based on convolution theory, where the impulse response of the heterogeneous model would be obtained and stored using an impulse in the time domain or space domain (spatially localized incident fields) or both, and convolved with the prescribed variation of the incident fields in time and space domains. We illustrate this procedure in the following with the example of the response of the model for exposure to pulses or transients of prescribed shapes [36]. For impulse response calculations, a narrow unit magnitude flat-top "impulse" of time duration $T' = 5$ to 10 δt is assumed. The impulse-induced current response $H_i(t)$ for the various sections of the body (such as sections through the eyes, neck, heart, liver, etc.) is calculated and stored. Induced currents $I_i(t)$ for these sections for a prescribed incident pulse $E(\tau)$ can then be calculated from the convolution integral

$$I_i(t) = \int_0^T E(\tau) \, H_i(t-\tau) \, d\tau$$

(16)

where the integration time T is a period in excess of the time duration of the incident pulse. An alternate procedure that has also been found to be equally applicable is to work with Eq. 16 in terms of the Fourier transforms $\mathcal{F}\{H_i(t)\}$, $\mathcal{F}\{E^{im}(t)\}$, and $\mathcal{F}\{E(t)\}$ of the induced currents $H_i(t)$, the broadband initial impulse $E^{im}(t)$, and the prescribed pulse $E(t)$ for which the induced currents $I_i(t)$ are desired. In terms of the Fourier transforms Eq. 16 can be written as

$$I_i(t) = \mathcal{F}^{-1}\left\{\frac{\mathcal{F}\{E(t)\}\,\mathcal{F}\{H_i(t)\}}{\mathcal{F}\{E^{im}(t)\}}\right\}$$

(17)

11

where the discrete Fourier transforms needed for Eq. 17 can be efficiently calculated using the Fast Fourier Transform (FFT) algorithm. Both of the above approaches are relatively simple and do not need a large computer memory, making it possible to use a small computer or PC for calculating the response of the human body to any desired incident pulse. We show in Figs. 12a and 12b the comparison of the vertical currents induced for a couple of representative sections of the body for the ultrawideband pulse of Fig. 3. In both Figs. 12a and 12b the time-domain variations of the currents calculated with the simpler impulse response and the convolution method are in excellent agreement with the results obtained from the exact simulation with the conventional $(FD)^2TD$ method.

A similar procedure may be also be usable for prescribed spatial variations of the incident fields.

CONCLUDING REMARKS

From the foregoing it can be seen that the FDTD method is very versatile and has been used for a number of important and meaningful problems in the field of bioelectromagnetics. Some of the future applications involve improving the efficiency of the code by techniques such as use of the expanding grid rather than the regular grid, elimination of the interior of the body at higher frequencies, since this region is relatively shielded from incident fields, and use of truncated models of the body at microwave frequencies where there is a lack of coupling between the various regions of the body. We also plan to develop the new convolution method for use with prescribed variations of the incident fields in time and space domains. In this method, high-resolution impulse response of the model, in time and space domains, would be stored and used for subsequent calculations. Since convolution integrals are relatively easy to calculate and do not need a large computer memory, high-resolution dosimetric calculations should be possible using smaller computers or PCs. We also plan to focus on computer graphical displays for visualization of the calculated data.

12

REFERENCES

1. D. M. Sullivan, D. T. Borup, and O. P. Gandhi, "Use of the Finite-Difference Time-Domain Method in Calculating EM Absorption in Human Tissues," *IEEE Transactions on Biomedical Engineering*, Vol. BME-34, pp. 148-15, 1987.

2. D. M. Sullivan, O. P. Gandhi, and A. Taflove, "Use of the Finite-Difference Time-Domain Method in Calculating EM Absorption in Man Models, *IEEE Transactions on Biomedical Engineering*, Vol. BME-35, pp. 179-186, 1988.

3. J. Y. Chen and O. P. Gandhi, "RF Currents Induced in an Anatomically Based Model of a Human for Plane-Wave Exposures 20-100 MHz," *Health Physics*, Vol. 57, pp. 89-98, 1989.

4. J. Y. Chen and O. P. Gandhi, "Electromagnetic Deposition in an Anatomically Based Model of Man for Leakage Fields of a Parallel-Plate Dielectric Heater," *IEEE Transactions on Microwave Theory and Techniques*, Vol. MTT-37, pp. 174-180, 1989.

5. C. Q. Wang and O. P. Gandhi, "Numerical Simulation of Annular-Phased Arrays for Anatomically Based Models Using the FDTD Method," *IEEE Transactions on Microwave Theory and Techniques*, Vol. MTT-37, pp. 118-126, 1989.

6. J. Y. Chen and O. P. Gandhi, "Currents Induced in an Anatomically Based Model of a Human for Exposure to Vertically Polarized EMP," *IEEE Transactions on Microwave Theory and Techniques*, Vol. MTT-39, pp. 31-39, 1991.

7. O. P. Gandhi and J. Y. Chen, "Numerical Dosimetry at Power-Line Frequencies Using Anatomically Based Models," *Bioelectromagnetics*, Suppl 1, pp. 43-60, 1992.

8. O. P. Gandhi, Y. G. Gu, J. Y. Chen, and H. I. Bassen, "Specific Absorption Rates and Induced Current Distributions in an Anatomically Based Human Model for Plane-Wave Exposures (at Frequencies 20-915 MHz)," *Health Physics*, Vol. 63 (3), pp. 281-290, 1992.

9. S. S. Stuchly, A. Kraszewski, M. A. Stuchly, G. W. Hartstgrove, and R. J. Spiegel, "RF Energy Deposition in a Heterogeneous Model of Man: Far-Field Exposures," *IEEE Transactions on Biomedical Engineering*, Vol. BME-34, pp. 951-957, 1987.

10. O. P. Gandhi, B. Q. Gao, and J. Y. Chen, "A Frequency-Dependent Finite-Difference Time-Domain Formulation for Induced Current Calculations in Human Beings," *Bioelectromagnetics*, Vol. 13 (6), pp. 543-555, 1992.

11. C. M. Furse, J. Y. Chen, and O. P. Gandhi, "A Frequency-Dependent Finite-Difference Time-Domain Method for Induced Current and SAR Calculations for a Heterogeneous Model of the Human Body," submitted for publication to *IEEE Transactions on Electromagnetic Compatibility*.

12. O. P. Gandhi and J. Y. Chen, "Absorption and Distribution Patterns of RF Magnetic Fields Used or Planned for MRI with Frequencies up to 200 MHz," to be

13

presented at the Meeting of the Bioelectromagnetics Society, Los Angeles, California, June 13-17, 1993.

13. A. W. Guy, S. Davidow, G. Y. Yang, and C. K. Chou, "Determination of Electric Current Distributions in Animals and Humans Exposed to a Uniform 60-Hz High-Intensity Electric Field," *Bioelectromagnetics*, Vol. 3, pp. 47-71, 1982.

14. O. P. Gandhi, J. Y. Chen, C. M. Furse, and Y. Cui, "A Simple Convolution Procedure for Calculating Coupling to the Human Body for EM Fields of Prescribed Time and Space Variations," to be presented at the Meeting of the Bioelectromagnetics Society, Los Angeles, California, June 13-17, 1993.

15. A. Taflove and K. R. Umashankar, "The Finite-Difference Time-Domain Method for Numerical Modeling of Electromagnetic Wave Interactions with Arbitrary Structures," Chapter 8 in *Progress in Electromagnetics Research PIER 2*, Michael A. Morgan, Editor, Elsevier Science Publishing Company, New York, New York, 1990.

16. O. P. Gandhi, "Numerical Methods for Specific Absorption Rate Calculations, Chapter 6 in *Biological Effects and Medical Applications of Electromagnetic Energy*, Om P. Gandhi, Editor, Prentice Hall, Englewood Cliffs, New Jersey, 1990.

17. R. J. Luebbers, F. P. Hunsberger, K. S. Kunz, R. B. Standler, and M. Schneider, "A Frequency-Dependent Finite-Difference Time-Domain Formulation for Dispersive Materials," *IEEE Transactions on Electromagnetic Compatibility*, Vol. EMC-32, pp. 222-227, 1990.

18. M. D. Bui, S. S. Stuchly, and G. I. Costache, "Propagation of Transients in Dispersive Dielectric Media," *IEEE Transactions on Microwave Theory and Techniques*, Vol. MTT-39, pp. 1165-1172, 1991.

19. D. M. Sullivan, "A Frequency-Dependent FDTD Method for Biological Applications," *IEEE Transactions on Microwave Theory and Techniques*, Vol. MTT-40, pp. 532-539, 1992.

20. R. Luebbers, F. Hunsberger, and K. Kunz, "FDTD for Nth Order Dispersive Media," submitted to *IEEE Transactions on Antennas and Propagation*, 1992.

21. R. J. Luebbers, F. Hunsberger, and K. S. Kunz, "A Frequency-Dependent Finite-Difference Time-Domain Formulation for Transient Propagation in Plasma," *IEEE Transactions on Antennas and Propagation*, Vol. AP-39, pp. 29-34, 1991.

22. R. M. Joseph, S. C. Hagness, A. Taflove, "Direct Time Integration of Maxwell's Equations in Linear Dispersive Media with Absorption for Scattering and Propagation of Femtosecond Electromagnetic Pulses," *Optics Letters*, Vol. 16 (18), pp. 1412-1414, 1991.

23. O. P. Gandhi, B. Q. Gao, and J. Y. Chen, "A Frequency-Dependent Finite-Difference Time-Domain Formulation for General Dispersive Media," *IEEE Transactions on Microwave Theory and Techniques*, Vol. 41, April 1993.

24. A. C. Eycleshymer and D. M. Schoemaker, *A Cross-Section Anatomy*, Appleton-Century-Crofts, New York, 1970.

14

25. C. H. Durney et al., *Radiofrequency Radiation Dosimetry Handbook*, Second Edition, June 1978.

26. R. L. Magin, R. P. Liburdy, and B. Persson, Editors, "Biological Effects and Safety Aspects of Nuclear Magnetic Resonance Imaging and Spectroscopy," *Annals of the New York Academy of Sciences*, Vol. 649, 1992.

27. U. S. Food and Drug Administration: Magnetic Resonance Diagnostic Device: Panel Recommendation and Report on Petitions for MR Reclassification. Fed. Reg. 53:7575, 1988.

28. National Radiological Protection Board, U. K., "Revised Advice on Acceptable Restrictions of Patient and Volunteer Exposure During Clinical Magnetic Resonance Diagnostic Procedures," 1990.

29. N. Orcutt and O. P. Gandhi, "A 3-D Impedance Method to Calculate Power Deposition in Biological Bodies Subjected to Time-Varying Magnetic Fields," *IEEE Transactions on Biomedical Engineering*, Vol. 35, pp. 577-583, 1988.

30. C. C. Johnson and A. W. Guy, "Nonionizing Electromagnetic Wave Effects in Biological Materials and Systems," *Proceedings of the IEEE*, Vol. 60, pp. 692-718, 1972.

31. P. A. Bottomley and E. R. Andrew, "RF Magnetic Field Penetration, Phase Shift, and Power Dissipation in Biological Tissue: Implications for NMR Imaging," *Physics in Medicine and Biology*, Vol. 23, pp. 630-643, 1978.

32. W. T. Kaune and M. F. Gillis, "General Properties of the Interaction Between Animals and ELF Electric Fields," *Bioelectromagnetics*, Vol. 2, pp. 1-11, 1981.

33. J. R. Mautz, "Mie Series Solution for a Sphere," *IEEE Transactions on Microwave Theory and Techniques*, Vol. MTT-26, p. 375, 1978.

34. D. W. Deno, "Currents Induced in the Human Body by High Voltage Transmission Line Electric Field -- Measurement and Calculation of Distribution and Dose," *IEEE Transactions on Power Apparatus and Systems*, Vol. PAS-96, pp. 1517-1527, 1977.

35. J. DiPlacido, C. H. Shih, B. J. Ware, "Analysis of the Proximity Effects in Electric Field Measurements," *IEEE Transactions on Power Apparatus and Systems*, Vol. PAS-97, pp. 2167-2177, 1978.

36. J. Y. Chen, C. M. Furse, and O. P. Gandhi, "A Simple Convolution Procedure for Calculating Currents Induced in the Human Body for Exposure to Electromagnetic Pulses, " submitted for publication to *IEEE Transactions on Microwave Theory and Techniques*.

15

Table 1. Debye constants for tissues.

$$\tau_1 = 46.2 \times 10^{-9} \text{ s}$$

$$\tau_2 = 0.91 \times 10^{-10} \text{ s}$$

(average of optimum for fat and muscle)

Tissue	ε_∞	ε_{s1}	ε_{s2}
Muscle	40.0	3948.	59.09
Bone/Cartilage	3.4	312.8	7.11
Blood	35.0	3563.	66.43
Intestine	39.0	4724.	66.09
Liver	36.3	2864.	57.12
Kidney	35.0	3332.	67.12
Pancreas/Spleen	10.0	3793.	73.91
1/3 Lung	10.0	1224.	13.06
Heart	38.5	4309.	54.58
Brain/Nerve	32.5	2064.	56.86
Skin	23.0	3399.	55.59
Eye	40.0	2191.	56.99

16

Table 2. Tissue conductivities used for calculations at the power-line frequency of 60 Hz..

TISSUE TYPE	σ S/m
Air	0
Muscle	0.52 or 0.11
Fat, Bone	0.04
Blood	0.6
Intestine	0.11
Cartilage	0.04
Liver	0.13
Kidney	0.16
Pancreas	0.11
Spleen	0.18
Lung*	0.04
Heart	0.11
Nerve,Brain	0.12
Skin	0.11
Eye	0.11

* We have used 33 percent lung tissue and 67 percent air for the dielectric properties of the lung.

17
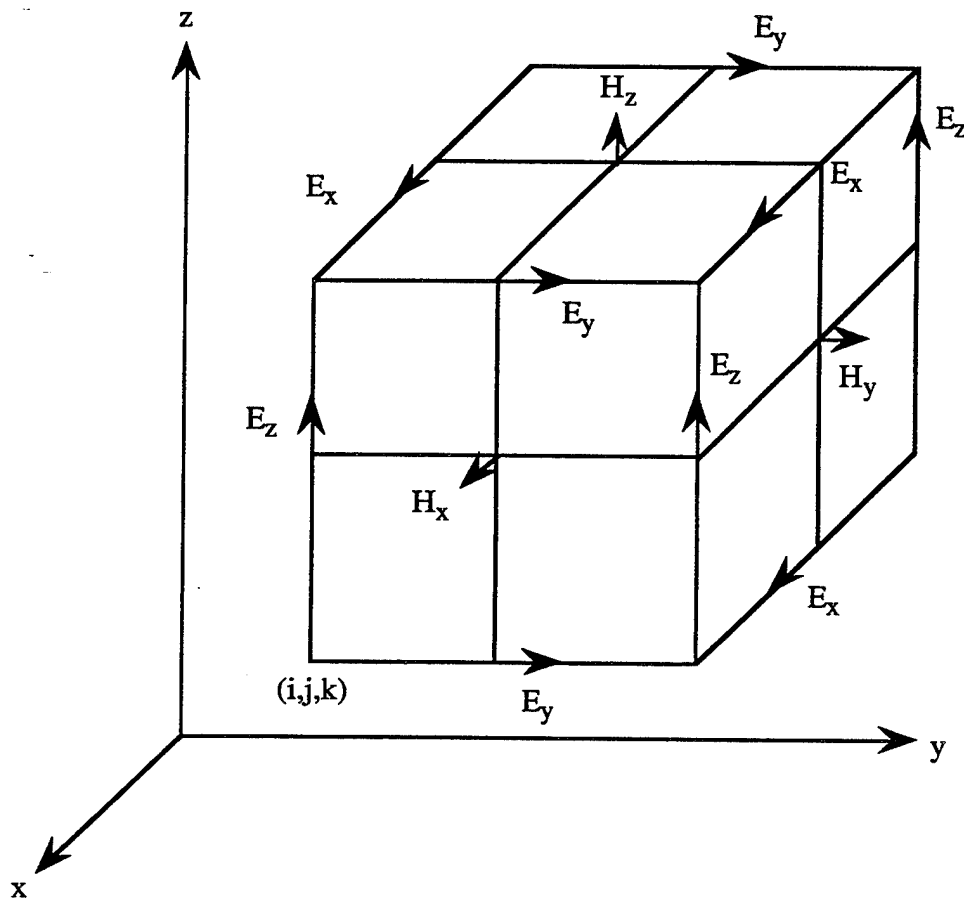
Fig. 1. Unit cell of Yee lattice indicating positions for various field components.
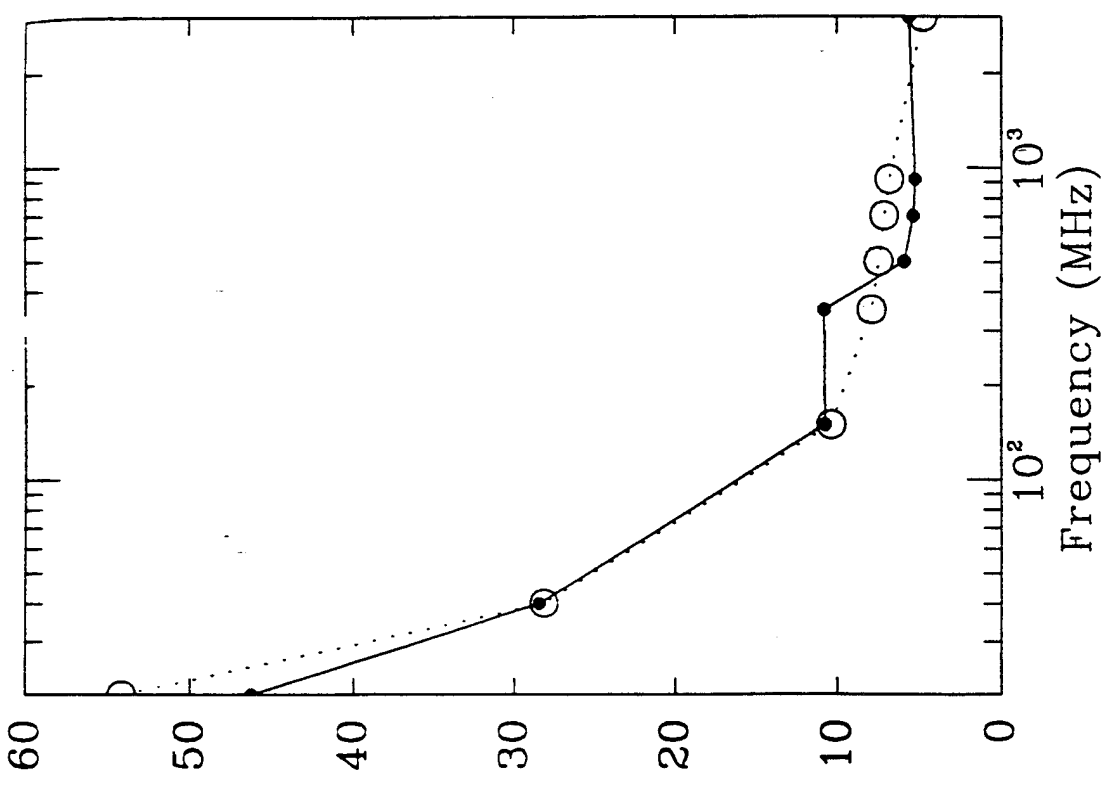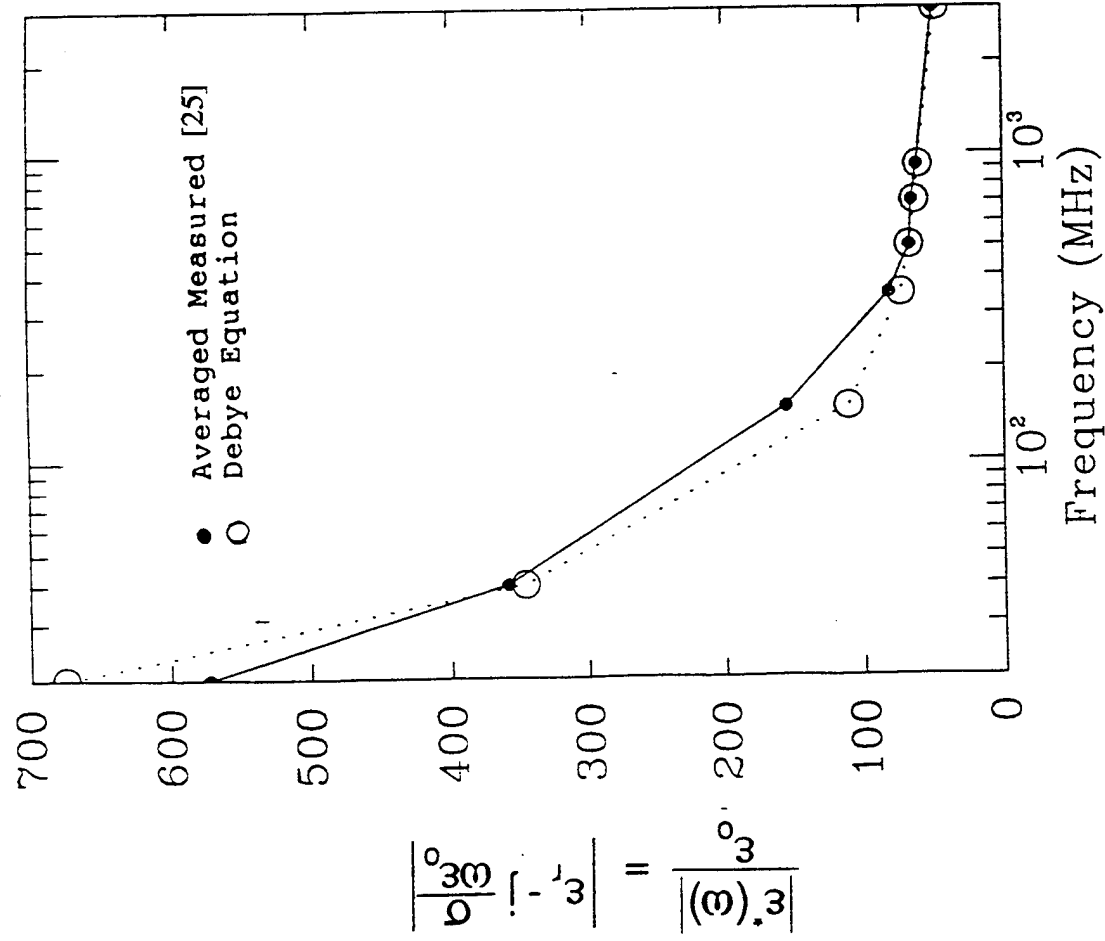
Fig. 2. Fit of Debye equations with two relaxations constants (5) to measured tissue properties of (a) muscle and (b) fat.

95
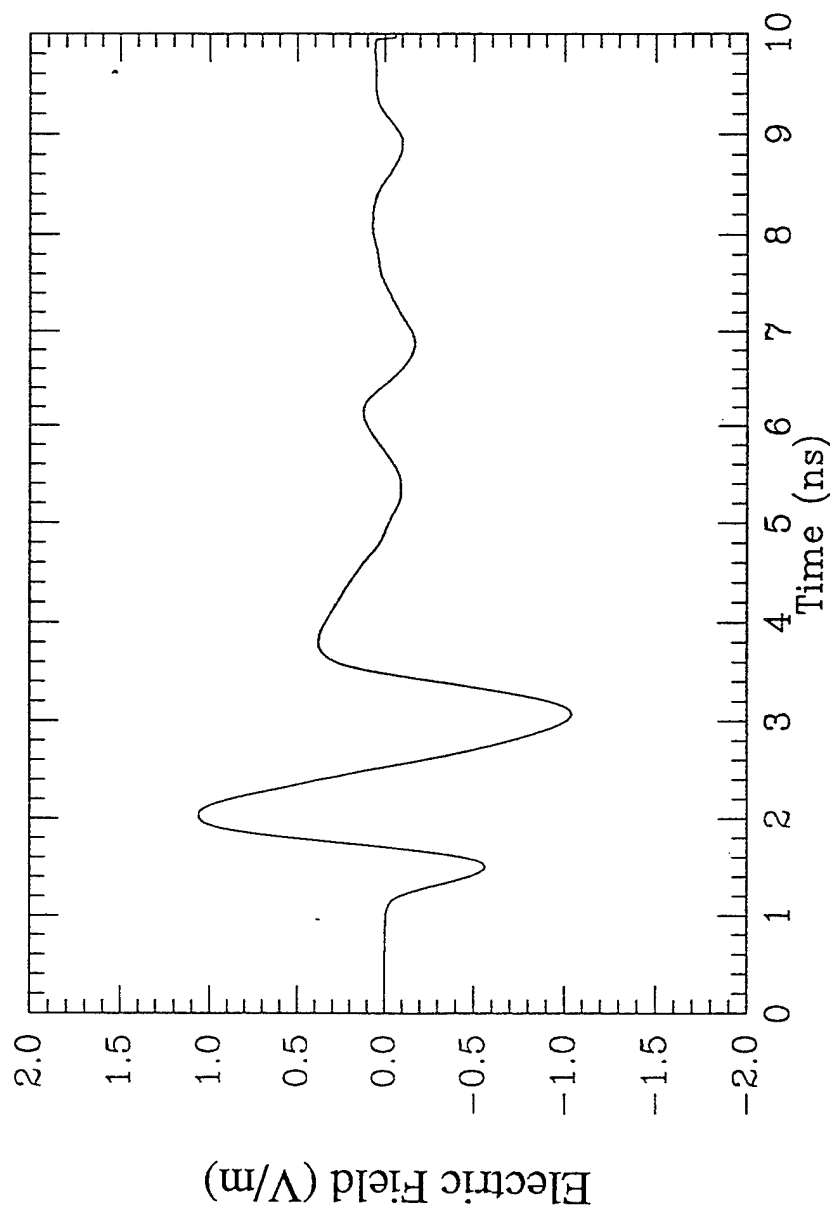
Fig. 3. The prescribed electromagnetic pulse. Peak incident field = 1.1 V/m.
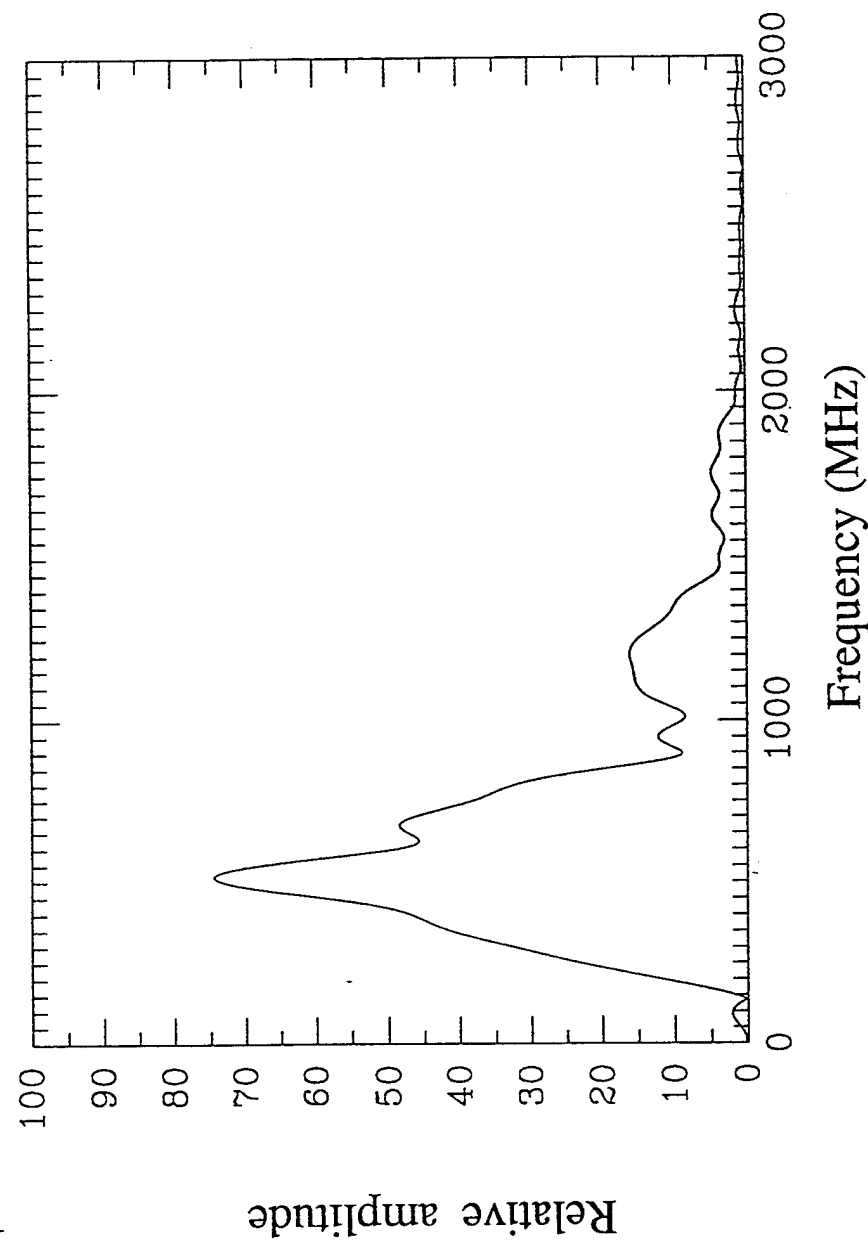
Fig. 4.   Fourier spectrum of the electromagnetic pulse of Fig. 3.

5a. Section through the eyes (height above the bottom of the feet = 168.3 cm).
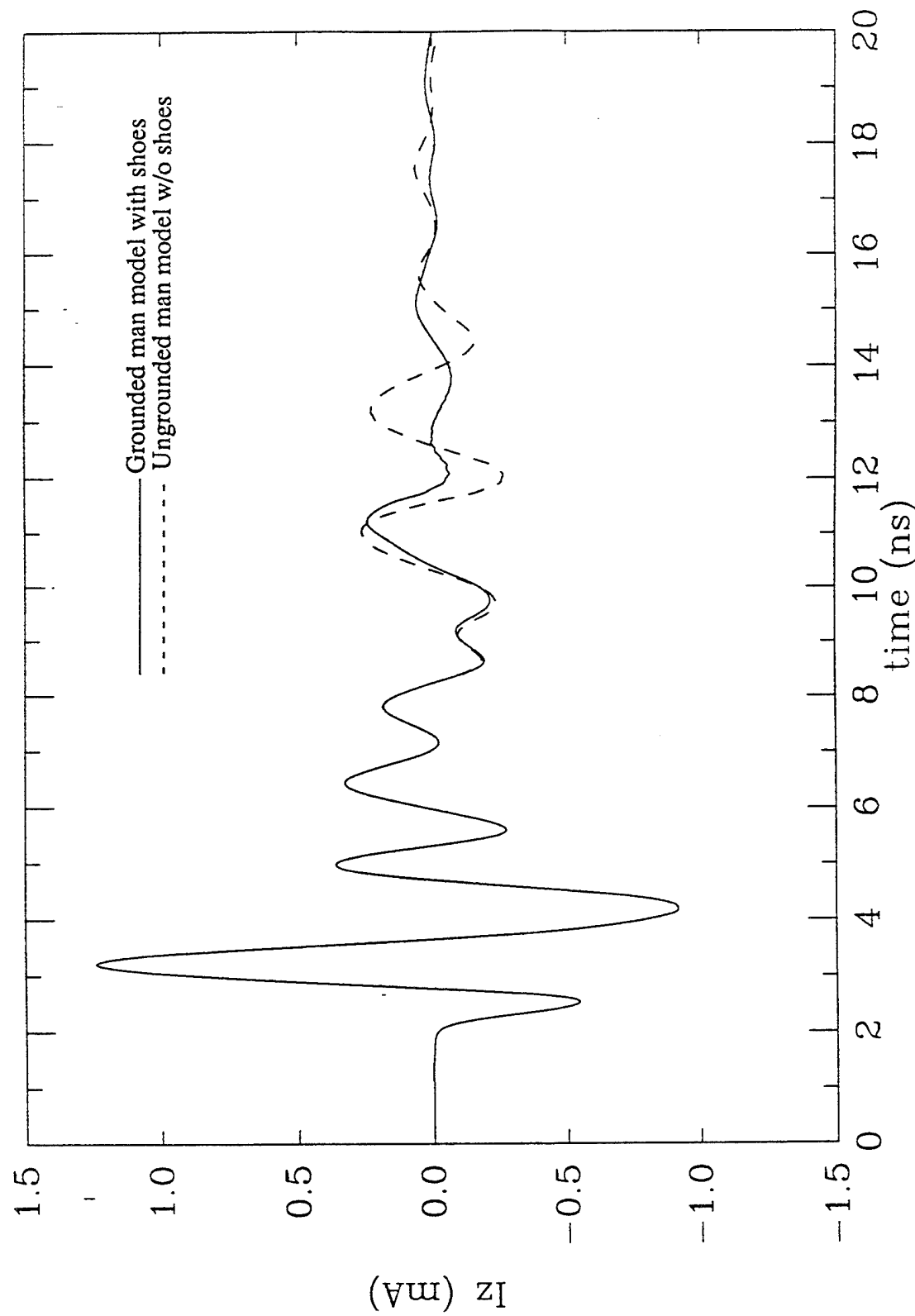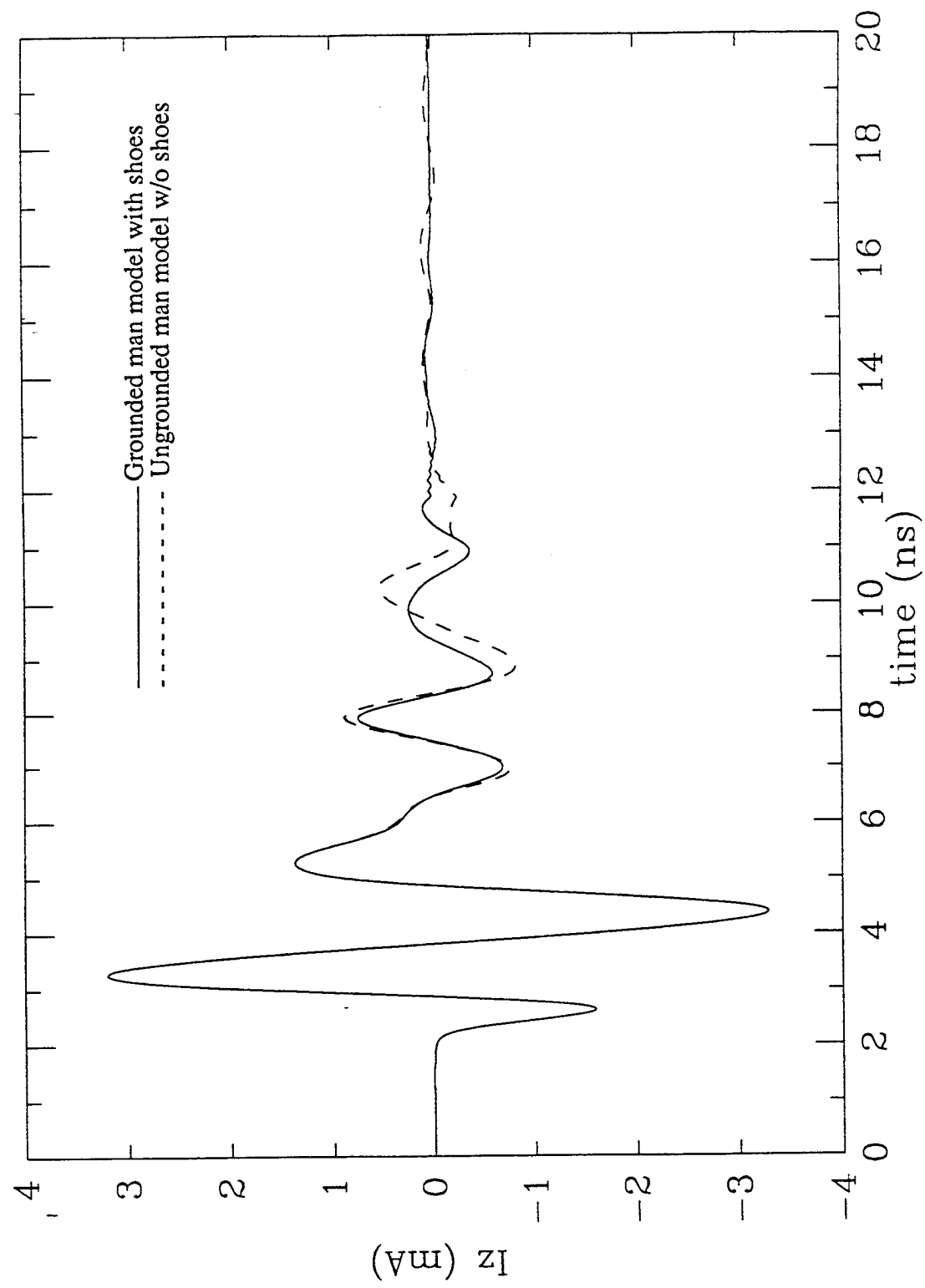
Fig. 5. Currents induced for the various sections of the body for shoe-wearing grounded and ungrounded conditions of exposure. $E_{peak} = 1.1$ V/m.

5b. Section through the bladder (height above the bottom of the feet = 91.0 cm)
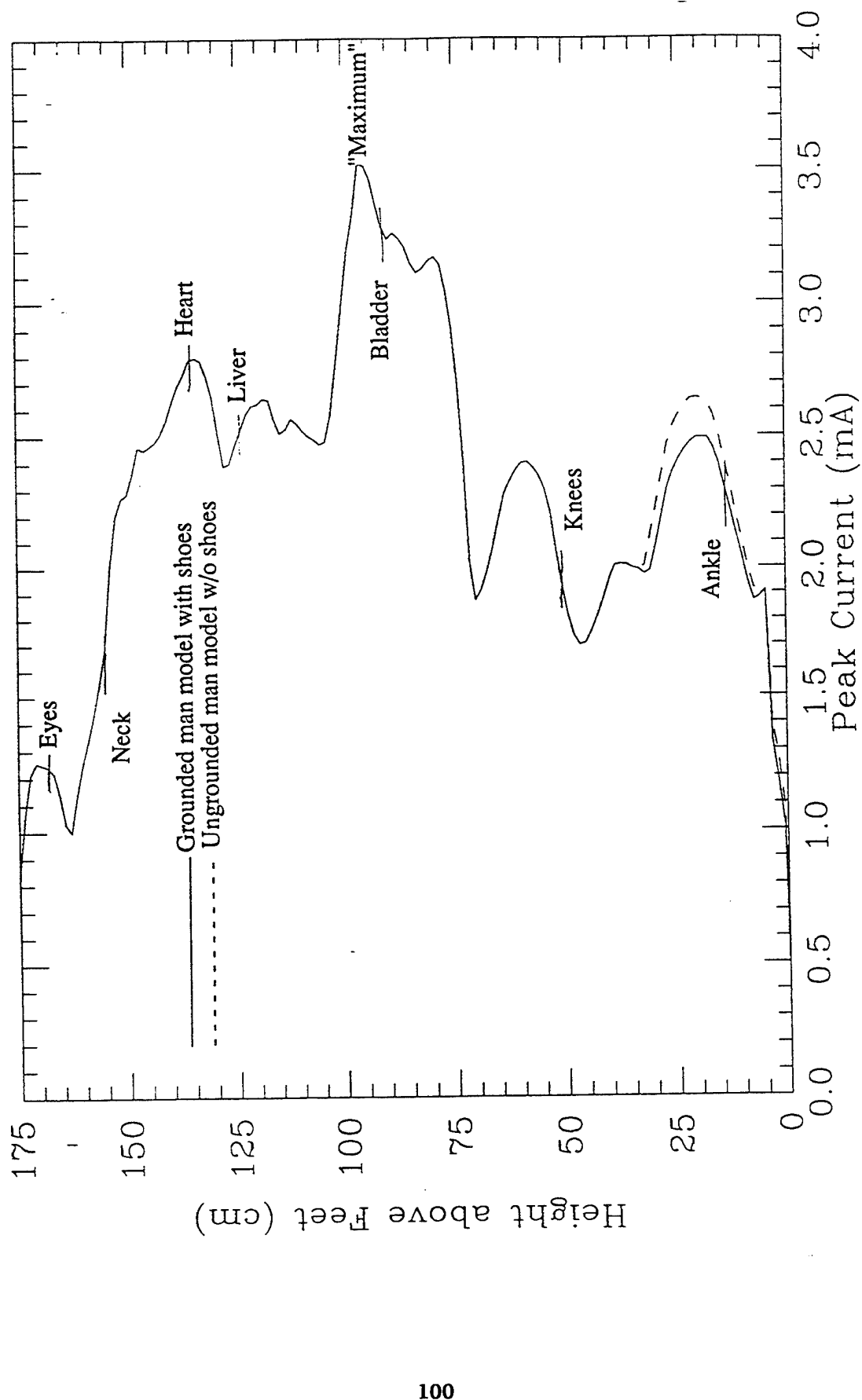
Fig. 6.   Peak currents induced for the various sections of the body for shoe-wearing grounded and ungrounded conditions of the model. $E_{peak} = 1.1$ V/m.
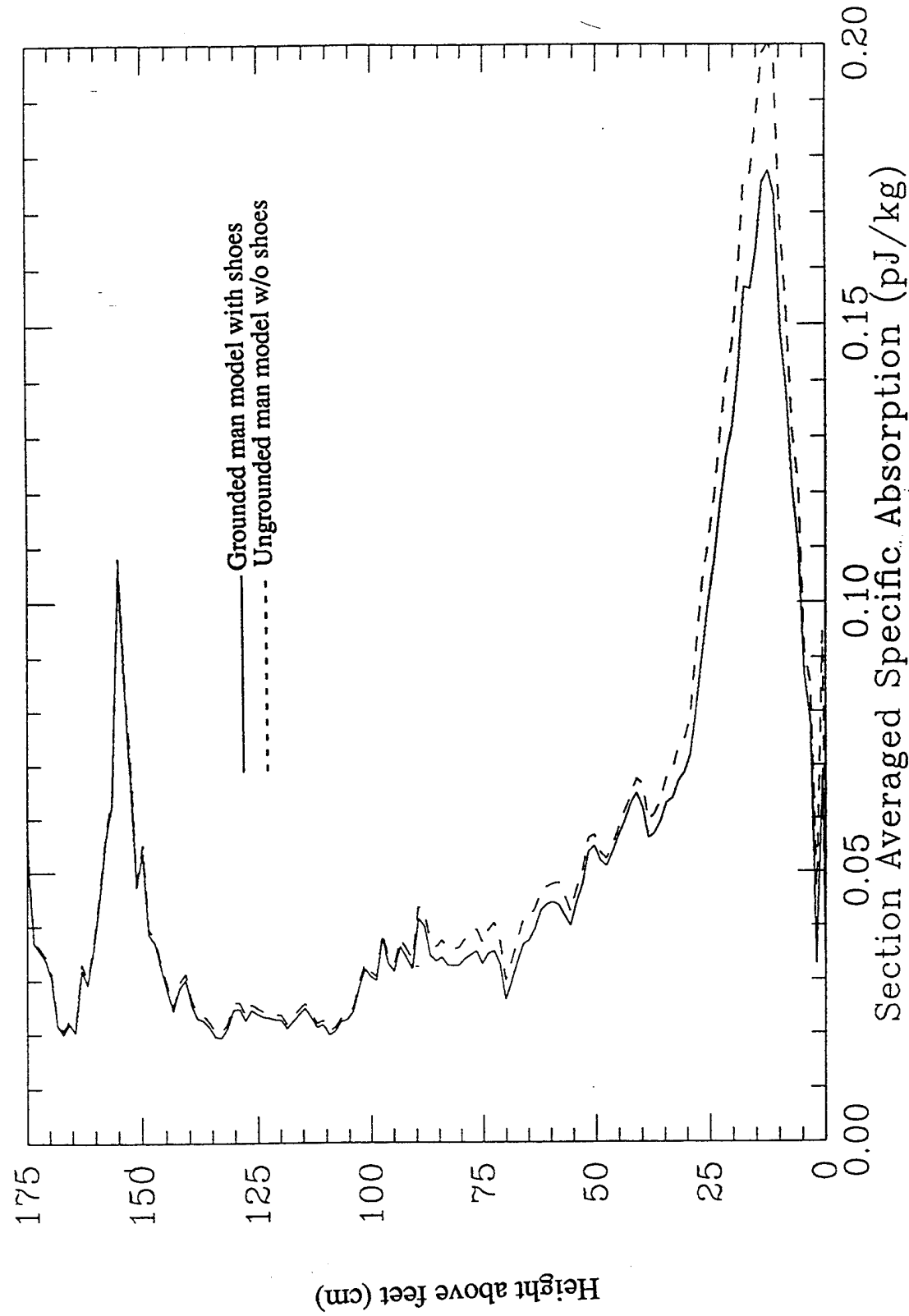
Fig. 7. Variation of section or layer-averaged specific absorption for the ultrawideband pulse of Fig. 3. $E_{peak} = 1.1$ V/m.

101
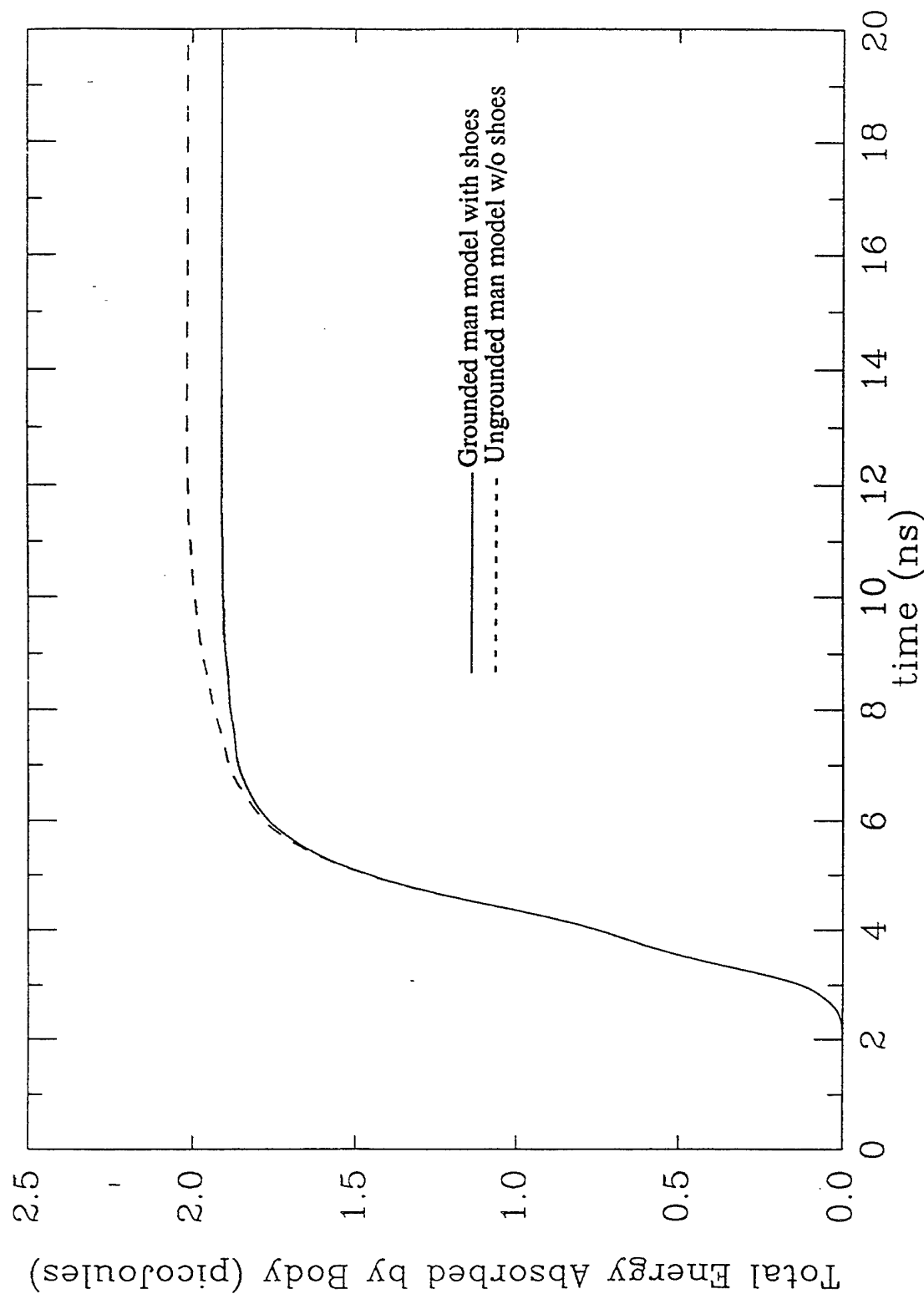
Fig. 8. Total energy absorbed by the body as a function of time.
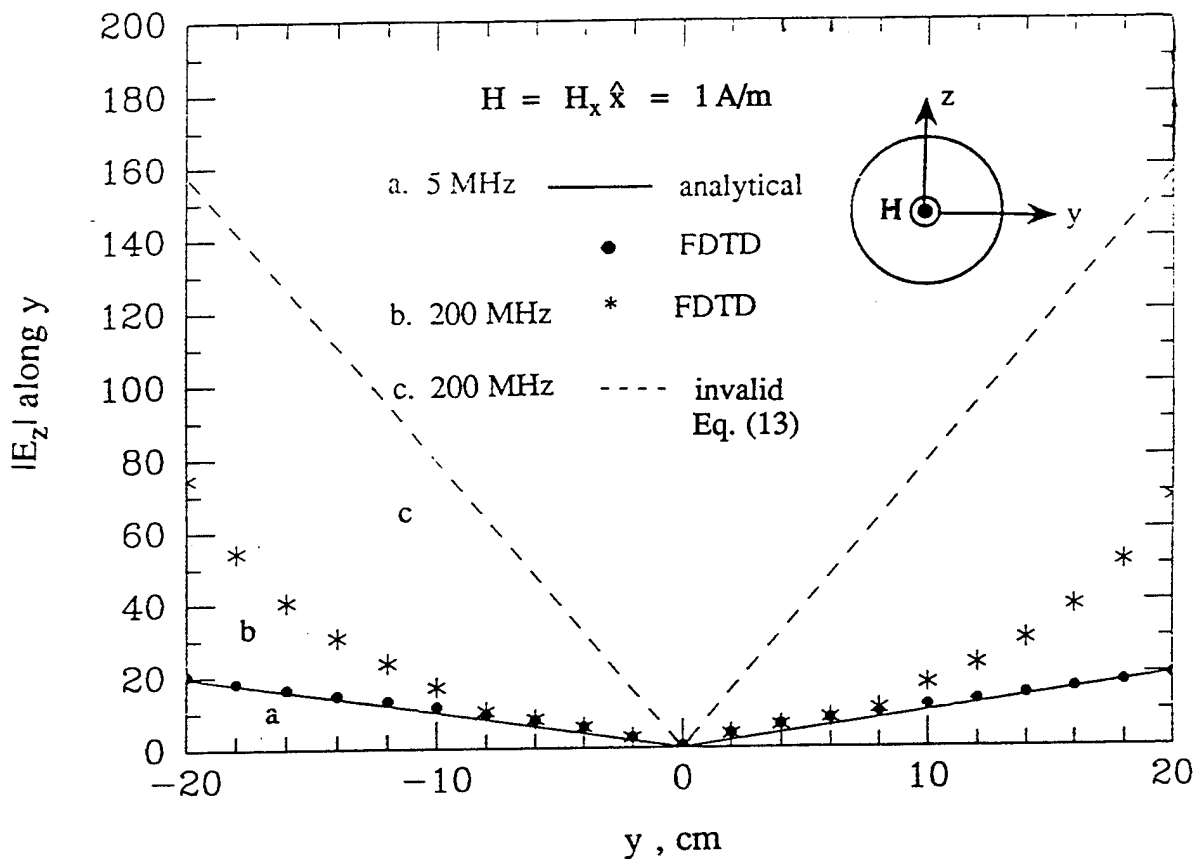
Fig. 9. FDTD-calculated and analytical variations of the magnitude of the induced E field for the central y axis of a homogeneous lossy sphere used as a test case. For a lossy sphere, radius = 20 cm; ε_r = 340, σ = 0.5 S/m at 5 MHz; ε_r = 37.0, σ = 0.85 S/m at 200 MHz. Note the considerably lower induced E fields (and, hence, SARs) than those projected by quasi-static analytical Eq. 13 for higher-frequency RF magnetic fields.
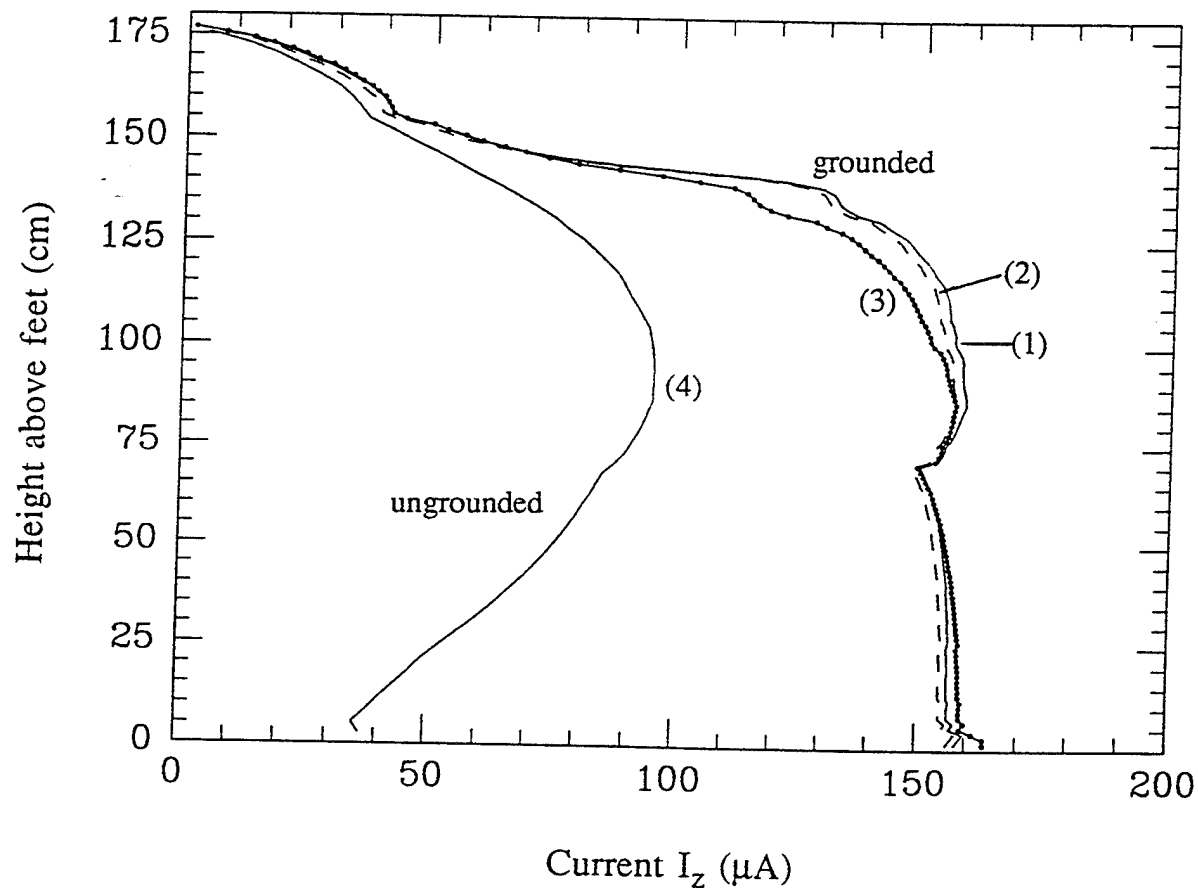
Fig. 10. Calculated layer currents for anatomically based grounded and ungrounded models exposed to EMFs at 60 Hz. For curves (1) and (2) σ = 0.52 S/m for skeletal muscle and σ = 0.11 S/m for the interior muscle. For curves (3) and (4) σ = 0.11 S/m for all of the muscle. E = 10 kV/m (vertical), H = 26.5 A/m from side to side for all of the curves except for (2) for which only E-field exposure is assumed.

```
                                69  65  21
                        50  68  63  92  76  65  61  53  20
                30  73  68  72  82  88 156 201 244 145 151  31  25
        59  97  63 117 114 117 106 109 108  81 254 285  75  31
        117  96 178 126 114 125  97  98 119 120  84  37  87  82  17
    102 100 181 147 121 109 105  98 101  94  93 114 147  55  58  10
    95 125 183 134 118 112 104 113 112  64  51  41  37  34  17  34
    91  72 188 132 127 128 104 104 102  55  45  39  48  45  46  57  44    F
    102 130 184 134 117 109 104 113 113  65  52  40  37  35  16  46
    125 105 181 147 120 109 105  95 100  93  96 124 162  57  55   8
        123  94 177 124 114 126  96  96 116 122  86  34  92  79  17
        43  91  59 116 111 105 100 108 109  88 208 264  70  31
            29  61  60  72  82  90 133 146 216 149 147  33  29
                30  45  45  54  67  66  54  39  18
                        38  36  12
```

a. Section through the brain (height above ground = 167 cm).

```
                        15  48  50  34
                26 149 281 192 121  82  13
            27 226 365 380 325 354 351  99  12
    29  81 356 370 379  45 108 425 381 181
    27  85 359 371 381 217 211 424 428 243
    20  78 351 360 374 344 360 388 394 178
        24 194 247 248 162 227 230 175  24
            13  26  32  33  34  37  39

     17  32 148 161 175 178 173 162 152  31  30
21   47 273 429 452 403 462 288 307 433 201 274 179 102  17
31  148 442 396 266 177 110  51  53 109  46  53 300 411 190  48
26  301 336 372  49 191  56  64  97  61  58  45  53 143 221 149  54
24  290 112 107  60  57  58 105 107  99  96  93  59  53  78 238 151  16
23  295  97  49  55  55  59 114 104 100  93 108 108  55  91 179 268  61
23  308 223 121  49  53  54  63 110 104  90  93 108  99 128 118 271 120
23  320 202 243  50  56  51  48  48  77 121  94  96 103 113 108 169 224  10
23  333 104 198  40  48  61 174  48  61 220  97  96 103 104 265 190  37
23  326 368  40  42  50  55 198  64  74 151 103  89 120 159 199 122 177  34    F
23  310 407  41  47  42  75 192  83 109 176 106 133 316 346 238  57  90
22  286 245  71  71  39  73 365  83 139 319  72 299 360 356 190  63  98
23  319 383  55  62  41  45  46  78 107 398 252 394 332 301  73  78 105
23  325 430  42  46  43  49  58  67 126 493 378 405 248  54  80 148 146
23  328 278  41  42 145 135  79  65  65 200 184 251 237  78 135 296 219
23  315 216  46  48 184 150  73 138  49  94 297  91 168 128 269 194
23  278 190  41  46  51  56  66 120  56 133 191 173  91  95 154 359  96
24  270  80  42  51  55  55  57  50  47  48  40  77  92 179 211 367  46
25  270  93  46  50  51 117 141  87  44  57  59 102 108 125 298 207  11
28  281 268 185  51  51 111  62 177  42  97 109 116 138 166 128  43
42  109 332 478 192  52  54  53  50  90 124 126 238 362 169 100
34   77 381 444 416 385 375 157 169 380 340 160 353 164  40  12
        23 116 265 356 364 364 347 339 247 154 136  22  10
        14  14  22  32  33  34  34  35  34

             2  65 100 100  76  91  95  54   8
        55 315 352 360 251 344 336 312  78
    17  78 348 361 372 339 293 411 417 233
    27  81 339 357 372  94 120 413 398 206
    48  66 297 342 367 140 220 374 216  66
        32  88 259 314 284 246 172  28
            35  28 102  65  27  17
```

b. Section through the heart (height above ground = 133 cm).

```
            215 616 982 807
    208 2610 4074 3317 5285 1652
    589 2629 6797 1216 1696 2879 316
    605  646 1651 1274  633 1693 153
        648  843  884  900


                                F


            678  884  906  912
    624  683 1702 1311  656 1661 150
    595 2610 6787 1213 1698 2869 315
    215 2606 4079 3308 5288 1658
        215  614  977  811
```

c. Section through the ankles (height above ground = 15.1 cm).

Fig. 11. Calculated total current densities in nA/cm^2 for the various cells ($\delta = 1.31$ cm) of a grounded anatomically based human model. Figures a-c are for combined E and H fields, E = 10 kV/m (vertical), H = 26.5 A/m (from side to side of the body), while Figs. d-f are for magnetic field alone.

```
                        2   2   1
                    2   2   4   4   1
            1       1   1   2   3   4   9  13  17  12  14   3   1
        1   1   3   1   2   4   5   6   7   7   5  21  25   7   3
        2   1   5   4   4   4   5   5   6   8   9   7   3  10  11   1
1       1   3   4   4   4   5   5   7   6   7  10  14   6   8   1
1       2   4   3   4   4   5   5   6   7   4   3   3   4   2   7
1       2   1   5   3   4   4   5   5   6   3   3   3   5   5   7   9   5     F
2       2   5   3   4   4   4   5   5   6   7   4   3   3   4   2  -7
3       2   4   4   4   4   5   6   5   6   8   7  10  15   6   8   1
        3   2   2   6   4   4   5   5   6   8   9   7   3  10  10   1
        2   2   2   4   4   4   5   5   7   8   6  18  24   7   3
            1   1   2   3   3   4   8  11  16  12  14   1
                    1   1   2   4   3   4   4   3
                        2       1   1
```

d. Section through the brain (height above ground = 167 cm).

```
                    5   6   1       1
        1  11  13   8   2   1   7   3
        4  18  13   7       7  13       9
        5  18  13   7   1   1   7  15  12
        4  17  12   7   2   2   7  14   9
        1  10   9   5   1   1   4   6   1

        1   5   3   2   2   4   5   6   1   1
    3  14  16  10   4   6   6   9  16  10  16  12   8   1
 1 10  23  15   6   2   1   1   1   4   2   3  20  33  17   4
   20  17  13   1   2       1   2   2   2   2   3  11  20  15   6
   19   5   3   1           2   3   3   4   5   4   4   7  24  17   1
   18   4   1   1   1   1   2   2   3   4   6   7   4   8  18  30   7
   19  11   5   1   1   1   1   2   3   4   5   7   8  11  11  31  15
   20  10  10   1   1           1   2   5   5   6   8  10  11  19  28   1
   21   5   8   1   1   1   2   1   2   9   5   6   8  10  11  31  24   4
   21  19   1   1   1   1   3   1   2   6   5   6  10  16  23  14  23   4
   20  21   1   1   1   1   3   1   3   7   5   9  27  36  28   7  12
   19  13   3   2   1   1   5   2   4  12   3  20  30  37  23   7  13
   21  20   2   2   1               1   3  15  12  26  28  31   9   9  14
   21  22   2   1   1       1   1   3  19  19  26  21   6   8  18  20
   21  14   1   1   3   2   1   1   2   7   9  17  20   8  14  35  29
   20  11   1   2   4   2   1   3   1   4  15   6   8  16  13  32  26
   18   9   1   1   1   0   1   3   2   5  10  11   8   9  15  42  12
   18   3   1   1   1   1   1   1   1   2   5   7  16  21  42   5
   19   5   2   1   1   2   3   2   1   2   3   6   8  11  30  23   1
 1 19  14   8   1   1   2   1   5   1   4   6   7  10  14  13   4
 1  7  18  19   4       1   1   1   3   6   7  15  27  15  10
    5  20  17  10   5   5   3   4  13  15   9  22  12   3   1
    1   6  10   9   5   4   7  10   9   7   7   1

        4   4   2   1   1   2   2
    3  17  13   8   2   2   7  12   4
    5  19  13   8   3   1   7  15  12
    5  18  13   8           7  14  11
 1  3  16  13   8   1   1   6   8   3
    4  10   8   3   2   3   1
        1   2
```

e. Section through the heart (height above ground = 133 cm).

```
        3  11  18  15
 3  46  75  63 104  33
10  46 125  23  33  58   6
10  11  30  24  12  34   3
    11  15  16  17
```
                                F

```
       12  16  17  18
10  12  31  25  13  34   3
10  46 126  23  33  59   6
 3  46  75  63 105  34
    3  11  18  16
```

f. Section through the ankles (height above ground = 15.1 cm).

Fig. 11 (continued)

a. Section through the liver (height above the bottom of the feet = 123.8 cm)
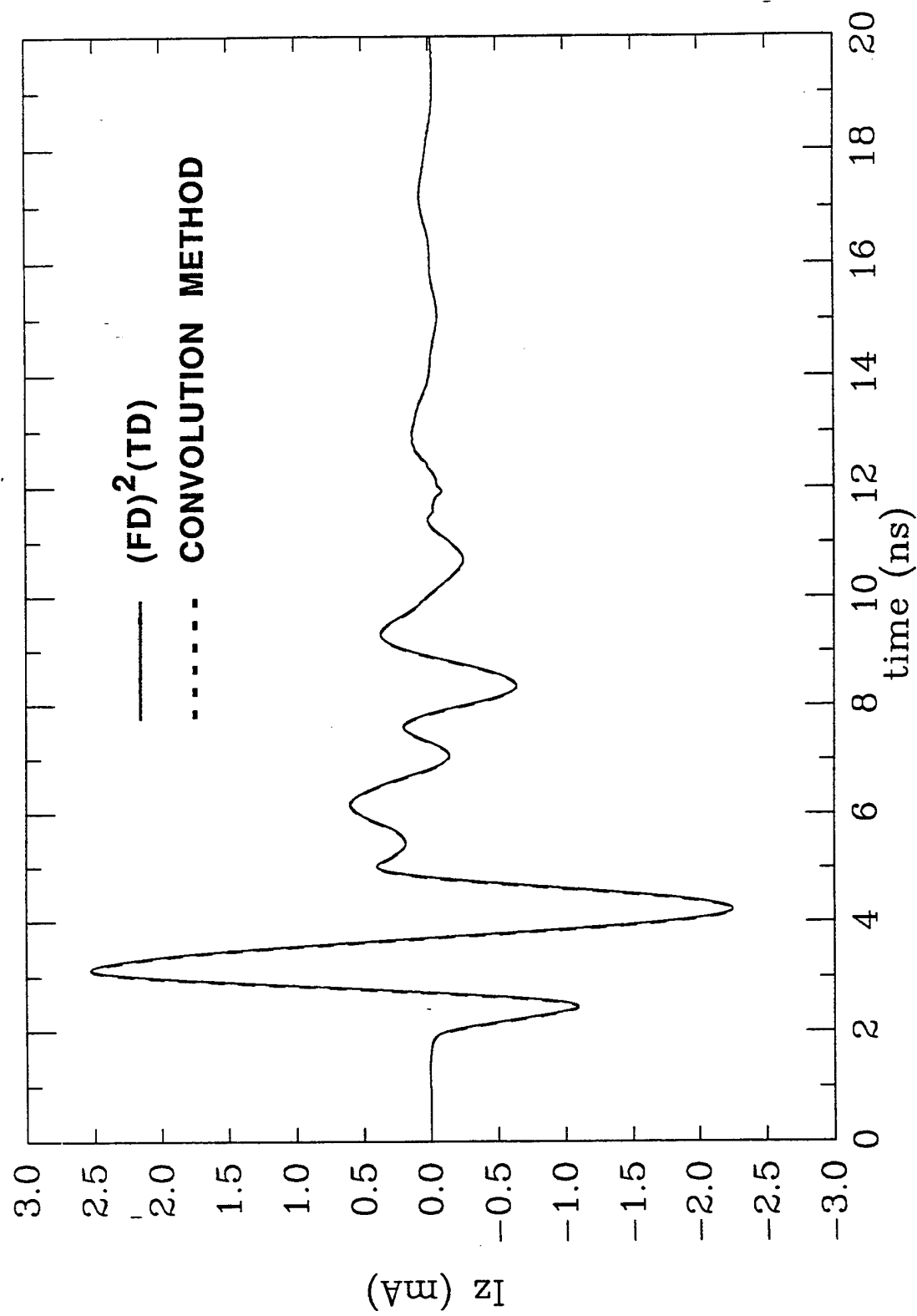
Fig. 12. Comparison of the induced currents calculated using the convolution method with the conventional $(FD)^2TD$ method for two representative sections of the body. Shoe-wearing grounded model of the body was used for the calculations.

b. Section through the knees (height above the bottom of the feet = 50.4 cm)
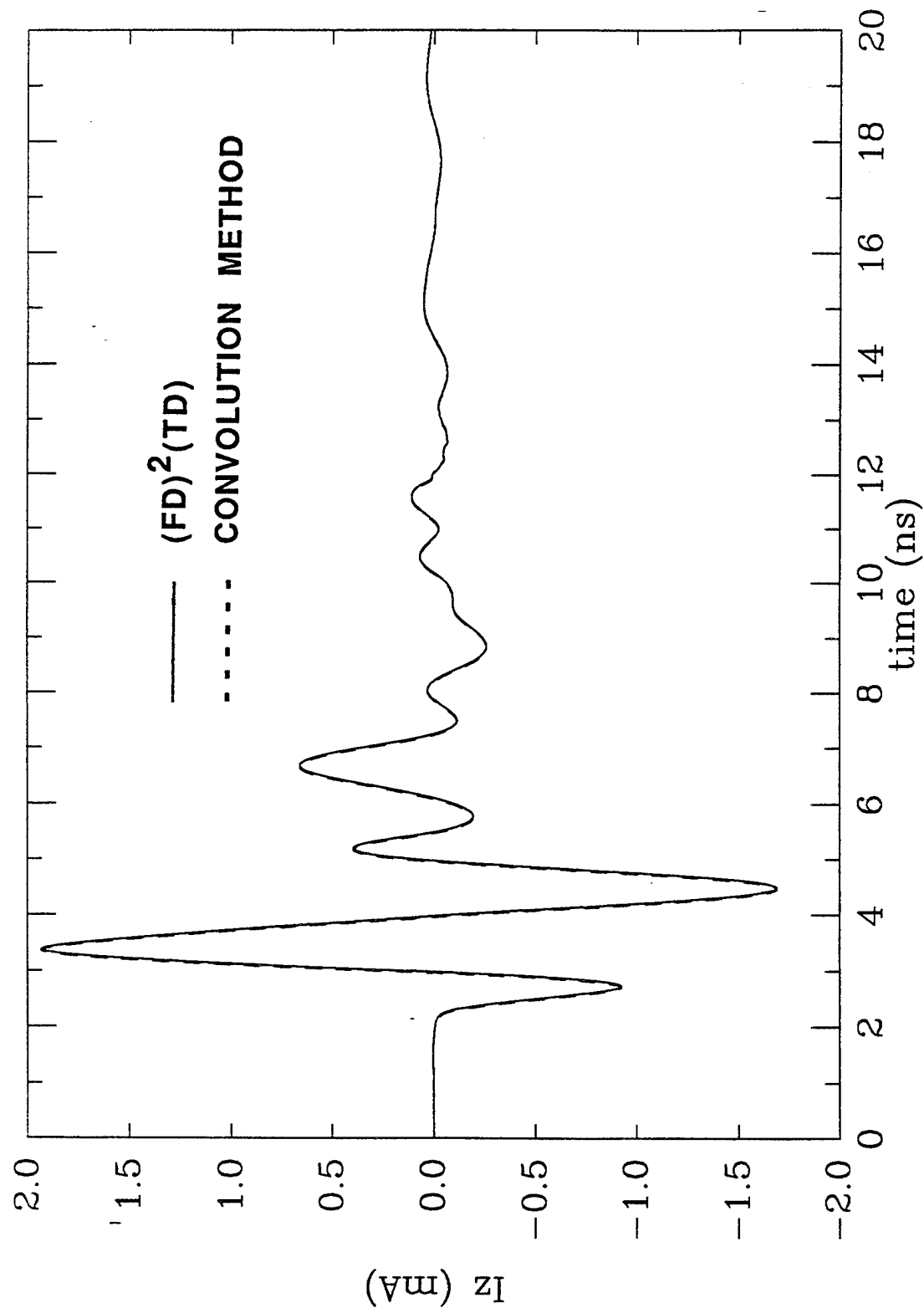
Fig. 12 (continued)

MATHEMATICAL CHARACTERIZATION OF ALGORITHMS FOR ELECTROMAGNETIC WAVE COMPUTATIONS

R. Albanese
J. Blaschak
P. Petropoulos

Special Projects Division
USAF Armstrong Laboratory

CHART 1: Title

Modern industrial and military activities, and modern lifestyles have resulted in the production of non-ionizing radiation fields with intensities that are far in excess of naturally occurring levels within specific frequency bands. Thus, it is essential that biomedical and allied scientists strive to understand the degree to which these fields penetrate the human body and then try to understand, in a very detailed manner, what the absorbed dose does within the body.

We believe that a detailed characterization of field penetration is important for the proper design and meaningful interpretation of experiments employing living subjects, and for the interpretation of epidemiological studies. Also, a knowledge of field penetration is essential when the occupational or environmental health specialist is faced with a new emitter or radiation condition and wishes to apply national guidelines to a consideration of human safety. The particular emphasis of our research group is on the issue of the penetration of ultra-short pulses of electromagnetic radiation and the formation of transients within the tissues of the body.

We believe it is not enough to simply calculate a result and present numerical answers as a function of position within the modeled human or animal body. We are convinced that it is imperative to provide a numerical estimate of the accuracy of the calculation given assigned values for the tissue dielectric constants and conductivities and the assigned body structural parameters. This emphasis on error analysis derives from a desire to see more precision in the interpretation of laboratory data, and epidemiological data and in the application of safety guidelines. In short, an important emphasis of our current research program is to provide quantitative error analyses for existing and, along with error analyses, to evolve algorithms which can be used to provide accurate results, more accessible to the non-specialist in numerical methods, and at decreased computational expense.

CHART 1

MATHEMATICAL CHARACTERIZATION OF ALGORITHMS FOR ELECTROMAGNETIC WAVE COMPUTATIONS

R. ALBANESE

J. BLASCHAK

P. PETROPOULOS

SPECIAL PROJECTS DIVISION

USAF ARMSTRONG LABORATORY

8 DECEMBER 1992

CHART 2: Outline

The topics to be covered during this briefing are shown, here. First, Dr Peter Petropoulos will present results of his analysis of errors present in numerical methods based on the popular finite-difference time-domain (FD-TD) approach for electromagnetic wave propagation computations. Dr Petropoulos will present the relationship between spatial sampling and total time of computation needed to control the effects of phase errors introduced by the difference scheme. Also, he will present the first analysis of the numerical properties of proposed FD-TD based schemes for the modelling of dispersive media. His analyses indicate the extent to which current FD-TD schemes for dispersive media misrepresent the true dispersion relation of the material and provide criteria to reduce the effects of cumulative phase errors and spurious dissipation introduced by the difference scheme. Examples will be presented to illustrate the utility of this analysis for the case of Debye media, a material model of fundamental importance for health and safety assessment of ultra-short pulsed electromagnetic field exposures.

The second part of the briefing will be given by Dr Jeffrey Blaschak, who will consider the effects of numerical errors introduced into direct scattering computations by the approximate radiation boundary conditions used in FD-TD codes. These errors are introduced because the operator applied on the boundary of the computational domain, in the standard implementation of the FD-TD algorithm, is an approximation to the exact operator satisfied by outward propagating scattered waves. Dr Blaschak will first review the derivation of these approximate radiation boundary conditions, which yield efficient, but inexact operators for use in FD-TD based codes. Next, he will present results of numerical experiments designed to measure reflection errors caused by approximate radiation boundary conditions and the resulting sensitivity of such computations to the position of the scatterer relative to the boundary of the domain. The nonphysical reflection of the scattered field, generated as it passes through a computational boundary employing an approximate radiation condition, will corrupt the accuracy of the computed interaction of illuminator fields with a biological model. Significant goals of this research effort are directed toward understanding the effects of this type of numerical error and eliminating its influence in time-domain computations.

Let us begin with Dr Petropoulos who will present some key results of his research.

112

CHART 2

OUTLINE

- INTRODUCTION

- ERROR ANALYSIS FOR FD-TD BASED NUMERICAL MODELS

- INFLUENCE OF RADIATION BOUNDARY CONDITIONS ON FD-TD BASED NUMERICAL MODELS

- SUMMARY

CHART 3: Sources of Error in FD-TD Based Numerical Models

Various sources of error enter in the building of models for physical phenomena. Here we are concerned with the description of electromagnetic pulse interaction with biological material, and the relevant model involves Maxwell's equations in the time domain coupled to ordinary differential equations that describe the evolution of the polarization excited by the incident signal. The desire to solve these models numerically introduces further errors. When the numerical approach of choice is the FD-TD method we can classify these additional sources of error as follows

a) Physical errors such as those incurred by the stair-step representation of smooth dielectric interfaces and by the approximation of the true Radiation Condition with approximate absorbing boundary operators, and

b) Numerical errors, i.e., those due to the phase error of the interior finite difference scheme, and those due to the discretization of the absorbing boundary operator.

In this section of the talk, I will be concerned only with the phase error due to the finite difference scheme used to discretize the time domain Maxwell's equations in non-dispersive dielectrics, and I will identify and quantify an additional source of error that contaminates computations done with extensions of the FD-TD approach for the modelling of scattering in dispersive media of Debye type.

CHART 3

SOURCES OF ERROR IN FD-TD BASED NUMERICAL MODELS

- **PHYSICAL ERRORS**

  - **STAIR-STEP REPRESENTATION OF SMOOTH DIELECTRIC INTERFACES ($\rightarrow 0$ as $\Delta \rightarrow 0$, Δ = Spatial Step)**

  - **APPROXIMATE RADIATION BOUNDARY CONDITIONS**

- **NUMERICAL ERRORS**

  - **INTERIOR SCHEME PHASE ERRORS**

  - **RADIATION BOUNDARY CONDITION DISCRETIZATION**

<u>CHART 4</u>: Relation of Phase Error to Time and Space Discretization

Working with the semi-discrete Maxwell's equations, which result from the discrete difference equations of the FD-TD method after letting the time step vanish, I derived a relationship for N_{ppw}, the number of sample points per wavelength, that gives the spatial sampling requirement for the highest frequency, k_*, that the simulation will attempt to resolve accurately.

In the expression for N_{ppw}, T_c is the total time of computation, T_* is the period associated with the highest frequency, θ is the propagation angle with respect to the grid, and e_ϕ is the designed phase error that will be accepted for the k_* component.

Then, the spatial step is defined as Δ and the time step follows from the Courant restriction for Δt, where CFL is the Courant number, v, and c is the speed of light in free-space. This simple formula implies that finer discretizations should be used as the computation time increases. Therefore, long computations should be done with a finer spatial step if one wants them to sustain the same phase error as a reference computation that takes less time.

CHART 4

RELATION OF PHASE ERROR TO TIME AND SPACE DISCRETIZATION

- SAMPLING REQUIREMENT FOR LARGEST WAVE NUMBER, K_*:

$$N_{ppw} \sim \sqrt{\frac{1}{3}\pi^3 \left(\sin^4\theta + \cos^4\theta\right) \frac{T_c}{T_* e_\phi}}$$

  WHERE,

  T_c IS THE TOTAL TIME OF COMPUTATION

  T_* IS THE PERIOD OF K_* COMPONENT

  θ IS THE PROPAGATION ANGLE W.R.T. THE GRID

  e_ϕ IS THE <u>DESIGNED</u> PHASE ERROR FOR K_* COMPONENT

- SPATIAL STEP FOR FD - TD ALGORITHM

$$\Delta = \frac{2\pi}{K_*} \times \frac{1}{N_{ppw}}$$

- TIME STEP FOR FD - TD ALGORITHM

$$\Delta t = CFL \times \frac{\Delta}{C}$$

CHART 5: Verification of Phase Error Formula

The formula for N_{ppw} was verified by numerically simulating a mode, propagating in a two-dimensional parallel plate waveguide of infinite length, accumulating phase error. The infinity of the waveguide was modelled by imposing periodic boundary conditions along the direction of propagation. On the waveguide walls, Dirichlet boundary conditions were imposed on the electric field component. The standard FD-TD scheme was initialized by computing the starting electric and magnetic fields from the exact solution.

The initial data was propagated for **P** periods and an estimate of the phase error was obtained. The discretization was determined from the expression for N_{ppw} using $\theta = 0$ so that 0.1 radians of phase error would be allowed to accumulate over a computation lasting for 10 periods. The results will be shown on the on Chart 6. Note that the observed phase error should be slightly better than the predicted one. This is because the waveguide mode actually propagates at a nonzero angle with respect to the grid, therefore, the value of N_{ppw} used for the computation was generous in that regard.

CHART 5

VERIFICATION OF PHASE ERROR FORMULA

WAVEGUIDE PROPAGATION EXPERIMENT

PERIODIC BC

PEC

y = 1

PEC

x = 1

PERIODIC BC

y = 0

x = 0
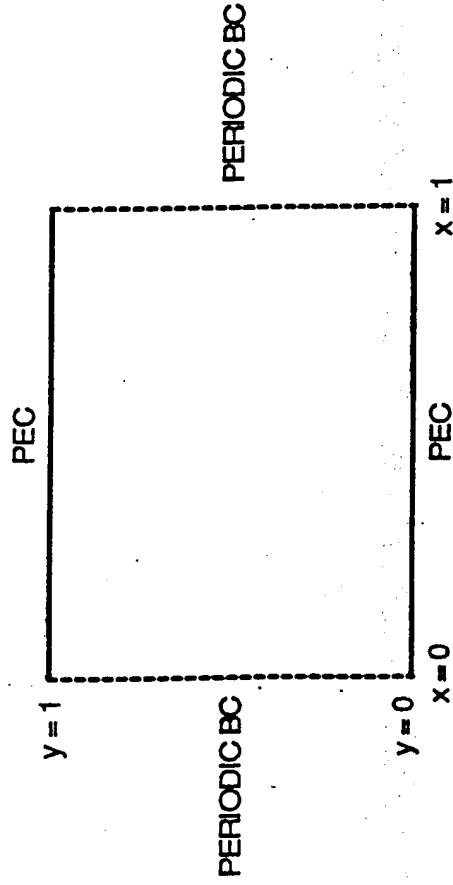
- INITIAL DATA FOR E_z, H_x AND H_y FROM EXACT SOLUTION

- PROPAGATE INITIAL DATA FOR $P = \dfrac{T_c}{T_*}$ PERIODS AND DETERMINE THE ACCUMULATED PHASE LAG

- COMPARE WITH DESIGN GOAL OF $e_\phi = 0.1 \dfrac{\text{RADIANS}}{\text{10 PERIODS}}$

CHART 6: Waveguide Propagation Experiment Results

For a designed phase error of 0.1 radians allowed to accumulate over a computation time length of 10 periods, the formula for N_{ppw} indicates that 32 points per wavelength should be used. From the Courant restriction we obtained the time step and it turned out that 1280 time steps were required to cover 10 periods. The results are as expected. The reason for the slight overestimation of the actual error is explained by the fact that the waveguide mode propagates at a nonzero angle with respect to the grid thus 32 points per wavelength is a generous estimate and less error is actually observed.

CHART 6

WAVEGUIDE PROPAGATION EXPERIMENT RESULTS

- **DESIGNED PHASE ERROR:** $e_\phi = 0.1 \dfrac{RADIANS}{10\ PERIODS}$

- **SPATIAL SAMPLING:** $N_{PPW} = 32$

- **TIME STEPS/PERIOD:** 1280
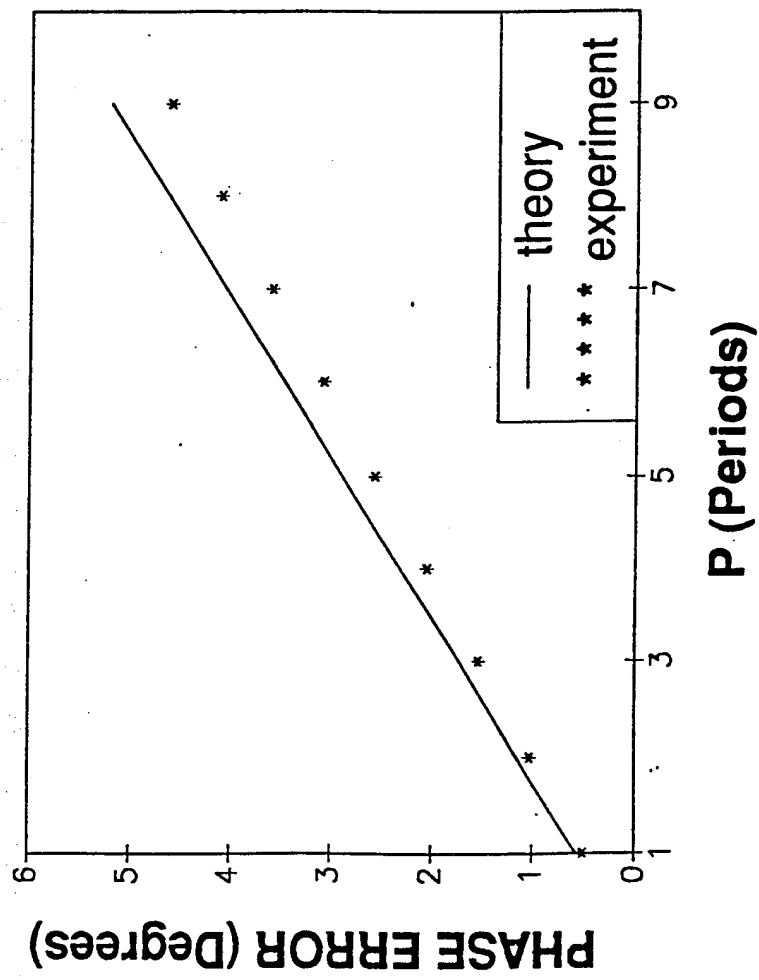
CHART 7: FD-TD Algorithm for Dispersive Media

I have analyzed four FD-TD based approaches for the modeling of pulse propagation in temporally dispersive media that are described by Lorentz or Debye type ordinary differential equations. I have completely characterized the schemes through studying the stability and phase error properties of the coupled difference equations corresponding to Maxwell's equations and to the equations for the dispersion. Guidelines have been developed for the *a priori* selection of correct discretization parameters so that there is a known small amount of artifacts due to the scheme present in the final results of the simulation.

For Debye media I have found that the discretization of the local-in-time differential constitutive relation method is totally equivalent to the method that uses the polarization differential equation. In the Lorentz medium case I have determined that the method that uses the polarization differential equation to model dispersion is to be preferred over the local-in-time constitutive relation method since the latter is weakly unstable for modes with wavenumber k such that $k\Delta x > \pi/2$. Here, only results relevant to the Debye medium are presented.

The continuous model dispersion relation corresponding to Maxwell's equations and a Debye dielectric is given by $k_c(\omega)$. The numerical model dispersion relation is found to be $k_N(\omega)$. By comparing the continuous and numerical dispersion relations, two features emerge that are solely due to the discretization of the ODE involved. First, the relaxation time, τ, of the medium is now as shown for the numerical model, i.e., the medium actually modeled by the numerics is one with *higher* relaxation time constant. This is also a source of artificial dissipation that will be explained later.

Further, for a fixed Δt, the cosine function is zero for a certain frequency component, ω, and infer that this frequency component will be adversely affected by the scheme since it will experience a medium of nonphysical constant conductivity. Such artificial dissipation can be controlled by choosing Δt so that the cosine term is close to 1 across the range of frequencies present in the short-pulse that propagates in the medium. Also, the actual frequency modeled by the numerical scheme is as shown. The phase error present in the numerical model is given by Φ.

CHART 7

FD-TD ALGORITHM FOR DISPERSIVE MEDIA

- ## DISPERSION RELATIONS: DEBYE MEDIA

  - ### CONTINUOUS MODEL

  $$k_c(\omega) = \frac{\omega}{c} \sqrt{\frac{\epsilon_s/\tau - i\omega}{1/\tau - i\omega}}$$

  - ### NUMERICAL MODEL

  $$k_N(\omega\Delta t) = \frac{2}{\Delta} \sin^{-1} \left[\frac{\Delta \tilde{\omega}}{2 c} \sqrt{\frac{\epsilon_s/\tau - i\tilde{\omega}}{1/\tau - i\tilde{\omega}}} \right]$$

  WHERE,

  $$\tilde{\omega} = \omega \operatorname{sinc} \left(\frac{\omega\Delta t}{2} \right)$$

  $$\tau = \frac{\tau}{\cos\left(\frac{\omega\Delta t}{2} \right)}$$

- ## DEFINITION OF PHASE VELOCITY ERROR

  $$\Phi (\omega\Delta t) = \frac{\left| k_N(\omega\Delta t) - k_c(\omega) \right|}{\left| k_N(\omega\Delta t) \right|}$$

CHART 8: Behavior of Phase and Dissipation Errors

The figure on the left shows the phase velocity error, Φ, as a function of the time step at a fixed Courant number, $\nu = 1$. At that Courant number the standard FD-TD in a non-dispersive dielectric is free of dispersion. Thus the effect of the discretization of the ODE is exemplified. On this transparency we also show that an additional error is introduced by the discretization of the ODE for dispersion.

The figure on the right was obtained with methods not described herein. This new error is named spurious dissipation since it represents the absolute value of the maximum eigenvalue of the finite difference equations at each time step, and this absolute value is now seen to be less than one and a function of frequency. To calculate the energy loss suffered by a particular mode **k** after NMAX number of time steps, we read from the figure on the right (drawn for a specific **h** and spatial step Δx) the value, **max** ξ, associated with that mode. Then we simply raise that number to the power NMAX to obtain the loss that particular mode suffered through the computation.

CHART 8

BEHAVIOR OF PHASE AND DISSIPATION ERRORS

- τ: DEBYE RELAXATION TIME, $\quad h = \dfrac{\Delta t}{\tau}$

- COMPUTATION AT COURANT NUMBER: $\quad \nu = \dfrac{c\Delta t}{\Delta x}$

SPURIOUS DISSIPATION

PHASE VELOCITY ERROR
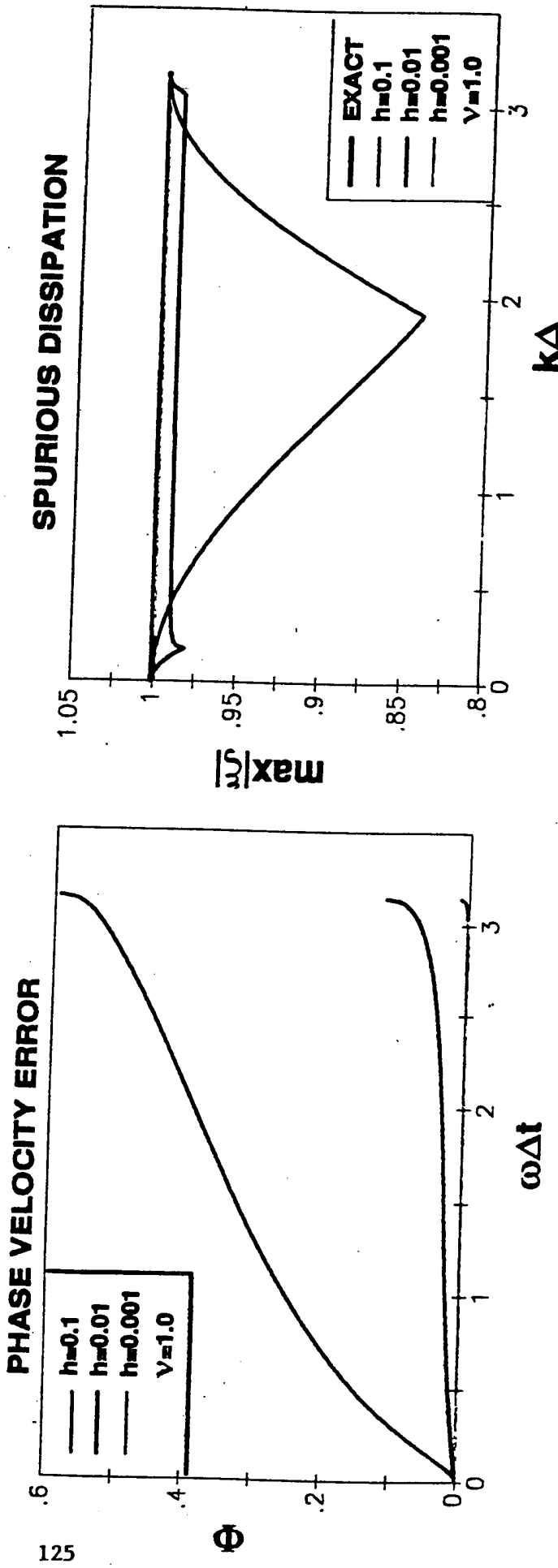
CHART 9: Outline

Dr Blaschak will now present results of his research in the area of absorbing boundary conditions for FD-TD based algorithms.

CHART 9

OUTLINE

- INTRODUCTION

- ERROR ANALYSIS FOR FD-TD BASED NUMERICAL MODELS

→ - INFLUENCE OF RADIATION BOUNDARY CONDITIONS ON FD-TD BASED NUMERICAL MODELS

- SUMMARY

CHART 10: Computational Domain and Boundary

I will begin with a quick review of the need for a radiation boundary condition. Radiation boundary conditions are also known as "absorbing boundary conditions" in the literature. I will use these terms interchangeably throughout this talk.

For finite difference or finite element based methods, designed to compute the time domain interaction of electromagnetic waves with biological models, an algorithm is derived from the partial differential equation form of Maxwell's equations, which yields a well define method to compute the propagation of fields within a computational domain, Ω. This interior wave propagation algorithm generates and propagates an incident wave, U_i, models the interaction of this wave with the scatterer and then propagates the scattered wave, U_s, outward to the boundary of the computation space. On the computational boundary, $\partial\Omega$, a boundary condition is applied, which is intended to simulate the propagation of U_s away from the scatterer to infinity. Mathematically, the scattering problem is defined on an infinite spatial domain. For computations, the algorithm must be implemented on a finite sized domain. An absorbing boundary condition is used to limit the size of Ω so that meaningful scattering computations can be performed within the bounds of available computer resources.

What is sought after and achieved with some success is a "local" absorbing boundary condition. The numerical implementation of local absorbing boundary condition operators yields efficient schemes to compute the solution on $\partial\Omega$ at each time step. By employing local operators, the computation at any boundary point depends upon data within a small "coupling region" near the boundary point. The complexity of the boundary computation is then of the same order as that for the algorithm used on the interior of Ω.

Local absorbing boundary condition operators, which are derived from approximation of the exact absorbing operator, introduce error in the form of nonphysical waves reflected from the computational boundary. The influence of these reflected waves on the overall accuracy of a finite difference based computation is a serious, practical concern.

CHART 10

COMPUTATIONAL DOMAIN AND BOUNDARY
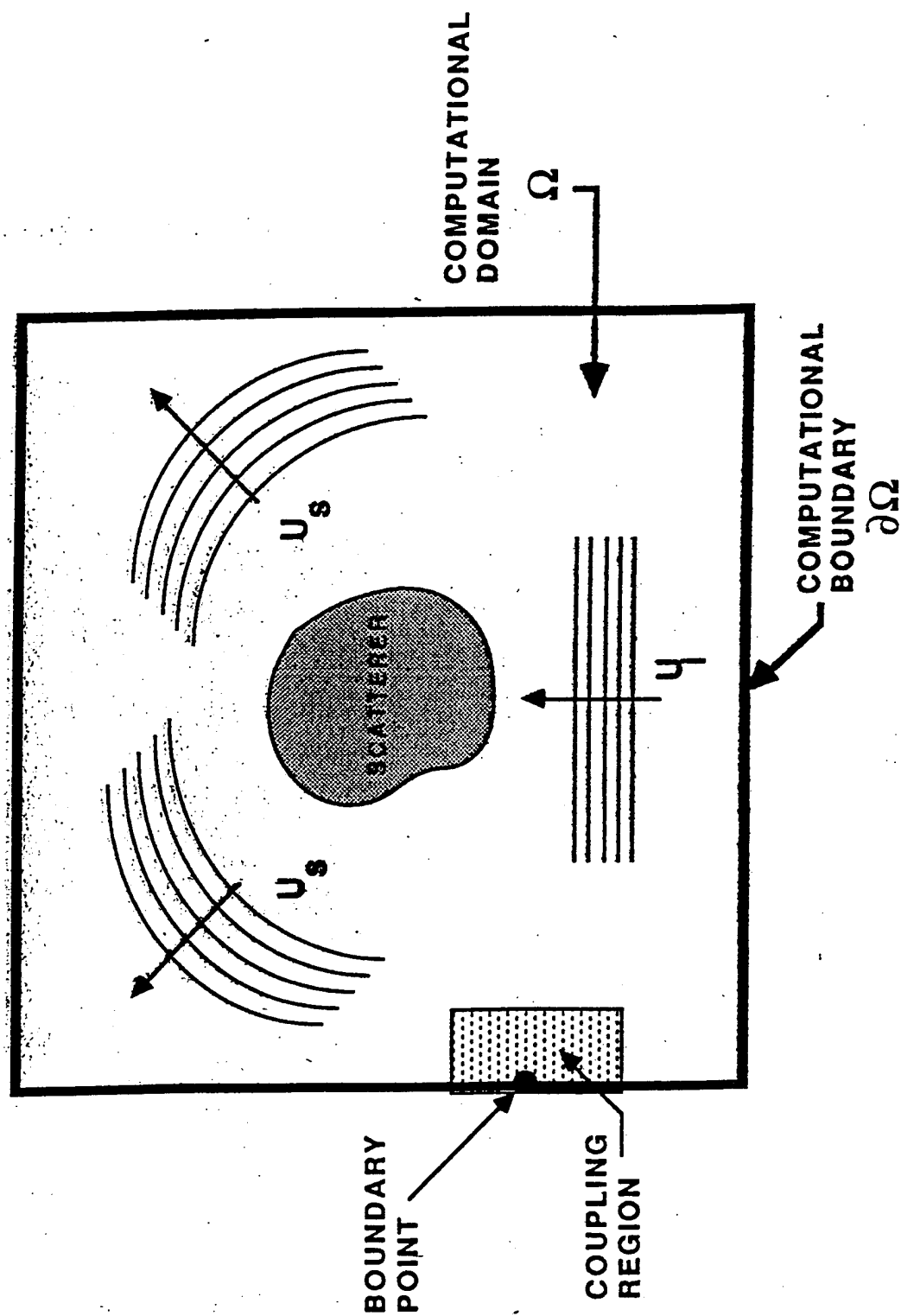
CHART 11: Linear Operator Factorization

The standard approach to the derivation of operators, which function as absorbing boundary conditions for propagating waves, is shown here.

The time dependent wave equation operator, L, is factored into a product of operators, L^+ and L^-. The factorization, shown here, is with respect to propagation in the x direction. D_x and D_t are the usual partial derivative operators with respect to x and t. The term, s, is the ratio of the y partial derivative operator to the t partial derivative operator and is related to the angle of incidence a plane wave makes with a boundary at a fixed x coordinate position.

CHART 11

LINEAR OPERATOR FACTORIZATION

- WAVE EQUATION

$$LU = U_{xx} + U_{yy} - \frac{1}{C^2} U_{tt} = 0$$

- FACTORIZATION IN X - DIRECTION

$$L^+ L^- U = 0$$

$$L^- = D_x - \frac{1}{c^2} D_t \sqrt{1 - s^2}$$

$$L^+ = D_x + \frac{1}{c^2} D_t \sqrt{1 - s^2}$$

- EXAMPLE: PLANE WAVE

$$s = \frac{k_y}{k} = \sin \theta$$
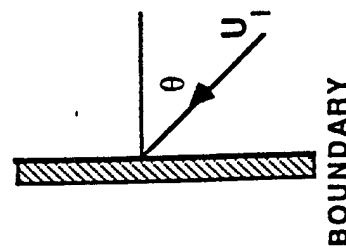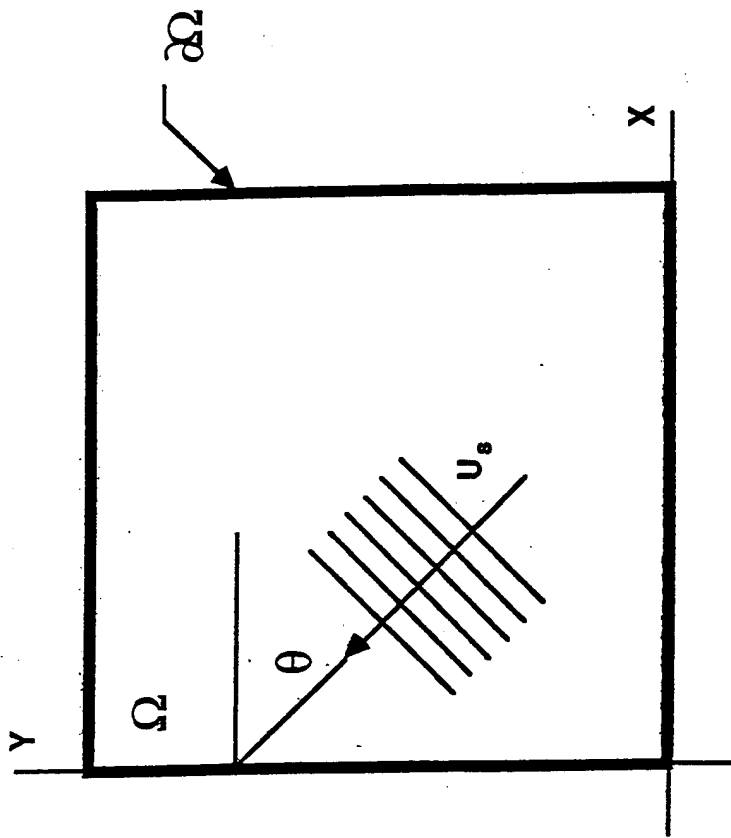
BOUNDARY

<u>CHART 12</u>: Exact Absorbing Boundary Condition

For a boundary at $x = 0$ in a two dimensional Cartesian domain, L^- functions as an exact absorbing boundary condition. Applying L^- at this boundary would have the effect of removing waves propagating in the -x direction from the computational domain without any nonphysical reflection. L^+ would serve the same purpose at the other x boundary. Similar operators are easily derived for the y boundaries.

The problem with trying to use L^- directly in a numerical code is that L^- is a non-local operator in space and time. Technically, L^- is a pseudo-differential operator, which couples the solution at any boundary point for any fixed time to the solution at all boundary points for all previous time. The non-local nature of L^- is clearly seen in its integral representation presented in the classic Engquist and Majda work, which introduced factorization and pseudo-differential operator concepts for the absorbing boundary condition problem. The popular view has been that non-local operators are inappropriate to use in numerical codes because of the heavy computational burden imposed by their numerical implementation. Therefore, much research effort has been directed toward deriving operators, based on approximations to L^-, which yield to efficient numerical implementation.

CHART 12

EXACT ABSORBING BOUNDARY CONDITION

$$L \cdot U = \left(D_x - \frac{1}{c^2} D_t \sqrt{1 - s^2} \right) U = 0$$

- NON - LOCAL BOUNDARY CONDITION
(REF: ENGQUIST AND MAJDA, 1977)

CHART 13: Approximate Boundary Conditions

Approximation of the square root portion of the L⁻ operator using a rational function approximant yields a partial differential operators whose numerical implementation is manageable. This approach was originally proposed in the Engquist and Majda work and was implemented in the case of Padé approximants.

The approach was generalized by the work of Trefethen and Halpren, who presented stability and well-possedness theorems for approximate absorbing boundary condition operators derived from general, rational function approximants.

CHART 13

APPROXIMATE BOUNDARY CONDITIONS

- **EXACT ABSORBING BOUNDARY CONDITION**

$$L \cdot U = \left(D_x - \frac{1}{c^2} D_t \sqrt{1 - s^2} \right) U = 0$$

- **RATIONAL FUNCTION APPROXIMATION**

$$\sqrt{1 - s^2} \approx r(s) = \frac{p_m(s)}{q_n(s)}$$

- p_m, q_n POLYNOMIALS
  (REF: TREFETHEN AND HALPREN, 1986)

CHART 14: Approximate Boundary Conditions, Second and Third Order Results

The simple, two term general polynomial approximant produces a second-order absorbing boundary condition operator. The next, higher order approximant yielding a stable boundary condition, is the ratio of two such terms producing the general, third-order absorbing boundary condition operator shown, here. Some of the work I have performed in this area produced stable difference schemes, which implemented these approximate absorbing boundary conditions for finite difference computations.

Local absorbing boundary conditions produce reflection error as they operate on scattered waves during the course of a time domain computation. Next, I will present results of numerical experiments designed to reveal the influence of reflection errors in finite difference computations.

CHART 14

APPROXIMATE BOUNDARY CONDITIONS

- **SECOND - ORDER ABSORBING BOUNDARY CONDITION**

$$\sqrt{1 - s^2} \approx p_0 + p_2 s^2$$

$$U_{xt} - \frac{p_0}{c} U_{tt} - cp_2 U_{yy} = 0$$

- **THIRD - ORDER ABSORBING BOUNDARY CONDITION**

$$\sqrt{1 - s^2} \approx \frac{p_0 + p_2 s^2}{q_0 + q_2 s^2}$$

$$q_0 U_{xtt} + c^2 q_2 U_{xyy} - \frac{p_0}{c} U_{ttt} - cp_2 U_{tyy} = 0$$

- **DIFFERENCE SCHEMES DEVELOPED**
  (REF: BLASCHAK AND KRIEGSMANN, 1988)

CHART 15: Square Cylinder Model Problem

For the remainder of this talk, I will focus on this model problem. An infinitely long cylinder of square cross section is illuminated by a plane wave, normally incident on one face, in the case of continuous wave (CW) sinusoidal illumination. The solution of this two dimensional scattering problem will be computed using the standard FD-TD formulation for the transverse magnetic (TM) polarization. The second-order Engquist and Majda approximate absorbing boundary condition is the standard absorbing boundary condition used in such codes.

Irrespective of the numerical method used to compute the solution of this problem, physical arguments suggest that the steady-state solution should be symmetric about the center line of the cylinder cross section that is perpendicular to the phase front of the illuminating plane wave. I will compare the computed results for two test cases:

Case 1: The square cylinder is positioned at the symmetry point in a square computational domain, Ω.

Case 2: The square cylinder is positioned 5 cells to the left of and 5 cells down from the symmetry point in the same computational domain.

The only difference between the two cases will be the position of the cylinder in Ω. In each case, the cylinder is illuminated by the same infinitely extended plane wave and one would expect no difference between the two computed solutions.

CHART 15

SQUARE CYLINDER MODEL PROBLEM

- **INVESTIGATE EFFECT OF APPROXIMATE BOUNDARY CONDITION**

- **INTERIOR SCHEME: STANDARD FD-TD, TM CASE**

- **RADIATION CONDITION: 2nd ORDER ENGQUIST-MAJDA**

CASE 1: SYMMETRIC PLACEMENT

CASE 2: ASYMMETRIC PLACEMENT
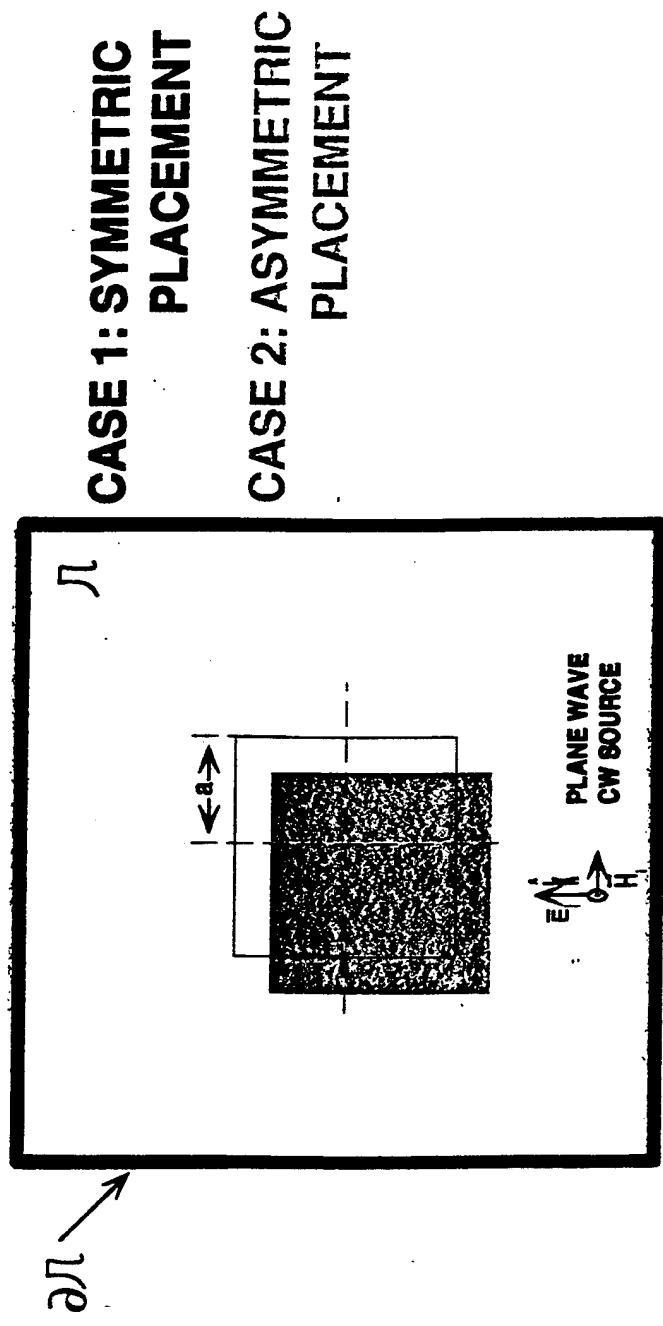
CHART 16: Square Cylinder Model Problem Results, PEC 50 x 50 Domain

Here are the results for this model problem in the case of a perfect electrically conducting (PEC) cylinder, 20 x 20 cell in size, positioned in a 50 x 50 cell computational domain. The frequency of the incident wave yielded **ka = 1**, where **k** is the incident wave number. At this frequency, the cylinder is not a large scattering object. For these computations, the incident wave was very well resolved at 62 sample points per wavelength (N_{ppw}). The FD-TD algorithm was executed for a number of time steps corresponding to 24 cycles of incident wave illumination, ensuring that the solution achieved the sinusoidal steady-state.

The solutions shown in the graph are the normalized (with respect to the magnitude of the incident H- field), steady state electric surface current densities induced on the back face of the cylinder computed for each of the two test conditions. The back face was selected because it is in a low excitation region and reflection errors from the absorbing boundary will be most noticable, there. Position 0 corresponds to the back left corner of the cylinder while position 20 corresponds to the back right cylinder corner when viewed relative to the front face.

In the case of symmetric placement, a symmetric and physically reasonable result is obtained. In the case of asymmetric placement, an unsatisfactory and nonphysical result is observed. There is at least a 15% difference between the two results in the region between positions 12 and 16, which was obtained by simply locating the cylinder a small distance away from the symmetry point of the computational domain.

My conclusion is that the accuracy of both solutions is suspect, because significant boundary condition reflections are present in this computational domain. In the case of symmetric placement, these reflection errors entered into the solution in a symmetric way, which obscured their observation.

CHART 16

SQUARE CYLINDER MODEL PROBLEM

- **PEC CYLINDER: 20 x 20 CELLS, Ka = 1**

- **COMPUTATIONAL DOMAIN: 50 x 50 CELLS**

- **STANDARD FD-TD: Nppw = 62**
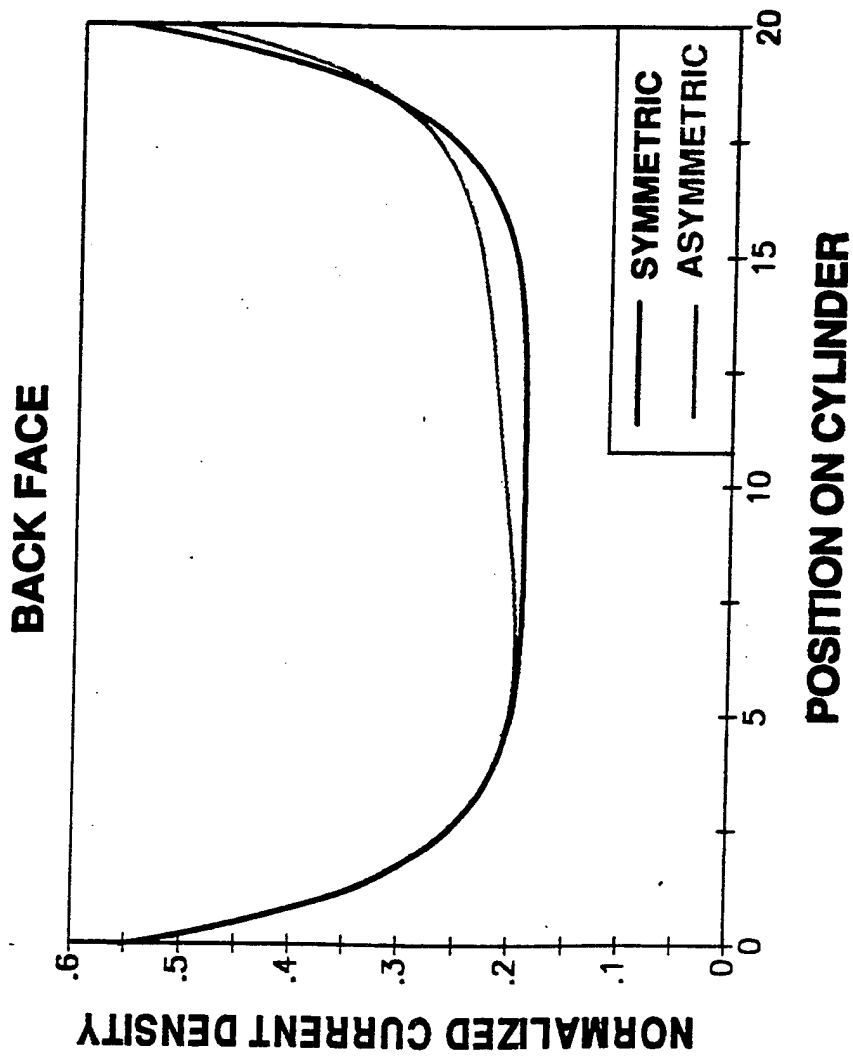
CHART 17: Square Cylinder Model Problem Results, PEC 100 x 100 Domain

We seek a solution using our standard FD-TD code, which is not corrupted by absorbing boundary condition reflection errors. A reasonable approach to resolve this problem is to repeat the computation on a larger domain, so that the computational boundary is located further from the surface of the scatterer, and again investigate to see if the solution is sensitive to the position of the scatterer within the domain.

Here are the results of that investigation. The computations were repeated on a 100 x 100 cell domain for the same two cases of relative scatterer position as was presented on the previous chart for the smaller domain and for the same number of time steps. The differences between the computed solutions for the symmetric and asymmetric cases are small, but the solutions, computed on the larger domain, were obtained at 4 times the effort needed to compute on the 50 x 50 cell domain. There is some asymmetry present in the solution obtained on the 100 x 100 cell domain in the case of asymmetric placement, but it is not observable on the scale of this graph. One might conclude that the scatterer is positioned in a "quiet zone" of the computational domain for which boundary condition reflections are not a problem, at least for the length of time corresponding to 24 cycles of incident wave illumination.

It is also interesting to investigate the sensitivity of the solution to variations in computational domain size. The computed solution for the case of symmetric placement within the 50 x 50 cell domain is also shown, with the conclusion that it is uniformly and as much as 10% larger than the corresponding result obtained on the 100 x 100 cell domain. This is further indication that FD-TD computation on a 50 x 50 cell domain is inappropriate for this problem.

CHART 17

SQUARE CYLINDER MODEL PROBLEM

- ## PEC CYLINDER: 20 x 20 CELLS, Ka = 1

- ## COMPUTATIONAL DOMAIN: 100 x 100 CELLS

- ## STANDARD FD-TD: Nppw = 62

143
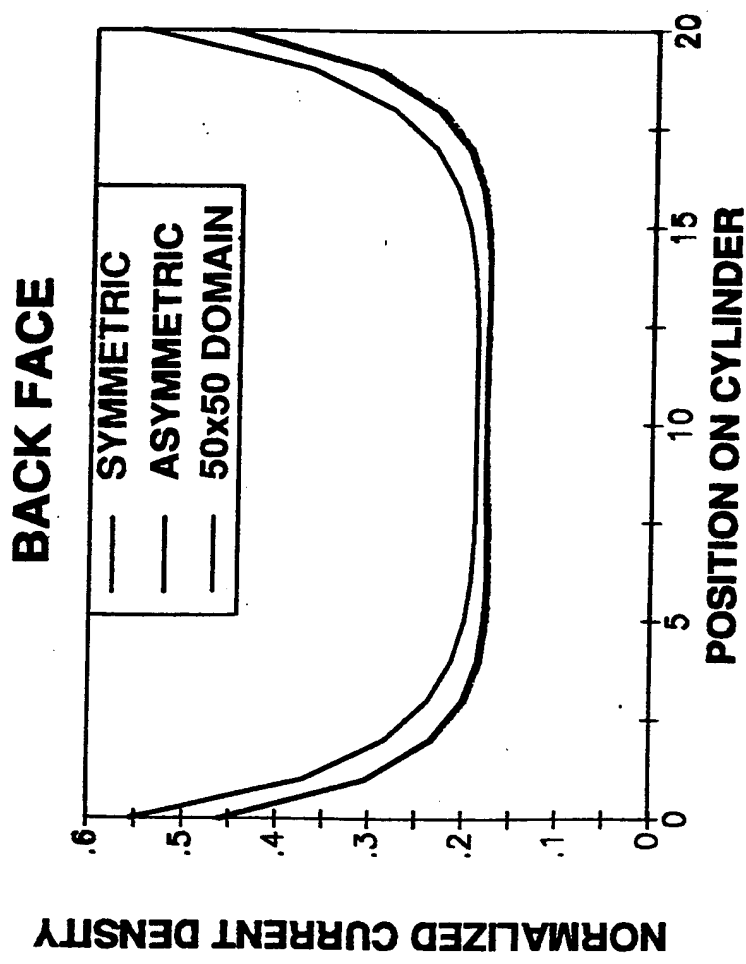
CHART 18: Square Cylinder Model Problem Results, Dielectric Cylinder 50 x 50 Domain

The previous results were obtained for the case of a perfectly conducting, impenetrable scatterer. Shown here are the results of the same sensitivity study repeated for the case of a square cylinder comprised of lossy dielectric material. The material parameters and incident wave frequency were selected to model muscle tissue at 300 MHz. Once again, the incident wave is TM polarized.

The computed solutions shown are for the penetrating electric field observed along the first row of grid points inside the back face of the cylinder. Again, computation on the 50 x 50 cell domain gives a nonphysical result when the cylinder is positioned 5 cells to the left of and 5 cells down from the symmetry point of the domain.

CHART 18

SQUARE CYLINDER MODEL PROBLEM

- **DIELECTRIC CYLINDER: 20 x 20 CELLS, Ka = 1**

- **MUSCLE TISSUE: $\in_r = 55$, $\sigma = 1$ S/M AT 300 MHz**

- **COMPUTATIONAL DOMAIN: 50 x 50 CELLS**

INSIDE BACK FACE
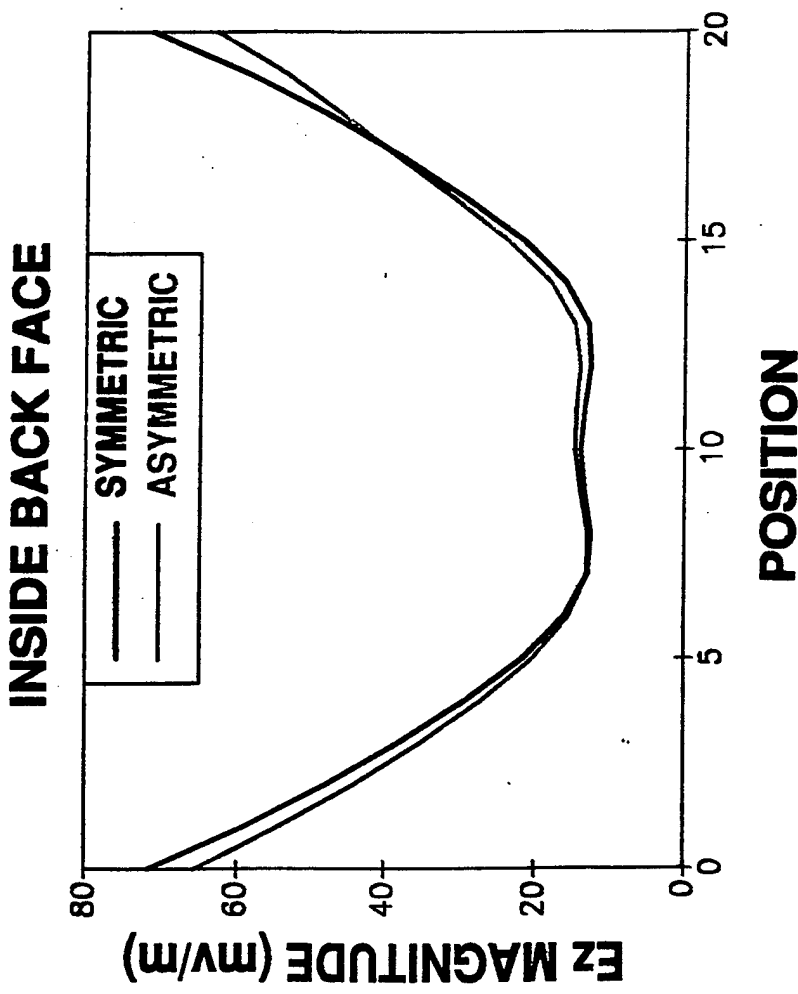
CHART 19: Absorbing Boundary Condition Opportunities

The results of our computations with our simple model problem indicate that there exists opportunities, and certainly a need, to improve the method used to compute the solution on the radiation boundary for FD-TD based algorithms. Some options we have considered for the direction of absorbing boundary condition research are shown, here.

One approach is to employ higher order approximations to the exact absorbing operator and derive local absorbing boundary operators, which generate smaller amplitude reflections compared to the second order operator in popular use. For the past five years, this has been a very active area of research. Operators of third order and higher present a serious implementation challenge and some progress has been made in the derivation of stable difference schemes for operators of third and fourth order. This approach does not address the fundamental problem, however, which is that any local operator is the *wrong* operator to use on the radiation boundary. All local operators will produce spurious reflections because they are approximations to the exact mathematical relation satisfied by outward propagating waves.

Another approach is to attempt to exploit the angular dependence inherent in all local operators. It is known that local absorbing boundary conditions work best for waves at certain "preferred" angles of incidence, which are determined by the coefficients of the approximation used in the derivation of the local operator. These coefficients are adjustable and yield a local operator with any desired angular performance. An adaptive algorithm could be defined, which adjusts these coefficients so that reflection errors are minimized. The adaptive algorithm would effectively "tune" the absorbing boundary condition for a specific scattering computation. Although this idea is interesting, it also does not address the fundamental problem, but proposes to minimize the negative consequences of using an inexact absorbing boundary condition.

We believe that the high risk, but high payoff approach to research in this area is to reconsider the exact operator and make a clear assessment of the complexity required for its numerical implementation. A successful global absorbing boundary condition algorithm would eliminate reflection errors from FD-TD based computations and permit computation on smaller sized domains. The practical utility of this trade off between domain size and the radiation boundary condition effort has not been effectively determined.

146

CHART 19

ABSORBING BOUNDARY CONDITION OPPORTUNITIES

- HIGHER ORDER LOCAL OPERATORS
  - 3RD AND 4TH ORDER CONDITIONS
  - IMPLEMENTATION CHALLENGE

- ADAPTIVE ABSORBING BOUNDARY CONDITIONS
  - EXPLOIT LOCAL OPERATOR ANGULAR DEPENDENCE
  - ESTIMATE SCATTERED WAVE DIRECTION
  - ADAPT OPERATOR COEFFICIENTS FOR MINIMUM ERROR

- EXACT GLOBAL OPERATOR
  - IMPLEMENTATION CHALLENGE
  - TRADE OFF DOMAIN SIZE AND BOUNDARY CONDITION COMPUTATIONAL EFFORT

CHART 20: Summary

The first item, shown here, is a brief statement of the philosophy and motivation of our research group. We believe that all numerical methods have limitations to their use. Conversely, all numerical methods have regimes of appropriate use. We simply want to know the extent of such limitations for any algorithm used to predict the penetration of electromagnetic fields into the human body. This is valuable and useful information for the RFR dosimetry community.

Progress has been made by Dr Petropoulos in the development of guidelines for choosing discretization parameters for FD-TD based computations in dispersive and non-dispersive media. His results indicated several shortcomings of the standard FD-TD method as applied to the modelling of pulse propagation in dispersive media. All of the work he presented is available upon request to interested parties in the form of two preprints.

Dr Blaschak presented results of sensitivity studies designed to detect the influence of radiation boundary condition reflection errors in FD-TD based computations. His results showed that reflection errors are easily observed in FD-TD computed solutions for simple model scatterers. He reviewed the present state of absorbing boundary condition practice for FD-TD based algorithms and future directions for absorbing boundary condition research.

Guided by these results, our ongoing research program will address these problems by exploring alternatives and improvements to the standard FD-TD algorithm.

CHART 20

SUMMARY

- NUMERICAL METHODS FOR RF DOSIMETRY PREDICTION REQUIRE RIGOROUS ANALYSIS AND UNDERSTANDING

- DEVELOPED GUIDELINES FOR CHOOSING DISCRETIZATION PARAMETERS FOR FD-TD BASED COMPUTATIONS IN DISPERSIVE AND NON-DISPERSIVE MEDIA

- SENSITIVITY STUDIES INDICATED THE INFLUENCE OF RADIATION BOUNDARY CONDITIONS IN FD-TD BASED COMPUTATIONS FOR SIMPLE SCATTERING OBJECTS

- FUTURE WORK:

  - ALTERNATIVES OR IMPROVEMENTS TO PRESENT FD-TD BASED METHODS

  - EXACT OPERATOR FOR RADIATION BOUNDARY CONDITIONS

REVIEW OF THERMOPHYSIOLOGICAL MODELS

Eleanor R. Adair, Ph.D.
John B. Pierce Laboratory and Yale University
New Haven, CT 06519

All animals, including humans, have a widely varying internal heat production and live in a thermal environment whose physical characteristics are constantly changing. In the absence of effective behavioral thermoregulation, the body temperature of homeotherms will be regulated by the autonomic (or physiological) mechanisms which control heat production, the distribution of heat in the body, and the avenues and rate of heat loss from the body to the environment. These mechanisms are well understood and quantified for the human body; thus it has been possible to develop mathematical simulation models of physiological thermoregulation in considerable detail and validate them against experimental data. Thermophysiological modeling becomes especially important when its purpose is to extrapolate variables that are not experimentally attainable and to simulate experiments that cannot be performed. The latter is one of the topics under discussion in this workshop.

In this brief overview, some of the general characteristics of thermophysiological models and their construction will first be presented. The model developed by Stolwijk and Hardy (1977) will be described as an example to illustrate some major characteristics of all simulation models. Some predictions by Stolwijk, and by others using elaborations of his model, will be mentioned that involve RF deposition in the body; some indication of the accuracy of these predictions will be attempted. Unfortunately, it is not possible to present here the detailed construction of any model, but appropriate and comprehensive references will be provided as required. Under the assumption that Dr. Wissler will provide a short description of his modeling efforts (Wissler, 1970), I will conclude with a brief description of Jurgen Werner's complex model that incorporates the true geometry and anatomy of the human body plus some summary observations.

The simplest basis for thermophysiological modeling is the energy balance equation, called by physiologists the heat balance equation. This is illustrated in Figure 1, a diagram developed by L. G. Berglund some years ago (Berglund, 1983). The figure shows the principal routes of energy exchange between a person and the environment. Heat is produced in the body by metabolism (M); additionally, heat may be generated in the body from the absorption of RF energy (AMicro). For the individual to maintain thermal balance, this energy must be continually transferred to the environment. The balance between energy production and loss is so regulated by behavioral and physiological adjustments that the temperatures of the skin and core of the body are maintained within quite narrow limits.

In Berglund's words (op. cit, p. 15), "Energy may be lost by doing work (force x distance) on the surroundings, through respiration and by heat transfer from the skin. Respiratory losses (Q_{res}) are generally small. In typical comfort situations, most of the

heat is lost from the skin by convection (Q_c) to the surrounding air and radiation (Q_r) to the surrounding walls and surfaces. In nonsweating situations, there is an additional small loss by the diffusion of water vapor through the skin (E_{diff}). In warm or hot conditions, the evaporation of regulatory sweat (E_{rsw}) can become a powerful mechanism for heat dissipation.

Convective heat loss increases with increasing air motion (V) and decreasing air temperature (T_a). At very low room air speeds, convection continues from the warm buoyant air rising next to the body. Radiation losses increase in proportion to the difference between the mean radiant temperature of the surrounding surfaces and the surface temperature of the individual. The mean radiant temperature (T_r) is defined as the temperature of an imaginary isothermal black enclosure in which an occupant would exchange the same amount of heat by radiation as in the actual nonuniform environment. . . . Respiratory heat losses depend on air temperature, humidity, and the rate of ventilation, which in turn are proportional to metabolism. The mass or evaporative heat transfer terms, E_{diff} and E_{rsw}, are both affected by humidity and air motion.

Two other parameters that affect the energy flow are metabolism and clothing insulation. Metabolism is characterised by a unit called the met. The energy produced by a resting person per unit body surface area (58 W/m^2) is arbitrarily defined as 1 met. Clothing is also important since it adds thermal resistance to the heat path between the skin and the surrounding environment. The resistance is characterized with the clo unit (1 clo or 0.155 Wm^{-2}C^{-1}). One clo of clothing insulation can keep a resting human 'comfortable' at 21 °C (70 °F).

In cool environments, the resulting losses may be burdensome even with autonomic and behavioral adjustments. Under such conditions, the overall nergy balance equation of Figure 1 indicates that absorbing microwave energy within the body is a novel way to supplement insufficient metabolic heat, balance the energy equation, and reduce the stress and discomfort of a cold environment."

As in all modeling efforts, thermophysiological models are based on simplifications of the actual system. In this case it is useful to separate the total physiological system into two major components: the regulated or passive system, and the regulatory or controller system. These are shown schematically in Figure 2 (adapted from Stolwijk, 1980). In all models, both of these systems are simplified to a degree necessitated by knowledge or required by the application. The controlling or regulatory part of the model consists of the structures which sense body temperatures and their response characteristics, the central neural integration, the neural effector pathways and the effector mechanisms themselves, including shivering or exercising muscles, secreting sweat glands, and the tone of peripheral blood vessels in the skin and other blood vessels elsewhere which control the convective heat transfer between different organs and structures of the body.

$$M + A\ Micro = WORK + Q_{res} + E_{diff} + E_{rsw} + Q_c + Q_r$$
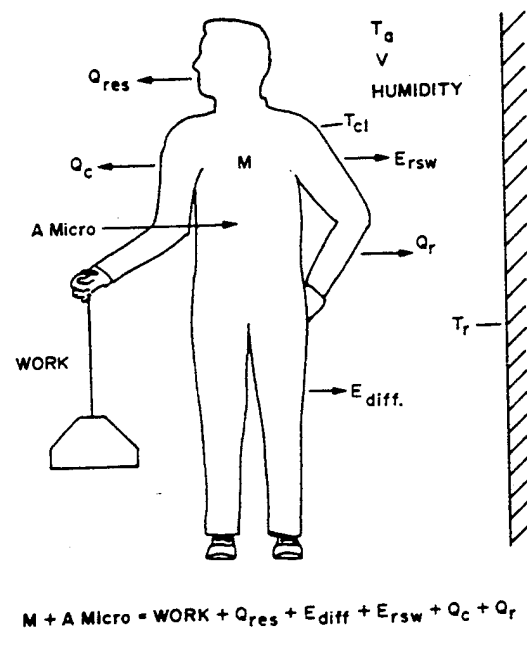
Figure 1. The energy flows between man and his environment. (After Berglund, 1983)
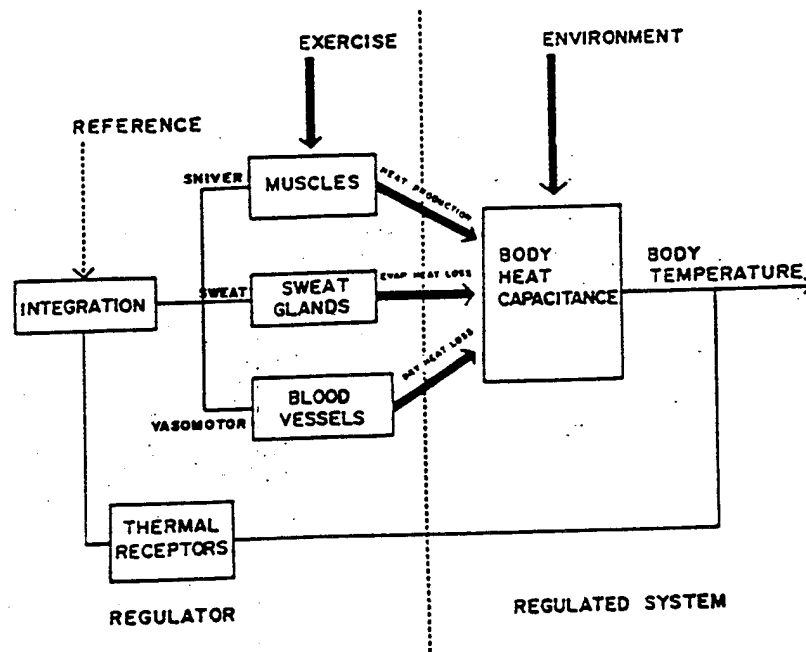
Figure 2. Simplified block diagram of the human thermoregulatory control system as presented by Stolwijk (1980).

The second component, the controlled system, consists of the simplified representation of the thermal characteristics of all the body tissues, including metabolic heat production, heat capacitance, local temperature, heat transfer via conduction and convection inside the body and heat transfer via evaporation, conduction, convection and radiation between the skin and the external environment. In the case of exposure of the whole body to an RF source, the absorbed energy will be added to metabolic energy generated in the body's core. Partial body exposure or allowance for distributive dosimetry will require the absorbed energy to be proportioned appropriately in various body compartments.

In the model of Stolwijk and Hardy, originally formulated in 1966, revised in 1971 and 1977, the human body is represented by 6 cylindrical elements, each consisting of 4 concentric cylinders, and a central blood compartment. The head is actually a sphere, rather than a cylinder. The concentric elements in each compartment correspond to the mass of skin, subcutaneous fat, muscle, and core tissues of the head, trunk, arms, hands, legs, and feet. Together with a central blood compartment, which exchanges blood and heat with each of the tissue compartments, there are a total of 25 tissue compartments. Each of these is characterized by a heat capacitance, a basal and exercise-related heat production rate, a blood flow rate indicating its convective connection to the central blood compartment, a heat conductance to adjacent compartments, and, for the skin, evaporative, radiant, convective, and conductive heat exchange with the environment. The model also provides for each compartment a temperature based on initial conditions and the integrated flows of heat into and out of the compartment.

The controlling system receives from the controlled system the instantaneous temperature of each of the 25 compartments. These temperatures are compared with reference or set point temperatures and summed with a relative weighting based on physiological measurements. The thermal sensors feeding into the integrator are located in the skin according to an experimentally determined distribution, and in the core of the head element which represents the temperature of the hypothalamus. The skin and head core signals, integrated with a relative weight of about 0.1 for the skin and 0.9 for the core, are converted into efferent commands to the sweat glands, to the muscles, or to the peripheral blood vessels controlling skin blood flow. These effector actions then will produce changes in heat production, heat loss, or heat transfer which will counteract the effects of internal or external loads which would otherwise change body temperatures away from preferred and regulated levels.

Stolwijk has used his model to predict the effects of deposition of RF energy into selected parts of the body. (Stolwijk, 1980) He first simulated the deposition of 100 watts of RF energy into the core of the head for 30 minutes in a thermoneutral environment (30 °C). The exposure caused only a modest elevation in brain temperature, because of the high rate of blood flow in the brain, and the mobilization of strong heat loss through sweating. Because the rate of heat loss in this case exceeded the rate of energy input, all body temperatures were predicted to fall. Secondly, Stolwijk presented the result of a simulation in which 500 watts of RF energy was

154

deposited into the trunk core for 30 minutes, again in a thermoneutral environment. Because the sweating response was disabled in this example the temperatures in all body compartments were predicted to rise and the thermoregulatory system was predicted to be overwhelmed by the RF exposure.

In a 1981 paper, Way, Kritikos and Schwan (Way, et al, 1981) introduced an additional compartment to Stolwijk's model, in the region of the hypothalamus, so as to consider partial heating due to hotspots that might be induced by microwaves. These authors found that because of thermoregulatory action, the hypothalamic temperature would not increase drastically until the rate of energy deposition exceeded a threshold level of 50 W/kg. The primary controlling physiological mechanisms in this case were found to be sweating and blood flow.

Not so successful was an adaptation of the Stolwijk model by Spiegel, Deffenbaugh and Mann (Spiegel, et al., 1980). They added a neck and subdivided the trunk, arms and legs so that they might introduce electromagnetic energy distributed in accordance with Hagmann's block model (Hagmann, et al, 1979) The local temperature at 61 discrete locations in the body, as well as the thermoregulatory responses of vasodilation and sweating were computed for a number of RF field intensities at 2 frequencies, 80 and 200 MHz. The incident power density vs duration necessary to obtain a hot spot of 41.6 °C was calculated for several parts of the body. Spiegel, et al. claimed to have demonstrated that hot spots were produced at much lower field strengths at 80 MHz than at 200 MHz and also that a 1 hour exposure to 80 MHz at 10 mW/cm^2 would generate a hot spot (temperature > 41.6 °C) in the core of the lower thigh. Unfortunately, their version of the model did not account for the great increase in blood flow known to occur at tissue temperatures of 40 °C and above (Cunningham, 1970; Guy and Chou, 1983; Sekins, 1981), a response which would have prevented elevations in tissue temperature of this magnitude.

- -

---A description of Prof. Eugene Wissler's thermophysiological model should be inserted here. ---

- -

With the advent of super-computers, it has become possible to incorporate a comprehensive data bank of the true geometry and anatomy of the human body into thermophysiological modeling. Prof. Jurgen Werner (Ruhr University, FRG) has developed such a model on the basis of photogrammetric analyses of anatomical models (Buse and Werner, 1984; Werner, 1975; 1986; Werner and Buse, 1988). In his model, Werner provides the contour lines of sections of the body, e.g., the trunk, with the major organs eliminated. For each body section, analogue sectional maps for each contour line or slice are made. A corresponding computer representation for each slice is then determined. In Werner's model of the human body, 63 types of tissue are differentiated. The local grid is 1 cm for the trunk and 0.5 cm for the other parts of the body, resulting in a digital representation of the body with about 400,000 points associated with the physical parameters of the tissue.

155

Compared to the Stolwijk and Hardy model, the details of the controlled or passive system and the controller are quite complex. Werner separates the controlling or regulating system into three categories, the receptors, the effectors and the controller. RF energy from the environment can theoretically be deposited directly in any part of the anatomy, yielding a localized temperature change. Werner's simulation model is principally based on partial differential equations for both the passive system and the controlling system. For the passive system, equations include 1) heat transport via heat conduction and capillary blood flow and incorporating localized metabolic heat production (absorbed energy could be added to M at this level), 2) heat transport via bloodflow in large blood vessels, 3) heat loss via the skin (including radiation, convection + conduction, and evaporation), and 4) heat loss via respiration. For the receptors and effectors, the equations contain terms representing afferent frequencies, 3-D location, time constants, gain and temperature. The equation for the controller also incorporates a coupling matrix between receptor and effector site. The passive system's equations and parameters are represented as exactly as possible in order to test how far the controller equations could be simplified and still obtain an adequate description of the system's operation. Details of the model may be found in Werner, 1986; Werner and Buse, 1988.

Werner's modeled physiological system has been implemented on a vector computer Cyber 205 by an implicit alternating direction method. In 1987 the solution needed a core capacity of 3.5 million 64-bit words.

Some examples of steady-state transverse temperature profiles for the head and the trunk at a thermoneutral ambient temperature of 30 °C are given in Werner, 1986. That for the head reflects the high metabolic heat production of brain tissue and high regional blood flow. The profile for the trunk is more convex but rather homogeneous and smooth. Significant details such as the cooler region of the spinal cord and the region of the heart with its higher heat production are clearly evident. In the same publication, sample steady-state isotherms in the trunk at the level of the collar bone were predicted for 4 ambient temperatures ranging from 10 to 40 °C. The cool periphery in the cold is demonstrated in the predictions to give way to vasodilated warmer skin in the warmer environments.

At last report, about 2 years ago, the simulation of dynamic or transient effects by Werner's model was judged to be possible but considerable expansion of computer memory was necessary. If this model is to be useful for the analysis of thermophysiological responses to RF energy deposition, dynamic analyses, as well as steady-state solutions, are essential.

Finally, it is useful to note that a new 3-D model developed at Kansas State University by Carol Smith (and as yet unpublished) is being further elaborated by Toshikazu Takemori in Japan. This model embodies 15 cylinders, each having axial, radial and circumferential segments. There are approximately 4648 elements, each having linear thermal gradients within them and there are a total of 2525 nodes. Although it is not

possible to discuss details further, I tempt your interest by reporting that detailed color-coded computer outputs of both peripheral and deep body temperatures have been generated acurately for both cold and warm environments. Although in a relatively early stage of development, this model may hold promise for future work in this area.

Some general conclusions about the utility of such models to predict the physiological consequences of RF energy deposition in the human body are appropriately offered here.

First, given the great advances in computer capability (both memory and speed), thermophysiological modeling that incorporates the results of a fine grained dosimetry model should be feasible and successful. Depending upon the specific questions asked, either the Wissler or Werner model would seem appropriate for this application.

Second, special consideration must be paid to the role of regional blood flow as local tissue temperature rises. For well vascularized tissues such as muscle, a tremendous increase in blood flow occurs when temperatures of 40 - 42 °C are exceeded. Data of Guy and co-workers (Guy and Chou, 1983; Sekins, 1981), Cunningham (1970), and many others bear on this point. Body regions, such as eyes and intestines, that are poorly perfused will be more vulnerable to localized high SARs than are those regions well perfused with blood.

Third, for attempts to incorporate the results of energy deposition models into thermophysiological models, the most effective way to achieve this marriage is to leave both systems as originally developed but transfer the localized SARs from the compartments of the deposition model to the differently-formulated, but corresponding, compartments of the thermophysiological model which can then predict the thermal and thermoregulatory output response (Stolwijk, 1983). The absorbed energy would most appropriately be added to the localized metabolic energy production, as has already been done successfully with simple modeling efforts (Adair and Berglund, 1986; 1989; 1992).

And finally, such a marriage seems feasible and useful at this time, but any predictions should always be interpreted with resonable caution and tested in a laboratory setting whenever possible.

REFERENCES

Adair, E.R. and Berglund, L.G. (1986) On the thermoregulatory consequences of NMR imaging. Magnetic Resonance Imaging 4:321-340.

Adair, E.R. and Berglund, L.G. (1989) Thermoregulatory consequences of cardiovascular impairment during NMR imaging in warm/humid environments. Magnetic Resonance Imaging 7:25-37.

Adair, E.R. and Berglund, L.G. (1992) Predicted thermophysiological responses of humans to MRI fields. Annals N.Y. Academy of Sciences 649:188-200.

Berglund, L.G. (1983) Characterizing the thermal environment. In: Microwaves and Thermoregulation. (E.R. Adair, Ed.) Academic Press:New York, pp. 15-31.

Buse, M. and Werner, J. (1984) Determination of temperature profiles within the human body by mathematical simulation. In: Lecture Notes in Medical Informatics (D.A.B. Lindberg, P.L. Reichertz, Eds.) Springer-Verlag:Berlin, vol.24, pp.471-476.

Cunningham, D. J. (1970) An evaluation of heat transfer through the skin in extremity. In: Physiological and Behavioral Temperature Regulation (J.D. Hardy, A.P. Gagge, J.A.J. Stolwijk, Eds.) Charles C. Thomas:Springfield, IL. pp. 302-315.

Guy, A.W. and Chou, C.-K. (1983) Electromagnetic heating for therapy. In: Microwaves and Thermoregulation (E.R. Adair, Ed.) Academic Press:New York, pp.57-93.

Hagmann, M.J., Gandhi, O.P. and Durney, C.H. (1979) Numerical calculation of electromagnetic energy deposition for a realistic model of man. IEEE Trans. Microwave Theory Tech. 27:804-809.

Sekins, K.M. (1981) Microwave hyperthermia in human muscle: An experimental investigation of the temperature and blood flow fields occurring during 915 MHz diathermy. Ph.D. Dissertation, University of Washington, Seattle, WA.

Spiegel, R.J., Deffenbaugh, D.M., and Mann, J.E. (1980) A thermal model of the human body exposed to an electromagnetic field. Bioelectromagnetics 1:253-270.

Stolwijk, J.A.J. (1971) A mathematical model of physiological temperature regulation in man. Report No. NASA CR-1855, Washington, D.C.

Stolwijk, J.A.J. (1980) Mathematical models of thermal regulation. Annals N. Y. Academy of Sciences 33:98-106.

Stolwijk, J.A.J. (1983) Evaluation of thermoregulatory response to microwave power deposition. In: Microwaves and Thermoregulation (E.R. Adair, Ed.) Academic Press:New York, pp. 297-306.

Stolwijk, J.A.J. and Hardy, J.D. (1966) Temperature regulation in man - a theoretical study. Pflugers Archiv. 291:129-162.

Stolwijk, J.A.J. and Hardy, J.D. (1977) Control of body temperature. In: Handbook of Physiology; Reactions to Environmental Agents (D.H.K. Lee, Ed.) American Physiological Society:Bethesda, MD, pp.45-68.

Way, W.L., Kritikos, H. and Schwan, H. (1981) Thermoregulatory responses in the human body exposed to microwave radiation. Bioelectromagnetics 2:341-356.

Werner, J. (1975) Zur temperaturregelung des menschlichen Korpers. Biol.Cybernetics 17:53-63.

Werner, J. (1986) Do black-box models of thermoregulation still have any research value? Contribution of system-theoretical models to the analysis of thermoregulation. Yale Journal of Biology and Medicine 59:335-348.

Werner, J. and Buse, M. (1988) Three-dimensional simulation of cold and warm defence in man. In: Environmental Ergonomics: Sustaining Human Performance in Harsh Environments. (I.B. Mekjavic, E.W. Banister, J.B. Morrison, Eds.) Taylor and Francis:Philadelphia, pp. 286-296.

Wissler, E.H. (1970) The use of finite difference techniques in simulating the human thermal system. In: Physiological and Behavioral Temperature Regulation (J.D. Hardy, A.P. Gagge, J.A.J. Stolwijk, Eds.) Charles C. Thomas:Springfield, IL, pp. 367-388.

Wissler, E.H. (1988) Mathematical simulation of human thermal behavior using whole-body models. In: Environmental Ergonomics: Sustaining Human Performance in Harsh Environments (I.B. Mekjavic, E.B. Banister, J.B. Morison, Eds.) Taylor and Francis:Philadelphia, pp. 325-373.

Heat Transfer Models for Vascularized Tissues

Kenneth R. Foster
Department of Bioengineering
University of Pennsylvania
Philadelphia PA 19104-6392

The well-known hazards of exposure to RF energy are associated with either excessive heating of tissue or with adverse physiological consequences of the absorbed power. In contrast to the SAR, which depends on physical and geometrical factors, the thermal response of an animal strongly reflects physiological and anatomical factors that are difficult to model exactly.

In calculating the thermal response, one can distinguish between a <u>local</u> problem (calculating the temperature rise at each point within the irradiated tissue) and a <u>global</u> problem (determining the thermoregulatory response of the animal). The first problem is one of heat transport; the second is one of thermophysiology. My comments address the first of these problems.

In studies of bioheat transport, the formulation that is by far the most widely used is Pennes' bioheat equation[1]:

$$\rho c_t \frac{\partial T}{\partial t} = \nabla(k\nabla T) - wc_b(T - T_a) + q \tag{1}$$

where T_t is the local average tissue temperature
T_a is the arterial supply temperature
k_t is the tissue thermal conductivity
W_b is the perfusion rate dependent parameter
q_t is the volumetric heat generation rate (the SAR)
c_t is the specific heat of the tissue
q_t is the density of the tissue
and t is the time.

Pennes' equation is easy to solve, contains few parameters, and its parameters can be given a simple interpretation in terms of measurable quantities such as blood perfusion or thermal conductivity. However, the model has obvious problems. For example, the blood perfusion is modeled as a heat sink: the heat just vanishes whereas in real life it must go somewhere. More generally, the model is a continuum approximation to heat transport by blood vessels, and the nature of the transport clearly depends on the geometry, configuration, and flow properties of the vessels.

In recent years, the problem of heat transport in vascularized tissue has been subject to renewed attention. Several investigators have pointed out that most heat exchange between blood and tissues does not occur in the capillary bed (as Pennes

assumed) but rather in larger thermally significant vessels.

An important parameter that describes exchange of heat and the surrounding tissue is the thermal equilibration length, i.e. the distance that blood has to flow in a vessel to equilibrate thermally with the surrounding tissue. As Chen and Holmes and others have shown [2] (Fig. 1) the thermal equilibration length ranges from several meters for the largest blood vessels, to less than 0.01 mm for capillaries. Capillaries are numerous, but they are fully equilibrated with the surrounding tissue and are ineffective at transporting heat. Most heat exchange occurs in small vessels of a few hundred microns diameter. These vessels are numerous and have thermal equilibration lengths in the cm range. Larger vessels are comparatively uncommon; smaller vessels are ineffective in transferring heat.

The result of this situation is rather confused. Pennes' equation has been employed by many investigators, often for calculating the temperature distribution in tissue subject to RF irradiation or for microwave hyperthermia. Despite its lack of theoretical basis, the hyperthermia community seems generally satisfied with the model -- perhaps because no better model is in sight that is practically useful in a clinical situation. However, continuum models such as that of Pennes must be approached very cautiously.

A more rigorous analysis would consider heat transfer from individual vessels, at least those that are large enough to be thermally significant. Such a vessel-by-vessel analysis would be feasible in principle, but too complex to be practical. An intermediate approach is to develop continuum models that are satisfactory approximations for a vascularized tissues.

This latter approach has been taken by several authors, notably Weinbaum and colleagues. These investigators have carried out detailed analyses of selected tissues (the upper cm of the rabbit thigh, the human arm) and developed approximate formulations of models that provide reasonable approximations without requiring a full vessel-by-vessel analysis[3][4][5]. This group experimentally measured the temperature distribution in surface layers of the rabbit thigh, and interpreted their data using a detailed model based on a vessel-by-vessel analysis.

Based on this work, Weinbaum and colleagues have proposed a new bioheat equation that is just the heat conduction equation in which the effective thermal conductivity k_e of a tissue is a function of the geometry of the vessels. For a tissue whose thermally significant vessels occur as countercurrent pairs,

$$k_e = k\left[1 + \frac{\pi^2}{4\sigma k^2}na^2k_b^2Pe^2\right] \tag{2}$$

where k is the thermal conductivity of the tissue excluding the blood vessels,

162

σ is a shape factor,
n is the number density of countercurrent vessels.
k_b is the thermal conductivity of the blood,
Pe is the Peclet number that characterizes the flow.

According to their model, the chief effect of blood flow is to increase the effective thermal conductivity of the tissue, in a direction parallel to that of the countercurrent vessels. This enhancement is proportional to the square of the blood velocity, through its effect on Pe. This model applies for tissues in which the heat transport is dominated by parallel blood vessels with countercurrent flow.

Our own group has explored a variety of other vascular models in an attempt to understand the conditions under which a continuum model might suffice. (This work, and many of the references in this present contribution) is described in the Ph.D. thesis of Baish as well as in the papers listed in the Bibliography).

Our models consisted of parallel arrays of vessels of varying diameter, with countercurrent or unidirectional flow, subject to volumetric heating (Fig. 2). These models are obviously oversimplified, but they can be rigorously solved and provide good insight into the transition between a vessel-by-vessel analysis and the continuum limit.

The results of an extensive series of simulations are summarized in Fig. 3. They show that heat transport in tissues can be described by a continuum model if the heat exchange is dominated by equilibrated (i.e. small) vessels. The continuum model that results depends on whether the vessels have countercurrent or unidirectional flow. For countercurrent flow, an effective conductivity model (the Weinbaum-Jiji model) results; for unidirectional flow a model results that resembles the classic problem of heat exchange due to a fluid that is percolating through a porous medium.

The continuum models do not work when the vessels are of intermediate size, i.e. when their equilibration lengths are comparable to the size of the heated region. Near large vessels, a full analysis is also needed to produce a detailed description of the temperature near the vessels. Surprisingly, near large vessels, something resembling Pennes' bioheat equation will provide a good estimate of the average tissue temperature. However, the term corresponding to the "perfusion" term in Pennes' equation is proportional to geometric factors, not to the "perfusion rate".

What is the result of all of this analysis? Clearly, Pennes' bioheat equation, at least in its naive interpretation, is not adequate to predict the temperature rise in tissue. While a continuum model might work reasonably well in many circumstances, the model needs to incorporate information about vascular geometry as well as perfusion. An exact analysis would require a detailed vessel-by-vessel analysis, which is likely to be too time consuming to be feasible in most cases. Investigators need to explore the use of approximate models, provided they are informed by adequate information about vascular geometry and perfusion.

What needs to be done? With isolated exceptions (the human arm, the upper cm of the rabbit thigh) there are few experimental tests of these new theories. There needs to be more experimental work on well-characterized biological preparations to relate heat transport to vascular geometry and flow. Several groups are now studying the canine or porcine kidney, which can be isolated and perfused. Other organs as well should be studied. The nature of heat transport in these organs will vary just as the vascular geometry varies.

For tissues subject to RF irradiation, there is often a need to predict the temperature increase and distribution of temperature increase. From the above considerations, it is clear that a range of approaches is possible for modeling the temperature response of a tissue. At one extreme, one could develop a rigorous vessel-by-vessel analysis to predict the detailed temperature distribution in a subject's body resulting form RF irradiation. This is, however, a major undertaking, which would probably be warranted only when the SAR is very high or the increase in tissue temperature must be known with high precision.

A far simpler, and more approximate, approach would be to apply a continuum model of bioheat transport to estimate the temperature increase within a region of tissue subject to RF irradiation. A still simpler approach would be to ignore heat transport within a tissue compartment entirely and consider only the exchange of heat between compartments and the effect of RF irradiation on the global energy balance. In view of the vast difference in effort involved in these different approaches, one needs to define very carefully the accuracy that is needed for any given problem.

Papers by Foster et al. on Bioheat Transfer

Small scale temperature fluctuations in perfused tissue during local
hyperthermia.
J. W. Baish, P. S. Ayyaswamy and K. R. Foster.
ASME Transactions on BioMechanical Engineering Vol: 108, Pages 246-250,
1986.

Perfused phantom models of microwave irradiated tissue.
J. W. Baish, K. R. Foster, and P. S. Ayyaswamy.
ASME Transactions on BioMechanical Engineering Vol: 108, Pages 239-245,
1986.

Heat transport mechanisms in vascular tissues: a model comparison.
J. W. Baish, P. S. Ayyaswamy, and K. R. Foster.
ASME Transactions on BioMechanical Engineering, Vol: 108, Pages 324-331,
1986.

Convective heat transport due to blood perfusion in volumetrically heated biological
tissue. J. W. Baish. Ph.D. dissertation, Department of Mechanical Engineering and
Applied Mechanics, University of Pennsylvania 1986

.Bibliography (see also the references in Baish's thesis).

1. H. H. Pennes, "Analysis of tissue and arterial blood temperature in the resting human forearm", J.
Appl. Physiol. 1:93-122 (1948).

2. Chen,M.M., Holmes,K.R., "Microvascular contributions tissue heat transfer,"
Thermal Characteristics of Tumors:Applications in Detection and Treatment.
Jain,R.K.,Gullino,P.M., eds. New York: The New York Academy of Sciences, 335:
137-150.
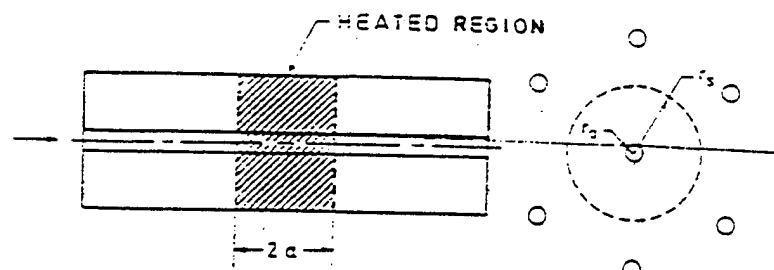
3. S. Weinbaum and L. M. Jiji, "A new simplified bioheat equation for the effect of
blood flow on the local average temperature," ASME J. Biomech. Eng. 107, 131-139
(1985).

4. S. Weinbaum et al, "Theory and experiment for the effect of vascular microstructure
on surface tissue heat transfer - I: anatomical foundation and model
conceptualization," ASME J. Biomech. Eng. 106, 321- 330 (1984).
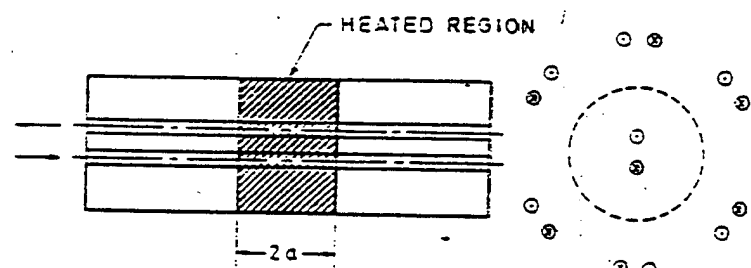
5. L. M. Jiji et al, "Theory and experiment for the effect of vascular microstructure on
surface tissue heat transfer - II: model formulation and solution," ASME J. Biomech.
Eng. 106, 331-341 (1985).

Equilibration Lengths
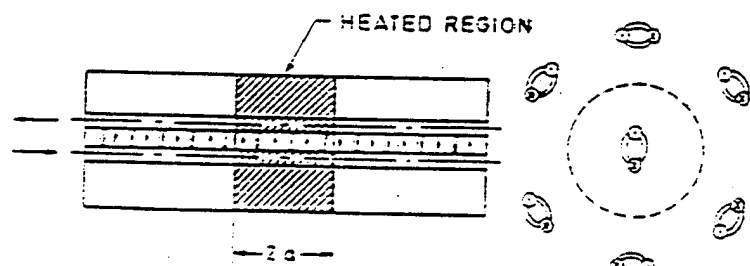
Vessel Type	Radius (microns)	Velocity (cm/sec)	L (UD) (cm)	L (CC) (cm)
Large artery	1500	13	440	300
Main arterial branch	500	8	29	21
Terminal branch	300	6	7.5	6
Small artery	200	2	1	0.8
Equilibrated vessel	<100	< 0.3	< 0.03	< 0.02

(Chen and Holmes)

166

(a) Unidirectional vessel configuration

(b) Countercurrent vessel configuration

(c) Large/small/large vessel configuration

167

Relationships between the Vascular Models

Relative Equilibration Length

	Long	Intermediate	Short
Unidirectional Flow	Heat Sink $a^2 n \bar{\sigma}_d (T_t - T_a)$	Full Unidirectional Model	Directed Perfusion Model
Countercurrent Flow	Heat Sink $a^2 n \sigma_\ell (T_t - (T_a - T_v)/2)$	Full Countercurrent Model	Effective Conductivity Model

168

DISPLAY OF COMPUTER-GENERATED DOSIMETRY DATA: I

Om P. Gandhi
Department of Electrical Engineering
University of Utah
Salt Lake City, Utah 84112

Abstract

With the development of high-efficiency numerical techniques and high-resolution anatomically based models of the human body, it is possible to determine internal electromagnetic fields and SARs for realistic exposure sources under near-field or far-field irradiation conditions. It is important, therefore, to develop computer graphical tools for visualization of the massive amounts of data that are generated. At the meeting, we showed video displays of induced currents for the various sections of the 1.31-cm resolution anatomically based model of the body for exposure to a lower-frequency electromagnetic pulse (0-100 MHz) and a wideband ultrashort pulse with bandwidth on the order of 1-1.5 GHz. For the latter pulse, the $(FD)^2TD$ method was used for calculations of internal fields and induced currents. We also showed a three-dimensional visualization of the new millimeter-resolution model of the human head obtained from the MRI scans of a male volunteer. This model has, to date, been used for calculations of SARs due to a cellular phone planned for a frequency of several GHz.

INTRODUCTION

With the advent of high-efficiency numerical techniques and high-resolution anatomically based models of the human body, it is now possible to determine the coupled electromagnetic fields and specific absorption rates (SARs) for an increasing variety of exposure conditions with a degree of realism that would have been unthinkable just a few years ago. To understand the massive data that is thus generated for the induced EM fields, currents, and SAR distributions, it is necessary to develop computer graphical tools for visualization of the data. For this presentation, we showed video displays of induced currents for the various sections of the 1.31-cm resolution anatomically based model of the human body [1] for exposure to a relatively lower-frequency (0-100 MHz) electromagnetic pulse (EMP) and an ultrawide band pulse (bandwidth on the order of 1-1.5 GHz). Also shown was a three-dimensional visualization of the new millimeter-resolution anatomically based model of the human head [2]. As previously described [2], the resolution for this latter model is 3 mm in the vertical direction and 1.875 mm for the orthogonal axes in the cross-sectional planes.

CURRENTS INDUCED IN THE HUMAN BODY FOR EXPOSURE TO AN EMP

The details of the calculations are given in reference 3. The exact shape of the EMP prescribed to us on a computer diskette and used for the calculations is given in Fig. 1. Only the first 400 ns of the pulse (to the first zero) was used for the calculations to save

1

computation time. We assumed the incident fields to be vertically polarized, since this is generally the situation as the fields are radiated from the EMP simulators. The calculated Fourier spectrum of the prescribed pulse is shown in Fig. 2. Note that most of the energy is at frequencies less than about 100 MHz. For the calculations of the internal E fields and induced currents, we used the finite-difference time-domain (FDTD) method and the frequency-independent properties of the various tissues at a midband frequency of 40 MHz [3]. A 45,024-cell anatomically based model of the human body described in references 1 and 3 was used for the calculations. This model has a resolution of 1.31 cm. The calculated internal electrical fields for the various cells of the model were used to obtain the vertical or z-directed currents for the various layers from the following relationship

$$-I_{k,z}(t) = \delta^2 \sum_{i,j} \left[\sigma(i, j, k,) E_z(i, j, k, t) + \varepsilon_o \varepsilon(i, j, k) \frac{\partial E_z(i, j, k, t)}{\partial t} \right]$$

$$(1)$$

where the summation over i, j means summation for all cells in a given layer k.

The calculated currents for several sections of the body are shown in Figs. 3a-e. The same sections of the body were used for the video displays, and the z-directed currents were shown for each of the cells with reds representing the positive values of currents and blues representing the negative values of currents. The Wavefront Technologies Data Visualizer Version 2, written and developed at the New York Institute of Technology, was used for the visualization. Negligible values of induced currents close to zero were shown by white on the screen. The hue of the color was used to represent the magnitude of the induced currents with deeper reds showing larger positive values and deeper blues showing larger negative values of the induced currents. Because of the sequential color pictures of the induced currents in the time domain, one could see the induced positive and negative cycles of induced currents similar to the diagrams in Figs.3a-e.

CURRENTS INDUCED IN THE HUMAN BODY FOR EXPOSURE TO AN ULTRAWIDEBAND PULSE

Some aspects of this work are discussed in a companion paper [1]. A typical ultrawideband pulse with a peak amplitude of 1.1 V/m as shown in Fig. 4 is assumed for the calculations. The calculated Fourier spectrum of this pulse is shown in Fig. 5. Because of the wide bandwidth, the frequency-dependent FDTD method described in references 1, 4, and 5 is used for the calculations. As in the previous section, a 45,024-cell anatomically based model of the human body is used for the calculations. We assumed the incident fields to be vertically polarized, since this polarization is known to result in the strongest coupling for standing individuals. The induced vertical currents for the various cells (i, j, k) and for the various cross sections of the body, can be calculated from $\partial D_z/\partial t$ as follows:

$$I_z(i, j, k, t) = \delta^2 \frac{\partial D_z(i, j, k, t)}{\partial t}$$

$$(2)$$

2

$$I_{z,k}(t) = \delta^2 \sum_{i,j} \frac{\partial D_z(i, j, k, t)}{\partial t}$$

(3)

where δ is the cell size (= 1.31 cm) and the summation in Eq. 3 is carried out for all cells in a given layer k. Using Eq. 3, the calculated layer currents for a couple of sections of the body (viz, the sections through the eyes and the bladder) have previously been shown in Figs. 5a and 5b of reference 1. Shown in Figs. 6a-e are the calculated currents for the sections through the neck, heart, liver, knees, and ankles.

As for the lower-frequency EMP discussed in the previous section, a video display of the currents induced for the various cells was shown as a function of time for the sections through the eyes, neck, heart, liver, bladder, knees, and ankles. As before, the reds were used to show the positive values and blues were used for the negative values of the induced currents. Because of the rapidly varying induced currents associated with the ultrashort pulse of Fig. 4 (see also Fig. 6), it was found that the currents could be positive for certain regions of a given cross section, say, the front section, while they were negative for the back region, and vice versa, at the same time. The calculations of the layer currents based on Eq. 3 and shown in Figs. 6a-e would, therefore, tend to subtract out negative from the positive values, giving somewhat reduced values than if the magnitudes of the currents had been summed up as a function of time. To correct this situation, we have also calculated layer currents by summing the magnitudes of the currents $\delta^2 \partial D_z/\partial t$ for each of the cells. The currents thus calculated are shown in Figs. 7a and 7b for a couple of representative sections, such as those through the heart and the liver, respectively..

MILLIMETER-RESOLUTION MODEL OF THE HUMAN BODY

Higher-resolution models with cell sizes on the order of millimeters are needed to extend dosimetric calculations to microwave frequencies where the penetration depths are generally less than 1 or 2 cm. They are also needed for nonuniform, at times highly localized, electromagnetic fields encountered in real life (cellular phones and hair dryers to name just two) where the exposed region is of the dimensions on the order of a few centimeters. As discussed in the companion paper [2], we are developing a new anatomically based model of the human body based on magnetic resonance imaging (MRI) scans of a male volunteer of height 176. 4 cm and weight 71 kg. These scans have been taken with a resolution δ_z of 3 mm along the height of the body, and a somewhat finer resolution $\delta_x = \delta_y$ of 1.875 mm for the cross-sectional axes. In developing the new higher-resolution model, we are also distinguishing between the skeletal muscle and internal muscle such as heart, etc., so that anisotropic conductivity of the skeletal muscle, bone, etc. that is important at power-line and other ELF frequencies can be accounted for in dosimetric calculations. To verify the accuracy of the model, we have compared the weights of the various organs and their parts (say, eye balls, eye lens, etc.), and find these to be in reasonable agreement with those for a "reference man" [6].

To date, this millimeter-resolution model has been used for SAR calculations in the human head and neck for electromagnetic fields of a cellular phone planned for a frequency of several GHz. We used the FDTD method for these calculations and modeled not only

3

the head but also the forward-tilted handset of the phone and the radiating antenna. At the meeting, a three-dimensional visualization of the millimeter-resolution model of the head used for these calculations was shown. Because of the high degree of resolution, it is possible to calculate the organ-averaged SARs in the ear, eye lens, sclera, vitreous humor, eye balls, brain, etc.

CONCLUDING REMARKS

Computer graphical tools for visualization of the calculated dosimetric data are likely to play an important role in understanding coupling of the fields to the exposed biological bodies. Of particular help would be the color-coded pictures of internal E fields, induced current densities, and SARs (wherever pertinent), both for 2D sections as well as for 3D representations of the body with or without the superimposed anatomical features for which the dosimetric data are shown.

4

REFERENCES

1. O. P. Gandhi, "Some Recent Applications of FDTD for EM Dosimetry: ELF to Microwave Frequencies," companion paper, this issue.

2. J. N. Lee and O. P. Gandhi, "Models of the Human Body: A Historical Perspective," companion paper, this issue.

3. J. Y. Chen and O. P. Gandhi, "Currents Induced in an Anatomically Based Model of a Human for Exposure to Vertically Polarized Electromagnetic Pulses," *IEEE Transactions on Microwave Theory and Techniques*, Vol. 39 (1), pp. 31-39, 1991.

4. O. P. Gandhi, B. Q. Gao, and J. Y. Chen, "A Frequency-Dependent Finite-Difference Time-Domain Formulation of Induced Current Calculations in Human Beings," *Bioelectromagnetics*, Vol. 13 (6), pp. 543-555, 1992.

5. C. M. Furse, J. Y. Chen, and O. P. Gandhi, "A Frequency-Dependent Finite-Difference Time-Domain Method for Induced Current and SAR Calculations for a Heterogeneous Model of the Human Body," submitted for publication to *IEEE Transactions on Electromagnetic Compatibility*.

6. International Commission on Radiological Protection No. 23, "Report of the Task Group on Reference Man," published by Pergamon Press, Elmsford, New York, 1992.

5
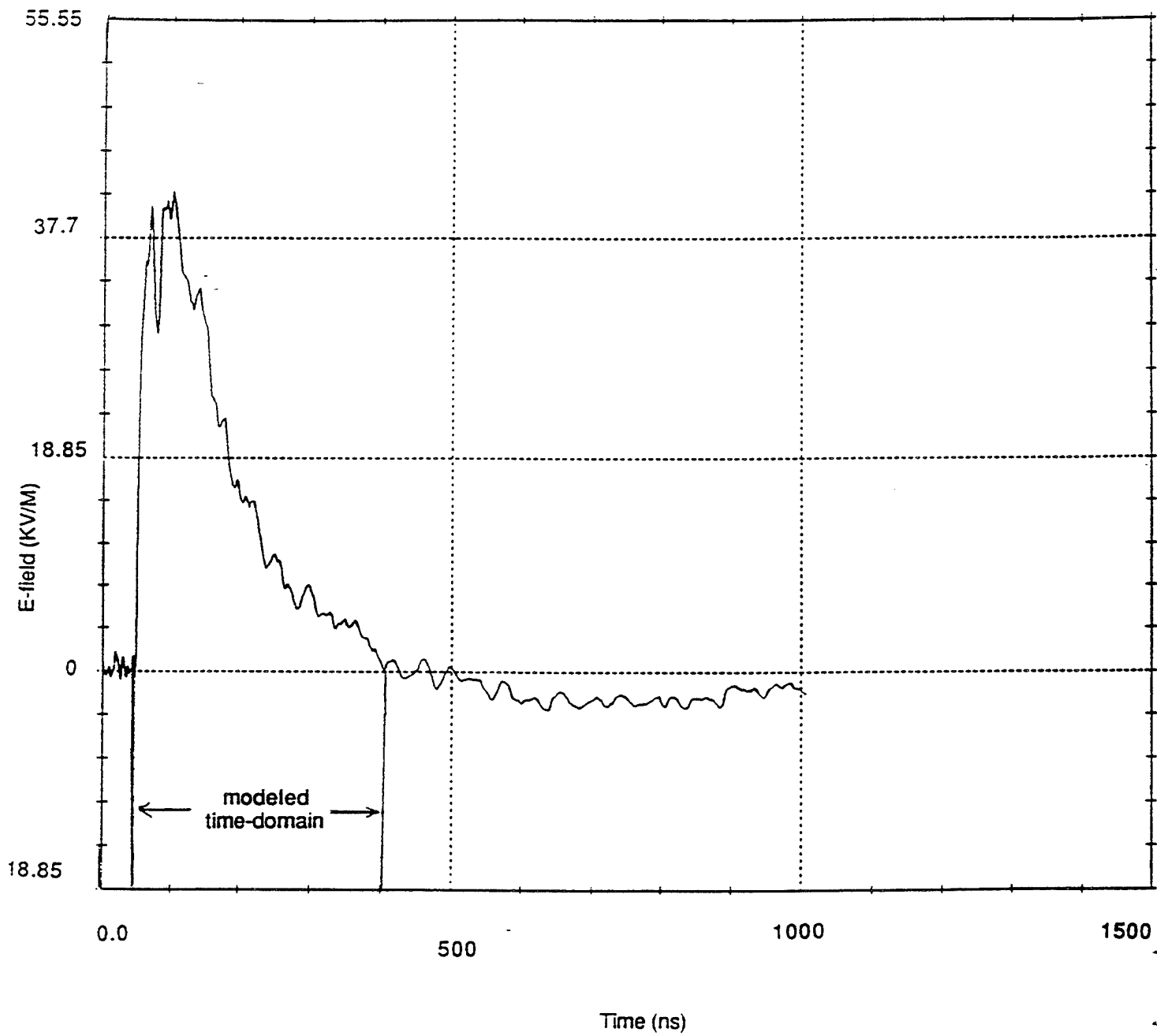
Fig. 1. The prescribed electromagnetic pulse in the time domain. Peak incident field = 41.5 kV/m.

6
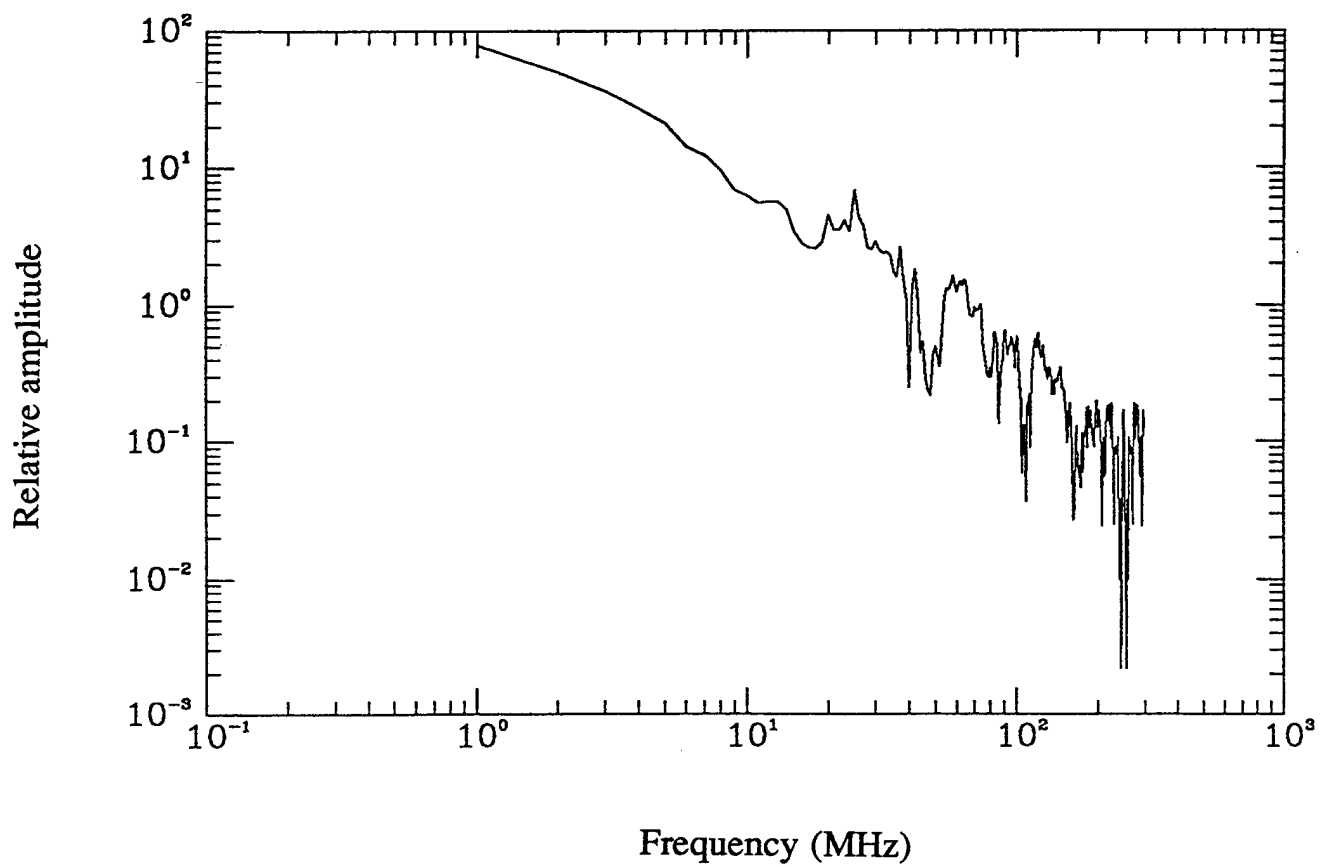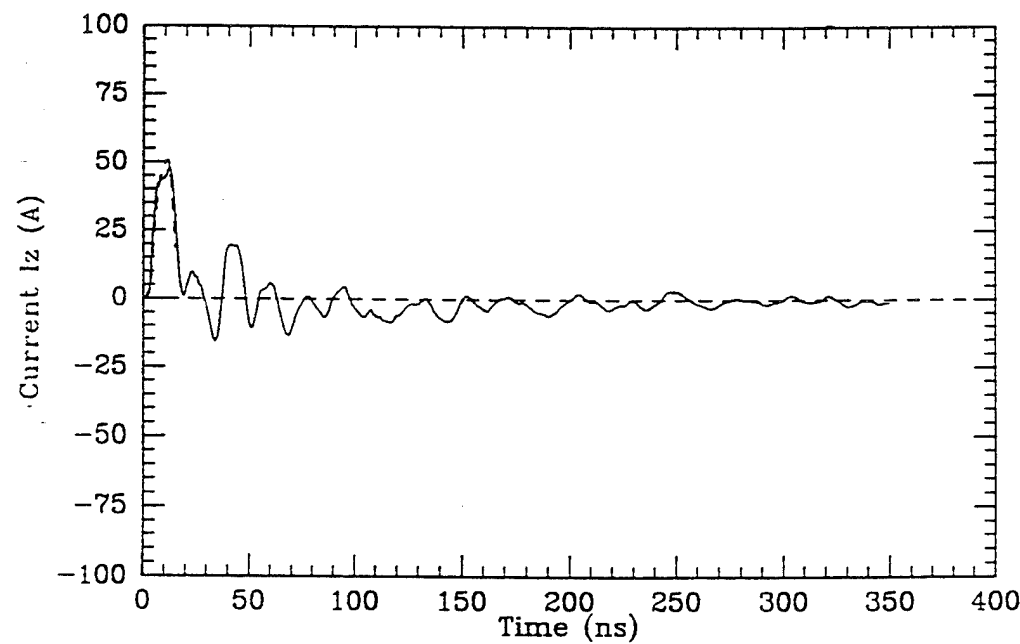
Fig. 2. Fourier spectrum of the EMP of Fig. 1.

a. Current through the neck section.

b. Current for the section through the heart.
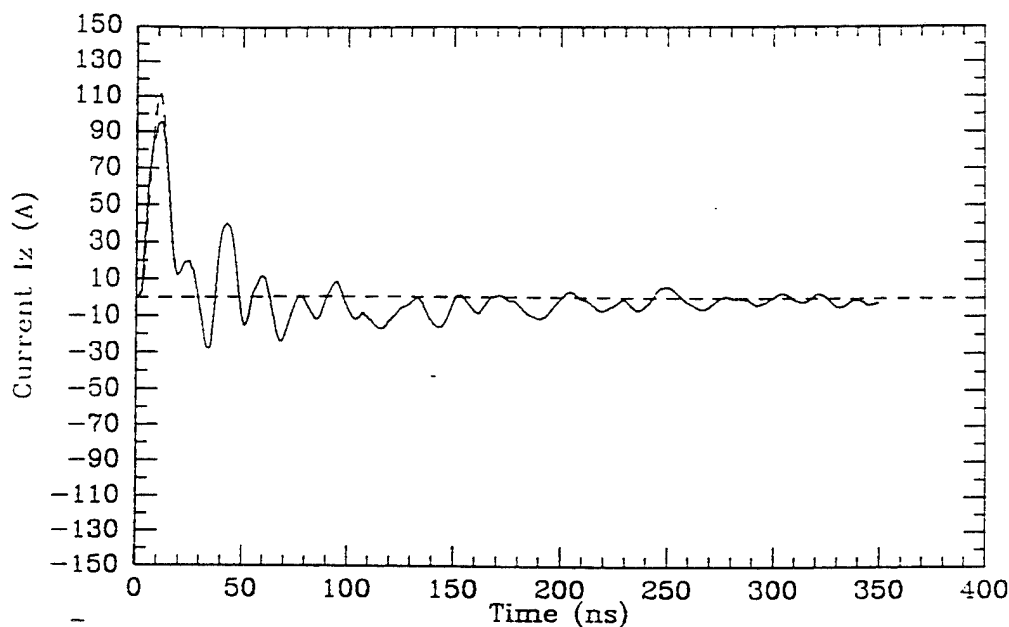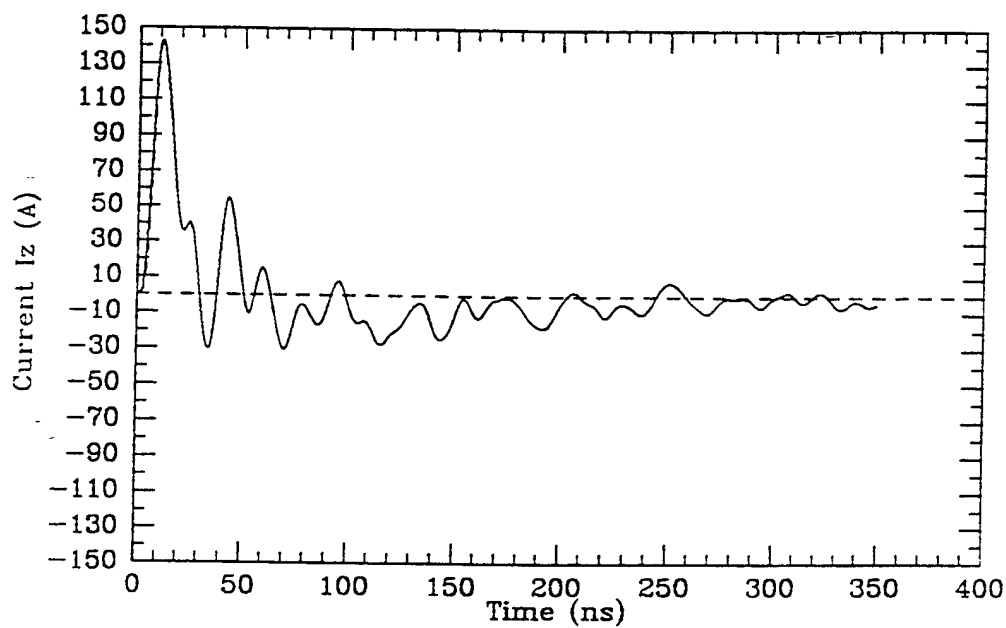
Fig. 3. Currents induced for the various sections of the body for the EMP of Fig. 1. Peak incident field = 41.5 kV/m.

8

c. Current through the knee section.

d. Current through the ankle section.

Fig. 3. (continued).

9
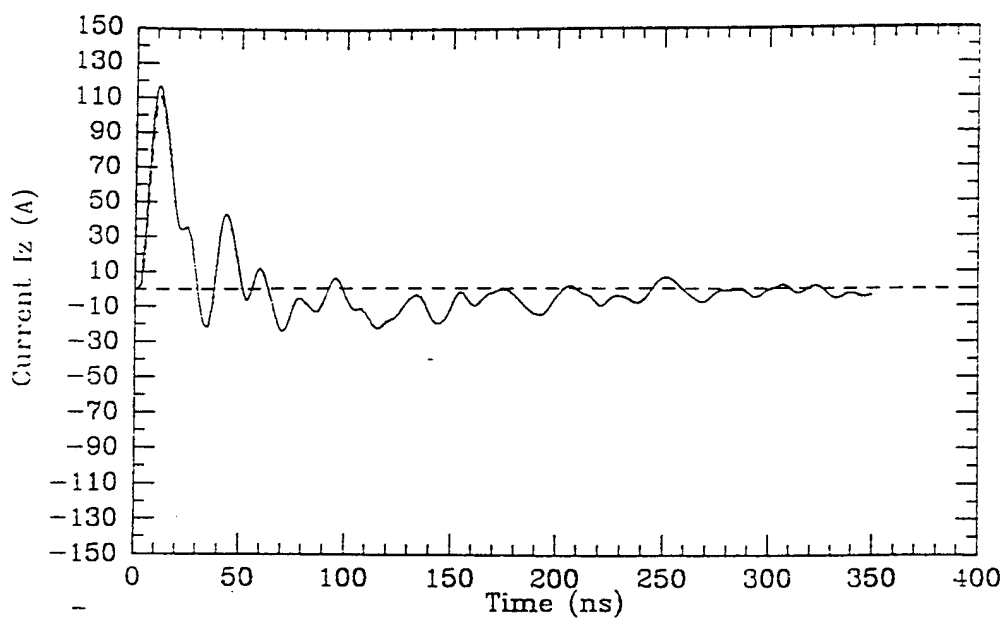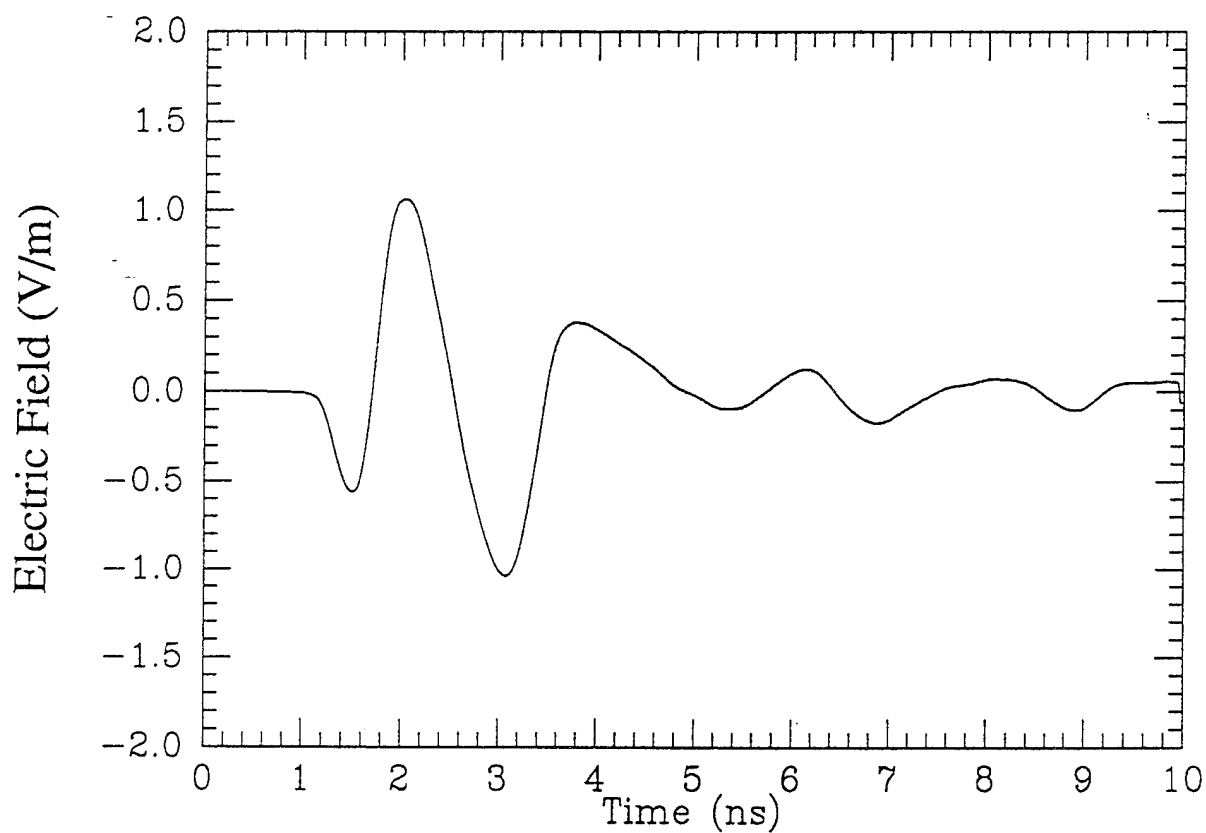
Fig. 4. A typical ultrawideband electromagnetic pulse. Peak incident field = 1.1 V/m.

10
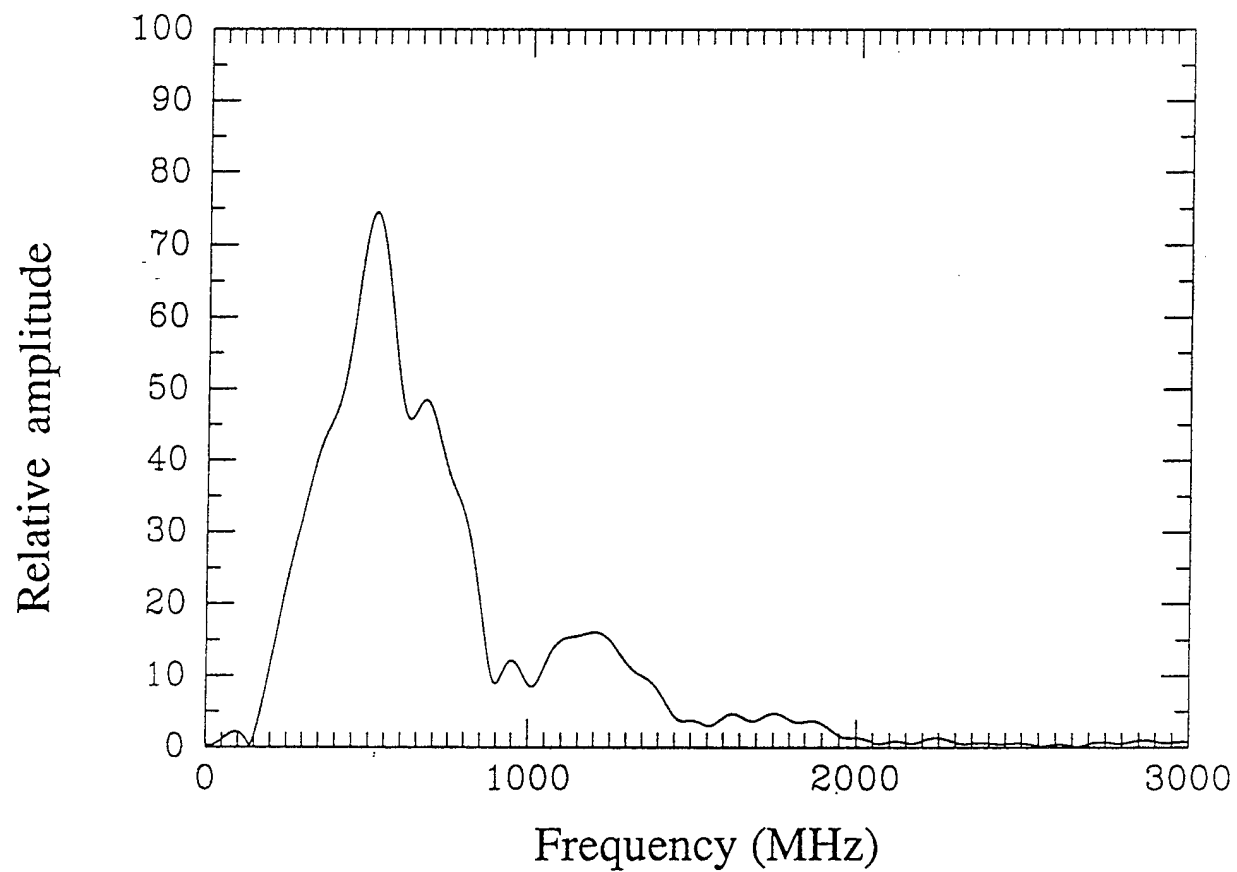
Fig. 5. Fourier spectrum of the ultrawideband electromagnetic pulse of Fig. 4.

11

a. Section through the neck (height above the bottom of the feet = 155.2 cm).
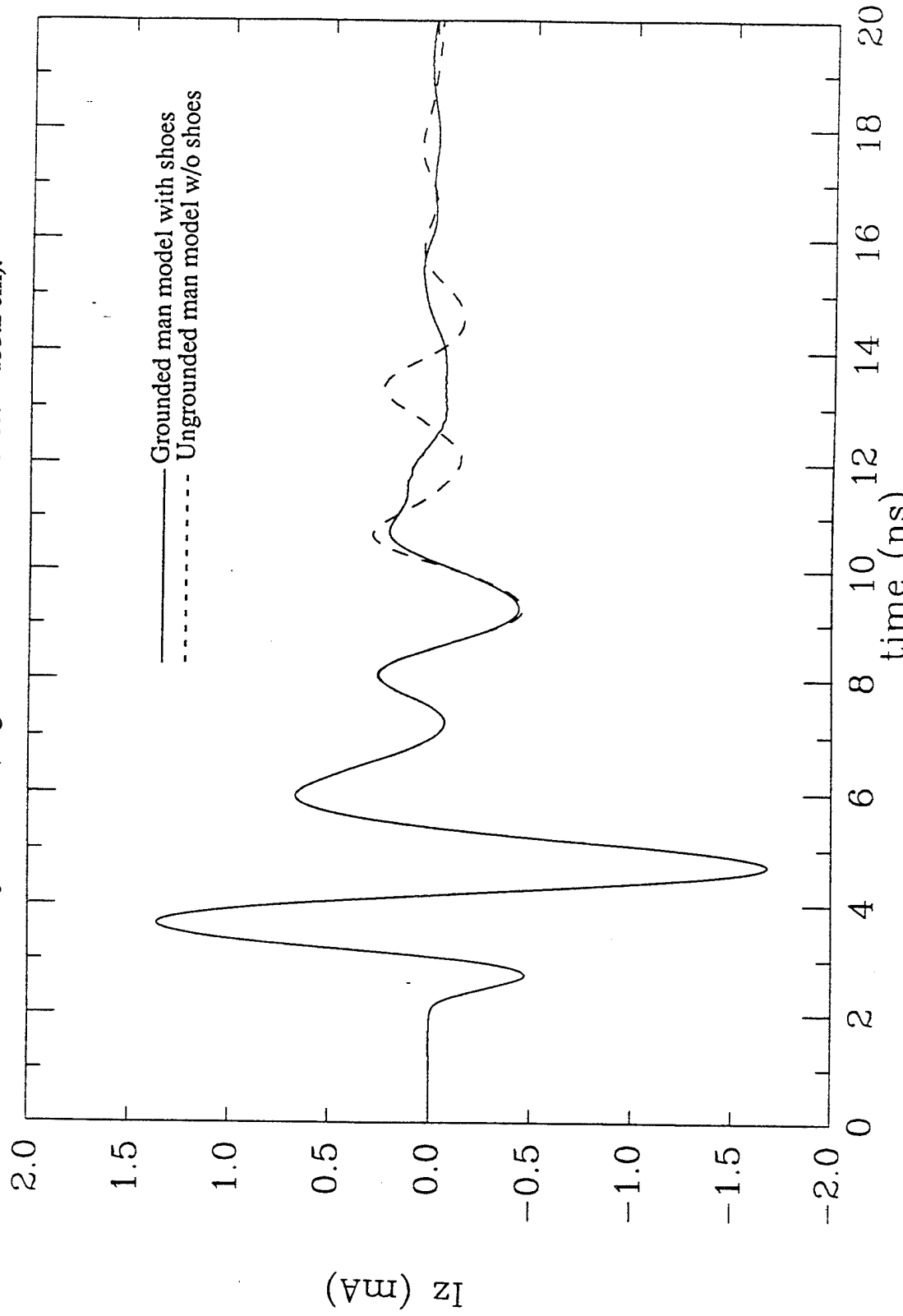
Fig. 6.   Currents induced for the various sections of the body for shoe-wearing grounded and ungrounded conditions of exposure to an ultrawideband pulse of Fig. 4. E_{peak} = 1.1 V/m.

b. Section through the heart (height above the bottom of the feet = 135.6 cm).
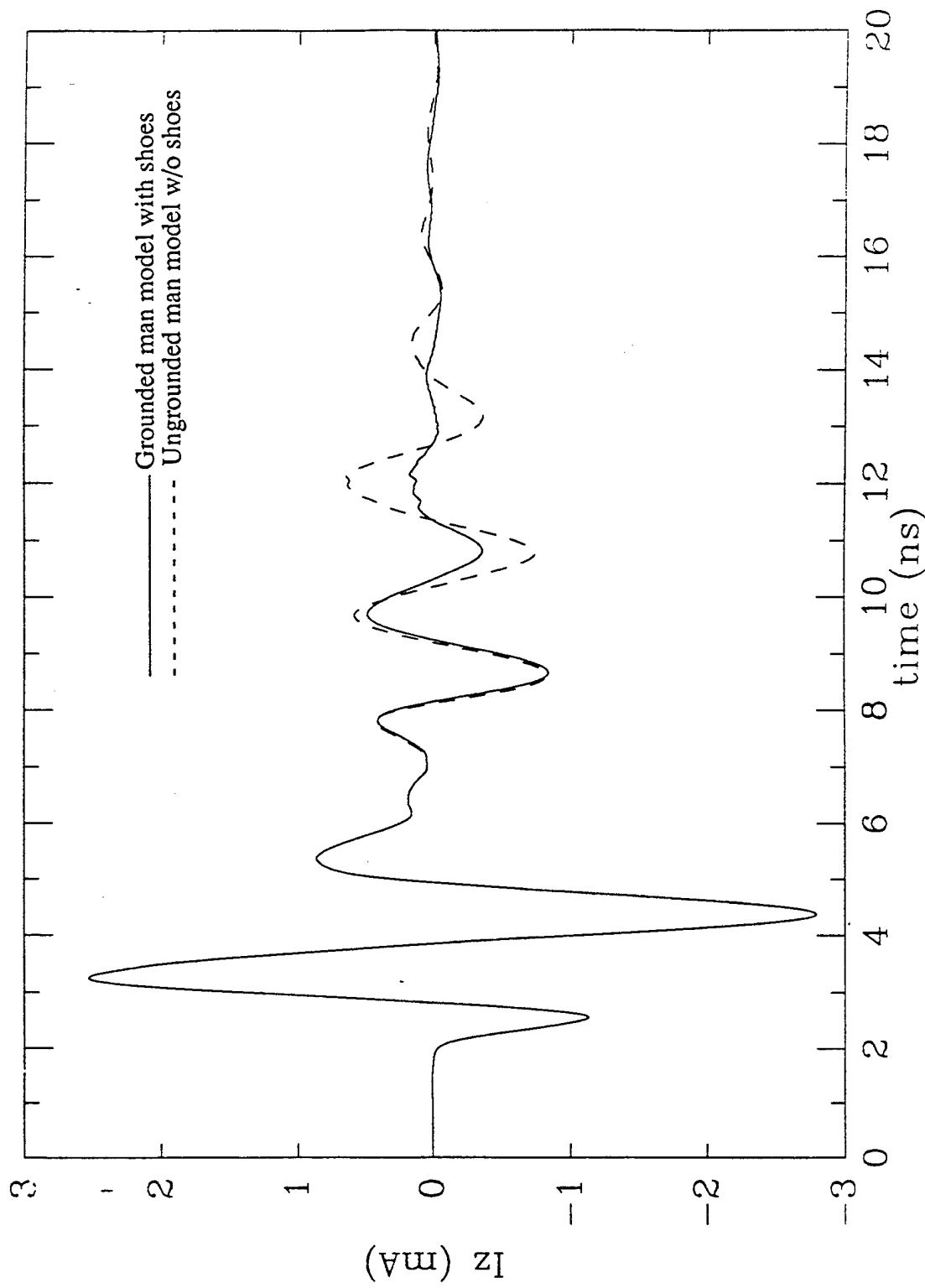
Fig. 6 (continued).

c. Section through the liver (height above the bottom of the feet = 123.8 cm).
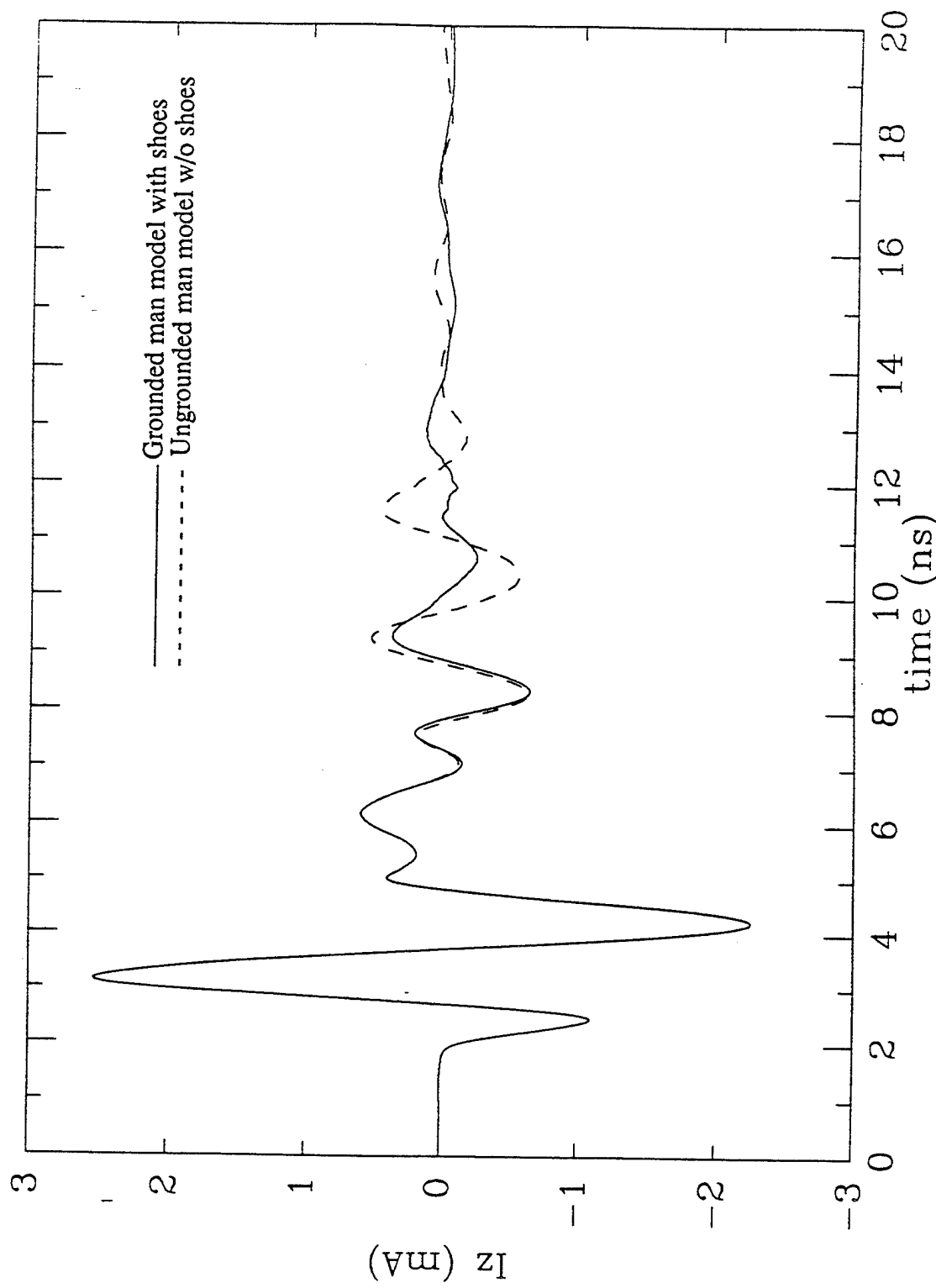
Fig. 6 (continued).

d. Section through the knees (height above the bottom of the feet = 50.4 cm).
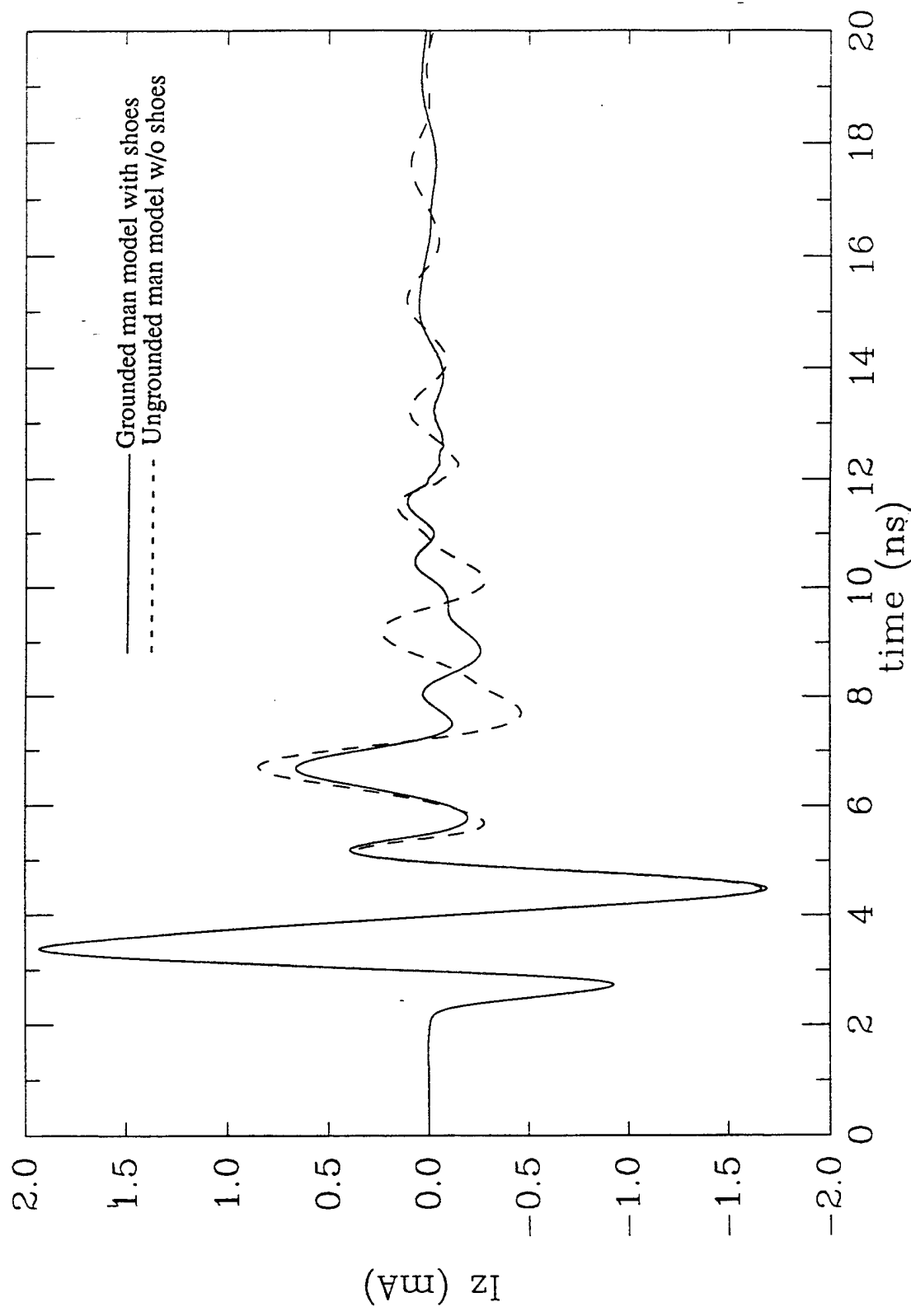
Fig. 6 (continued).

e. Section through the ankles (height above the bottom of the feet = 13.76 cm).
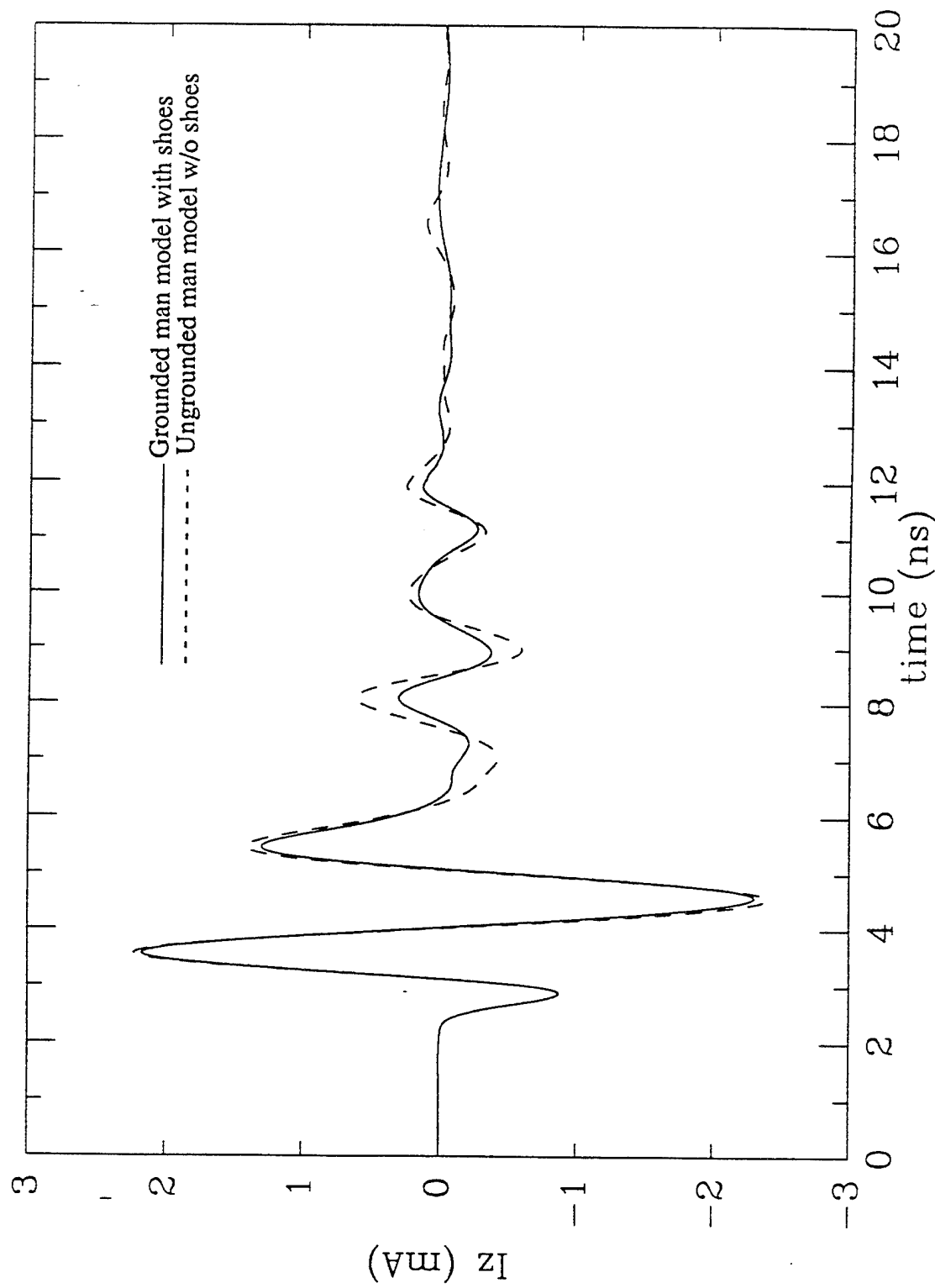
Fig. 6 (continued).

a. Section through the heart.
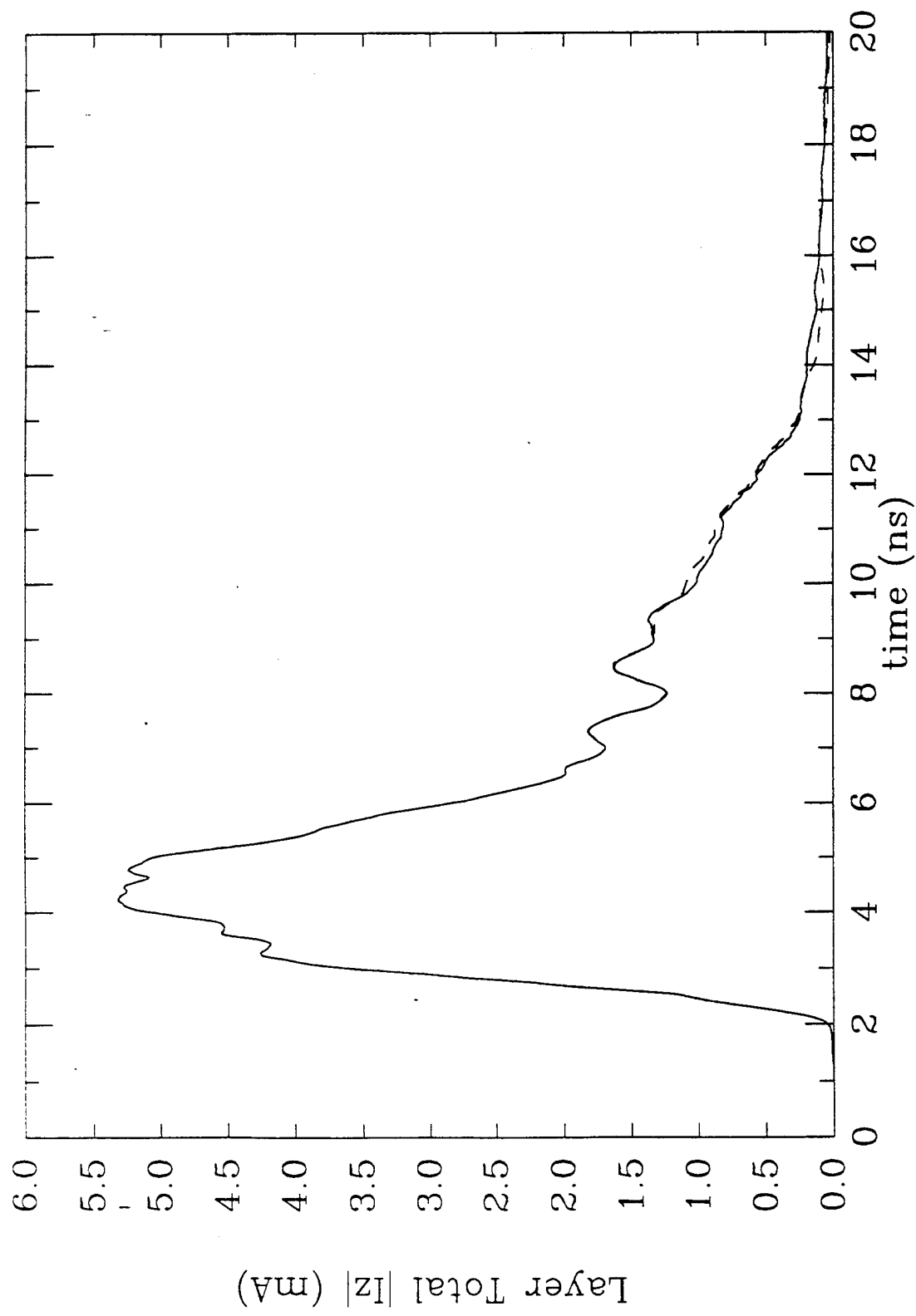
Fig. 7. Sum of the magnitudes of the vertical currents induced in the various cells for a couple of representative sections of the body. The ultrawideband pulse of Fig. 4 was assumed for the calculations. Note that because of the summation of the currents, the magnitudes are larger than those in Figs. 6b and 6c where the existence of simultaneous positive and negative currents for various regions of a given section tended to cancel part of the currents.

b. Section through the liver.
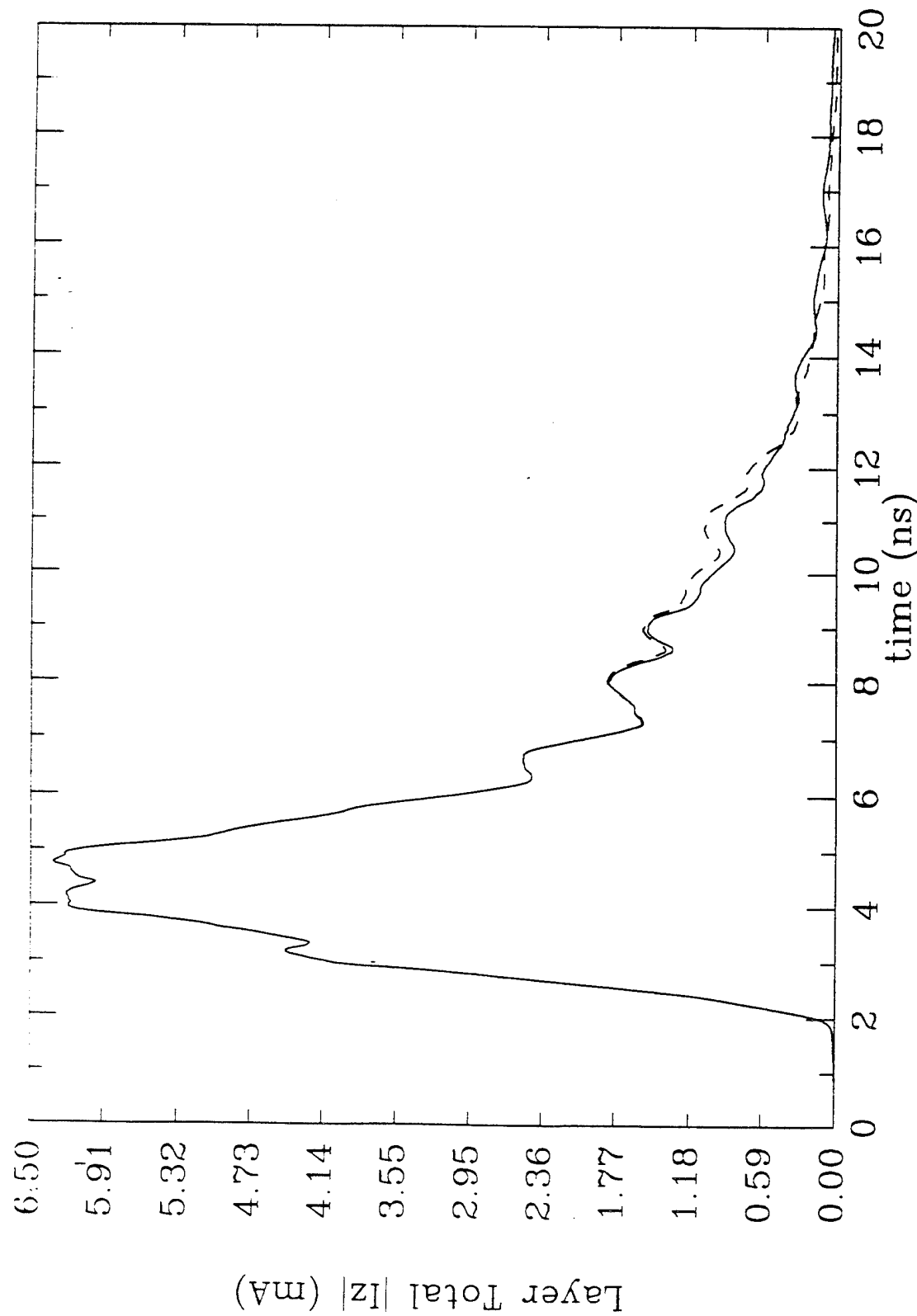
Fig. 7. (continued).

VISUALIZATION AND DISPLAY OF DOSIMETRY DATA

John Peifer, James Toler, and Wesley Shelton _

Bioengineering Center
Georgia Institute of Technology
Atlanta, Georgia 30332

This paper provides an overview of the tasks and considerations that are involved in scientific visualization as related to the display of dosimetry data. A discussion of the tools that are required and the resources that are available for various types of displays is presented. And at the end of the paper, examples of visualization in bioengineering applications illustrate some of the modeling and display capabilities that exist today.

"Visualization" is a frequently used word in the computing world today. While visualization techniques have always been employed by scientists to present research findings, recent advances in computer technology have made it much easier to organize, manipulate, and display large amounts of numeric data. In a broad range of applications, researchers are using computer graphics to display and clarify three-dimensional and temporal information that previously could only be evaluated in 2D plots or as temporal snap shots. The bottom line is that today's graphics capabilities make it easier for people to assimilate complex spatial, temporal, and functional relationships such as the distribution of electromagnetic fields in biological systems.

In any scientific visualization application, the basic steps are very similar. First, the **visualization objective** - that is what we are trying to illustrate - **must be clearly defined**. The next step is to **design the display format** that illustrates the main concept.   In the display design step, the data, geometry, and presentation format are established. This includes selecting the scale and range for the data variables to be displayed. After the format has been designed, the next step is to **process or organize the data** to convert the raw data into a format that the computer understands. This typically involves assigning color and intensity values to scalar and vector data. In addition, data files often must be created with special header information at the beginning of the file which describes the data types and visualization parameters. The final step in the visualization process is to **render the visualization output to a computer display, printer, or video tape**. A variety of rendering algorithms are used in computer graphics: vector or wireframe drawings, simple polygon shading, ray tracing, radiosity, and volume rendering.

Visualization tools can enhance the study of bioeffects and the display of dosimetry data. The **display considerations cover a wide range of choices** for the visualization objective, the display design, and the rendering approach. For example, 3D graphics can be used to display the electromagnetic field distribution in space illustrating the relationship between the radiation source and the exposed body, or graphics can be focused on displaying the internal or in vivo field distributions within the exposed body. Multivariable relationships can be illustrated in simple 2D graphs or with advanced 3D graphics. Computer animation provides a very effective means for displaying the temporal relationships associated with body motion, heat flow, or dynamic field variations. Anatomical geometry and composition are important factors in evaluating radiation bioeffects. Field induced interactions or alterations can be displayed at a macro level in which such variables as total body temperature is considered or at the micro level in which such factors as physiology, vascular cooling, and cellular effects are studied.

Traditional 2D and 3D graphs illustrating multivariable relationships will continue to play a role in evaluating dosimetry data, but these standard tools can be significantly augmented by many new 3D visualization techniques. Color maps of temperature and field distributions can be generated for 2D cross sections or mapped onto 3D surfaces or volumes. 3D "ribbon" displays that have been used to present meteorological data provide an effective way to illustrate field lines

or thermal flow. Another method for displaying field or thermal flow information is to use 3D vector displays in which a collection of small arrays are drawn pointing in the direction of the vector field, and the color or size of each arrow is associated with the local field intensity (or any other scalar value of interest). 2D and 3D iso-contour maps and intensity profiles are often useful for evaluating flow patterns in both static and dynamic conditions. Anatomical cross sections based upon tomographic medical images provide information describing geometry, physiology, and dielectric properties. Both predicted and measured dosimetry data can be effectively mapped back into these anatomical cross sections. 3D geometric modeling of exposed biological systems can be based upon these medical images or created as generic anatomies. Temporal relationships are often best illustrated by animation tools. Animation can be as simple as showing the time variations of a 2D plot or as complex as showing the temporal fluctuations in temperature distribution as the various layers of the body are peeled away. Many flow visualization techniques employed for computational fluid dynamic studies are closely related to bioeffects studies. Computational grids and flow results can be used to study the complex relationships between anatomy, field and thermal distributions, and blood flow. And finally, it is often useful to combine several of these graphics techniques to produce a more complete picture.

Many powerful visualization tools are available today for a variety of budgets. Basic components for a complete visualization workstation include the hardware, software, anatomical models, and data. Computer technology continues to rapidly improve as the price-to-performance ratio drops. Thus, it is important to evaluate the capabilities of top of the line systems as well as the systems that are affordable today. Within a few years, the prohibitively expensive techniques of 1992 may become standard options on the commodity workstations of 1996. The software selection is just as important as the selection of the hardware, and unfortunately, the prices for special purpose application software have not fallen as fast as the hardware prices. In fact, it is not unusual to pay almost as much as the price of the system for a single application package. SUN, SGI, HP, and IBM all offer good workstations for around $10,000; however, some of the top data visualization and modeling packages cost much more than $10,000. Under these conditions, it is better to first identify the software that satisfies the application requirements, and then purchase the system that best supports the software.

Visualization hardware consists of a variety of components. The CPU controls the operation of the system and provides a platform for running application programs and software development. For many visualization systems, however, performance is significantly enhanced by special graphics acceleration boards. These add-on boards can provide additional graphics memory that improve pixel and color resolution and hardware transformations that dramatically speed up 3D translations and rotations. Another component that is becoming increasingly important is the communications hardware that provides high speed data transfer supporting distributed processing and remote access. Visualization projects often demand massive storage capacities to handle high resolution color image files. Magnetic tape storage remains a popular method for storing data, but many mass storage users are now switching to optical and magnetic disk based systems that provide faster access times. Output options for the visualization system include CRT display monitors, printers, and film and video recorders. High resolution color monitors often come as standard equipment today, but color printers, film, and video options are almost always add-on items.

Software components for a visualization system include the underlying operating system, programming languages and development tools, and various special-purpose application graphics packages. The operating system and development tools are of primary importance when creating or customizing a visualization application. Real time performance may be improved or limited depending upon the development tools and operating system options. Today powerful visualization tools can be purchased off-the-shelf that generate many standard 2D and 3D displays. The best choice depends upon the visualization objective, and there is a good selection to choose from in each category. Software tools can be grouped into the following categories: 1). data

analysis, plotting and display packages, 2.) volume rendering tools, 3.) geometric modeling programs, and 4.) advanced 3D modeling and choreography

Data analysis, plotting and image display packages provide tools for importing 2D and 3D numeric data and creating charts, graphs, and displays through a menu of options. Data analysis examples are:

PV Wave by Precision Visuals,
Application Visualization System (AVS) from Stardent,
IDL (Interactive Data analysis Language) by Research Systems, Inc, and
Public domain tools: NIH Image, NCSA's XImage and XDataSlice.

Volume rendering tools are sometimes included in the data analysis packages, but I have listed it separately because volume rendering demands a much higher level of system performance. Volume rendering tools operate on a volume of data and provide tools to view the volume from different orientations, to slice through the volume with arbitrary cutting planes, to generate 3D iso-surfaces by thresholding, and to create semitransparent displays of the 3D data volume. Some of the more powerful data analysis and volume rendering packages include:

Voxelview by Vital images,
Data Visualizer by Wavefront Technologies,
SUN Vision from Sun Microsystems, and
Analyze by the Mayo Clinic

Geometric modeling programs also provide tools for displaying 3D information, but these modeling tools operate on geometric models constructed from simple geometric primitives that have been extracted from the data. Some 3D modeling tools are now available on PC workstations, and one of the better modeling products is Studio 3D from the makers of Auto Cad.

Advanced 3D packages provide more sophisticated modeling, rendering, and choreography or animation capabilities. The high end systems provide sophisticated special effects such as 3D textures, advanced lighting and reflection models, deformable geometry, and inverse kinematics. The major competitors are Wavefront Technologies, Thomson Digital Image, SoftImage, and Alias Research, and the products range from $10K to $100K.

Anatomical models must be considered as another component for a dosimetry data display system. Accurate anatomical models take a long time to build, and it is important to factor this component into any consideration of a new dosimetry visualization system. No complete model of any biological system exists today; however there are a variety of resources available that can provide partial models. Viewpoint is one commercial source that sells 3D geometric models for all types of applications. These models are generally limited to a 3D mesh of polygons that describe surface. A new product called A.D.A.M (for Animated Dissection of Anatomy for Medicine) offers an impressive interactive 2D medical atlas that includes many layers of detail. A modification of their approach could be used to display dosimetry data throughout the anatomy. At the University of Hamburg, Karl Heinz Hohne is creating a detailed 3D atlas of human anatomy from medical images and illustrations. His model will include a large amount of detail, but it will require powerful graphics hardware to achieve practical levels of interactive performance. From the Visible Human Project, the Air Force has collected large amounts of anthropometric data in 3D format that may be very useful for RFR bioeffects studies and dosimetry data visualization. And, not to be overlooked, there is a growing database of 3D models that is available in the public domain for free or for nominal handling charge. Available anatomical models should be utilized whenever possible.

The final component in the dosimetry display system is the most obvious - dosimetry data.

Over the years, the Air Force has assembled a large database of measured and simulated dosimetry data. This resource should ideally be converted to a standard digital format - perhaps on compact disk - that can be easily distributed and readily accessed by a variety of visualization workstations. A standard data organization and numeric format will accelerate the interpretation and evaluation of past, present, and future dosimetry data.

At Georgia Tech many researchers are actively involved in various aspects of scientific visualization, electromagnetics, and bioeffects studies. Computer processing and specialized graphics hardware resources are shared through a collaboration of interdisciplinary researchers devoted to advanced computer visualization. Modeling, analysis and visualization software products are also shared resources, and Georgia Tech serves as test site for many of the advanced visualization products developed by companies such as Silicon Graphics, Digital Equipment, IBM, Wavefront Technologies, and Thomson Digital Image. A high speed, fiber optic network connecting all Georgia Tech facilities significantly increases the accessibility of resources and is often used to distribute CPU-intensive processing tasks. Visualization resource centers can be established in many different ways, but interdisciplinary collaboration and sharing of resources provides the best organization for advancing the visualization objectives. Visualization techniques applied on selective bioengineering studies at Georgia Tech illustrate some of the visualization ideas that are discussed above. A video tape of these visualization examples was presented at the RFR Dosemitry Workshop at San Antonio in December 1992.

1. A unified approach to cardiac imagery

In this study, information is combined from two different cardiac imaging modalities - x-ray angiography and nuclear perfusion studies - to produce a new 3D representation that more clearly displays and quantifies the relationship between defects in the coronary arteries and blood supply to the heart muscle. This arterial model is created from a pair of planar X-ray angiograms. Tomographic nuclear studies display blood supply to heart muscle, and a computer animation shows the 3D unified model from an animal experiment in which a defect was created by blocking an artery. Similar vascular models may be very useful in evaluating heat dissipation in biological systems, and the same techniques for mapping blood perfusion values onto the heart model can be applied to dosimetry data in other parts of the anatomy.

2. Computer modeling of the abdominal aorta from MR images

In another 3D vascular modeling project, the coronary artery modeling tools have been extended to model the abdominal aorta from a pair of magnetic resonance images. Although MR angiography is still not capable of resolving details in small vessels, the resolution is adequate for large vessels. The geometric model of the aorta can be displayed from any orientation and superimposed on other images to display the relationship of the vasculature to the surrounding anatomy. Combining anatomical models with cross sectional images can clarify the 3D geometry while displaying the 2D image details.

3. Multimodality modeling of AVMs in the brain

On another project , we have explored methods to improve surgery planning for arteriovenous malformations (AVMs) of the brain. The video shows an example of volume rendering using magnetic resonance images from a patient with an AVM. The volume has been sliced to display the AVM in relation to the surrounding anatomy, and rendered using Analyze volume rendering software from the Mayo Clinic.

4. Magnetic resonance flow visualization

On this study, the goal is to evaluate the time varying hemodynamic flow patterns through

the abdominal aorta using in vivo MR velocity measurements. Studies suggest that there is a relationship between atherosclerosis and flow, but without visualization tools it is difficult to interpret the MR velocity images. This visualization combines 2D and 3D computer animation. The 2D waveform in the lower left represents time varying flow volume over the cardiac cycle, and the corresponding 3D velocity profiles in the main portion of the display represent the point by point velocity measurements from a cross section of the abdominal aorta just below the renal arteries. A transparent green plate is inserted at the zero velocity level to highlight reverse flow conditions.

5.   Aortic arch mapping

This project uses texture mapping and model deformation tools to represent plaque formation along the interior walls of the aortic arch. Investigations have shown that atherosclerotic plaque tends to form at specific sites along the arch of the aorta. Autopsy studies have produced statistical 2D color maps that display the distribution of the most common plaque formation sites. At Georgia Tech, we are interested in the correlation between these sites and the local hemodynamic flow conditions. Using texture mapping and model deformation tools, the autopsy results are mapped back into a 3D computer model that can be used to perform the computational hemodynamic studies. The 3D aortic arch model is created by deforming the 2D plaque distribution into a tube and then bending the tube into an arch.

6.   Modeling of aortic aneurysms for surgical planning

This project demonstrates a 3D visualization approach for improving surgery planning for aortic aneurysms by creating a 3D display combining geometric models and single-slice magnetic resonance (MR) images. The aneurysm model is created by extracting the geometry of the aorta from tomographic images. This model is then combined with image slices showing the surrounding anatomy at the maximum extent of the aneurysm in the bottom slice and above the neck of the aneurysm in the top slice. This presentation is of particular interest to the surgeon as it is critical to locate the "neck" of the aneurysm in relation to the renal arteries and veins. The outer wall of the aneurysm is modeled in a semi-transparent blue so that it is possible to see the diameter of the patent portion of the aorta through which the blood still flows.

7.   Propulsed endoscope

Computer animation demonstrates the geometry and function of a new self-propelled endoscope for evaluating intestinal ulcers and cancer. The experimental device moves by selectively inflating and deflating the front, middle, and rear sections. The animation is created by interpolating between a collection of 3D geometric models at different stages in the cycle of inflation and deflation. Some of the latest modeling techniques for deformable geometry and inverse kinematics may simplify this type of animation. In another animation, the outer layers of the endoscope are peeled away to reveal the inner components. Reflection mapping is used to produce the metallic appearance of the end components.

8.   Eye surgery simulation

In a collaboration with the Medical College of Georgia, we are developing a computer based simulation for training eye surgeons. The approach is to display a realistic computer model of the eye that can be manipulated by simulated medical instruments. Photographic images of the eye have been texture mapped onto simple geometric models of the various component in the eye. The position and orientation of the scalpel is controlled by a Polhemus 3D digitizing device. A simple incision is simulated by drawing on the surface of eye when the scalpel tip makes contact. Another example shows experimental deformation of the eye when pushed by an instrument. A high performance Silicon Graphics VGX workstation provides the computing power to manipulate

the 3D models in real time.

9.   Olympics, motion analysis, and other multimedia projects

Georgia Tech's Multimedia Lab grew out of the Olympics project. An extended team of computer scientists, engineers, and graphics experts combined to create the interactive presentation that demonstrated Atlanta's proposed facilities to the International Olympics Committee. The resources and experience from the Olympics project have since been directed into a wide variety of interdisciplinary projects including medical imaging, surgical planning, and scientific visualization. An early contribution to the Olympics project was a three-dimensional computer model of a "golden athlete" that includes a highly detailed 3D model of anatomy and natural human motion. Projected Olympic facilities and stadium were created from a 3D data base of geometric specifications from a local architectural firm. The multimedia Lab is now working on developing a faster and cheaper method for digitizing 3D objects. A 3D model of Ga Tech's President Cresine has been created using this new digitizer. During the scanning procedure, 2D profiles are stored as the object is rotated, and the post processing 3D reconstruction produces the complete 3D geometry. The multimedia lab is also developing a motion analysis capability for sports, medical, and rehabilitation applications. The system can playback recorded human motions from any perspective and produce a wide variety of motions parameters that can be evaluated. Motion data are collected by a computer controlled set video cameras that track motion sensors attached to the anatomy. Interactive tools allow great flexibility in displaying and evaluating the results. Both the 3D digitizer and the motion analysis technologies could be useful in creating models for dosimetry and bioeffects studies.

10. Distribution of electromagnetic fields in biological systems

We have also created a few 3D modeling examples displaying field distributions related to radiation bioeffects studies. In this first example we display the temperature distribution for a homogeneous sphere exposed to electromagnetic radiation. The analytic solution is incorporated in a program that computes field values for any point in a sphere. A 3D geometric model of the sphere is created from polygonal elements with color values, corresponding to temperature, assigned to every vertex.

Changes in polarization and frequency affect the field distribution within the exposed body, and different models can be created for changes in polarization and frequency to illustrate these effects. In this animation, the model on the left represents a slice through the volume in the E-field plane, and the model on the right represents a slice through the volume in the H-field plane. The color distribution changes as the frequency is varied from 500 MHz to 100 MHz.

The field distribution within the volume can be displayed by cutting or slicing away portions of the surface. In this animated sequence, the spherical volume is divided into sections that are slid apart and rotated to show the temperature distribution at different locations within the volume. The slices are modeled by polygonal elements with color values corresponding to temperature computed at every vertex.

Also using Wavefront modeling software, a simple geometric model of Chatterjee and Ghandi's block man was created. The geometry of the block man is scanned in from the figure published in the RFR Dosimetry Handbook (3rd Edition), and the SAR values are mapped into a color for each block in the model. A simple color scale maps lower SAR values into blue and increasing values into red, yellow and white. The animation of the block man is choreographed to display the 3D SAR distribution as the block man is rotated and the leg of the block man is raised and lowered to demonstrate very simple body motion. Here the SAR values do not change as the leg is rotated, but in reality, body position and motion do affect the field and temperature distributions. In another example, the three layers comprising this simple block man are peeled

away revealing the SAR distributions in each layer.

A final example with the block man illustrates a dynamic color change that could have resulted from changes in the field properties. This type of animated display communicates the field distribution changes much more effectively than can be accomplished by reading through tables of data.
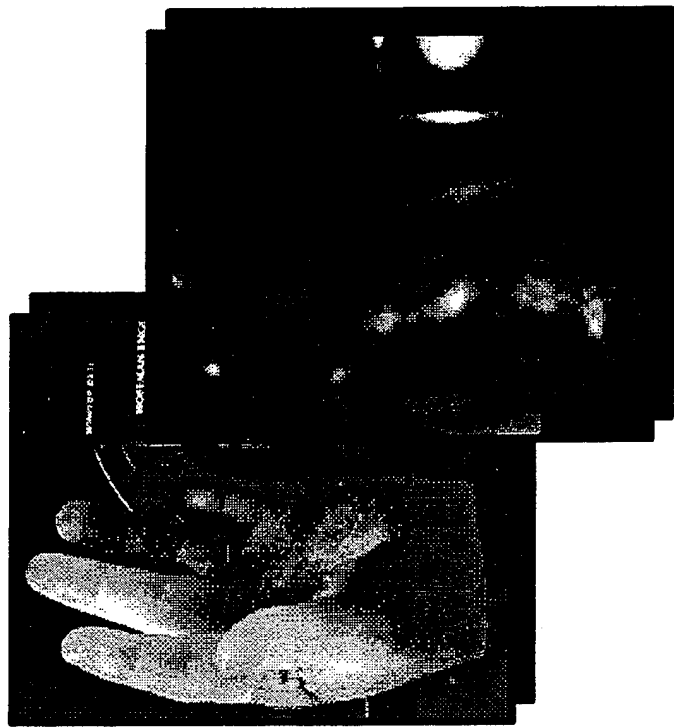
The Wavefront Technologies software tools on a Silicone Graphics workstation are used to define and render these animated sequences. Wavefront's Choreography tool defines the animation sequence and Wavefront's Image renders the images to disk. After the rendering is completed, the image sequences are transferred to the Abekas digital video image storage device for high speed playback. The animated visualization can be directly displayed in real time from the Abekas, and video tapes in 1/2 inch standard VHS, 3/4 inch Sony U-matic, or 1 inch broadcast quality formats can be can be produced.

SUMMARY

New visualization tools can significantly enhance the examination and interpretation of dosimetry data, and many new avenues of investigation will open up as detailed anatomical models and advanced display techniques are employed.

QUANTITATIVE LUMINESCENCE IMAGING SYSTEM
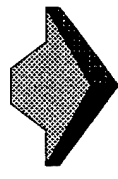
CR Batishko

KA Stahl
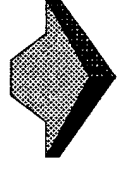
BA Fecht

US DOE/Pacific Northwest Lab
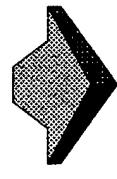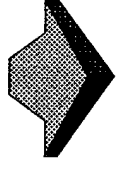
RF ➡ ORGANISMS+DALM ➡ VISUAL SPECTRUM LIGHT ➡ DISTRIBUTION DETECTION ➡ ANALYSIS

IMAGE DETECTION...
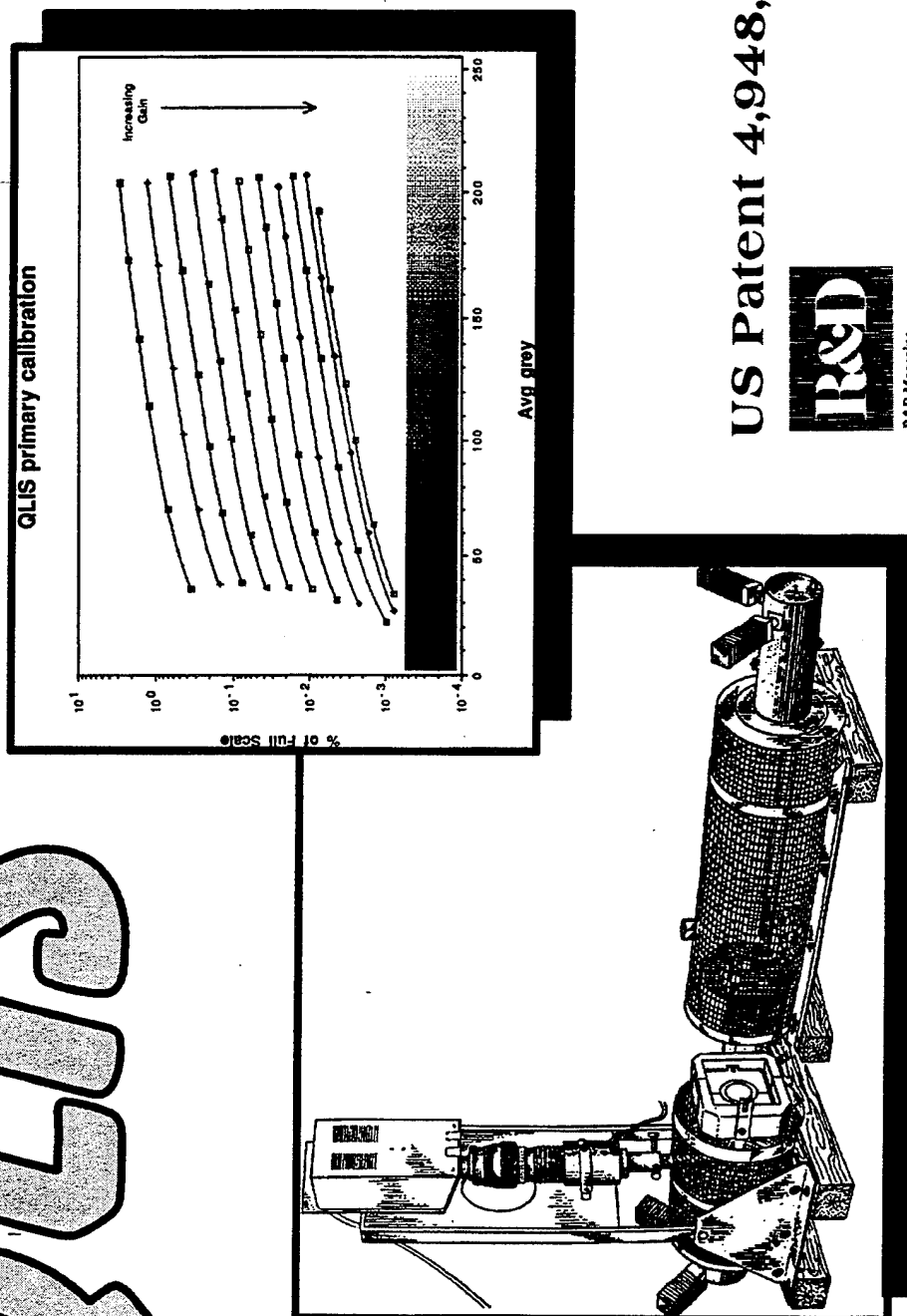
	INTENSIFIED VIDEO:	COOLED, SLOW SCAN, CCD:	RESISTIVE ANODE ENCODER:
COST	$10k-25k	$15k-50k	>$75k
SENSITIVITY	mid	mid-high	high
DYNAMIC RANGE	10-7	10-9	<10-9
IMAGE FILE FORMAT	8-bits	12-16 bits	unlimited?
COMPATIBILITY	standard	special	special
FRAME RATE	video	integrated	integrated
MATURITY	off-the-shelf	state-of-art	moderate

QLIS primary calibration

US Patent 4,948,975

R&D Magazine
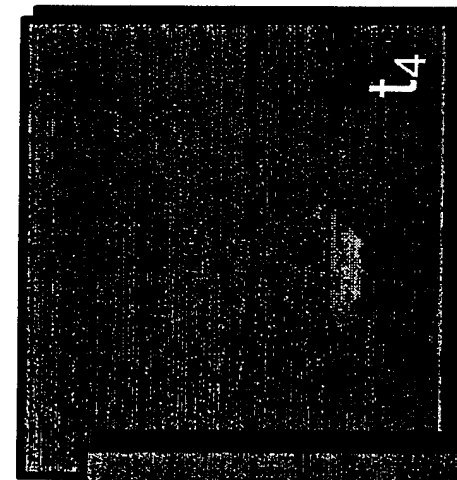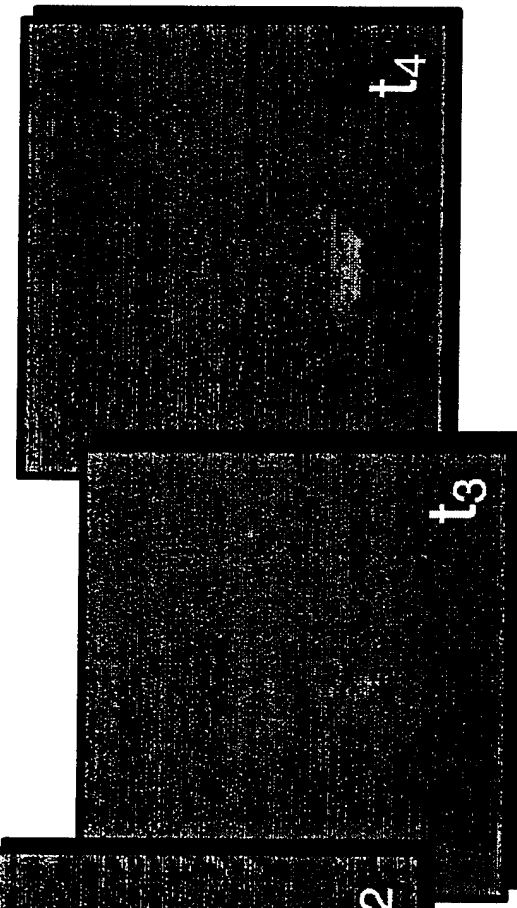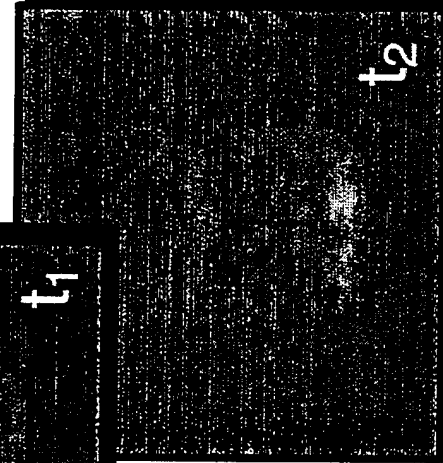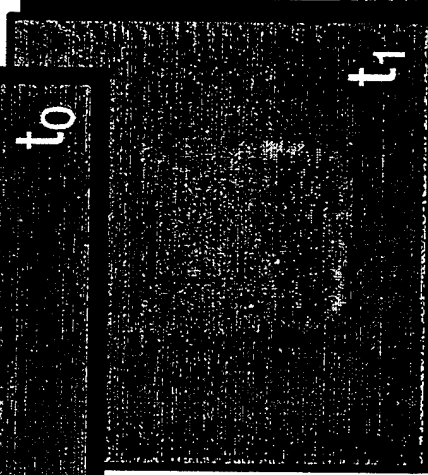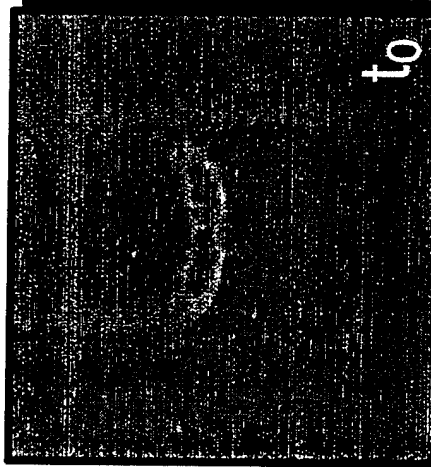
crb/EOS/11.10.92
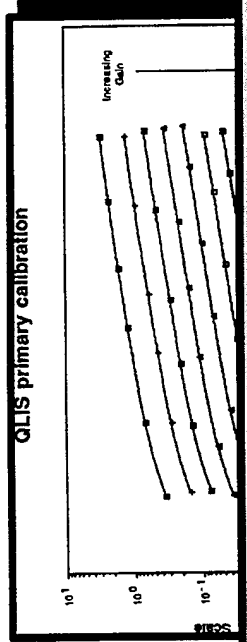
CHEMILUMINESCENCE
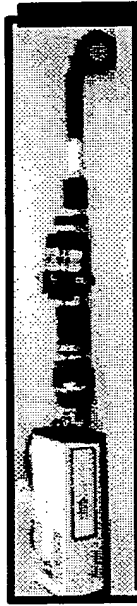
(LUMINOL IN DMSO, IN 1 CM X 1 CM CUVETTE, ACTIVATED WITH SODIUM HYDROXIDE)

SELECTED FRAMES FROM VIDEO RATE RECORD

crb/EOS/11.9.92

QLIS

8 BIT DETECTION...

results 2×10^5 **PHOTONS/SEC/CM^2**

QLIS primary calibration

Increasing Gain

Avg grey

calibration curve relates gray value (0-255), gain and RELATIVE brightness

normalize for camera spectral response and sample emission spectrum

$$\eta_c \cdot \frac{\int_{\lambda_1}^{\lambda_2} Q(\lambda)c(\lambda)\,d\lambda}{\int_\lambda c(\lambda)\,d\lambda} \qquad \eta_s \cdot \frac{\int_{\lambda_1}^{\lambda_2} Q(\lambda)s(\lambda)\,d\lambda}{\int s(\lambda)\,d\lambda}$$

RADIANCE equation:
$$L = [V_s\, S(V_s, g_s)\, \eta_s\, L_c] / [V_c\, S(V_c, g_c)\, \eta_s]$$

SOLID ANGLE equation:
$$\Omega = 4\pi \sin^2\!\left[\tfrac{1}{2}(\sin^{-1} N.A.)\right]$$

RADIANT FLUX equation:
$$P = LAn\Omega$$

PHOTONS/SECOND equation:
$$N_{ph}(\lambda) = F(\lambda)P/E_p(\lambda)$$

where...
$$F(\lambda) = \frac{\int_{\lambda_1}^{\lambda+10} S(\lambda)\,d\lambda}{\int_{\lambda_1}^{\lambda_2} S(\lambda)\,d\lambda}$$

QLIS

entrance face of fiberoptic image conduit

microchannel plate intensifier

fiberoptic reducer

transfer lens

vidicon-type video camera

fiberoptic housing/coupler

fiberoptic image conduit
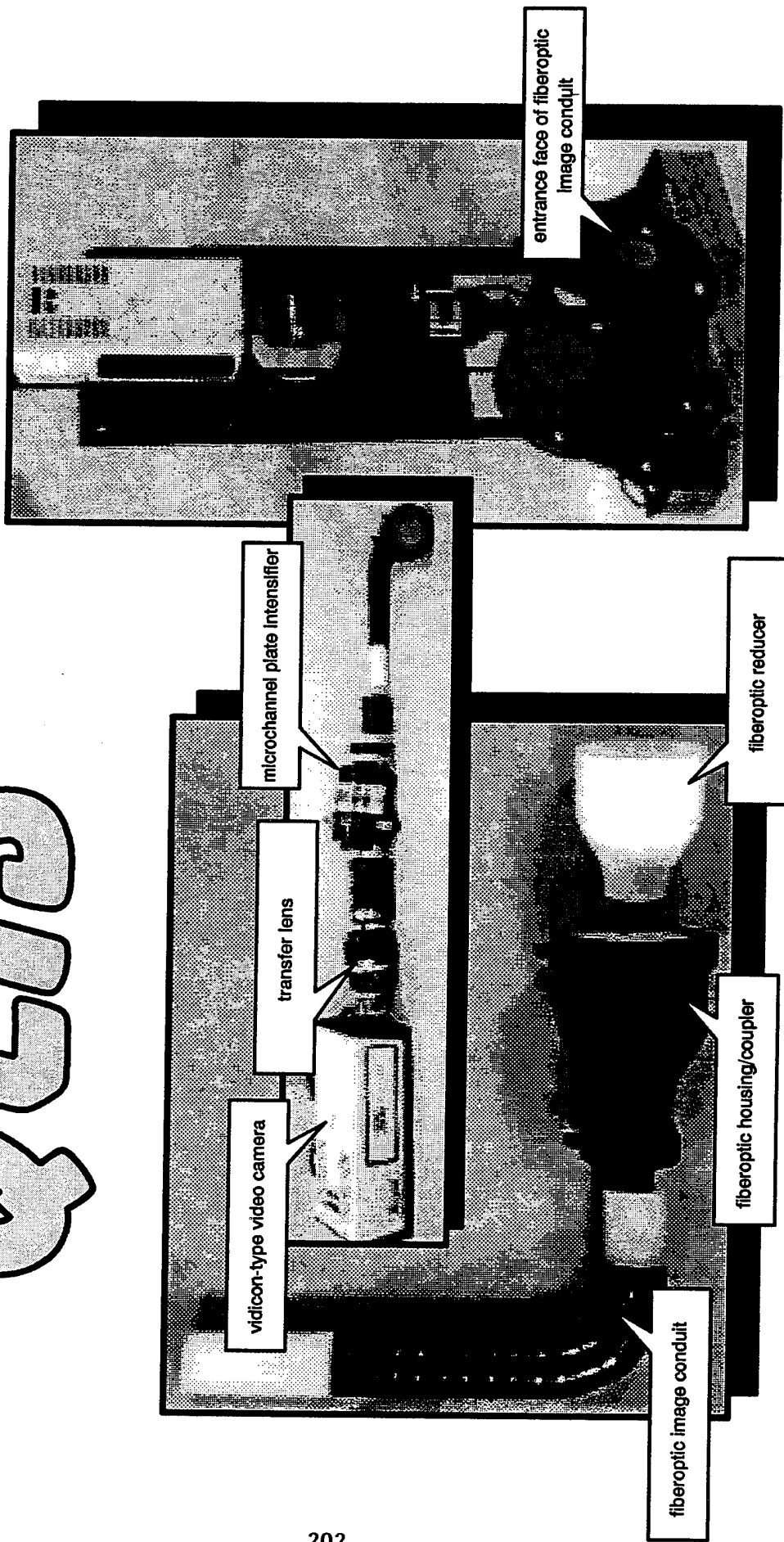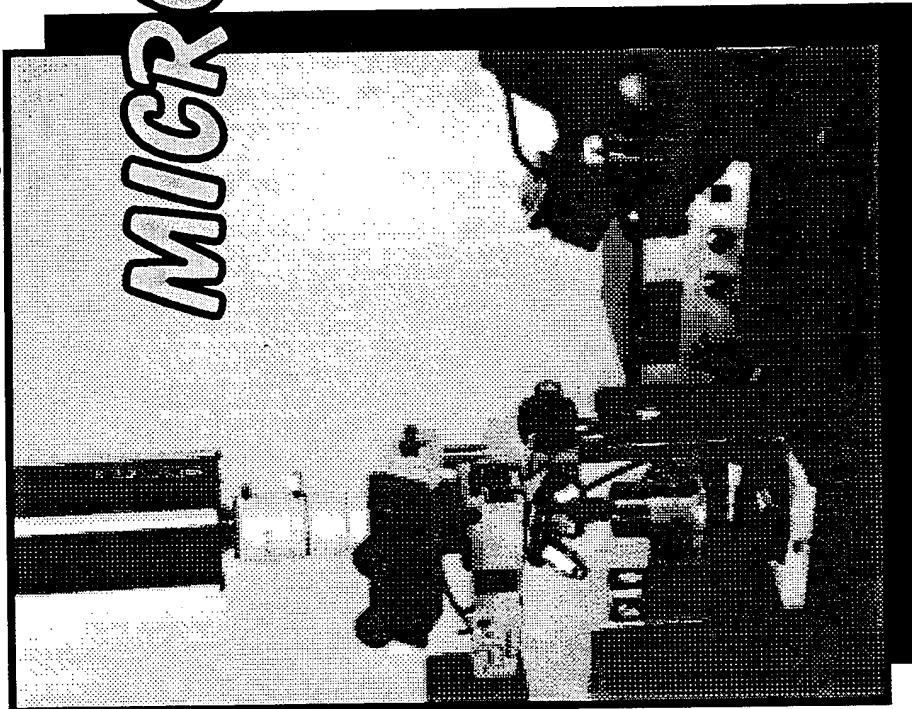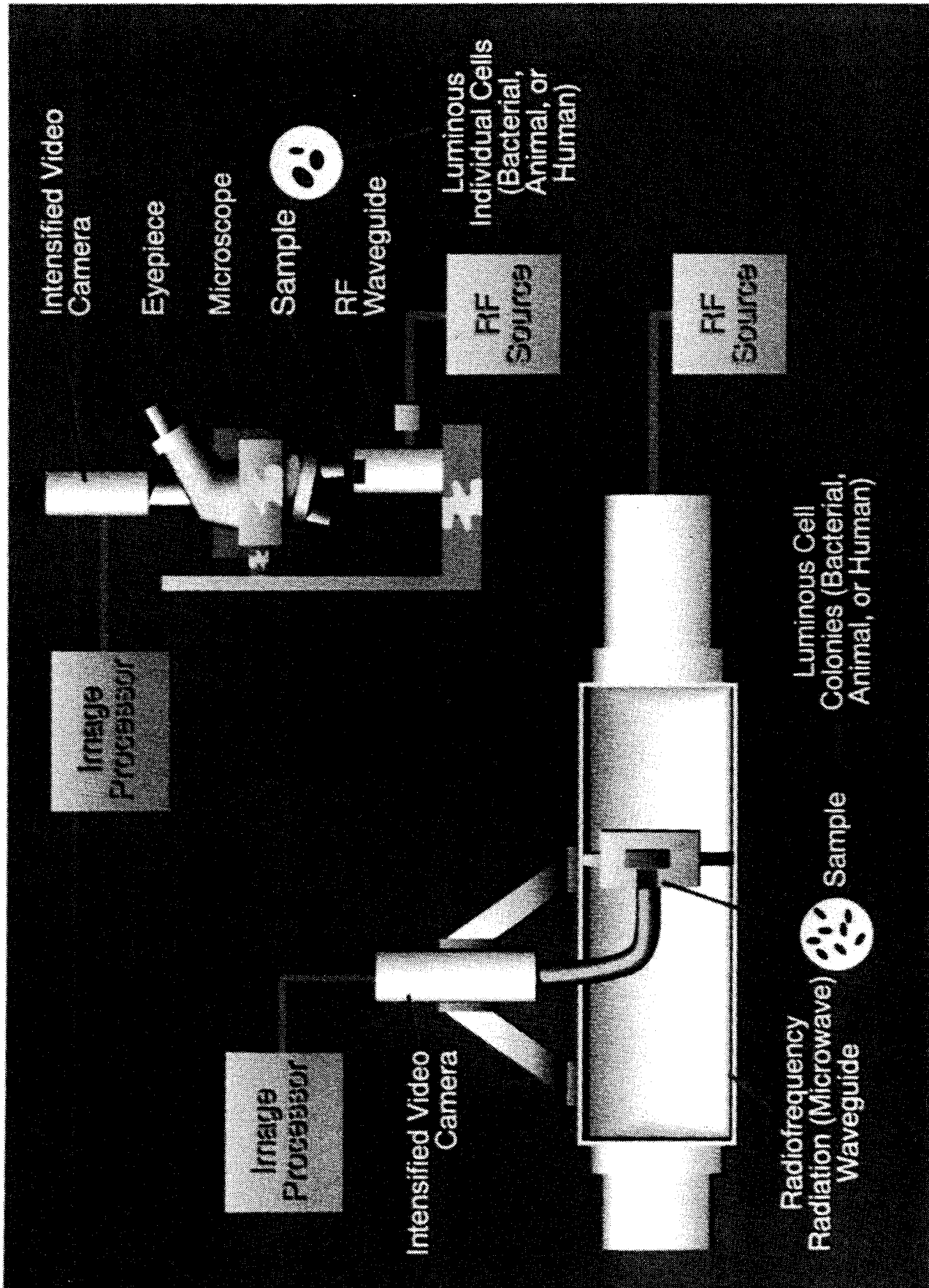
M-QLIS

MICROSCOPE-QLIS

- Olympus post-mounted microscope
- ITT intensified video camera
- NIST traceable calibration standard
- Gateway 2000 486/33 PC-AT computer
- 650 MB erasable optical drive
- 640x480 pixel frame grabber
- IMAGE PRO PLUS™ software
- PNL developed custom RF radiator

Intensified Video Camera

Eyepiece

Microscope

Sample

RF Waveguide

Luminous Individual Cells (Bacterial, Animal, or Human)

RF Source

RF Source

Image Processor

Image Processor

Intensified Video Camera

Luminous Cell Colonies (Bacterial, Animal, or Human)

Sample

Radiofrequency Radiation (Microwave) Waveguide
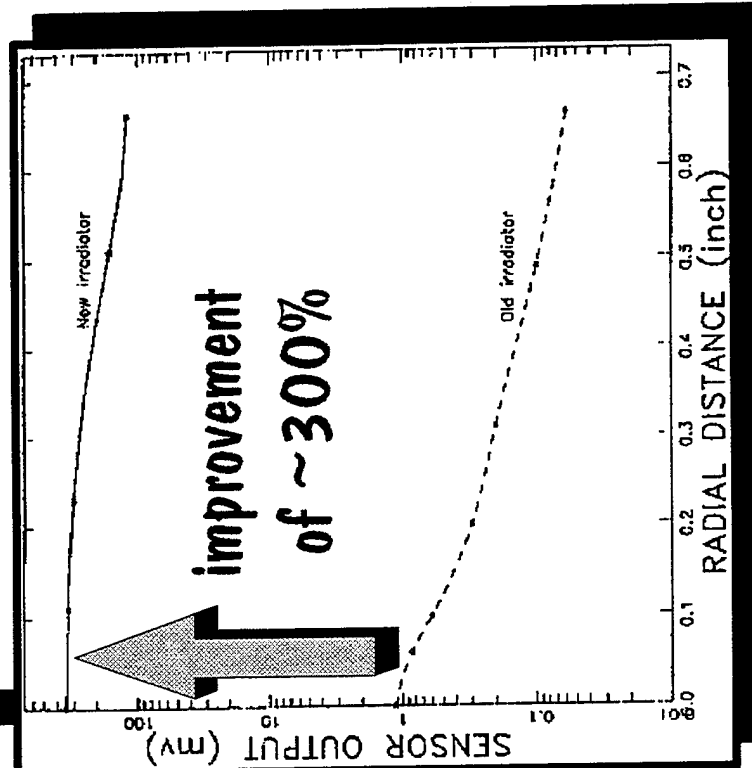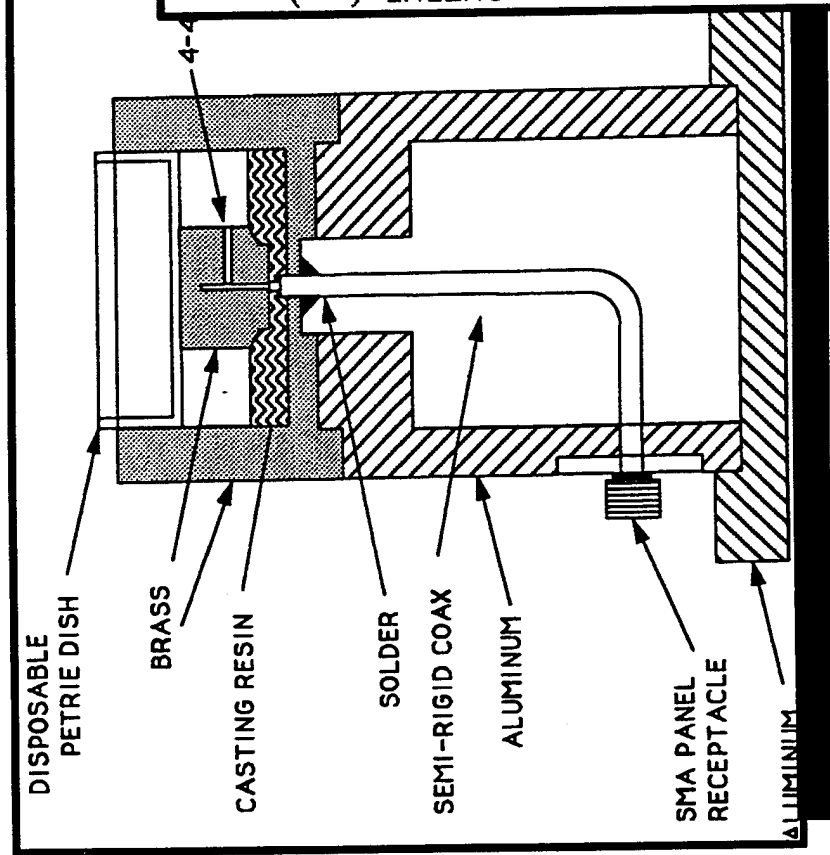
M-QLIS
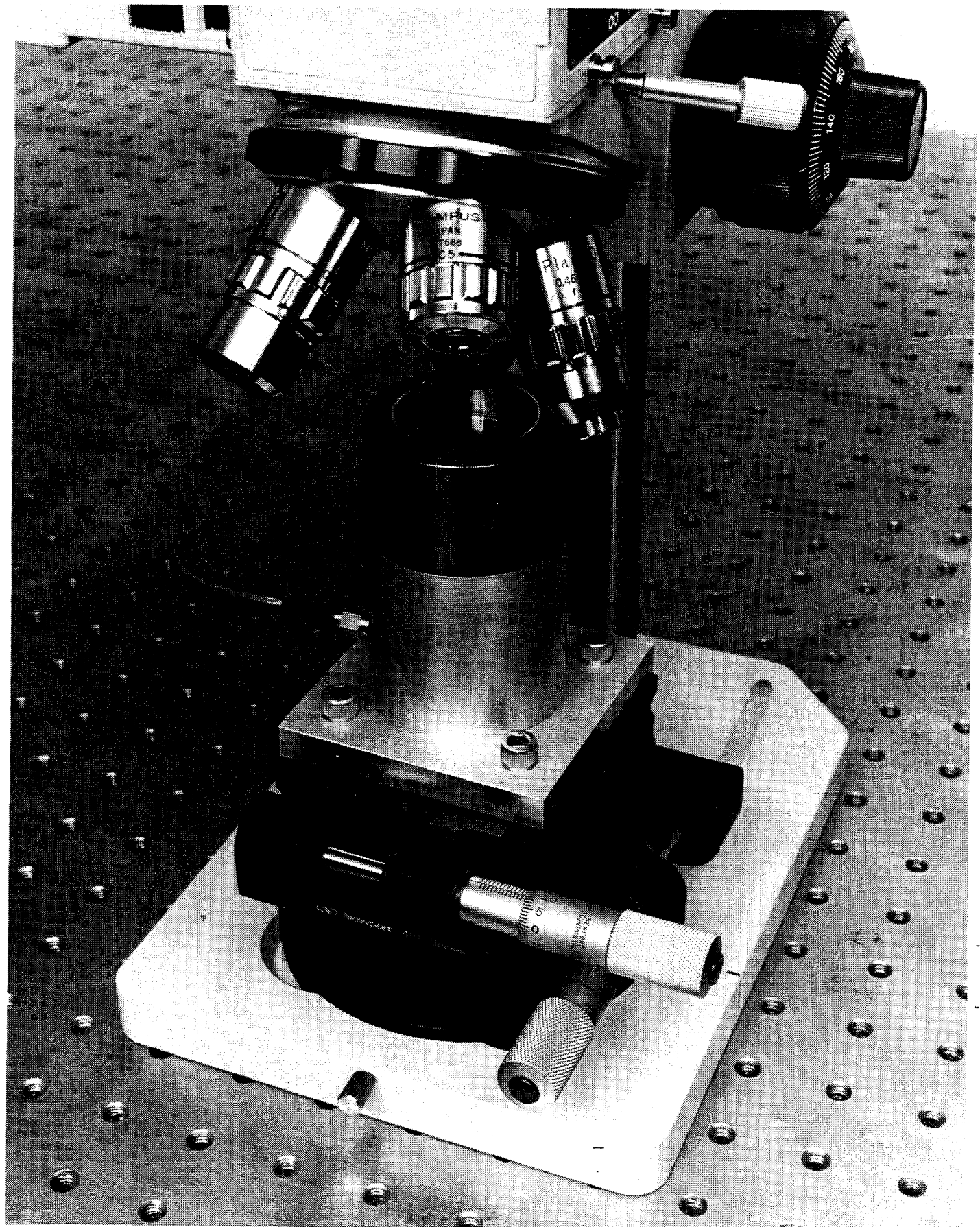
RADIOMETRIC DETECTION LIMIT

2.5X	8×10^7 PHOTONS/SEC/CM^2
5X	1×10^8 PHOTONS/SEC/CM^2
10X	2×10^8 PHOTONS/SEC/CM^2
20X	9×10^8 PHOTONS/SEC/CM^2
50X	2×10^{10} PHOTONS/SEC/CM^2

M-QLIS

PNL DEVELOPED CUSTOM RADIATOR

improvement of ~300%

SENSOR OUTPUT (mv)

RADIAL DISTANCE (inch)

New irradiator

Old irradiator

DISPOSABLE PETRIE DISH

BRASS

CASTING RESIN

SOLDER

SEMI-RIGID COAX

ALUMINUM

SMA PANEL RECEPTACLE

ALUMINUM

L-QLIS...
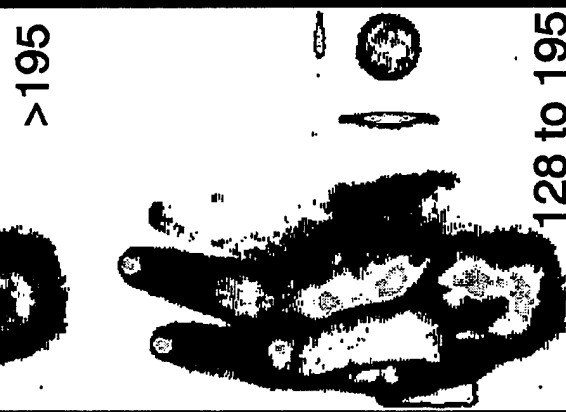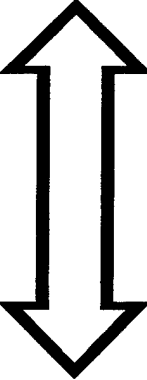
LARGE-SCALE QLIS

ITT INTENSIFIED CAMERA
FUJINON 25 MM. F/0.85 LENS

crb/EOS/11.20.92
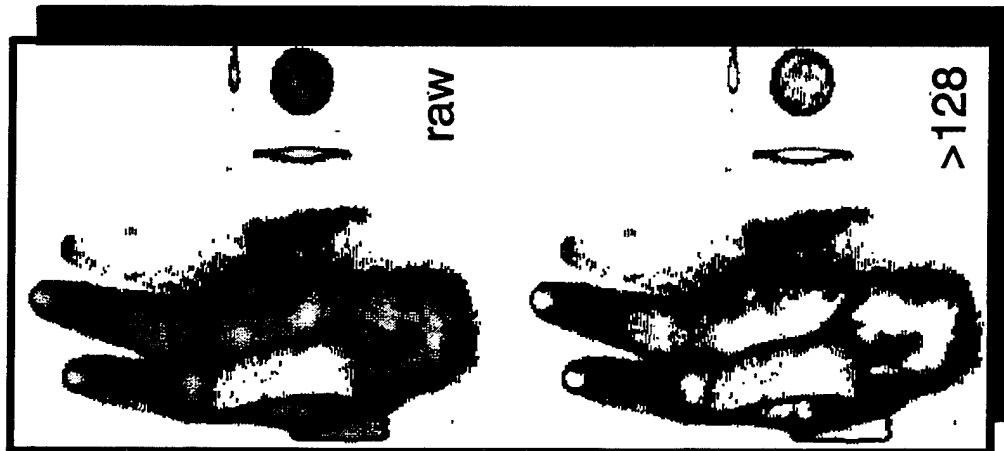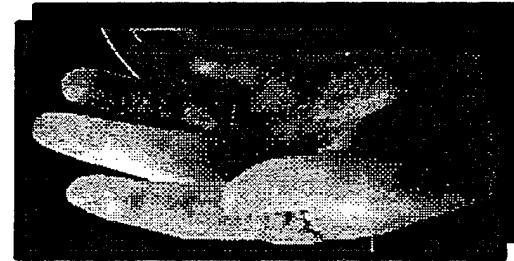
L-QLIS – IMAGE RADIOMETRY

LOW LIGHT THRESHOLDED

REFLECTED LIGHT

>195

128 to 195

raw

>128
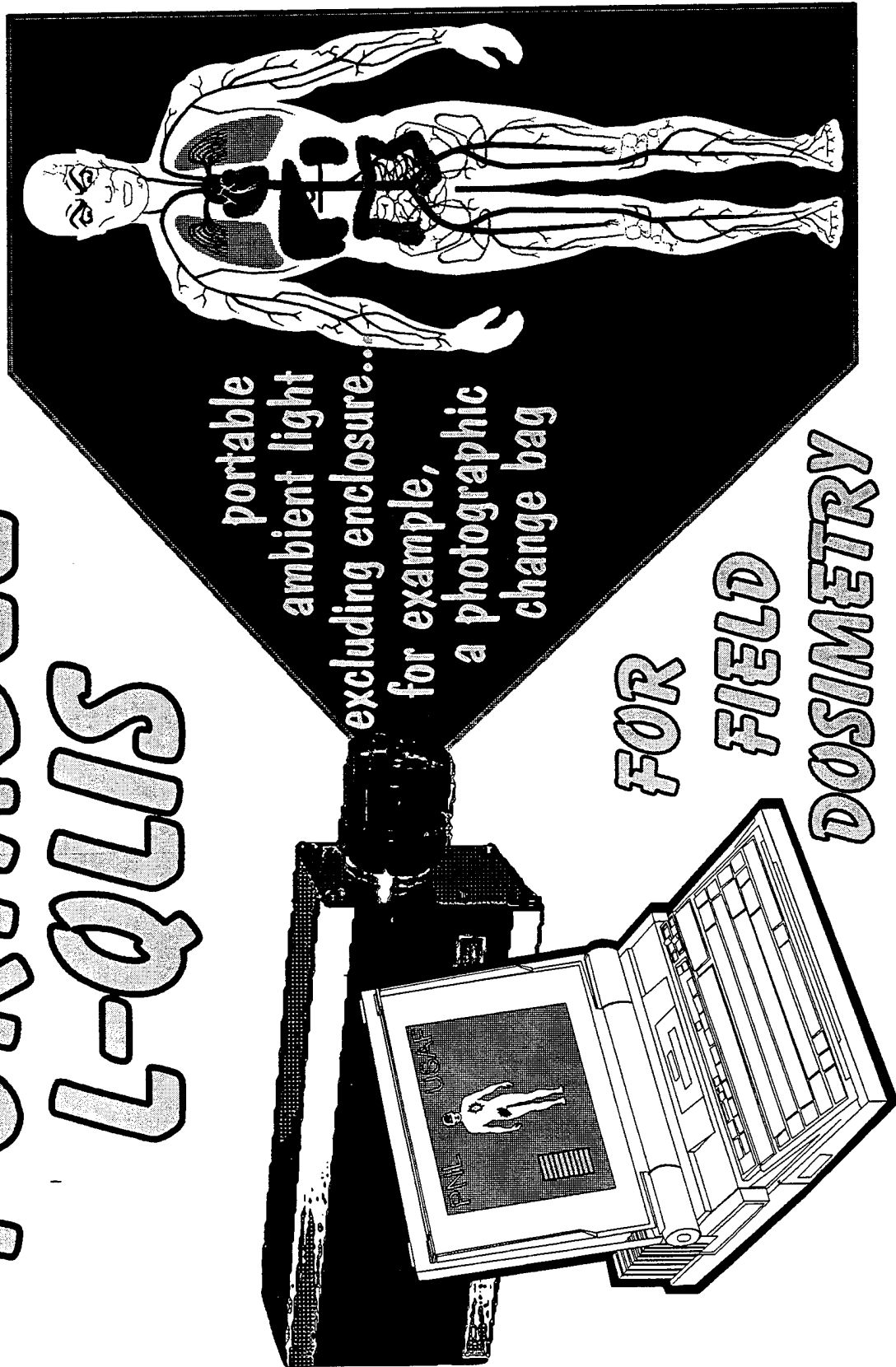
**PORTABLE L-QLIS**
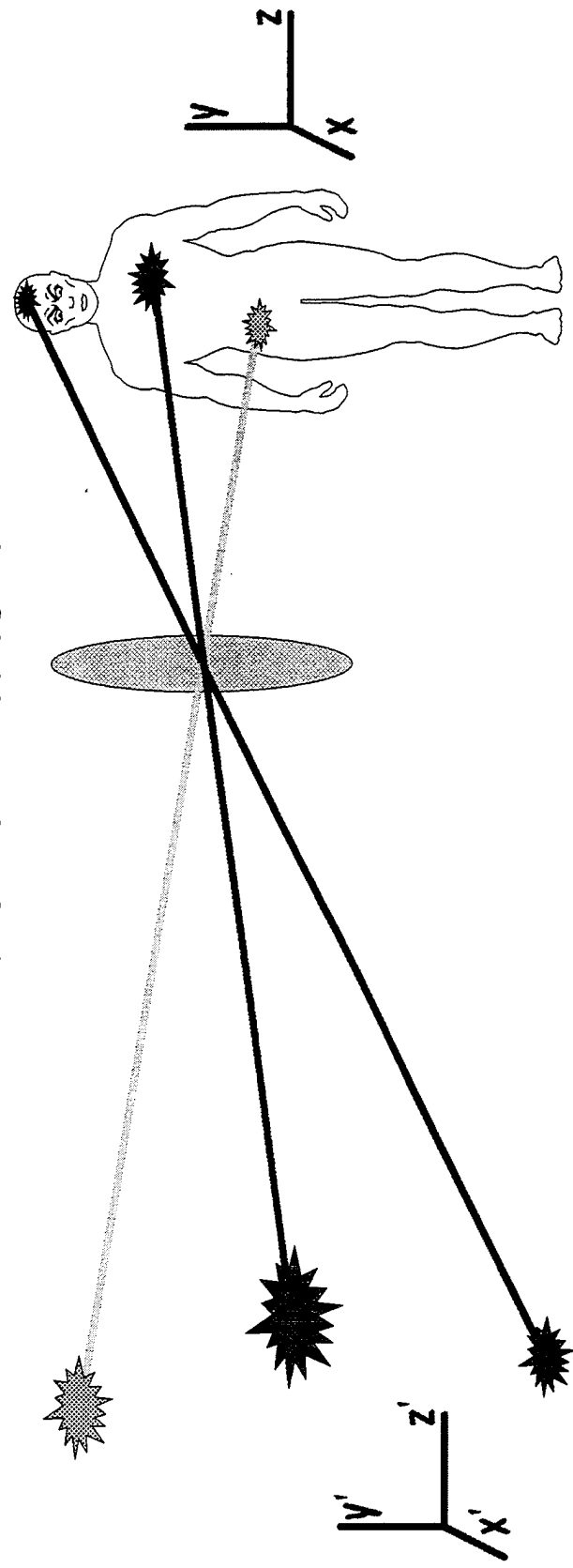
portable ambient light excluding enclosure... for example, a photographic change bag

FOR FIELD DOSIMETRY

L-QLIS...3-D

to map
volumetric chemiluminescence distributions
into a three-dimensional dataset

L-QLIS...3-D

* multiple cameras (IMAGE ANALYST™ on Macintosh)

* focal scanning with defocus removal (MICROTOME™)

* rotating phantom, single camera

* other tomography?
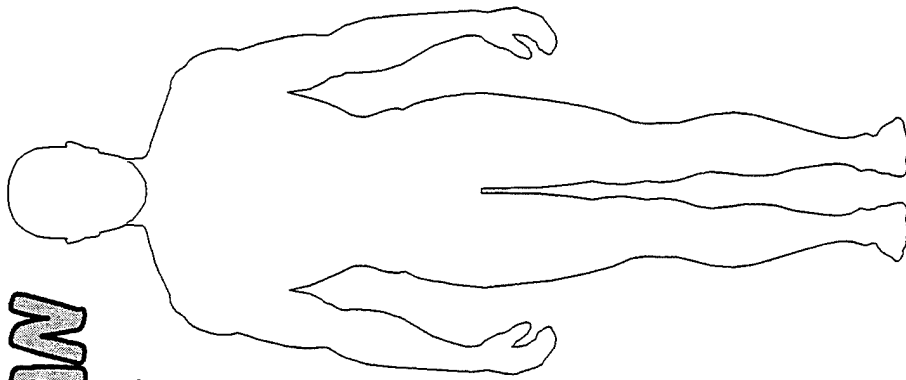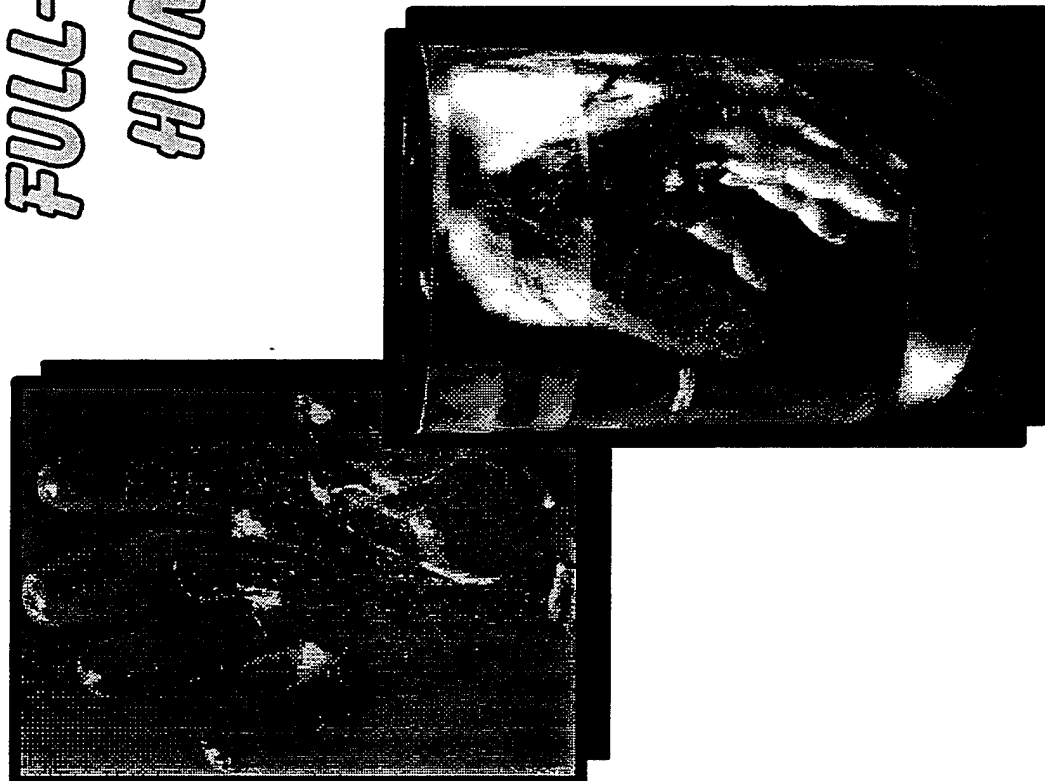
PHANTOMS
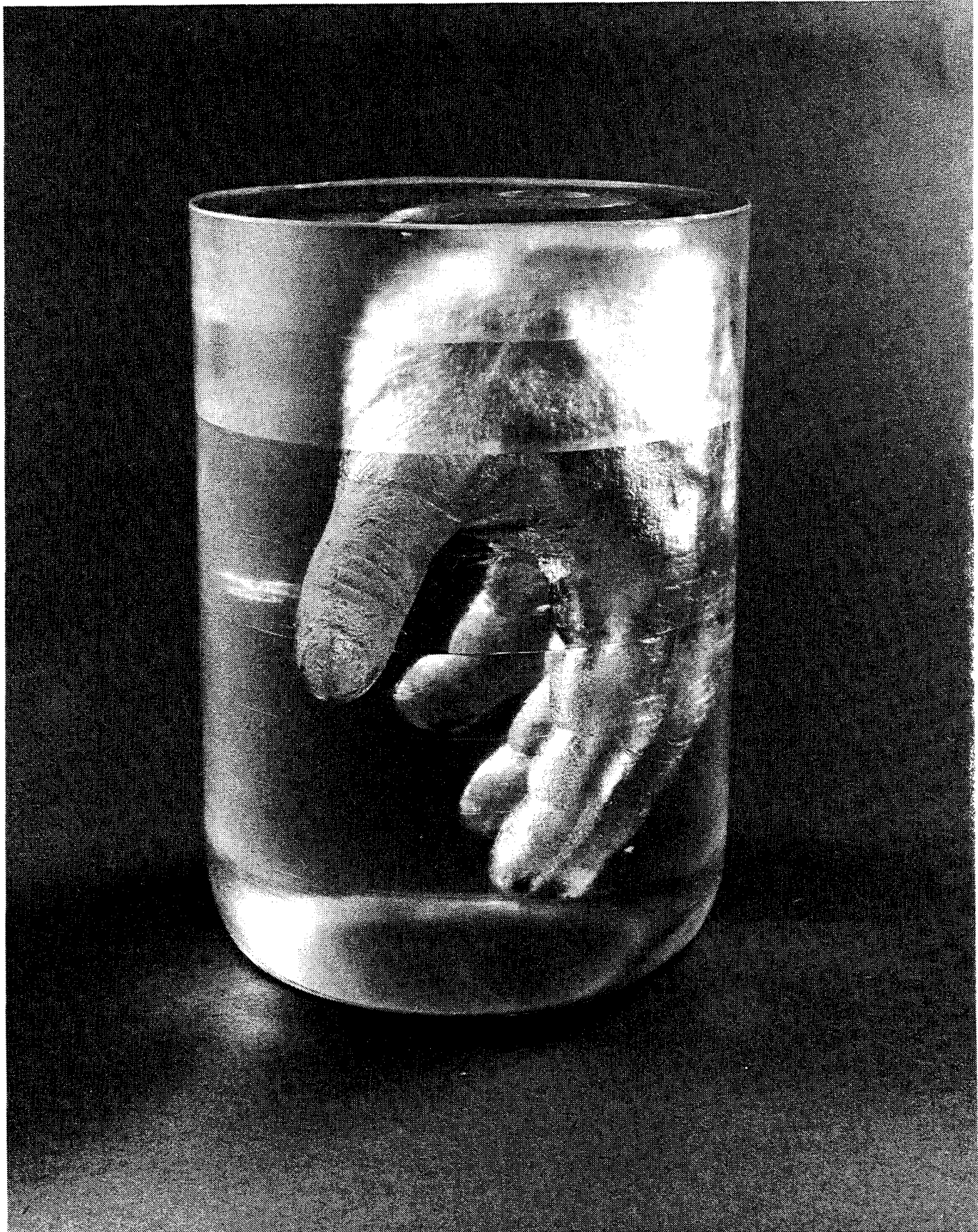
FULL-SIZE HUMAN

HUMAN PARTS
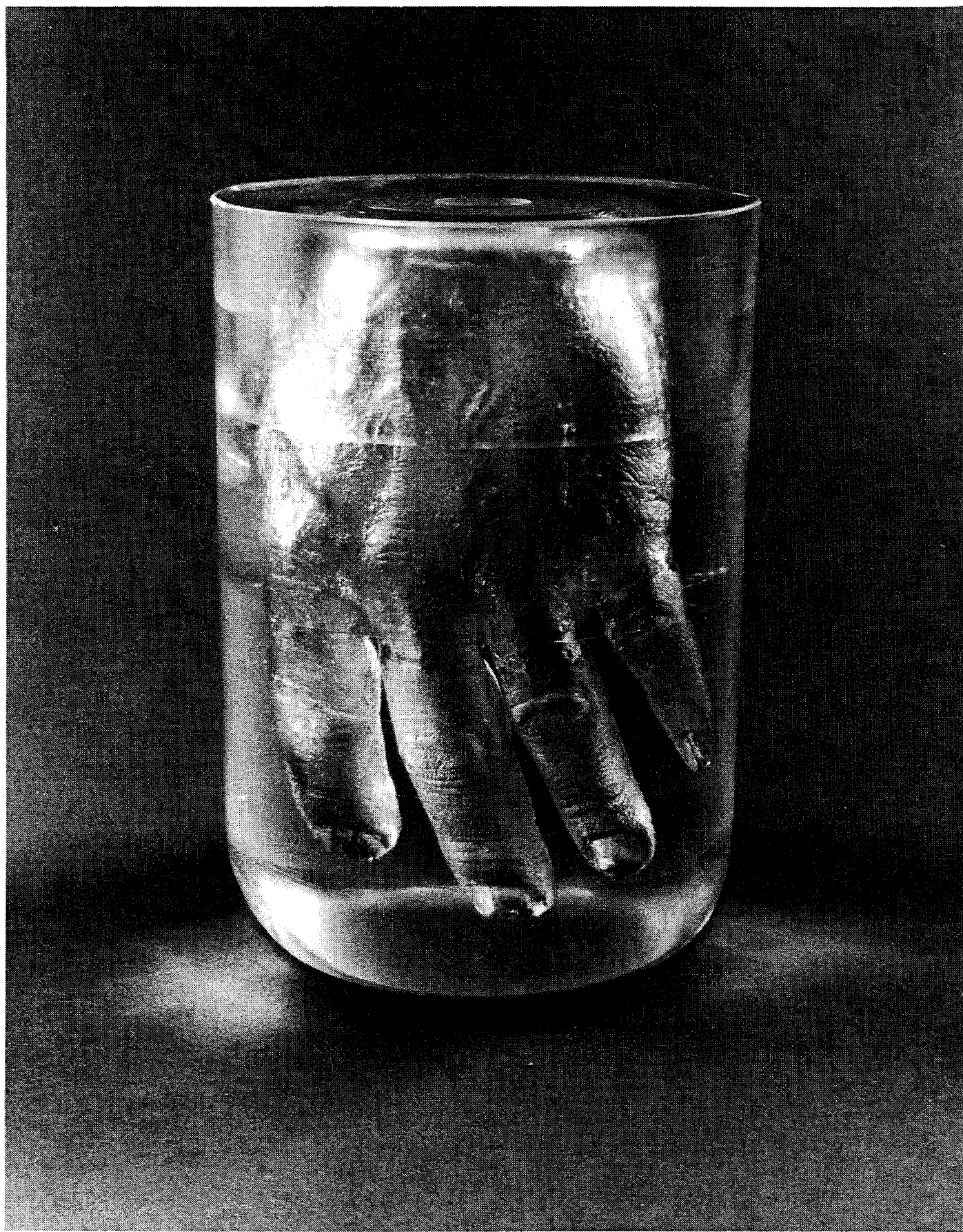
RATS
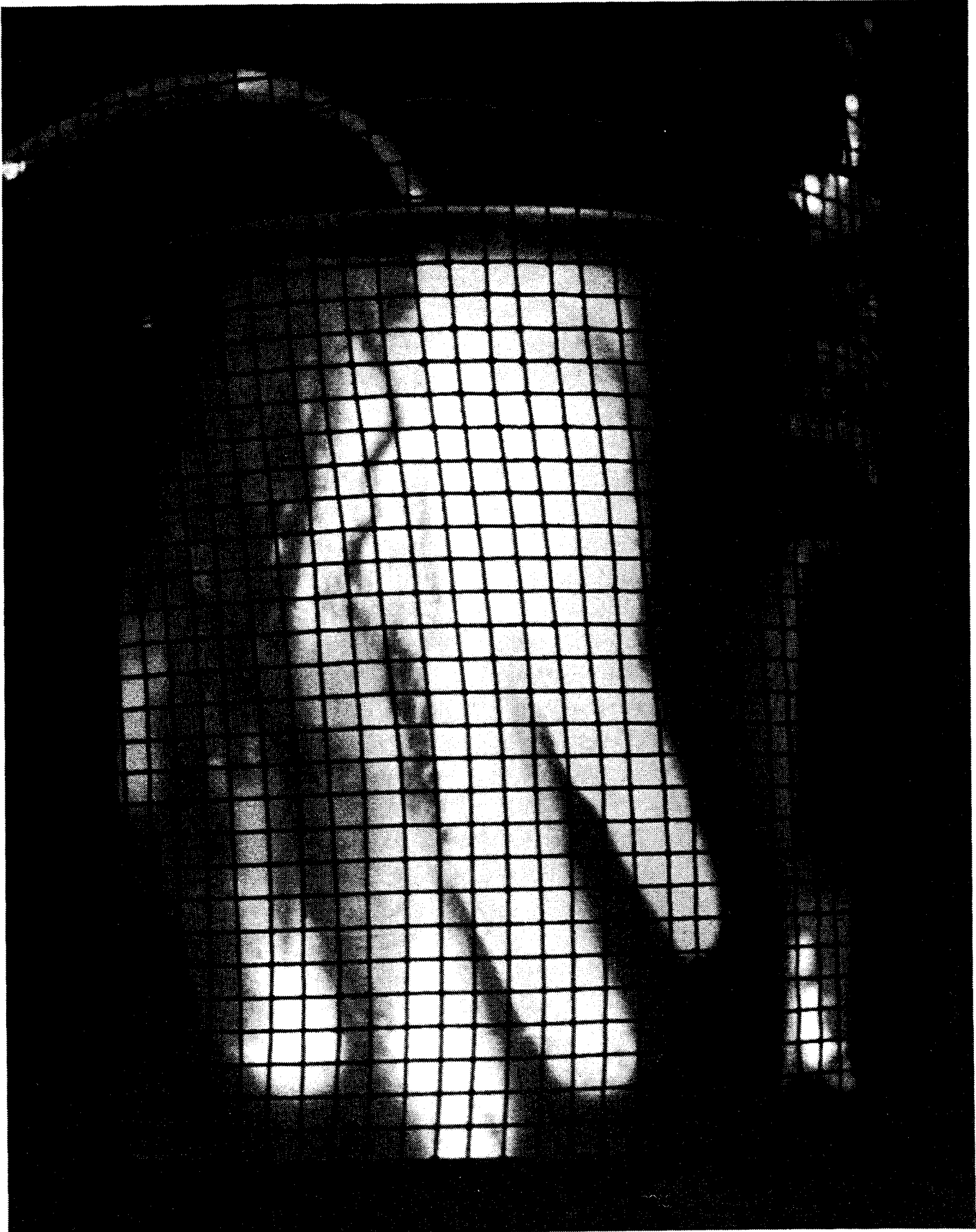
CHIMP
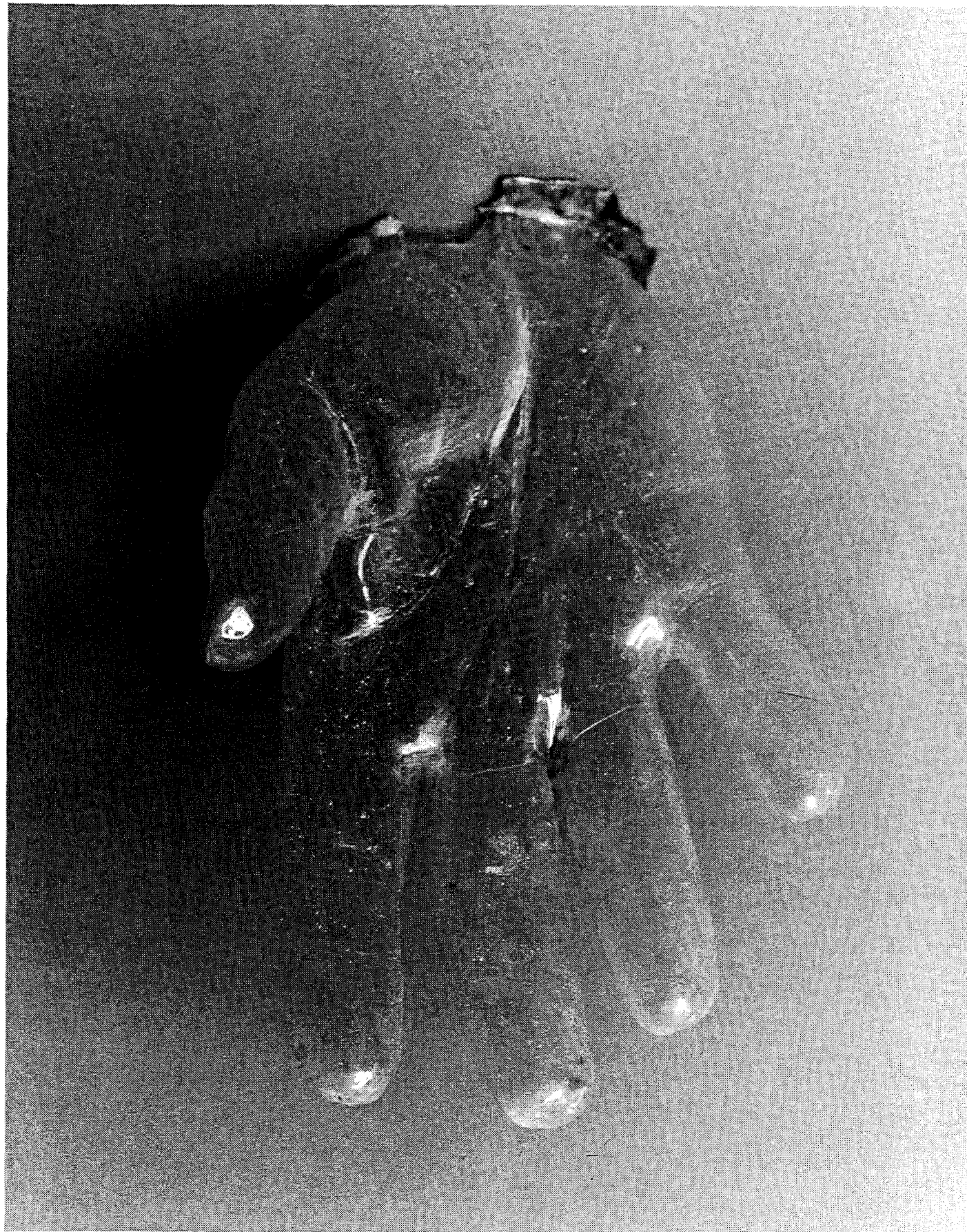
OTHERS?

PHANTOMS
MATERIALS

* requirements...
  chemically inert to DALM
  optically/RF transparent and non-scattering

* tested...
  cyanoacrylate butyrate
  polyethylene teraphthalate
  cellulose acetate butyrate
  epoxies
  silicone

* using...
  DOW 334 epoxy
  Texaco Jeffamine 403 hardener

crb/EOS/12.4.92

219

PHANTOMS

CURRENT/NEAR FUTURE

* thin (2-3 mm) shells in general
* human hand(s)
* human head
* human limbs
* rat (with and without imbedded skeleton)

UPGRADES

* camera sensitivity
* camera dynamic range (12-16 bit)
* RF/thermal/optical system integration
* laptop portability
* computing power/speed
* networking

SUMMARY...

✳ **QLIS** - delivered, upgraded, in use

✳ **M-QLIS** - delivered, improvement required

✳ **L-QLIS** - delivered

✳ **Phantoms**

    thick hand delivered; thin hand delivered

    mid-thickness hand imminent

    head or rat next

✳ **RF M-QLIS Radiator** - delivered

✳ **Upgrades** - computers, peripherals, cameras

✳ **Current Development** - 3-D, portable, integration

RFR DOSIMETRY WORKSHOP

REVISED AGENDA

WEDNESDAY, DECEMBER 9, 1992

9:00 a.m.   DISCUSSION ON WORKING GROUP TOPICS, SUGGESTED INITIAL COMPOSITION OF GROUPS, AND POSSIBLE APPROACHES.

9:30 a.m.   BREAK INTO WORKING GROUPS.
EACH WORKING GROUP TO ELECT A MODERATOR AND A RAPPORTEUR.

9:45 a.m.   BRAINSTORMING BY EACH WORKING GROUP ON FUTURE RESEARCH DIRECTIONS.

10:30 a.m.   Break

10:45 a.m.   FORMALIZATION OF BRAINSTORMING BY EACH WORKING GROUP INTO PREPARATION OF WRITTEN RECOMMENDATIONS.
(Includes what sort of experimental validation, testing, and verification, etc., is required.)

11:45 a.m.   Lunch at Brooks Club.

1:00 p.m.   VERBAL PRESENTATION OF RECOMMENDATIONS OF EACH WORKING GROUP BY RAPPORTEURS.

2:00 p.m.   DISCUSSION AND INTEGRATION OF REPORTS BY GROUP AS A WHOLE.

3:00 p.m.   CONCLUSION OF WORKSHOP.
Transportation from Brooks AFB To San Antonio Airport.

RFR DOSIMETRY WORKSHOP

SUGGESTED WORKING GROUPS

1. MODELLING

TADEUSZ BABIJ

JEFFREY BLASCHAK

PETER DIMBYLOW

CARL DURNEY

ALAN FENN

CAMELIA GABRIEL

OM GANDHI

ARTHUR GUY

MARK HAGMANN

WILLIAM HURT

~~GREGORY KRIEGSMANN~~

PETER PETROPOULOS

WESLEY SHELTON

MARIA STUCHLY

DENNIS SULLIVAN

2. PHYSIOLOGICAL RESPONSE

ELEANOR ADAIR

RICHARD ALBANESE

DAVID ERWIN

KENNETH FOSTER

~~JOHNATHAN KIEL~~

SALLY NUNNELEY

MICHAEL REPACHOLI

3. INTERFACE AND GRAPHICAL PRESENTATION.

CHARLES BATISHKO

C-K CHOU

KEN JOYNER

JAMES LIN

RICHARD MAGIN

RICHARD MEDINA

JOHN PEIFER

KURT STAHL

JAMES TOLER

WORKING GROUP 1

MODELLING

General Recommendations

1.   A two-year effort to develop a fifth edition of the dosimetry handbook based on new developments in dosimtery made since the publication of the fourth edition. This edition would be based on current state of the art techniques. It would include both a published bound copy and software. The handbook would consist of two parts, one part for researchers, a second part for others, such as public health workers. We estimate the effort would require about two year's effort and would cost about $400 to $500k.

2.   A research program that would advance the state of the art, leading to a sixth edition (and possibly later editions). Specific recommendations for this research are:

A. modeling
   1. sources
   (a) identify, characterize, and model EM sources, including transient and pulsed field sources, occupational exposures and new technologies (wireless).
   2. methods
   (a) identify the most effective modeling methods for various frequency ranges and types of exposure and verify codes
   (b) develop (user-friendlyr two or three methods (among them FDTD), determine the range of applicability and error bounds
   (c) consider parametric studies
   (d) implement conformal cells
   (e) nonlinear effects
   (f) develop models that combine SAR calculations with heat transfer.
   (g) include self tests of the software
   3. computation
   (a) model exposure to complex spatial and temporal fields in selected occupational and envioronmental situation including bodies in motion, portable transmitters, applicances, surroundings.

B. Database
   Develop public-domain (e.g. Internet) data base consisting of (but not limited to: .
   * full-scale anatomical models of man and animal
   * SARs for fetuses
   * tissue permittivity vs frequency
   * basic dosimetry curves (average SARs)
   * phantom formulas
   * numerical codes
   * bulletin board with new software

C. Experimental
   Determine SARs, E field, temperature in a few selected realistic models.

D. Phantoms

Review the existing data and develop as necessary appropriate phantoms for EM and thermal modeling

E. Permittivity

Compile the existing data.
Identify what is missing.
Perform needed measurements.
Present the data in the frequency and time domains for modeling.

F. Models

Develop computer models of man, woman, child and experimental animals. The models should be compatible with the numerical codes and also suitable for thermal modeling.

G. Instrumentation.

Develop small E-field probes suitable for wide-band and in-vivo measurements.
Develop instrumentation to measure induced currents and their distribution and shock hazards under CW and pulsed conditions.

H. Graphics

Develop user-friendly visualization techniques to display simulultaneously anatomical details and computed fields and to display fields while performing FDTD calculations.

Working Group #2

Physiological Response Modelling

Goals
   To provide models of human responses to EM fields (DC to 300 GHz).
      a. General design of experimental studies (power, sample size, quality control etc.)
      b. Validation and verification (incorporation of animal data, extrapolation).

Projects
   1. Model selection/specialization
         1a. Endpoint selection.
         1b. Computational complexity.
         1c. Applications and scope.
         1d. Thermal effects on electromagnetic deposition.
         1f. Accomodate ambient conditions (temperature, humidity, work, metabolic rate etc.)
         1g. Accomodate field specific factors with physiological impact.
         1h. Develop rules of thumb for temperature rise and thermal time constants, thermal gradients and uncertainties in modeling.
         1i. Expert system to assist with model selection and use.
         1j. Hot links to biomedical data bases.
   2. Not necessarily thermal models
         2a. Replication of non-thermal bioeffects.
         2b. Long term animal experiments to assess cancer production and co-promotion.
         2c. Understand electromagnetic coupling: coherent molecular motion to thermal transition.
         2d. Startle and shock.
         2e. Sensory organs, nervous system and behavior.
   3. Thermal modeling
         3a. Basic thermal 70 kg man.
               3ai. Sensory organs, nervous system, behavior (thresholds, systemic and/or regional)
               3aii. Thresholds for responses: thermoregulatory behavior/thermal damage.
               3aiii. Identify hot spots, micromodel key sites, prevent injury, dose tumors
               3aiv. Additional loads and combinations of stresses.
         3b. Special thermal models
               3bi. Effects of drugs
               3bii. Fetal effects
               3biii. Regions of special sensitivity
               3biv. Partial body exposure
               3bv. Effects of age, body size, body composition, gender,

227

acclimatization, people with thermal
                                    compromize
                    3bvi.   Microthermal modeling
                    3bvii. Effects on implanted devices, RFR local
                                    hot spots
                    3bviii. Influence of fever and other illness.
                    3bix.   Tissue repair.
4. Applications.
            4a. Hyperthermia
            4b. RF re-warming
            4c. Tissue repair
            4d. Pound proposal
            4e. Thermal tolerance by RF treatment
            4f. Design of RFR bioeffects studies
            4g. Hot links between models and bieffects database.

Working Group 3

ELECTRONIC EDITION OF DOSIMETRY HANDBOOK

I.   Introduction

II.   How to Use

III.   Tutorials

            Measurements
            EM Basics
            Dielectrics
            Hypertext

IV.   Modelling

V.   Physiological Responses

VI.   Graphical Dosimetry

        Appendices

DEFINE DESIRED OUTPUT

        Who will users be?
             BEM community
               Medical
               Environmental
               Research
               Occupational
               Legal
        User friendly
        2D/3D contours
        Color Coding
        Variety of computers
        Realtime
        Zooming
        User responsive

DATABASE

Anatomical Models
Existing data
Experimental/Theoretical
Standards
    Graphical presentation
    Data format
    Grey scales
Distribution
Taxomony

DATA ALGORITHMS

Formulas
Calculations
    SAR
    Safety
Interpolation/Extrapolation
PW vs CW
Scaling
Expert Systems
Special Purpose Applications
    Building layout vs fields

INTERFACE AND DISPLAY

Hardware
    Displays
    Platform
Software
Operating System Independent

DATA DISTRIBUTION

Database Central/Manager
Networks
CD's
Hardcopy
ROM

A.   Platform-Independent CD-ROM

   o Exportable format
    - o Text
      o Images
      o Table
      o Formulas (Spread sheets)
   o Viewers
   o Index

B. Interactive Tool Kit

o Graphics Applications Templates
  o 2D graphs/charts
  o 3D geometry
  o 3D volume
  o animation

C. Long Term

o Advanced Tool Kit
  o Expert System
  o Automated Design Tool
o Network
o Remote Processing